UNIVERSITY OF SOUTHAMPTON

THE NUMERICAL STUDY of 3-DIMENSIONAL LAMINAR HYPERSONIC BLUNT FIN INTERACTIONS

By

Sameera Jayanishka Vithana

Ph.D. Thesis

SCHOOL OF ENGINEERING SCIENCES

June 2007

UNIVERSITY OF SOUTHAMPTON

ABSTRACT

SCHOOL of ENGINEERING SCIENCES

DEPARTMENT of AERONAUTICS and ASTRONAUTICS

Doctor of Philosophy

THE NUMERICAL STUDY of 3-DIMENSIONAL LAMINAR HYPERSONIC BLUNT-FIN INTERACTIONS

By Sameera.J.Vithana

The three-dimensional numerical simulation of a Mach 6.7 perfect gas, with a unit Reynolds number of $7.6 \times 10^6 m^{-1}$, over several configurations of a blunt-fin attached to a flat plate are carried out. The resulting interference flowfield is reported in this thesis.

The laminar Navier-Stokes code developed by Navarro-Martinez [47] has been modified to solve any general three-dimensional problem, and the complete Navier-Stokes equations. The numerical scheme is operator split, allowing independent numerical schemes to be used on each of the individual contributions to the Navier-Stokes, which can be combined later to advance the entire solution in time. The inviscid part uses a first order Godunov method with a HLLC approximate Riemann solver; second order accuracy is achieved through the MUSCL approach. The viscous contribution is modeled by a centered difference scheme. An iterative matrix solver is used to advance the implicit solution in time. To handle large three-dimensional grids, the code is implicit and run on a parallel computer cluster.

The three-dimensional results from the various blunt-fins simulated show a complex rich three-dimensional structure, with several horseshoe vortices formed within the separated flow. Extremely large heat transfer rates have been measured along the path of these vortices on the plate surface, and on the leading edge of the unswept blunt-fin. In particular cases heat transfer rates as high as $(h/h_u) \simeq 60$ were measured for the $5mm$ diameter fin. The $5mm$ fin results show remarkable similarity to the experimental results obtained by Schuricht [53]. The results obtained using a swept fin, and a fin of doubled fin diameter also show good agreement with the trends observed by Schuricht and others for a laminar interaction.

Acknowledgements

As usual, the author of this work is one, but many are the people who in different ways, and at different degrees, contributed to the finalization of this thesis. I would like to thank some of the many people who made this work possible.

First of all I would like to thank Prof. Tutty and Dr. Roberts, for giving me the opportunity to work with them on this project. Their guidance and enthusiasm have been essential in overcoming the obstacles that I found myself facing sometimes. A special acknowledgement goes to Dr.Martinez for his continuous support, willingness to share his knowledge with me, and above all, patience in teaching me the basics of the job. Without him I would still be running my laminar calculations.

On a more personal note there are many more people that, most likely unknowingly, have helped me finish my studies and grow as a person. I wish to thank my best friend *Tariq Dawood*, for helping me get through the difficult times, and for all the comraderie, entertainment, and advice you gave.

I wish to thank my entire extended family for providing a loving environment for me during this period; especially my sisters *Lokku Akka* and *Chuti Akka*, brother-in-laws *Sanjeeva Wimalasena* and *Viji Wickramasinghe*, and all others for being particularly supportive. I would also like to give out a special thanks to my fianće *Tharaka Chandrakumar*, whose patient love, emotional support and advice enabled me to complete this work.

Lastly, and most importantly, I wish to thank my parents, *Rathna Vithana* and *Sujatha Vithana*. They raised me, supported me, taught me, and loved me. And with that in mind I wish to dedicate this thesis to my loving dearly departed mother *Sujatha Vithana*.

Contents

List of Tables

List of Figures

Nomenclature

List of Common Symbols

a	Higher order terms in Richardson extrapolation *Chapter 3*
a_1, b_1 and b_2	Pressure coefficients in a strong and weak interaction
$\mathcal{A}$	Jacobian matrix of a transfomation
b	Constant in Richardson extrapolation *Chapter 3*
c	Sound speed
$\boldsymbol{C}$	Constant in Richardson extrapolation *Chapter 3*
C	Chapman-Rubesin constant
$C^{'}$	Stretching factor in z
C_p	Constant pressure expansion coefficient
C_v	Constant volume expansion coefficient
C_f	Skin Friction Coefficient
$\mathcal{C}_{BC}$	Boundary condition matrix
CFL	Courant number used in the computation of Δt
CFL_{max}	Maximum CFL number
D	Diameter of blunt-fin
DE	Discretization error in Richardson extrapolation *Chapter 3*
E	Total specific energy
f	Flux function
$F_{1,2..}$	Focus point
F, G, H	Vectors of inviscid fluxes
F_v, G_v, H_v	Vectors of viscous fluxes

$\mathbf{F}$	Inviscid flux vector (F, G, H)
$\mathbf{F}_v$	Inviscid flux vector (F, G, H)
$\hat{F}_k$	Space averaged flux across k-th surface
$\tilde{F}_k$	Space averaged flux across k-th surface
h	height
h_a	Minimum height of fin required to produce asymptotic behaviour
h_x, h_y	x and y components of height from cell centre
h	Heat transfer coefficient
h_u	Undisturbed Heat transfer coefficient
$\mathbf{K}$	Hypersonic similarity parameter, Gladstone-Dale coefficient
$\mathbf{I}$	Identity matrix
Kn	Knudsen Number
L	Length
L_{ref}	Characteristic reference length of the body
M	Mach number
m_{N_2}	Molecular mass of Nitrogen
n	Nodal point
$\mathbf{n}$	Normal vector of surface
N	Number of cells in the system
$\mathbf{N}$	Nodal point
N_f	Number of faces in one polyhedral
p	Pressure
Pr	Prandtl number
q_w	Heat transfer
r_ρ	Ratio of densities
$\mathbf{R_{1,2..}}$	Reattachment line
R	Universal gas constant
R_N	Gas constant for Nitrogen
Re	Reynolds Number
Re/l	Unit Reynolds Number
Re_{trans}	Transitional Reynolds Number
Res_ρ	Density residual

Res_A	Residual of the matrix solver
s	Saddle point
S	Surface Area
ΔS_k	Area of k-th face of the cell
$\mathbf{S}$	Saddle point
$\mathbf{S_{1,2..}}$	Separation line
S_L, S_R	Left and right sonic wave speeds
S_M	Contact wave speed
S_t	Stanton Number
t	Time
Δt	Time step
Δt_{CFL}	Inviscid time step
Δt_C	Viscous time step
T	Temperature
u, v, w	Velocity components in x, y, z
U	Vector of conserved variables
U_∞	Freestream velocity
$\mathbf{v}$	Velocity vector
V_i	i-th cell volume
V_T	Volume of tetrahedra in cell
x, y, z	Cartesian coordinates
x_p, y_p	Coordinates of cell centre
x_S	Separation distance
$\Delta x, \Delta y, \Delta z$	Cell length in each coordinate x, y, z

Greek Characters

$\alpha_1, \alpha_2, \alpha_3$	Viscous coefficients
β	Dimensionless wave number
β_1	Oblique shock angle
$\bar{\chi}$	Viscous interaction parameter
γ	Ratio of specific heats

δ	Boundary layer thickness
$\Delta\xi, \Delta\eta, \Delta\zeta$	Cell length in each coordinate ξ, η, ζ
κ	Coefficient of thermal conductivity
λ_μ	Viscosity coefficient
λ_i	Eigenvalue of the i-th conservation law or characteristic speed
Λ	Sweep of blunt-fin
ω	Vorticity $\omega = \nabla \times \mathbf{v}$
ω_n	Vorticity perpendicular to the plane $\omega.\mathbf{n}$
$\sigma, \epsilon_i/k$	Lennard-Jones parameters
$\tau_{i,j}$	Shear stress tensor
τ_w	Skin friction at the wall
$\mathcal{O}$	Truncation error
θ	Momentum thickness
θ_S	Angle of separation shock
ϕ	Rotation angle around blunt-fin
μ	Coefficient of dynamic viscosity
ρ	Density
ξ, η, ζ	Generalised coordinate system

Subscripts

a	Adiabatic state
A	Primary separation line
e	Edge of boundary layer
G	Ghost cell
i, j, k	Spatial index
r	Recovery temperature
l, r	Left/right states of the discontinuity
L, R	Left/right states of the discontinuity
S	Separation point
w	Wall quantities
∞	Freestream values

Superscripts

- $*$ Evaluated at reference temperature *Chapter 2*
- $*$ Intermediate state in the Riemann Fan *Chapter 3*
- n Time index

Abbreviations

AUSM	Advection Upstream Splitting Method
Bi-CGSTAB	Bi-Conjugate Gradient Stabilised
CFD	Computational Fluid Dynamics
CFL	Courant-Friedrich-Levy
CPU	Central Processing Unit
HLLC	Harten-Lax-van Leer-Contact
LU-SGS	Lower Upper Symmetric Gauss-Seidel
MPI	Message-Passing Interface
MUSCL	Monotone Upwind Schemes for Scaler Conservation Laws
PV	Primary Vortex
SV	Secondary Vortex
SULPICT	Southampton University Light Piston Isentopic Compression Wind Tunnel
TSL	Thin Shear Layer
TVD	Total Variation Diminishing

Chapter 1

General Introduction

The work described in this thesis concern the numerical simulation of a hypersonic interference flowfield involving a blunt-fin on a flat plate. Particular emphasis is made of the resultant heating distribution on the flat plate and blunt-fin.

The significance of hypersonic interference heating and its implications on hypersonic vehicle design was demonstrated by the catastrophic failure of a pylon on the *X-15* rocket/ramjet during the final stages of flight trials in the *X-15* program. For this particular flight a dummy ramjet was attached to the lower fuselage surface by a pylon. During hypersonic flight, a shock wave from the ramjet nacelle intersected the bow shock which had developed on the pylon, and the resulting shock/shock interaction lead to a hole being burned in to the Inconel pylon skin surface (Inconel has a melting temperature of 2800 degrees Fahrenheit) causing it to fail. It was later discovered that the pylon-fuselage interaction also caused local heating damage to the bottom surface of the *X-15* [65].

The surface of a hypersonic vehicle is basically exposed to two heating sources, energy from the propulsion system and aerodynamic heating, of which the latter is usually far more significant. Modern hypersonic vehicles generally carry sensitive electronic equipment, a valuable payload, and possibly human occupants. For example, a hypersonic vehicle traveling above Mach 10 in the stratosphere will have an adiabatic wall temperature - the temperature the vehicle surface will asymptote to in the absence of any heat loss - that exceeds 3430 °C (assuming constant γ). This is above the melting point of all metals

(e.g. the melting point of Tungsten is 3411 °C). Although it is unlikely that the surface would actually reach this temperature (due to radiative heat losses to the surroundings), it is quite clear that steps have to be taken to protect the contents of the vehicle and the structure from such temperature levels which could result in material destruction.

On a modern hypersonic vehicle there exists many regions which are prone to interference heating effects such as shock/boundary layer and shock/shock interactions which must be accounted for in the design of a vehicle,(see Figure 1.1). The areas usually of most concern are stagnation regions and areas of flow reattachment.

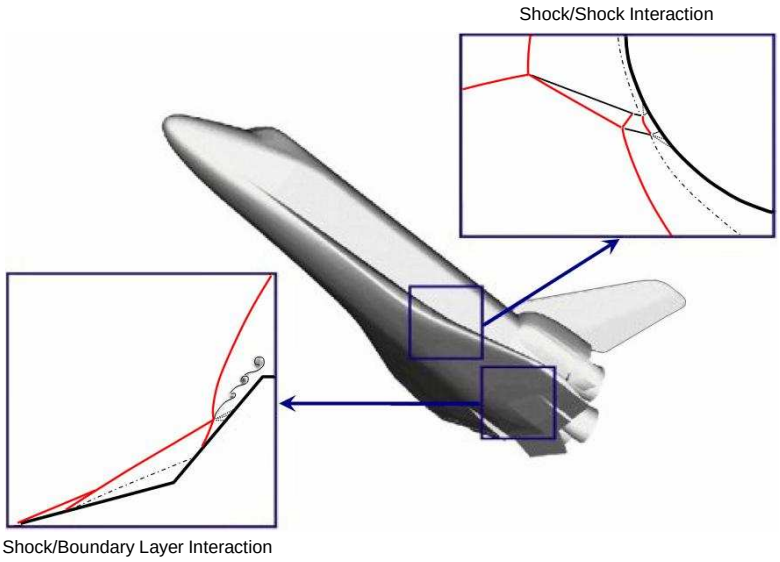

Figure 1.1: Illustration of a reentry vehicle showing regions of interaction between shocks and boundary layers [52]

Flow separation is of great importance for hypersonic flight: it causes adverse effects on vehicle control and performance as well as contributions to thermal loading caused by subsequent flow reattachment. The configurations of fin-body or wing-body junctions are particularly prone to flow separation because of the interaction of the fin or wing bow shock wave with the boundary layer on the surface of the body. As well as producing high levels of heating, these interference effects can also significantly modify the pressure profiles of a lifting surfaces and control surfaces, and may adversely affect their aerodynamic performance, [43]. Following the experience from the *X-15* program, designers of hypersonic vehicles have treated regions prone to interference heating effects with a con-

siderable amount of conservatism. Unlike stagnation regions, where the positions of the localised peaks in heat transfer are almost intuitive, the "hot spots" caused by interference flowfields are not as straightforward to identify or locate, [30]. This is largely due to the fact that they are extremely localised and move around as the attitude of the vehicle changes during flight.

Due to the complexity of the phenomena involved, elucidation of the mechanisms and accurate estimation of the pressure and heating levels generated in interference flowfields is extremely difficult, but necessary. The conservative approach taken by designers on thermal protection has invariably resulted in over protection of hypersonic vehicles, leading to reduced payload capacity, reduced performance, and higher costs, [30]. This is exemplified by the shuttle orbiter design where the thermal protection system accounts for approximately 10% of the vehicle dry mass [53]. Alternatively, under design of the thermal protection systems could lead to disastrous consequences, failure or inability of the vehicle to adequately accomplish its mission. A tragic demonstration of this occurred in February 2003, when the space shuttle *Colombia* exploded after a heat insulation tile on the wing was blown away by debris. This resulted in the wing being exposed to the intense atmospheric heating on the leading edge, which led to a catastrophic chain of events that resulted in the loss of the shuttle and its crew [1].

Over the last thirty years many experimentalists and theoreticians have studied all manner of interference flowfields and have now understood some of the basic flow phenomena and have developed empirical and computational methods to estimate heat transfer rates, predict flow structures, and pressure profiles.

These empirical methods can give reasonable approximate estimates for the locations and magnitudes of peak heating and pressure levels on the surface or on a section of the flow but, can not yield results for the full interaction region. On the other hand, a numerical solution has the advantage in being able to provide the values of the various parameters in space (more particularly at the grid points of the computational domain). This data can then be transformed into images of the flowfield by applying post-processing techniques.

Computational Fluid Dynamics (*CFD*) codes over the years have become increasingly

[1]- The following reference is taken from the official NASA site on the world wide web: www.nasa.gov

sophisticated, and the accuracy achieved by these *CFD* codes has brought about a new dimension in the solution of these problems. Numerical simulations in hypersonic dynamics, specially with *CFD* codes, are often cheaper than wind tunnel testing. The flexibility of computers allows savings in experimental measurements and reduces the final cost of design; furthermore, it is possible to simulate a more realistic environment. However, these numerical techniques are only asymptotical approximations of reality and they can have a lot of uncertainties and inaccuracies. Nevertheless, the computational methods have progressively gained respect and increased in accuracy.

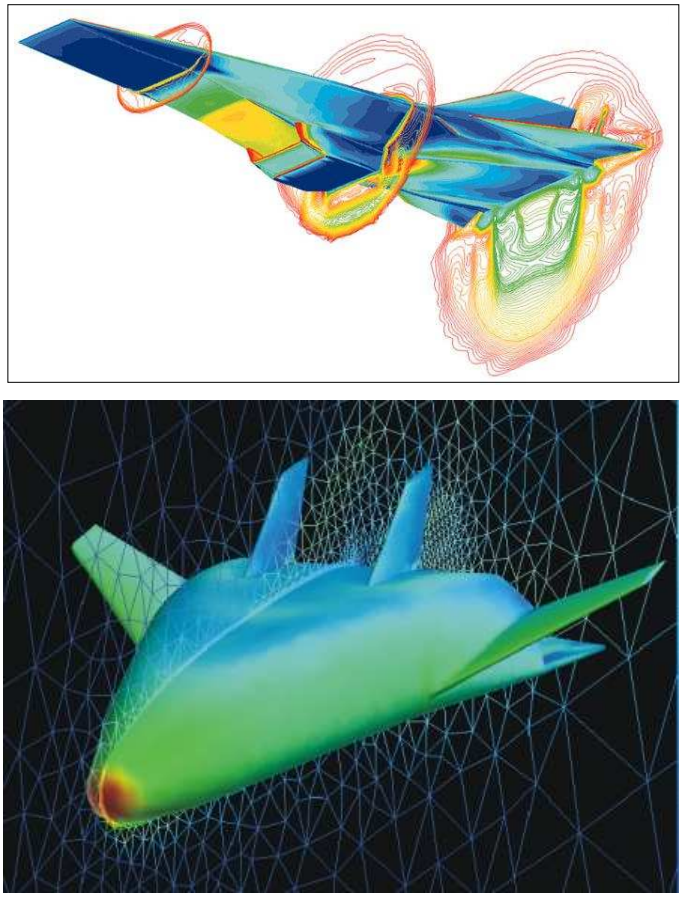

Figure 1.2: (**top**) Illustration of how CFD is used in the X-43 design - Pressure contours around the vehicle structure at Mach 7 [46] (**bottom**) Illustration of an un-structured computational grid built around a model of the X-33 [31]

Development of future hypersonic platforms like the terminated *X-33* program and current *X-43* program have used extensive computational resources in their design and develop-

ment [52] (see Figure 1.2). Considerable attention has been given to reconstruction of the flow around and near control surfaces like flaps and wings, and fin-body junctions like wing-fuselage or tail-fuselage areas on the vehicle. The flow around these junctures is very complex and is illustrated well by the fact that current experimental data from wind tunnels and reentry measurements do not show great agreement with *CFD* results for these cases. These discrepancies have been attributed to turbulence associated with the flow and the three-dimensional effects which are not taken into account in most two-dimensional simulated results [23].

The need to improve these simulation tools, whilst simultaneously reducing the computational cost has been challenging to designers and programmers alike. In order to alleviate the costs associated with extensive use of computational resources, newer faster processors are being developed and intensive parallel algorithms created.

The objective of this work is to accurately predict the interference heating effects around a blunt-fin on a flat plate in a hypersonic flow, mainly along the regions of separation and reattachments in the vicinity of the fin. Particular attention is paid to laminar boundary layer interactions which, as will be discussed in Chapter 2, have been largely ignored in past works. Laminar interactions generally produce more complex and extensive interference flowfields compared to turbulent flows, and it also avoids the uncertainty associated with the use of turbulence models which may not have been validated for hypersonic conditions. However the heating levels associated with laminar interactions are generally lower than those seen in fully turbulent interaction flowfields. The blunt-fin interaction is an important case to study because fins are one of the primary methods of stability and control for many atmospheric high speed vehicles and missiles. As mentioned previously, the interference flowfield created by the fin bow shock-boundary layer interaction creates regions of increased heat transfer close to the fin which must be allowed for in the thermal protection system design. Local peaks in heating rate in the interaction region can be orders of magnitude greater than the stagnation value [16] [56].

In the current work, the laminar-Navier-Stokes code developed by Navarro-Martinez [47] has been modified and improved to solve the blunt-fin flowfield, which is highly three-dimensional. The current code uses an implicit Godunov method with the HLLC Rie-

mann solver as the basic inviscid method. Special features include higher order schemes *(MUSCL, minmod)* to improve accuracy. The scheme was validated for a basic laminar flat plate configuration and a three-dimensional cylinder case. The final improved scheme is able to handle any generic three-dimensional problem. Coupled with a full three-dimensional viscous solver, the method is applied to the three-dimensional analysis of fin-plate situations.

This thesis has six Chapters. Following the introductory remarks made in this first Chapter, an overview of the physics involved in hypersonic interference flowfields is presented in Chapter 2 with reference to previous published work by other researchers. In Chapter 3 a detailed explanation of the methods used in the current numerical scheme is provided. The results of the validation test cases are presented in Chapter 4. Chapter 5 contains the results from the various blunt-fin/plate models simulated, with an extensive detailed study of the unswept $5mm$ diameter blunt-fin. Chapter 6 contains the conclusion of this work along with a number of suggestions for future work and improvements that could be made to the current numerical algorithm. The Appendices contain extra detail about the numerical scheme and supplementary results to complement Chapter 5.

Chapter 2

Literature Review

There are many disciplines involved in studying the physics of hypersonic flow, which basically deals with a compressible fluid flow at high speed, high temperature and in some specific circumstances low density. From an engineering point of view however the definition of the hypersonic regime arises from the differences of design criteria between a supersonic aircraft and a hypersonic vehicle. Although the flow phenomena are similar, there are large differences of behaviour which are strongly dependent on the speed leading to difficulties in the design of hypersonic compared to supersonic vehicles.

Due to the wide scope of this subject area, it is not possible here to detail all the physical aspects relating to hypersonic flow conditions. For example we will not discuss ionisation problems, chemical reactions of gases or low density situations common to many hypersonic flows since these do not form part of the investigation in this present work. However, it is important to discuss some basic detail about the flow regime primarily because these definitions will be used later when analyzing the related numerical results.

The initial part of this Chapter will give a general overview of the physical phenomena affecting hypersonic flows. Then some consideration is given to the mechanisms which lead to heating enhancements on hypersonic vehicles like viscous interaction, shock/boundary layer and shock/shock interactions. This then leads to a review of the current knowledge on blunt-fin interactions with emphasis on previous computational work in the field and some discussion on the scope of the present study.

2.1 Fundamentals of Hypersonic Flow

As a basic definition it is generally accepted that the hypersonic region of flight begins at Mach numbers greater than about 5. The free stream Mach number is defined as the ratio between the stream velocity (U_∞) and the sound speed in this medium (c_∞).

$$M_\infty = \frac{U_\infty}{c_\infty} \tag{2.1}$$

This is not a definitive physical limit, Mach numbers as low as 3 and as high 10 can be also considered as the limit of supersonic-hypersonic transition. Rather, it is better to say that the hypersonic regime is where certain physical phenomena become progressively more important as the Mach number is increased [2]. These hypersonic effects include strong shock waves, thin shock layers, entropy layers, viscous interactions, high temperature phenomena and low density conditions. All these phenomena are intimately coupled and reinforce each other, increasing the difficulty in analyzing hypersonic flows.

The region between the bow shock wave and the body is called the shock layer. It can be shown analytically that, as the Mach number increases, the angle between the shock wave and the body becomes smaller [3]. If high-temperature, chemically reacting effects are included, the shock wave angle will be even smaller [3]. It is a basic characteristic of hypersonic flows that shock waves lie close to the body, and that the shock layer is thin. In turn, this can create some physical complications, such as the merging of the shock wave itself with a thick, viscous boundary layer growing from the body surface - a problem which becomes important at low Reynolds numbers. However, at high Reynolds numbers, where the shock layer is essentially inviscid, its thinness can be used can be used to theoretical advantage, leading to a general analytical approach called "thin shock layer theory" (see [2]). Highly curved shock waves, like those around the nose of blunt bodies, generate entropy gradients resulting in an entropy layer with strong vorticity associated. The boundary layer lies inside this entropy layer and is strongly affected by it, modifying the conditions of analysis. This effect is known more commonly as vorticity interaction.

As previously stated a large amount of kinetic energy is dissipated either by shock waves

or through viscous effects (which is discussed later), causing an increase in the stream flow temperature. This dissipation process can produce very high thermal energies, reaching even above molecule dissociation energy levels. At the same time at high enough temperatures, a chemically reacting layer is developed within the boundary layer. For example, in the *Apollo* mission since the vehicle re-enters the earth's atmosphere at Mach numbers in excess of thirty, the temperatures in the shock layer exceeded $6600K$ and gas temperatures behind the leading bow shock reached $11000K$ [18]. The vehicle's surface was exposed to radiative and convective heating. At such temperatures the air ionises and the flow behaves like a partially ionised plasma. Furthermore, at this temperature radiation effects become important, increasing the thermal load on the hypersonic vehicle. The radiative heating becomes more severe for some planetary entries due to even higher velocities and can be the major contribution to the total heat transfer. An example is the *Galileo* mission to Jupiter, in which the radiative contribution to the probes heating was larger than the convective contribution [18]. However, for most Earth re-entry situations, the convective contribution is normally greater than the radiative as illustrated in Figure 2.1.

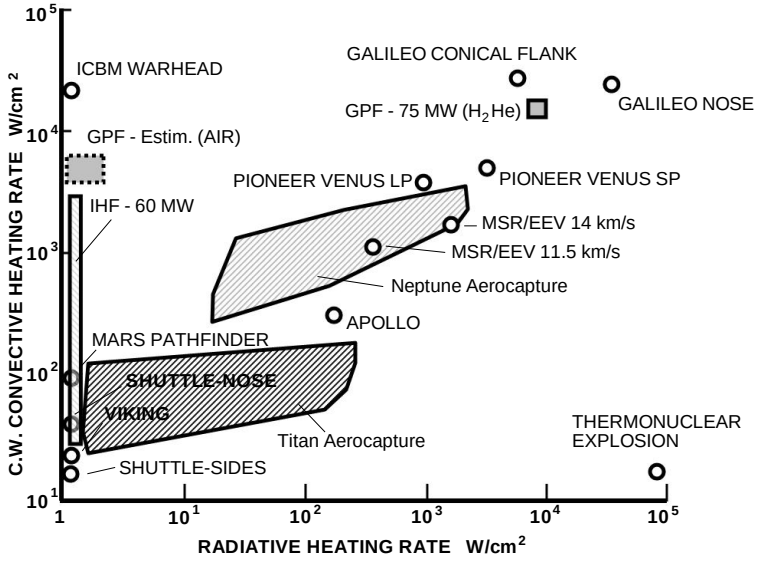

Figure 2.1: Convective vs Radiative heating [23]

The high temperature reached in hypersonic regimes modifies the behaviour of the flow, altering the gas model initially considered. The ideal gas assumptions no longer holds and more realistic models need to be introduced. Also all the transport properties vis-

cosity, conductivity etc. are strongly affected by the temperature, differing from ambient conditions. Simulating these high temperature conditions in ground based wind tunnel facilities, whilst also matching the Mach number and Reynolds number is practically impossible, and is another reason why CFD has been increasingly used as a design tool for the development of hypersonic vehicles in recent years.

In the upper layers of the atmosphere, the air is rarefied. Under these conditions the air is no longer a continuum fluid and it behaves under a free molecular regime described by the kinetic theory. The transition from the usual continuum level to the free molecular regime is controlled by the Knudsen number, (Kn), which is the ratio between the mean free path of the gas (λ) and a characteristic length associated with the body (L).

$$Kn = \frac{\lambda}{L} \tag{2.2}$$

The Knudsen number indicates the regime of application of the different flow equations. For low $(Kn \ll 1)$, the continuum hypothesis holds and the fluid mechanics equations (Euler or Navier-Stokes) may be applied. When (Kn) becomes large $(Kn > 1)$ the Boltzmann equations come into play, and in the limit $(Kn \to \infty)$, the collisionless Boltzmann equations are applicable. At this point, the flow is so rarefied, with very few non-interacting molecules, that it can for all intents and purposes be described as that seen in outer space.

2.2 Viscous Effects in Hypersonic Flow

The designers of vehicles that are to fly at hypersonic speeds have long recognized that the locally severe heating rates produced by viscous interactions and by shock/shock interactions can cause catastrophic failures, as noted in the example *X-15* in Chapter 1. The interaction between a shock wave and a boundary layer is a problem of many practical hypersonic flows. As an example Figure 1.1 shows regions on a reentry vehicle that are typical for problems of shock boundary layer interactions and shock/shock interactions.

Consider a flat plate exposed to a hypersonic freestream, near the leading edge, the boundary layer grows rapidly where the region outside the boundary layer is assumed to be

inviscid and the viscous effects are confined to the boundary layer. The presence of the boundary layer causes the hypersonic flow to decelerate creating a shock wave on the leading edge (see Figure 2.2).

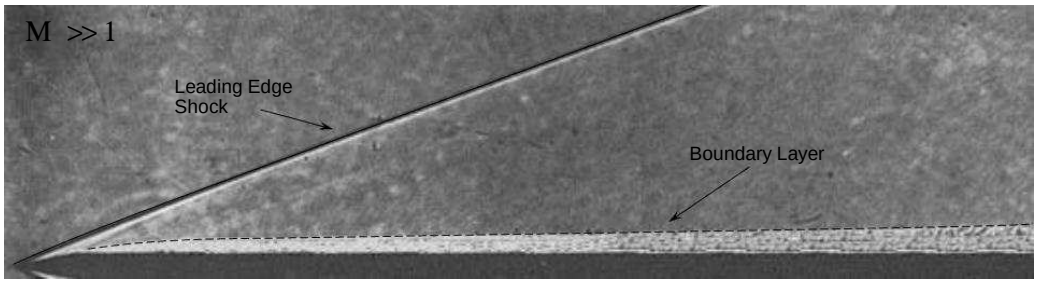

Figure 2.2: schlieren image of a hypersonic flow over a flat plate [27]

For a hypersonic freestream Mach number of (M_∞), the compressible laminar boundary layer thickness, (δ), increases over a flat surface approximately as [3],

$$\frac{\delta}{x} \propto \frac{M_\infty^2}{\sqrt{Re_x}} \tag{2.3}$$

where the Reynolds number at distance x is defined as,

$$Re_x = \frac{\rho_\infty U_\infty x}{\mu_\infty} \tag{2.4}$$

where (ρ_∞), (U_∞) and (μ_∞) are the density, velocity and viscosity respectively of the free stream flow. The Reynolds number is a well known parameter characterizing the ratio of the viscous forces in the gas to the inertial forces. In hypersonic applications, unit Reynolds number (Re/l) ranges from extremely low values on entry to the outer regions of the atmosphere up to $\sim 10^8/m$ for low altitude hypervelocity missiles. This range of Reynolds number encompass the full range of boundary layer flows from full laminar, through transitional, to fully turbulent.

Another useful parameter used when discussing hypersonic flows is the Prandtl number, (Pr).

$$Pr = \frac{C_p \mu}{\kappa} \tag{2.5}$$

where (C_p) is the specific heat at constant pressure and (κ) is thermal conductivity. The Prandtl number is commonly described as being the ratio of momentum diffusivity (kinematic viscosity) to thermal diffusivity. It can be related to the thickness of the thermal and velocity boundary layers, where it is actually the ratio of the velocity boundary layer to thermal boundary layer. In cases where $(Pr > 1)$ the thermal boundary layer is thinner than the velocity boundary layer and vice versa for $(Pr < 1)$. When (Pr) is small it means that heat diffuses very quickly compared to velocity (momentum).

From examining Eqn 2.3 it is clear that boundary layers under hypersonic flows are relatively thick compared to supersonic or subsonic cases due to the Mach number square dependence. The reason for this is that high velocity hypersonic flows lose a considerable amount of kinetic energy when slowed down due viscous effects in the boundary layer. A significant amount of the kinetic energy of the flow is converted to internal thermal energy via viscous dissipation. As a result this increases the local temperature but, because the pressure in the normal direction is constant across the boundary layer, the density falls. Consequently, in order to pass the required mass flow through the boundary layer at reduced density, the boundary layer enlarges. Due to this rapid boundary layer growth the inviscid flow is strongly affected, increasing the interaction between them and modifying the aerothermodynamics loads. This phenomena is known as viscous interaction and is discussed later in this section.

Looking at Figure 2.2 again, the shock wave compresses the flow throughout the surface of the plate and affects the fluid variables in the inviscid region of the flow. The increase in pressure past the shock immediately in-front of the flat plate leading edge changes the profile of the compressible boundary layer near the shock wave leading edge, reducing its thickness and increasing the local heat transfer and the skin friction. Within the boundary layer the local surface shear stress - skin friction - (τ_w) can be defined as,

$$\tau_w = \mu \left. \frac{\partial u}{\partial \zeta} \right|_{\zeta=0} \tag{2.6}$$

where (u) is the tangential flow velocity and (ζ) is a direction perpendicular to the surface. The rate of heat transfer per unit area - heat flux - $(\dot{q}_w)$ is given by:

$$\dot{q}_w = \kappa \frac{\partial T}{\partial \zeta}\bigg|_{\zeta=0} \tag{2.7}$$

The surface shear stress and heat flux are commonly presented using non-dimensional coefficients, the skin friction coefficient (C_f) and the Stanton number (St) given by:

$$C_f = \frac{\tau_w}{\frac{1}{2}\rho_\infty U_\infty^2} \tag{2.8}$$

and

$$St = \frac{\dot{q}_w}{C_p \rho_\infty U_\infty (T_r - T_w)} \tag{2.9}$$

here (T_r) and (T_w) are the recovery and surface temperatures respectively. The recovery temperature (T_r) is a function of the conditions at the boundary layer edge and on the boundary layer state.

To predict the surface shear stress and heat flux in high speed flows Eckert [19] proposed an empirical approach called the "reference temperature method", which is widely accepted for its simplicity and general good agreement with the boundary layer theory. This approximation is based on correcting the results for classical incompressible boundary layer by incorporating compressibility effects defined at a reference temperature (T^*) given by:

$$T^* = \frac{1}{2}(T_\infty + T_w) + 0.22(T_r + T_\infty) \tag{2.10}$$

where (T_e) is the temperature at the outer edge of the boundary layer, (T_w) and (T_r) were defined earlier as the wall temperature and recovery temperature respectively. (T_r) is given by:

$$T_r = T_e + \frac{r U_e^2}{2C_p} \tag{2.11}$$

The recovery temperature is identical to the adiabatic wall temperature. For a laminar boundary layer the recovery factor, (r), is taken as,

$$r = \sqrt{Pr} \tag{2.12}$$

Eckert assumed the same functional dependence on the skin friction coefficient (C_f) and the Stanton number (St) number with the Reynolds and Prandtl numbers as for incompressible boundary layer theory. The Stanton number and skin friction coefficient are now evaluated as,

$$C_f = \frac{0.664}{\sqrt{Re_x^*}} \sqrt{\frac{\rho^* \mu^*}{\rho_\infty \mu_\infty}} \tag{2.13}$$

and

$$St = 0.5 C_f Pr^{*-2/3} \tag{2.14}$$

Variables with the asterisk indicates quantities evaluated at the reference temperature, (ρ^*) can be obtained through the equation of state assuming that the pressure remains constant across the boundary layer. The Eckert relationship for Stanton number in Eqn 2.14 will be used throughout this work to compare with our numerical approximation for hypersonic flows over a flat plate. The heat transfer may then be obtained from Eqn 2.9, where (C_p) is obtained from a polynomial fit or perfect gas assumptions. The reference temperature method agrees well with solutions obtained from the integration of the compressible boundary layer equations, especially in the flat plate case.

The boundary layer analysis carried out by Eckert [19] to predict the skin friction and heat flux did not take viscous interaction into account. It is therefore not expected to provide reliable estimates in the region of strong interactions which occur near the leading edge as highlighted by Figure 2.2. Further downstream of the leading edge, the growth of the boundary layer is smaller and as a result has a diminished effect on the inviscid outer flow. In these areas, as highlighted earlier Eckert's comparison for heat transfer and skin friction should agree with compressible boundary layer theory [25].

2.2.1 Interaction parameters

When regarding the flat plate at hypersonic Mach numbers as depicted in Figure 2.2, it is noticed that the pressure over the plate is significantly influenced by the rapid boundary layer development over the plate (the boundary layer thickness develops according to Eqn 2.3). Due to the boundary layer growth the leading edge shock is curved near the plate which considerably influences the flow properties on the plate. This can be described by applying the tangent-wedge formula to an effective body described by the local slope of the displacement thickness $\left(\frac{d\delta^*}{dx}\right)$. Results and derivation of the viscous interaction theory are summarized in [2]. The viscous interaction can be divided into two cases: a strong interaction where $\left(\frac{d\delta^*}{dx}\right)$ is large so $\left(\mathbf{K}^2 = \left(M_\infty \frac{d\delta^*}{dx}\right)^2 \gg 1\right)$ and a weak interaction where $\left(\frac{d\delta^*}{dx}\right)$ is moderate so $\left(\mathbf{K}^2 = \left(M_\infty \frac{d\delta^*}{dx}\right)^2 \ll 1\right)$. In both interactions the equation for the pressure depends solely on one governing similarity parameter which controls laminar viscous interaction. This parameter is called the viscous-interaction parameter, (χ), which in a characteristic length is defined by:

$$\bar{\chi} = M_\infty^3 \sqrt{\frac{C_w}{Re_{/x}}} \tag{2.15}$$

where (Re/x) is the Reynolds number based on a specified reference length (L_{ref}), and (C_w) is the Chapman-Rubesin constant. As before, subscripts (∞) and (w) refer to freestream and wall conditions respectively, where the Chapman-Rubesin constant is given by [26].

$$C_w = \frac{\rho_w \mu_w}{\rho_\infty \mu_\infty} \tag{2.16}$$

It is obvious that the viscous interaction grows very rapidly with the cube of the Mach number. For large values of $(\bar{\chi})$, there is a strong interaction between the viscous and inviscid flow, while for small values of $(\bar{\chi})$ the interaction is called weak, and the inviscid flow is practically unaltered. Following equations Eqn 2.4 and Eqn 2.15 $(\bar{\chi})$ decays as $(x^{-1/2})$, giving a strong interaction near the edge and a weaker one when (x) increases along the flat plate. A practical limit of $(\bar{\chi} \approx 3)$ is considered to distinguish between

strong and weak interactions. The transition from a domain of strong interaction to a region of low interaction can be seen schematically in Figure 2.3.

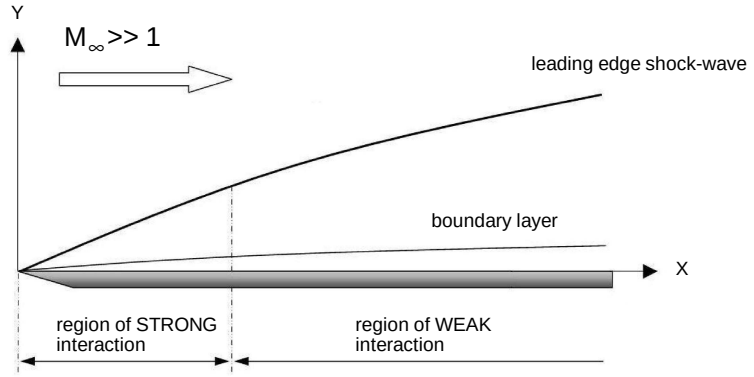

Figure 2.3: Illustration of viscous interaction of a hypersonic flow over a flat plate [47]

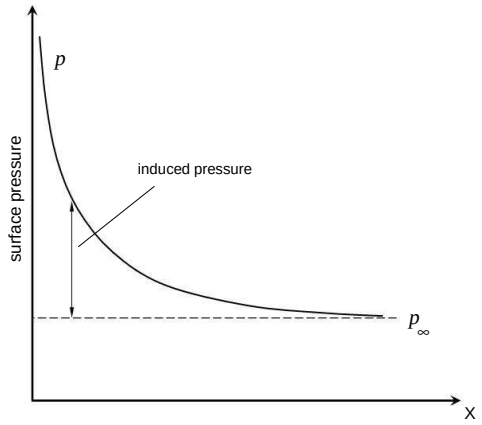

Figure 2.4: Schematic diagram of distribution of the surface pressure of a hypersonic flow over the flat plate

The effect of the viscous interaction can be seen in the distribution of the pressure displayed in Figure 2.4. In the strong interaction region, the induced pressure follows a linear function of $(\bar{\chi})$ [2].

$$\frac{p}{p_\infty} = 1 + a_1\bar{\chi} \tag{2.17}$$

while, in the weak interaction region the pressure variation becomes quadratic.

$$\frac{p}{p_\infty} = 1 + b_1\bar{\chi} + b_1\bar{\chi}^2 \tag{2.18}$$

with (a_1), (b_1) and (b_2) constants which depend on the gas properties [2].

The reference temperature method can be corrected taking into account the pressure difference along the flat plate [2]. The pressure corrected Stanton number (St) and skin friction coefficient (C_f) were given earlier in Eqn 2.13 and Eqn 2.14.

2.3 Shock/Boundary Layer Interaction

As described earlier, shock/boundary layer interactions are unavoidable on hypersonic vehicles, due to the necessity of using control mechanisms such as flaps, fins and jets. Initially, for the basic purpose of identifying the mechanisms involved in a shock/boundary layer interactions, a two-dimensional shock/boundary interaction is described, as this contains many of the features found in the more complex three-dimensional interactions. The qualitative physical aspects of a general two-dimensional shock wave/boundary layer interaction are shown in Figure 2.5.

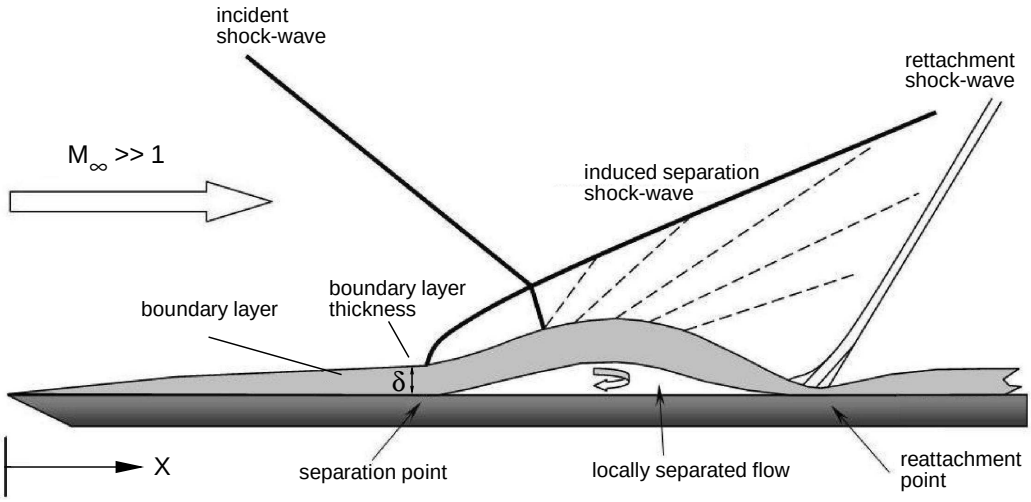

Figure 2.5: A two-dimensional swept shock/boundary layer interaction [53]

In the configuration illustrated an incident shock wave impinges on a flat plate boundary

layer downstream of the leading edge. The large pressure rise associated with the shock imposes a severe adverse pressure gradient, and this causes the boundary layer to separate. As the subsonic portion of the boundary layer allows the higher pressure in the post shock region to feed upstream, the separation point is located ahead of the incident shock impingement point. Separation of the boundary layer compresses the freestream flow above it, creating an induced separation shock. Subsequently the separated boundary layer turns back towards the flat plate and reattaches, creating an enclosed region of locally separated flow. Expansion waves are generated between separation and reattachment points as the flow turns back towards the surface compression waves are generated and further away from the flat plate surface these merge to form the reflected shock wave predicted by inviscid theory. The latter is known as the reattachment shock.

At the reattachment point a local thinning of the boundary layer and high pressure result in a region of high local heat transfer. The incoming boundary layer state affects the extent and severity of the interaction region. Laminar boundary layers separate more readily than their turbulent counterparts, due to the less full velocity profile. Thus, for a given shock strength a laminar shock/boundary layer interaction will be larger in extent than a turbulent interaction.

In laminar interactions, thickening of the boundary layer due to the adverse pressure gradient creates a reduction in heat transfer around the separation point, due to the reduction in convective currents. This heat transfer reduction reaches a marked minimum before rising to a peak associated with the reattachment. In contrast, for an oncoming turbulent boundary layer the heat transfer rises at separation and reaches a plateau through the separation region, rising again near the rear of the separation region to a peak associated with the reattachment. This rise at separation is therefore opposite to that exhibited by the laminar case. Stollery [56] suggested that the effect may be due to the large increase in turbulent intensity occurring in the vicinity of the separation point. The large eddies which then form can promote energy exchanges between the wall region and the outer high enthalpy flow, thus leading to an increase in heat transfer to the surface.

It should be noted that even if the oncoming boundary layer is laminar the impingement of an incident shock is sometimes usually enough to trip the boundary layer into transition,

and therefore, after laminar separation, heat transfer levels may be higher than expected at the reattachment point, due to the reattachment of a turbulent boundary layer.

2.3.1 Three-Dimensional Separation

Three-dimensional separation is radically different from two-dimensional separation which was described earlier. In two-dimensional flows separation is identified by a region of backflow, and at the wall by a zero shear stress solution. This difference is illustrated in Figure 2.6: in two-dimensional separation the separation point and reattachment point are connected by a ($u = 0$) velocity line and a dividing streamline. The region is closed and the streamlines inside are closed. In a three-dimensional separation, the separation and reattachment points cannot be connected by a streamline to form a closed vortex [13]. The concepts of separation and reattachment points, recirculation regions or dividing streamlines as mentioned above need careful redefinition.

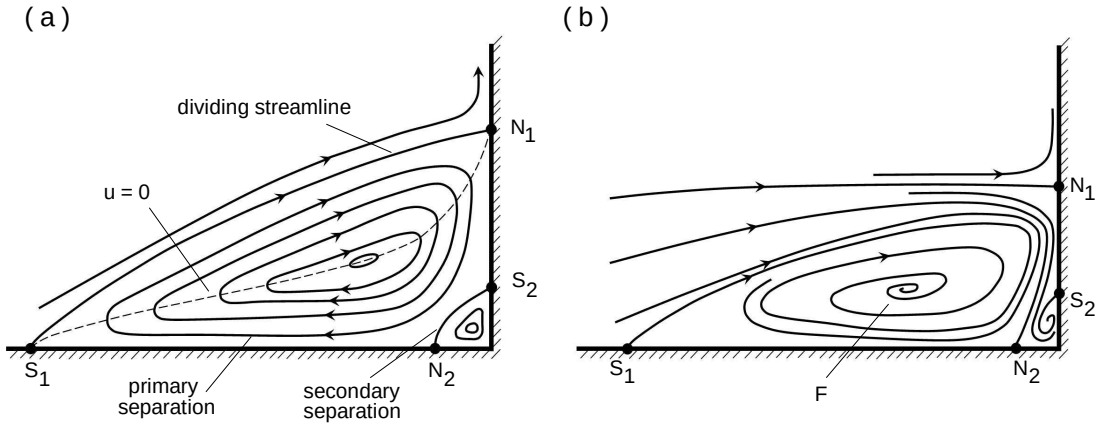

Figure 2.6: (**a**) A flow which exhibits two-dimensional separation (**b**) A flow with three-dimensional separation [45]

To identify three-dimensional separated regions, one focuses on the shear stress at the wall, which is a vector field in three-dimensional flows. The trajectories of this field are the skin friction lines, sometimes called limiting streamlines because they are the limit of a streamline when the distance to the wall becomes zero. The set of the skin friction lines covering a body constitutes a skin friction line pattern, and separation is defined from

examination of this pattern. However, the sole inspection of the skin friction line pattern is far from being sufficient to define and describe three-dimensional separation. Considering orthogonal coordinates in the two-dimensional space (x, z) of the body surface, we denote $\big(\ \tau_x(x,z)\ \big)$ and $\big(\ \tau_z(x,z)\ \big)$ the components of the skin friction vector $\big(\tau_x\big)$ along (x) and (z) respectively. The skin friction lines are defined by the following (time independent) differential equation:

$$\frac{dx}{\tau_x(x,z)} = \frac{dz}{\tau_z(x,z)} \tag{2.19}$$

These equations define an infinity of solution curves called characteristic lines or trajectories that are associated with the skin friction lines introduced above. In general, one and only one trajectory passes through a point on the surface. The only points that do not satisfy this rule are the singular points of the system where the skin friction vanishes, that is, where we simultaneously have

$$\tau_x(x,z) = \tau_z(x,z) = 0 \tag{2.20}$$

Around such singularities, the shape of the skin friction lines are evaluated through a first order Taylor series expansion, written in tensorial form as

$$\tau = \mathcal{A}\mathbf{x} \tag{2.21}$$

where $\big(\ \tau = (\tau_x, \tau_z)\ \big)$ and $\big(\ x = (x,z)\ \big)$, $(\mathcal{A})$ is the Jacobian of the above transformation. Depending on the values of $(\mathcal{A})$ it is possible to classify the different types of singular points. One method of classification is according to the eigenvalues of the Jacobian, where real eigenvalues produces (**nodes**) if $\Big(|\mathcal{A}| > \mathbf{0}\Big)$, **saddles** if $\Big(|\mathcal{A}| < \mathbf{0}\Big)$ or a combination of both if $\Big(|\mathcal{A}| = \mathbf{0}\Big)$. The most common singular points are presented in Figure 2.7.

Singular points may be classified as two types: **nodes** and **saddle** points (see Figure 2.7:(**a**) and 2.7:(**b**)). When the skin friction lines converge to, or diverge from a point, the point is called **node** - nodal point of separation or attachment - respectively

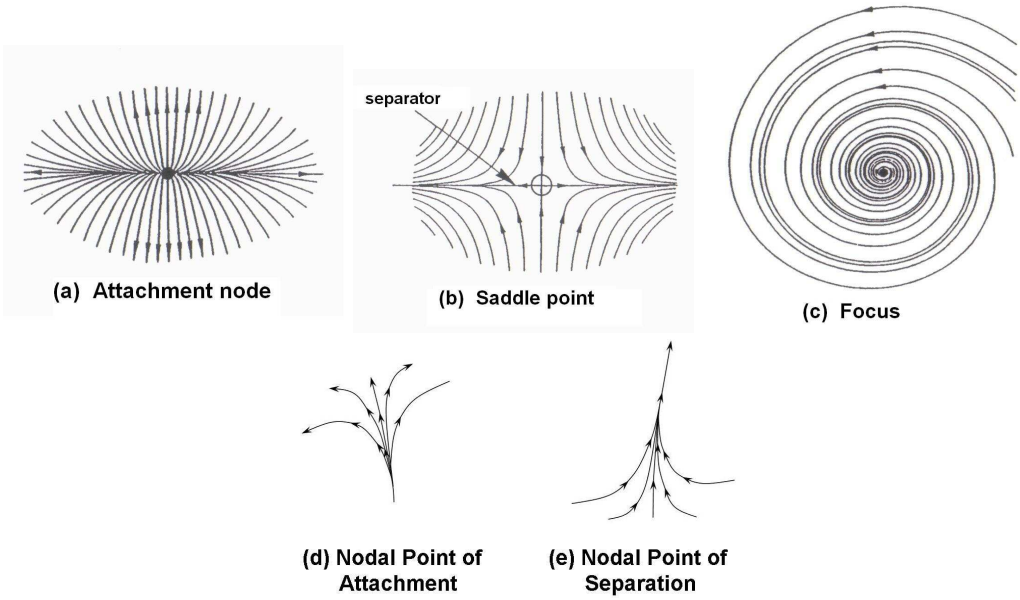

Figure 2.7: Most typical patterns near critical points [13] (**a**) Attachment node (**b**) Separation saddle (**c**) focus (**d**) Nodal point of attachment (**e**) Nodal point of separation

(see Figure 2.7:(**e**) and 2.7:(**d**)). Nodal points can have one line to which all skin friction lines are tangent to, or none. In the latter case the node is called **focus** - of separation or attachment (see Figure 2.7:(**c**)). Nodal points of separation and attachment can be viewed as sinks and sources of skin friction, respectively. Nodal points of attachment are typically stagnation points on a forward facing surface (like a blunt nose).

There are cases where the skin friction lines deviate from a point as from a stagnation point. There are only two lines (normal to each other) through the point, which is called **saddle**. Skin friction lines diverging from nodal points cannot cross, due to the presence of a saddle point between them. One of the lines through the saddle is a separation line.

Nodal points of separation and attachment have other interesting features: they become edges of vortex cores. In some cases there is also a distinction between primary and secondary lines of separation. Devices most commonly used for the study of three-dimensional separation include prolate spheroids, blunt and pointed cones at incidence, where non-axisymmetric vortex formation appear (all axisymmetric bodies at incidence are very prone to flow separation with consequent instability).

The existence of these critical points in the surface indicates the presence and types of separation. A flow is separated if the skin friction lines configuration contain at least one saddle point [58]. Accordingly, a separation line would form a separation surface which usually rolls up in a vortical structure, as demonstrated in Figure 2.8. A combination of saddle and nodes in the surface would give rise to the different types of separation, like the bubble of the horseshoe vortex type (1 saddle and 1 node).

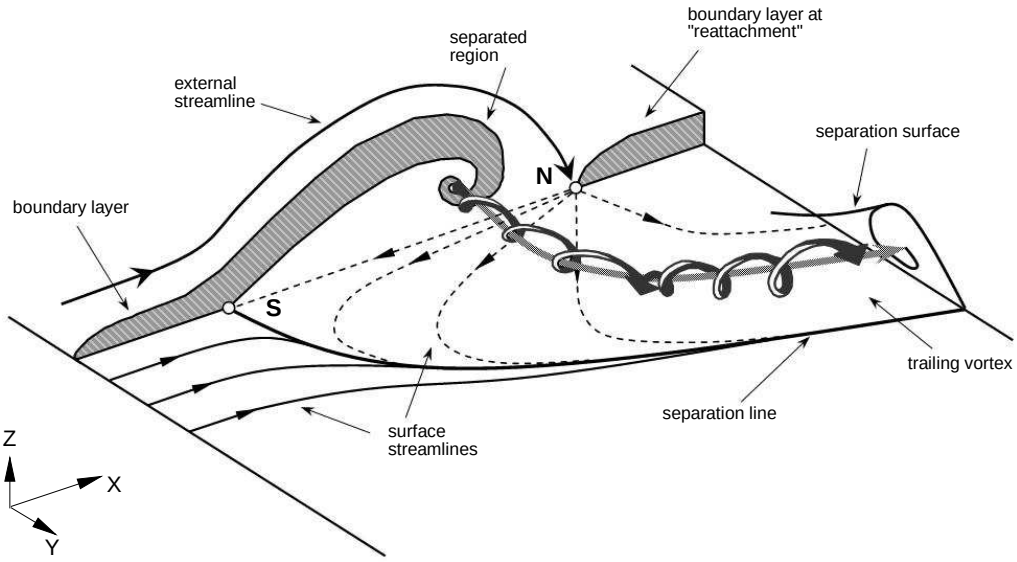

Figure 2.8: Horseshoe or bubble separation. S marks the saddle point at separation and N denotes the node point at reattachment [47]

A topological rule has been developed for streamlines on a vertical plane cutting a surface that extends to infinity both upstream and downstream [58].

$$\left(\sum\nolimits_N + \frac{1}{2}\sum\nolimits_{N'}\right) - \left(\sum\nolimits_S + \frac{1}{2}\sum\nolimits_{S'}\right) = 0 \tag{2.22}$$

The singular points in this rule are defined as half-nodes ($N^{'}$), half-saddles ($S^{'}$), saddles (S), and nodes (N). This rule has been used to describe the upstream plane of symmetry for an obstacle mounted on a wall [58].

2.4 Shock/Shock Interaction

Edney [20] in 1968 presented one of the most comprehensive studies of shock/shock interference effects, concentrating on the mechanisms by which these interactions arise, and how they generate severe heating and pressure levels on nearby aerodynamic surfaces. His study involved measurement of the heating and pressure levels on a hemisphere/cylinder model injected into Mach 4.6 - 7 flow. An impinging shock from a wedge was traversed across the bow shock from the hemisphere, encompassing the full geometric range of shock/shock interactions possible. A sketch illustrating the approximate relation between the location where the impinging shock wave intersects the bow shock on the hemisphere and the shock/shock interference patterns is reproduced in Figure 2.9:(**left**).

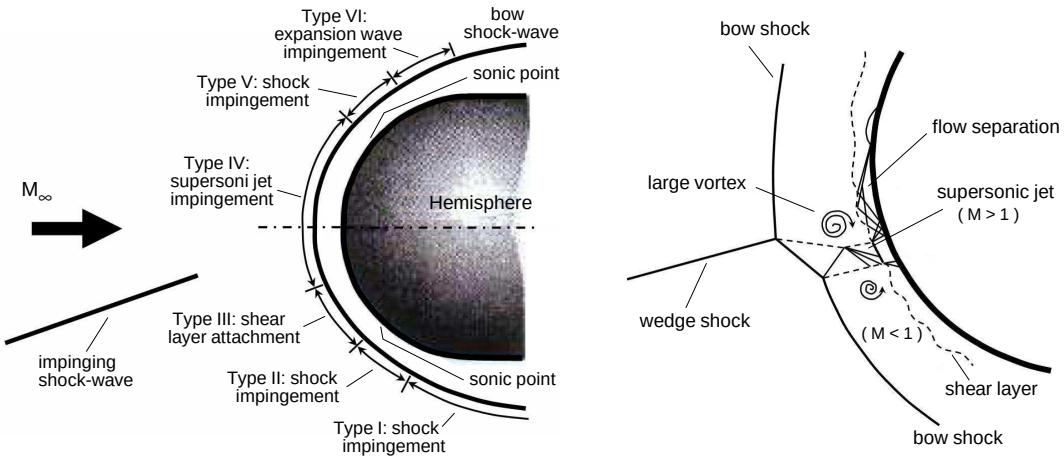

Figure 2.9: (**left**) Approximate relation of the shock/shock geometry and the type of interference pattern [20] (**right**) Supersonic jet and vortex pattern from a Type IV interference [28]

Edney observed that there were 6 different types of shock/shock interference of varying degrees of severity and complexity. The interference heating types were categorised as types I to VI. He explained that the enhanced heating and pressure levels were produced by shock/boundary layer interactions for types I, II, IV and V, stability and attachment of free shear layers for type III, impingement of a supersonic jet for types IV and V. Edney discussed the practical implications of his work mentioning that blunt fins attached to a fuselage would experience one of three types of interference, IV, V, or VI depending

on their degree of sweep as shown in Figure 2.9:(**left**). At zero or small angles of sweep, type IV will prevail, at around 30° sweep, type V will take over and further sweep will yield type VI interference.

Edney predicted that the most severe levels of heating and pressure would be produced by a type IV interaction. This interaction arises when an oblique shock is incident close to the normal region of the bow shock, as illustrated in Figure 2.9:(**right**). In high Reynolds number flows, shock/shock interaction produces an essentially inviscid slipstream - which Edney termed a "jet" - in which the supersonic flow is efficiently compressed by a series of compression and expansion waves. This jet, which is bounded by shear layers, is terminated by a normal shock just ahead of the surface to produce a narrow stagnation region. The path of the jet is such as to maintain the same pressure either side in the subsonic regime and the jet can curl upwards, downwards or even divide before it impinges on the body.

The region of flow surrounding the embedded supersonic jet is largely subsonic and the flow is unsteady and highly rotational, and results in the formation of several small vortices, as indicated in Figure 2.9:(**right**). The efficient compression process produces high localised pressures, and very large velocity gradients in the small stagnation region that can cause large heating rates relative to the heating generated by undisturbed flow. These surface thermal and pressure stresses for a laminar flow can be 30 times greater than stagnation conditions [28]. Edney also observed that for the type IV interaction, the peak pressure, heat transfer rates and pressure distributions are sensitive to upstream thermodynamic flow conditions, shock strength, and Mach number. It was also observed that the heating rates derived from the type IV interaction vary widely depending on whether the flow is laminar, transitional or turbulent as well as whether the gas is considered perfect or real [64].

2.5 Fin Interference Flow fields

Fin/plate interference flow fields, which are simplified examples of fin-fuselage interference configurations - particularly because they avoid additional three-dimensional effects that would otherwise be present on curved surfaces, such as a fin-fuselage configuration - are of great practical importance in the design and operation of hypersonic vehicles. Due to the complex nature of three-dimensional interference flowfields, experimentalists and CFD code developers alike initially confined their studies to simpler two-dimensional interference flows, such as ramp type flows. Numerous studies of various two-dimensional interaction flow fields [8] were made, and these flows became reasonably well understood; researchers then directed their attention to three dimensional flows where research has continued from the early 1960's right up until the present day. Excellent review papers on experimental results have been presented by [30, 43] on the different types of fin interference flow fields.

Broadly, there exists two types of fin/plate interaction: the sharp-fin interaction and the blunt-fin interaction, the latter being the configuration investigated in this study. The complexities in both these flow fields arise when the fin shockwave interacts with the oncoming boundary layer growing on the plate. This interaction generates shock/boundary layer and shock/shock interaction effects. For most fin/plate interactions, flat plate heating rates well in excess of undisturbed values have been measured in the region of flow reattachment lines by many researchers. The characteristics of these interactions depend on numerous geometric and flow parameters such as: Mach number, Reynolds number, state of the undisturbed boundary layer on the plate, local boundary layer thickness, protuberance height, fin leading edge diameter (for blunt-fin interactions only), fin incidence, and fin sweep. An excellent review encompassing all aspects of blunt-fin type interactions can be found in [56, 37, 14, 17, 16, 54, 15].

It is noted that in certain regions of the interference zone the flowfield for a blunt-fin resembles that of a sharp-fin, as a result a brief description of this type of interaction is given.

2.5.1 Sharp-fin Interaction

The simplest example of a swept shock/laminar boundary layer interaction, also commonly classified as "corner configurations", consists of a sharp-fin attached normally to a flat plate at a certain distance behind its leading edge. The oblique swept shock generated by the sharp-fin is attached at the fin leading edge as shown in Figure 2.10.

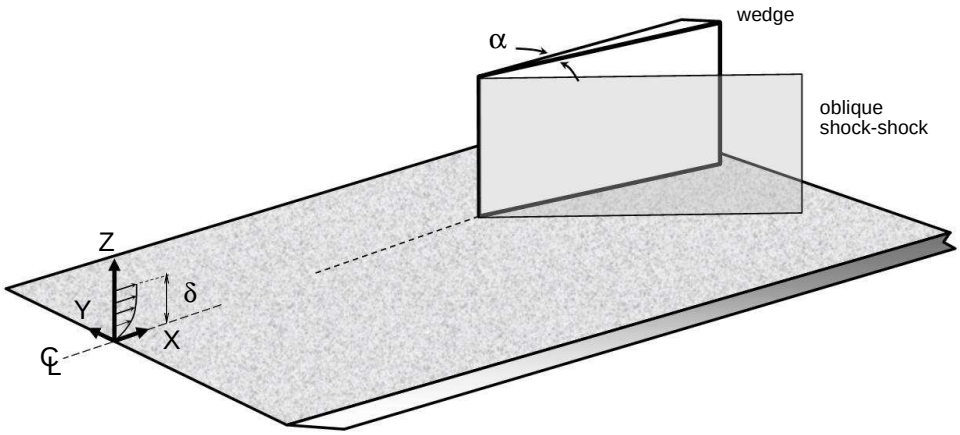

Figure 2.10: Sharp-fin/plate configuration

Impingement of the shockwave on the flat plate surface creates a pressure rise in the flat plate boundary layer. Provided the fin angle of incidence is small the flow does not separate. However, if the angle of incidence is sufficiently large the adverse pressure gradient is such that the flow separates ahead of the shock forming an oblique separation shock, with the flow reattaching further downstream. As a result of the shock interaction a "lambda" shock profile is formed which is overlaid over a quasi-conical flattened separation vortex. The vortical flow, starting from the fin apex and growing as it travels downstream, dominates the separated flow region. The conical vortex carries high-energy air from the external flow to its reattachment region, causing the appearance of peak heating and high values of pressure in this region. A small corner vortex is observed close to the fin/plate junction. A flow model containing the following features was put forward by Kubota and Stollery [44] and is illustrated in Figure 2.11.

In general, the interaction domain in this type of flow is quasi-conical; i.e., it grows almost

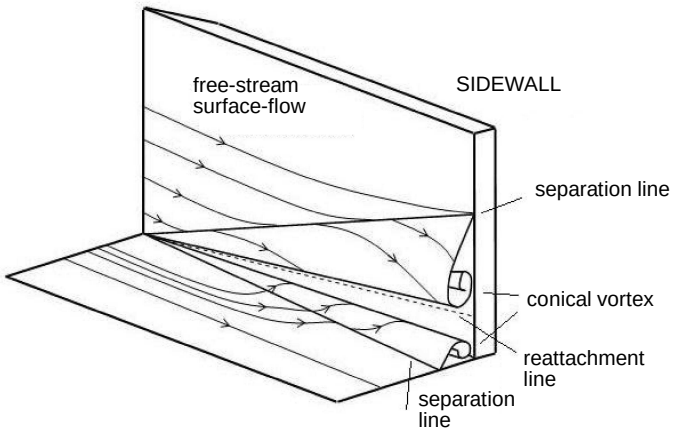

Figure 2.11: Fin/plate configuration flow model suggested by Kubota and Stollery [44]

linearly in the downstream direction [1]. According to experimental results, a small region close to the fin leading edge appears to deviate from the standard conical behaviour. This area is called the "inception zone" [13], and is characterised by a curved separation line. Downstream of the inception zone the surface features follow rays from a virtual common origin located upstream of the fin leading edge.

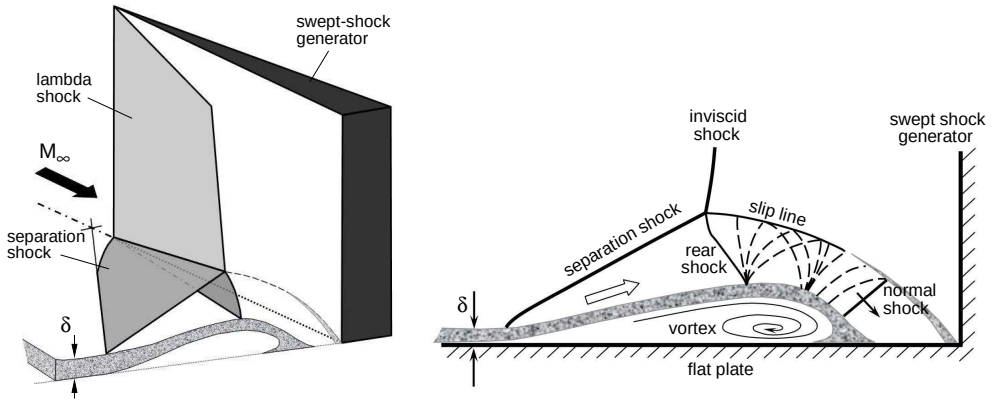

Figure 2.12: (**left**) Swept-shock quasi-conical interaction flowfield [49] (**right**) A schematic of the features observed in corner flows [49]

[1]This feature has been observed experimentally by many researchers, but it is also a conclusion of a theoretical study by Inger [39]. More specifically, through an order-of-magnitude analysis of the governing equations, Inger found that a swept interaction can approach a quasi-conical state at a large distance from the origin of the flow.

A typical flowfield cross-section of a sharp-fin interaction is illustrated in Figure 2.12, and the dominant features of the flow are:

- A main shock, a separation shock and a rear shock all meeting at the triple point.
- A slip line caused by the velocity difference in streamlines passing above and below the triple point.
- Transonic shocklets in the expansion region which terminates with a normal shock.
- A primary separation and vortex core.
- An impinging jet structure defined on the outer edge by the slip line and on the inner edge by the primary separation bubble.
- For moderate interaction strengths, an apparent secondary separation occurs inside the primary separation bubble but the exact nature of this feature is still unclear

Tests have shown that for sharp-fins the interaction scale, in both streamwise and spanwise directions, depends on δ, the incoming boundary layer thickness. The sharp-fin interaction shares quite a few common flow features with the blunt-fin example, primarily in regions downstream of the leading edge. In general, the interaction generated by the blunt-fin is stronger and far more severe than the sharp-fin interaction and always leads to flow separation well ahead of the fin protuberance.

2.5.2 Blunt-fin Interaction

The earliest known investigations of blunt-fin/plate interactions were carried out in the 1960's [50] and involved heat transfer measurements using thermocouples in the interference regions generated by the blunt-fin attached to a flat plate. Since then interest in this type of interference flowfield has grown and more research into this area has been undertaken. The schematic in Figure 2.13 illustrates the general physical features seen to occur in a blunt-fin interaction. The following section will attempt to describe the processes that lead to the creation of this flow structure and their effects.

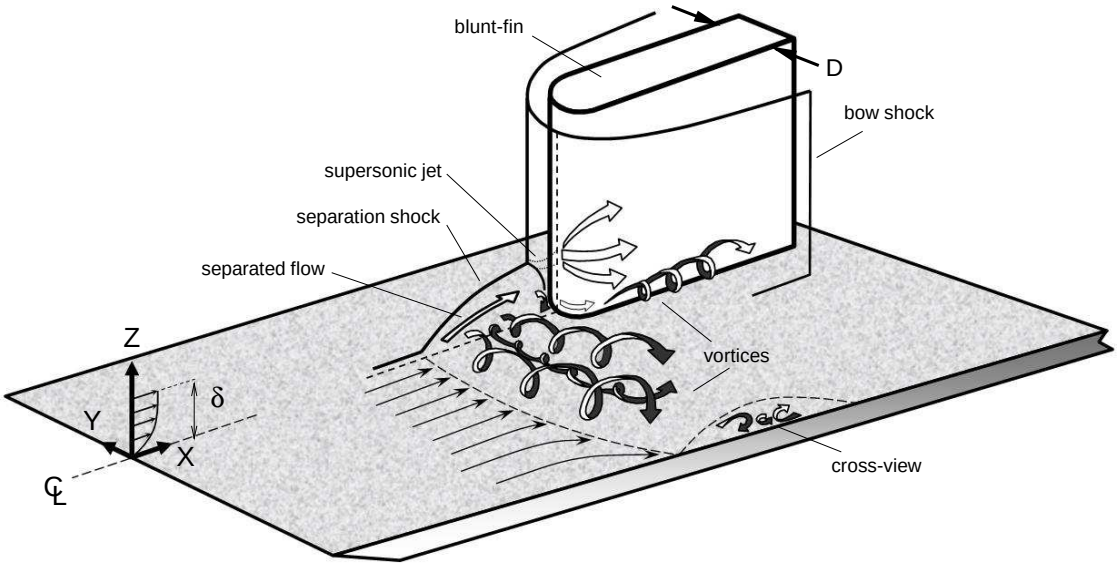

Figure 2.13: General features occurring around a blunt-fin on a flat plate

When a hypersonic flow field first interacts with the blunt-fin/plate model, two initial structures are produced. The first is a bow shock wave that forms in front of the blunt-fin so that the hypersonic flow can slow down and change direction. The second important structure is the boundary layer that forms on the flat plate in front of the fin. A portion of this layer contains subsonic flow, which allows information about the presence of the fin to travel upstream and influence the boundary layer; in particular its separation from the surface. In the initial stages of the development of this shock-wave/boundary-layer interaction, the pressure gradient caused by the bow shock travels upstream through the subsonic section of the boundary layer. This causes the boundary layer to separate from the plate and form an oblique shock, known as shock induced boundary layer separation shock. As a result of the boundary layer separating, a large disturbed flow pattern appears which covers covers a significant part of the flow upstream and downstream of the inviscid shock position.

Across the separation shock an equilibrium condition is reached that allows the mass of air entering the separated region to equal the mass of air exiting it. Downstream of the oblique separation shock the flow remains supersonic, and when this oblique shock intersects the leading edge bow shock an *Edney* Type *IV* shock-shock interaction occurs, and a third

resultant reflected shock. This shock structure creates a "lambda" type profile in the centerline plane (see Figure 2.15), and the point at which the three shocks meet is know as the "triple point". The separated region is bounded downstream by the reattachment of the boundary layer. As a result of the *Edney* Type *IV* shock-shock interaction, a supersonic jet is produced as described in Section 2.4. The impingement point of this jet on the fin produces very high pressure and heating rates on the fin surface [28].

The flow below the separation shock can be subdivided into two main regions, which are separated by a shear layer. Between the separation shock and the shear layer, the flow is effectively inviscid and travelling at supersonic speeds. Between the shear layer and the flat plate, the flow is viscous, subsonic and highly rotational, containing one or more "horseshoe" vortices. If the Reynolds number - based on the reference length, which is the distance from the leading edge of the flat plate to the front leading edge of the blunt-fin - is much less than the transitional Reynolds number the separated flow region is expected to exhibit laminar behaviour. However, if the Reynolds number is much greater, the separated flow is expected to exhibit fully turbulent behaviour. Under the latter conditions the separated region is expected to fluctuate in size and shape. Because of the large perturbations caused by the flow separation, the separated flow region may exhibit some unsteadiness below the transitional Reynolds number. However, this unsteadiness will be of lower frequency when compared with the fully turbulent case [32]. The transitional Reynolds number for this flow is assumed to be $\left(Re_{trans} = 1.3 \times 10^6\right)$ [32].

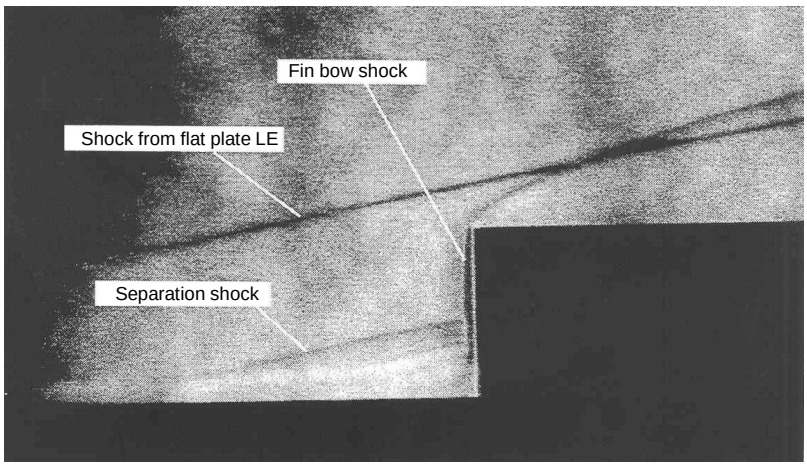

Figure 2.14: schlieren image of the interaction for a blunt-fin [53]

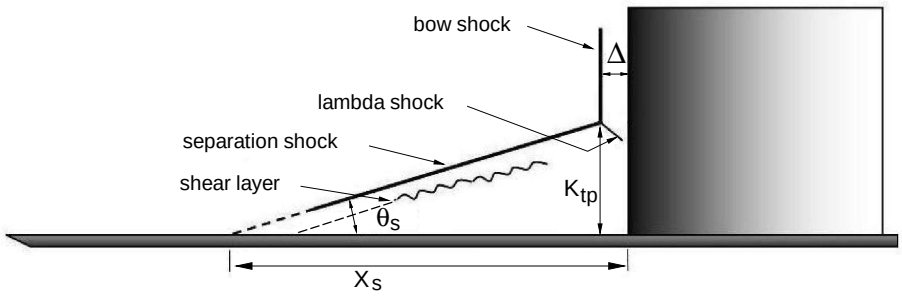

Figure 2.15: Representation of hypersonic flow over a blunt-fin on a flat plate in the plane of symmetry [32]

The schlieren image in Figure 2.14, which highlights the distribution of density gradients within a transparent medium, clearly captures the major features described above, such as the leading edge shock, fin bow shock and boundary layer separation shock. A graphical representation of the schlieren image in the plane of symmetry is shown in Figure 2.15, and indicates that the salient inviscid features produce some geometrical parameters which can be measured and be used as the basis of comparison between experimental and theoretical results. These parameters are: the shock standoff distance (Δ); the angle (θ_S) that the separation shock makes with the surface of the plate; the height (K_{tp}) measured from the plate to the triple point of the shocks; and the distance (x_S) measured from the foot of the separation shock to the fin root. These parameters will depend on the prevailing flow conditions and the geometry of the model. Since these conditions can be recreated in the numerical model, they turn out to be good variables for comparison.

The height of the triple point is an important parameter in blunt-fin interactions as it controls the approximate height for the impingement of the supersonic jet generated by this interaction which, as shown by Edney [20], results in localised regions of extremely high pressure and heat transfer. Using an un-swept cylinder mounted on a flat plate - cylinder examples are commonly used to study this type of interference flowfield because ahead of protuberance they produce the same interaction features found in blunt-fin interactions - Westkaemper [66] deduced an expression for estimating the height of the triple point using simple geometric considerations. This relationship was expressed in terms of the shock stand off distance, the angle of the separation shock and the primary separation distance. The relationship showed good agreement for a Mach number range of 2.0 - 5.0:

$$K_{tp} = (x_S - \Delta) tan\theta_S \tag{2.23}$$

From the above expression, (Δ) the shock stand-off distance in diameters can be estimated using the equation from [28] for an unswept cyclinder, as shown below:

$$\frac{\Delta}{D} = 0.76 + \frac{4.8}{(M_\infty^2 - 1)} + \frac{2.8}{(M_\infty^2 - 1)^2} \tag{2.24}$$

The shock angle (θ_S) can be found from knowledge of (M) and the pressure rise across the bow shock wave (δP) using shockwave tables.

Bogdonoff [15] and other experimentalists reasoned from experimental evidence that the shock structure was responsible in governing the scale of the interaction upstream of the fin. Consequently, changes to parameters such as fin leading edge diameter (D), fin height (K), leading edge sweep (Λ), boundary layer state and unit Reynolds number (Re/l) can affect the fin bow and oblique separation shock locations, and as a result alter the scale of the interaction. This interaction zone or length is generally measured in terms of the distance (x_S), which is measured from the initial boundary layer separation point to the fin leading edge.

- **Effects of Leading edge Diameter** (D)

  Price *et al* [50] was one of first researchers to study the effects of leading edge diameter on the scale of the interaction zone in blunt-fin interactions. It was found that for a fixed sweep, the fin leading edge diameter controlled the extent of upstream influence and the levels of subsequent interference heating on the plate and the fin. The relationship between the upstream influence and the leading edge diameter was approximately linear and apparently independent of boundary layer thickness. In addition the pressure in the disturbed flow region increased with increased fin diameter. Further work by Dolling [17] showed that in the case of the blunt obstacle, one has to distinguish two regions: Close to the obstacle in a region 2 - 3 fin diameters from the fin root, coined the "inner region", is a domain where the flow is dominated by the leading edge influence, and the flow is similar to that of a circular cylinder;

outside of this region there exists an "outer region" where the interaction properties are independent of the fin bluntness and are essentially the same as those for a sharp fin. Within the inner region, the flow properties are dictated purely by the diameter (D) of the leading edge and are nearly independent on the incoming boundary-layer thickness (δ). In particular, the upstream influence length, defined as the distance between the obstacle and the onset of the pressure rise, is particularly unaffected by a change of (δ/D). Thus, the upstream influence is a function of (D) only, nearly independent of (M) and (δ). Sedney and Kitchens [55] further demonstrated that for a cylinder obstacle the primary separation length (x_S), depends mainly on the diameter (D) and height (K) of the cylinder, and to a lesser extent the Mach number (M) and (δ).

- **Effects of Leading edge Sweep** ($\mathbf{\Lambda}$)

  Haq [28] did extensive tests with swept blunt-fins with turbulent boundary layers and Schuricht [53] using laminar boundary layers. Both showed that sweeping the fin was found to dramatically reduce the extent of the disturbed flow and significantly reduced overall levels of heating on the flat plate and swept-fin especially around the fin root. The pressures generally reduced throughout the entire interaction region. Overall the shock stand-off distance was observed to reduce and hence the upstream influence decreased. All the features on the interaction were observed to be compressed in to a smaller disturbed flow region.

- **Effects of Reynolds Number** (Re/l)

  The variation of the surface flow structures with unit Reynolds number was reported in detail by Özcan & Holt [11] [2]. It was observed from their experiments that a delicate balance existed between the vortical structures in the separated flow, and the unit Reynolds number. Özcan & Holt reported that several vortical structures could be observed, with transition from one structure to the other, occurring for small changes in the unit Reynolds number, and being perfectly reproducible. They reported that the number of separation lines dropped from 3 to 2 and from 2 to 1 as (Re/l) was increased from 1.9×10^5 to 2.3×10^6. Young et al. [70] reported similar

[2]The unit Reynolds number of the freestream was altered by changing the tunnel stagnation pressure while keeping the other freestream conditions constant. Reynolds number dependency was tested for a constant (D/δ)

findings for laminar flows past fins at ($M = 3$) and 5. This behaviour suggests a delicate balance in the separated flow, which is easily modified by slight changes in the initial conditions. Sedney and Kitchens. [55] observed for a given obstacle height, and a fixed upstream Mach number (M), the separated flow structure can change considerably with unit Reynolds number [55]. For a given boundary layer type, the effect of increasing the unit Reynolds number was seen to move the location of the pressure rise, following separation, further upstream of the fin leading edge. Furthermore, it was observed in all the experiments that the separation length increased with increasing Reynolds number.

- **Effects of Boundary Layer State**

  The state of the incoming boundary layer has a large effect on the physical scale of the interference interaction. When exposed to an adverse pressure gradient, a laminar boundary layer will separate far more readily than its turbulent counterpart because the flow in the boundary layer has very low energy (relative to the freestream) and is more easily driven by changes in pressure. Thus, for a laminar boundary layer blunt-fin interaction the initial separation point is further upstream of the fin leading edge than in the equivalent turbulent interaction. This was verified by Hung and Clauss [36] who showed that upstream separation points changing from 2.0 - 3.0 diameters in turbulent cases to 8.0 - 9.0 diameters in corresponding laminar cases; the test example was a cylinder mounted on flat plate in a ($M = 5.3$) flow. As a consequence of a larger separated region, laminar interactions have a more extensive, and complex flow structure associated with the separated region, when compared to the same region in turbulent flows.

The distributed pressure profile measured along the centerline on the plate surface ahead of the blunt-fin appears to show similarities to the profile observed over a two-dimensional forward facing step, however there are distinct differences as highlighted in Figure 2.16.

Both profiles show a rise in pressure just ahead of the separation point but, for a step flow the surface pressure typically reaches a plateau behind the separation pressure rise before final compression, however this plateau does not occur in the three-dimensional case. The range of upstream influence is dependent on the Mach number and Reynolds number [33],

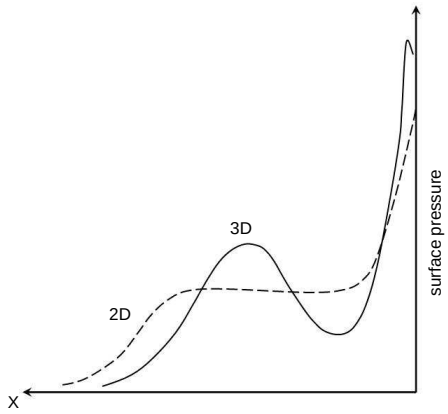

Figure 2.16: Two-dimensional vs three-dimensional pressure profile [45]

and the level of the plateau pressure is based on the free-interaction theory discussed by Chapman, Kuehn & Larson [9]. If there is a low pressure region behind the separation pressure rise in two-dimensional flow, one would expect a secondary separation in that region in response to the favourable pressure gradient. In contrast to the two-dimensional case, three-dimensional flow exhibits low pressure behind the separation pressure rise, due to a reversed high-speed flow in the primary vortex. In addition, near the junction, there exists a second peak due to flow reattachment attributed to the existence of a secondary vortex. Also, it is observed that the peak pressures encountered in the three-dimensional interactions were generally less than equivalent two-dimensional interactions due to the pressure relief present in the three-dimensional blunt-fin, allowing the compressed flow to escape around the sides.

As a result of strong entropy gradients in the shear layer of the separated region, the separated flow contains a high degree of vorticity that causes the formation of one or more horseshoe vortices depending on the geometric and flow parameters. The primary upstream separation point ($\mathbf{S}_1$), caused by the adverse pressure gradient as described above, results in the formation of a single vortex along the centerline with a strong reattachment occurring at the foot of the fin, this reattachment ($\mathbf{R}_1$) is often accompanied by large surface heat fluxes [32]. The reverse flow within this vortex initially encounters a favorable pressure gradient but, upon encountering the upstream flow is forced to separate also. This secondary separation along the centerline leads to the formation of several secondary

vortices [28]. Flowfields with 2, 4 and 6 vortices have been observed (see Figure 2.17), with the number of vortices dependent on the Reynolds number (Re/l), the Reynolds number depending on the diameter of the fin or cylinder [55]. For steady vortex systems the relative position of the vortices on the plate can be determined from the pressure distribution on the plane of symmetry upstream of the fin, which shows a pressure minima at the vortex locations.

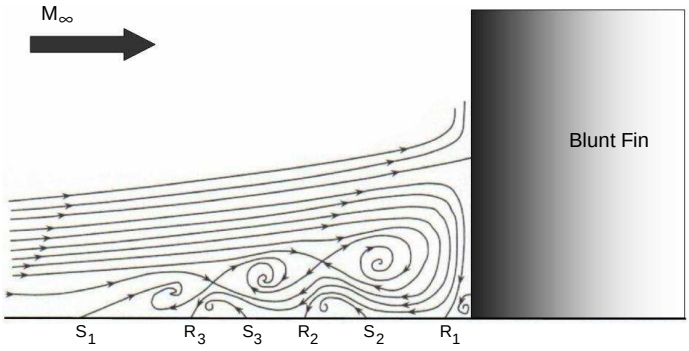

Figure 2.17: A schematic of a suggested vortex profile in the separated region for a blunt-fin [28]

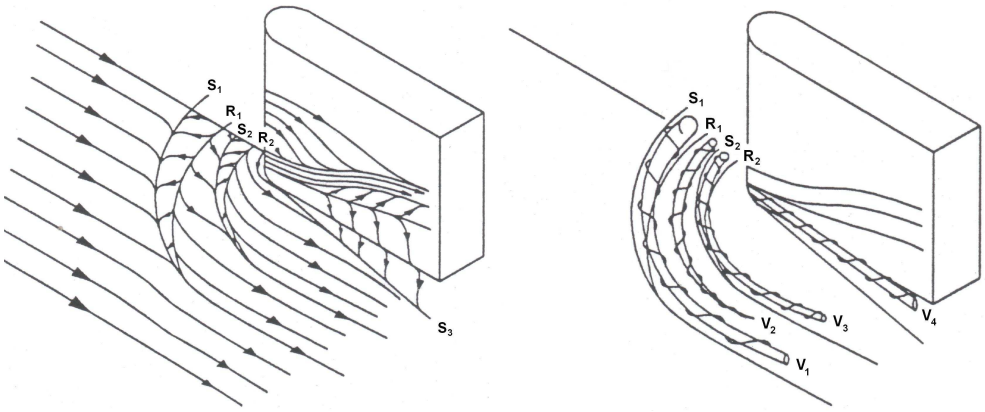

Figure 2.18: (**left**) Separation and reattachment lines for a blunt-fin [28] (**right**) Vortex skeleton presentation [28]

Examination of available experimental evidence reveals that, as the Reynolds number increases, the topology of the three-dimensional separation evolves from a single primary vortex to multiple vortices with further increases in the unit Reynolds number leading to unsteady laminar horseshoe vortex behaviour [61]. Tobak [58] hypothesized that the locations of the vortex centres in these unsteady cases are time dependent, but the streamline

pattern given in Figure 2.17 can be considered as one of the possible streamlines which succeed each other in time, thus giving a cyclic vortex structure [11].

A schematic of a suggested vortex pattern found in the separated region is shown in Figure 2.17 and the locations of the separation and reattachment lines $\big($labelled $(\mathbf{S}_1)$, $(\mathbf{S}_2)$ and $(\mathbf{R}_1)$, $(\mathbf{R}_2)$, respectively$\big)$ on the plate surface are shown in Figure 2.18.

The flowfield downstream of the blunt leading edge, which is within this large disturbed region, is dominated by effects of the fin-sidewall/plate junction. The flow structure near this junction is very similar to the observations made for a sharp-fin and exhibit the features shown in Figure 2.12. The bow shock generated at blunt leading edge intersects an oblique separation shock and as indicated a *Edney* Type *IV* shock-shock interaction occurs. The interaction point is characterised by the slip line that bounds several reflected shocklets which terminate with a normal shock as indicated in Figure 2.12. The separated region contains one or two vortices and additionally the junction of the blunt-fin/flat plate also contains a corner vortex as was found in sharp-fins.

Stollery [56] showed through oil streaks on the side of the fin several distinct features. An attachment line was observed along the windward side on the fin; emerging from the leading edge of the fin in the vicinity of the triple point shock interaction. Stollery implied that the attachment line was generated by the supersonic jet produced by these types of shock interactions. He also detected two other separation lines, one of which was thought to be related to the high pressure jet of gas trapped at the root leading edge of the fin due to the presence of a supersonic jet.

Three-dimensional fin interference heating

For thermal design purposes the peak heating in front of blunt-fin/plate junctions is of particular interest. Hung and Clauss [36] reasoned that in general, the peak interference heat factor, $(h/h_u)_{max}$ which is the heat flux on the plate or fin surface normalised with the respective undisturbed flow heat flux, can be assumed as a function of (D), (K), boundary layer thickness (δ) and free stream Mach number (M_∞). A typical dimensional anaylsis will yield:

$$(h/h_u)_{max} = f(D/\delta, K/\delta, M_\infty) \tag{2.25}$$

Hung and Clauss [36] discovered that a heating increase with (K) was obvious until (K) reached a certain value where further increase in (K) caused no significant heating increase. They stated that this could as a result be used as a criteria for defining short and long protuberances (such as fins and cylinders). Since then many authors have attempted to classify protuberances in a supersonic/hypersonic flow as either large/long or small/short, depending on certain parametric relationships generally involving the fin height (K), and to relate the interaction scale to other flow and protuberance properties. It is generally considered that a protuberance is large/long if it produces an "asymptotic result"; a condition where an increase in the fin height no longer produces an increase in the interaction extent. This limit is generally accepted to be reached when the (K/D) ratio is greater 2.5.

For short protuberances in laminar flow [3], the largest (h/h_u) ratio can be estimated from the following relations,

$$h/h_u = (2.5 \sim 4.25)(K/\delta)^{1.5} \tag{2.26}$$

and in turbulent flow

$$h/h_u = (5.2 \sim 7.3)(K/\delta)^{0.863} \tag{2.27}$$

where (h) is heat transfer coefficient for the interference flowfield and (h_u) is the local undisturbed (no protuberance) heat transfer coefficient. For a long cylinder, the observed heating trend for both laminar and turbulent flows is,

$$h/h_u = (4.2)(D/\delta)^{1.38} \tag{2.28}$$

[3]- The following relations are referenced from the work of Haq [28]

The boundary between small and large protuberances depends on the boundary layer state, and the conditions set by Hung and Clauss [36] are ($D/\delta \sim 2$) for a turbulent layer and ($D/\delta \sim 6$) for a laminar flow. The expressions appear to highlight a significant difference between small and large protuberances. It appears that for a small protuberance (h/h_u) depends on (K/δ) whilst for a long protuberance (h/h_u) is scaled by (D/δ).

2.6 Overview of Previous Computational Work

With a considerable database of experimental results available for turbulent and laminar blunt-fin flowfields, the development of numerical schemes to compute these flowfields has grown steadily throughout the years. Initially all computational methods developed were for solving turbulent boundary layers, this bias is partly based on the fact that at the time there was a greater volume of available data for turbulent cases compared to laminar flows. Reflecting this trend in history in the following section, outlined are three different cases of blunt-fin turbulent interactions studied and, two laminar cases from the last thirty years.

2.6.1 Turbulent Computational Work

One of the earliest successful computations of the blunt-fin interaction was presented by Hung and Buning [33] in 1984, and was achieved by solving the Reynolds averaged Navier-Stokes equations for a turbulent flow. The flow was supersonic (M = 2.95), with a (Re/l = 6.3×10^7) using a ($\kappa - \epsilon$) turbulence model over a blunt hemi-cylindrical fin with a (D/δ = 7) at zero incidence. They compared their computations to the experimental results of Dolling and Bogdonoff [16].

Predictions of the pressure field on the nose of the blunt-fin correlated well with the experimental data, but the peak pressure on the stagnation line (related to the impingement of the supersonic jet) was under predicted. Comparison of the streamwise pressure distribution on the plate ahead of the fin and at two outboard stations correlated well within experimental data and all the main features such as the upstream influence, the pressure

rise due to the separation shock, and the double pressure peak (see Figure 2.16), were well simulated.

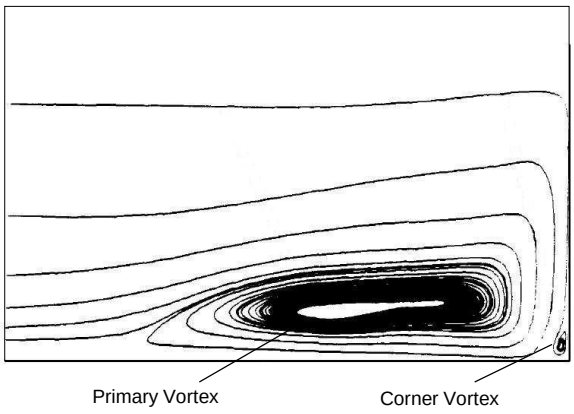

Figure 2.19: Horseshoe vortex flowfield, particle paths in the plane of symmetry [34]

Calculated particle paths in the plane of symmetry of the interaction (see Figure 2.19) indicated the presence of a large flattened horseshoe vortex structure well ahead of the fin and another smaller secondary corner vortex close to the fin-plate junction. For the case calculated, the separation shock was very weak and was smeared out over several mesh points, therefore, a sharp triple point at the intersection of the bow shock and separation shock was not observed. A strong Mach number variation in the region behind the bow shock close to the predicted pressure peak was not apparent, and so the computations had failed to predict the presence of the supersonic jet which is characteristic of this type of interaction. However the computations indicated that the size and location of the horseshoe vortices is dominated by the inviscid characteristics of the interaction, in particular the bow shock. As a result they summarised the effect (D) has on the flow.

The researchers concluded that agreement between the computed results and measured pressure distribution was very good despite the limited mesh resolution. However, the computational techniques needed refining particularly in the areas of shock capturing and, an improved resolution via increased density of mesh points.

In 1994 Tutty *et al* [60] simulated a turbulent flow over a blunt-fin/flat plate configuration, and specifically looked at the heat flux on the flat plate and fin. The flow was hypersonic (M = 6.85), with a ($Re/l = 5.4 \times 10^7$) and a ($K/D = 2.8$) at zero incidence. The code used

was termed SPIKE, a Navier-Stokes code developed by Fluid Gravity Engineering containing a Baldwin-Lomax turbulence model. The computational model was built around a blunt-fin with a diameter of $10mm$ at zero incidence and sweep. Contour maps of the heating distribution around the fin for both experiment and computation were presented.

General agreement on the shape of the features was noted. However, the numerical calculations overpredicted the location of the initial rise in heat flux upstream of the fin. This discrepancy was thought to be due to the rather coarse grid used in this preliminary study. Reasonable agreement was also shown for the centerline heating distribution, although the computation predicted that, close to the fin leading edge, the heat transfer coefficient peaks at 25 times the undisturbed value at the fin leading edge location. Comparison of experimental oil flow and heat transfer data with the numerical results indicate that the peak in heat transfer close to the fin is due to the impingement of the small corner vortex on the flat plate, and that the peaks and valleys in heat transfer correspond to the local reattachment and separations of the vortical flow structure.

Since then several turbulent numerical studies have been undertaken in hypersonic blunt-fin interactions. A very detailed study of swept and unswept blunt-fin interactions using a turbulent boundary layer were undertaken in 1998 by Yamamoto *et al* [68]. The flow was hypersonic (M = 3.92), with a ($Re/l = 1.26\times10^7$) and a ($D/\delta = 10$). The numerical scheme was a high-resolution finite-difference method based on a fourth order compact MUSCL ,TVD scheme with a modified AUSM and the maximum second-order LU-SGS scheme was employed to simulate unsteady flows associated with shock/shock and shock/turbulent boundary layer interactions.

The results obtained for the unswept blunt-fin showed a cyclic system associated with a system of separation shocks produced by several separation bubbles in the separated region. These produce multiple shock/shock interactions with a resultant mixture of several supersonic jets which combine to influence the characteristics of the separated flow (see Figure 2.20). Finally a flow accelerated by the jets becomes a large-scale supersonic jet. The jet streams into the separation bubbles and disturbs them, which causes the number of bubbles to change according to the strength and direction of the jet. This cyclic system was found to dominate the unsteady flow mechanism of the shock/turbulent

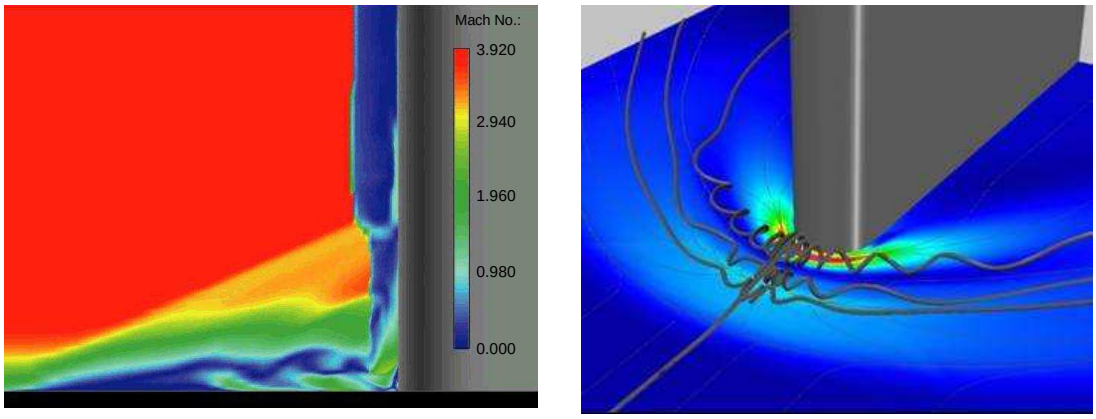

Figure 2.20: (**left**) Mach contours in the plane of symmetry of the flow [68] (**right**) Streamline vortex core paths around the blunt-fin [68]

boundary layer interaction. The results also appeared to indicate that the locations of the vortex centers were time dependent, but the time-averaged surface locations where the vortices are shed remain approximately constant.

Yamamoto also looked at swept blunt-fins and concluded that sweeping the fin from $0°-30°$ degrees resulted in a dramatic reduction in the upstream influence, a sharp decline in the final peak pressure levels, and generally reduced pressures throughout the entire interaction region. The streamlines in the symmetry plane confirmed that the horseshoe vortices were progressively weakened and reduced in size with increasing sweep.

2.6.2 Laminar Computational Work

In 1994 Lakshmanan and Tiwari [45] analysed a supersonic laminar boundary layer blunt-fin/flat plate junction through computation. They employed a three-dimensional Navier-Stokes code utilising the MacCormacks time-split, finite volume technique and investigated the effect of Mach number and Reynolds number on the flow. The flow was supersonic (M = 2.36), with a ($Re/l = 2.7 \times 10^6$) and a (D/δ = 7-30) at zero incidence.

They reported that increasing the freestream Mach number, decreased the extent of separation ahead of the fin. This was caused due to the subsequent reduction in the bow shock stand-off distance, which would be expected to reduce the size of the interaction region.

The parametric study also revealed a dependency of the number of vortices with the flow Mach and unit Reynolds number. Moreover, with an increase in the freestream Mach and unit Reynolds numbers, the primary horseshoe vortex bifurcated into two vortices rotating in the same direction (see Figure 2.21). Increasing the Mach number is also reported to reduce the maximum reverse flow velocity close to the plate and in addition lower the height of the reverse flow region.

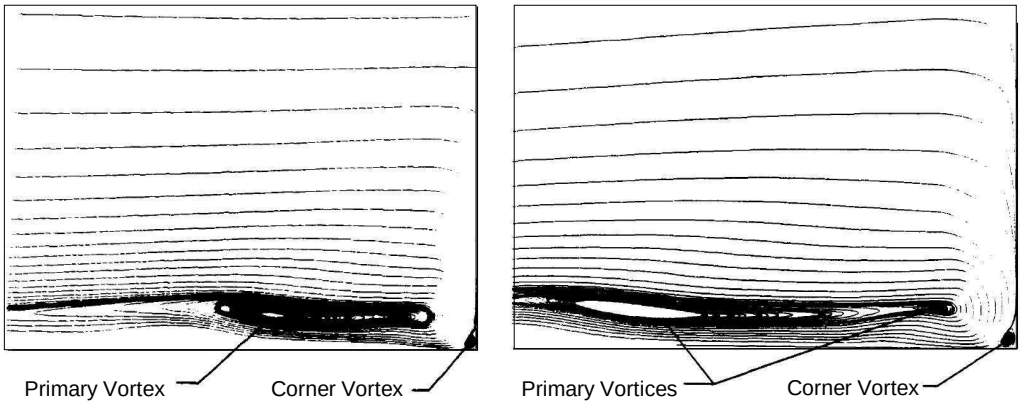

Figure 2.21: Horseshoe vortex flowfield, particle paths in the plane of symmetry [34] (**left**) $Re/l = 1.2 \times 10^6$ (**right**) $Re/l = 5.0 \times 10^6$

The most recent numerical studies to date using laminar boundary layers was done by Houwing *et al* [32]. However the numerical simulations were used mainly as a supplementary tool and for some comparative correlations with experimental results. The flow was hypersonic (M = 6.1 - 6.9), with a ($Re/l = 4.5 \times 10^6$) and a ($K/D = 2.63$) at zero incidence.

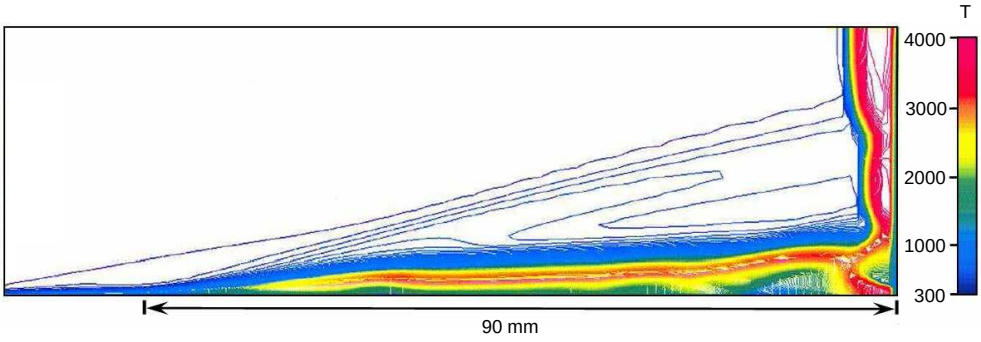

Figure 2.22: Temperature field in the plane of symmetry of the flow [32]

Nevertheless some good detail was obtained from the simulations. For example, Figure 2.22 shows the contour profiles for temperature in the centerline symmetry plane. Clearly visible are the shear layer, the separated boundary layer beneath and fin bow shock. These CFD results provide insight into the complexity of the separated flow region, which because of the limited experimental data available, had previously remained as conjecture.

2.7 Motivation for Present Study

The review of past published work covering hypersonic blunt fin interactions has shown that recent computational work has focused mainly on the study of turbulent boundary layer/fin plate interactions, leaving the laminar boundary layer flowfield under-studied.

The scope of the present study is therefore to advance the knowledge of hypersonic laminar boundary layer/fin plate interactions and to compare with or corroborate laminar hypersonic experimental data obtained at the University of Southampton by Schuricht [53].

From the numerical simulations it is hoped to observe the following points:

- The complex three-dimensional nature and major flow features associated with laminar blunt-fin interactions, in particular mapping the path of the horseshoe vortices present in the separated region of the flow.
- The effects of blunt-fin diameter and height on the general scale of the interaction including for example correlation of separation lengths.
- The effects of fin sweep on the general scale of interaction, including correlation of separation lengths.

The primary interest would be to explore the similarities/differences in flat plate heating profiles between the numerical analysis and the experimental data. If there are differences, possible mechanisms for the differences will be postulated.

Chapter 3

The Numerical Method

3.1 Introduction

Computational Fluid Dynamics (*CFD*) is the numerical simulation of flowfields through the approximate solution of the governing partial differential equations for mass, momentum, and energy conservation coupled with the appropriate relations for thermodynamic and transport properties. The approximate solution of the governing equations requires that the domain be subdivided into many small control volumes. The accuracy of the solution depends upon a variety of factors; the most critical factors are the size of each control volume, the orientation of its boundaries relative to a variety of flow features, and the order of accuracy of the discretization.

Although *CFD* methods have recently become a popular tool in engineering design to complement experimental data, the nature of hypersonic flows which routinely involve extremes of pressure, density, and temperature separated by shocks, expansions, shear layers, and boundary layers; these extremes in conditions and topology of flow structure complicate and present significantly larger challenges in the development of computational capabilities for analyzing hypersonic flows compared to subsonic or supersonic flows.

The main problems in hypersonic continuum *CFD* are the physical-chemical modelling of non-equilibrium flows, surface treatments (catalytic effects) and shock capturing - however

in present study these issues are ignored.

Solving the equations in a supersonic/hypersonic regime produce shocks and sonic lines, i.e. "discontinuities". These discontinuities can be described as extremely thin regions with sudden changes in flow properties, and the modelling of such discontinuities is disturbed by local losses of accuracy and smearing out, related to the numerical discretization of the hyperbolic inviscid Navier-Stokes (or Euler) equations.

In addition, the ability to orient a grid with evolving flow structures is another particularly challenging feature of hypersonic flows. For example, accurate simulation of heat transfer requires adequate resolution of the boundary-layer and accurate representation of conditions at the boundary layer edge. In turn, conditions at the boundary-layer edge particularly in the stagnation region of hypersonic flows are dependent on entropy carried along streamlines from the shock. Any irregularities in the captured shock create associated irregularities in entropy that feed the rest of the domain.

Taking into account some of the difficulties highlighted above, the inconsistencies in results produced by various computational methods because of inherent differences in the numerical technique has not promoted confidence in hypersonic *CFD* codes.

However, due to the lack of available ground facilities for realistic testing at high Mach numbers and due to the complex and integrated nature of the flowfield, traditional wind-tunnel based design and analysis techniques are not adequate. Further complicating experimental analysis of such flows is the limited range of experimental diagnostic techniques available for "probing" flows, particularly at high Mach numbers. This becomes an important issue for complex flows such as those considered here. Consequently, *CFD* methods for simulating hypersonic flows have received considerable attention in the recent past and have been pushed forward to become an important asset in understanding and highlighting key problem areas of complex flows. *CFD* methods also provide considerable benefits in terms of cost and time efficiency, due to the ability of performing computations at vastly reduced time scales compared to setting up and running an experimental facility. In addition, results obtained by *CFD* and experimental data are generally complementary and help improve our understanding of the flow physics involved, and are proving to be a promising alternative for analysis, design, and even optimization of hypersonic vehicles

and propulsion systems.

The following points highlight the properties essential to any numerical algorithm used in fluid dynamics; these being "consistency", "accuracy", "stability" and "convergence".

Consistency

- Discretization should become exact as the grid spacing (or time step) tends to zero.
- Truncation error $\longrightarrow 0$ as $(\Delta x \rightarrow 0)$ and $(\Delta t \rightarrow 0)$.
- *Truncation error* (τ_h): difference between the differential conservation equation $(\Im)$ and the corresponding discretized algebraic equation (L_h) on grid level h:
$\Big[\Im(\Phi) = L_h(\Phi) + \tau_h\Big]$ where (Φ) is the exact solution of the differential equation $(\Im)$.

Accuracy

- Accuracy of a solution means how close the solution is to the actual physical field.
- Most of the errors produced in the numerical simulation of a system can be removed by careful programming but systematic errors are always present.
- Many sources of error contribute to reduced accuracy:

Modelling error: difference between exact solution of mathematical model (conservation equations) and actual physical flow.

Discretization error: as defined above.

Convergence error: difference between the iterative solution and the exact solution of the algebraic system of equations.

- If exact (physical) solution is not known, absolute accuracy can only be estimated.

Stability

- Solution is called stable (bounded) when the method does not magnify the errors from iteration to iteration.
- Despite the accumulation of errors (truncation or discretization errors, and round-off errors caused by machine precision) solution should not diverge.
- The most common approach to stability of an algorithm is the von Neumann's linear method which gives the domain of stability of the solution, relating flow properties with grid spacing (Δx) and time step (Δt).

Convergence

- Solution is called convergent when the exact solution of the discretized equation tends to the exact solution of the differential equation as (Δx), (Δt) tend to zero.
- Discretization error $\longrightarrow 0$ as $(\Delta x \rightarrow 0)$ and $(\Delta t \rightarrow 0)$.
- *Discretization error* (ϵ_h^d): difference between exact solution of the mathematical model (Φ) and exact solution of the discretized algebraic system (ϕ_h): $\left[\Phi = \phi_h + \epsilon_h^d\right]$.
- "In a well-posed problem, consistency and stability are necessary and sufficient conditions for convergence."

3.2 The Numerical Scheme

The current numerical method in its initial form was developed and implemented by Navarro-Martinez [47], on the basis of the work of Amaratunga [1]. For a detailed background on the numerical preliminaries to the numerical method, see [47]. The author has modified the algorithm accordingly to account for the present characteristics of the problem. However for completeness, a general description of the workings of the entire numerical method shall be outlined.

This Chapter shall give a basic overview of the characteristics of the numerical algorithm. In the numerical scheme, a brief description is given of the two different time stepping methods; the explicit and implicit method used in this study. Which is followed by a description of the methodology for evaluating both the Inviscid and Viscous contributions to the Navier-Stokes equations. The formulation of the explicit and implicit boundary conditions for the numerical method is then outlined along with the methodology for solving the non-linear equations in the implicit method. This is then followed with a description of how the numerical scheme was modified to run on a parallel platform to allow for large three-dimensional calculations. Finally, the methods used to generate the different computational grids used in the simulation and the convergence criteria for the different simulations runs is followed by the Interpolation schemes used to save computational time.

It is important to note that, due to the actual complexity of the real flowfield, viscous forces cannot be neglected and in hypersonic flow viscous forces play an important part,

particularly near body surfaces and separated regions. Under these conditions it is necessary to integrate in time the full set of Navier-Stokes equations until a steady-state (if existent) is reached. A full description of the Navier-Stokes equations and their underlying assumptions can be found in Appendix B.

Outlined below are the two numerical schemes implemented in the existing code. The first section looks at the explicit formulation and the implicit method is then described in the following section.

3.2.1 Explicit Method

To take into account the multi-dimensional nature of the flow, the Navier-Stokes equations found in Appendix A are written in their integral form. Here we introduce the vectors ($\mathbf{U}$), ($\mathbf{F}$) and ($\mathbf{F}_v$), which are the vectors of m-conserved variables $\left(u_i(x,t) \right)$ and fluxes of the inviscid and viscous components (F, G, H) and (F_v, G_v, H_v) respectively.

$$\frac{\partial U}{\partial t} + \nabla \mathbf{F} = \nabla \mathbf{F_v} \tag{3.1}$$

Upon integrating the above Eqn 3.1 over a control volume (V), we obtain the following relation

$$\int_V \frac{\partial U}{\partial t} dV + \oint_S \mathbf{F}.\mathbf{n}\, dS = \oint_S \mathbf{F_v}.\mathbf{n}\, dS \tag{3.2}$$

where ($\mathbf{n}$) is defined as the outward normal vector of the surface (S) limiting the volume (V). At this point we introduce the definition of an average state ($\bar{U}$) as

$$\bar{U} = \frac{1}{V} \int_V U dV \tag{3.3}$$

Substituting the above expression into Eqn 3.2 we obtain the following semi-integral form

$$V\frac{\partial \bar{U}}{\partial t} = \oint_S (\mathbf{F_v} - \mathbf{F}).\mathbf{n}\, dS \tag{3.4}$$

Discretising the computational domain into a collection of polyhedral cells, the control volume (V) is replaced by the volume of the i-th cell which is bounded by (N_f) faces, thus making it possible to split Eqn 3.4 into an expression that is the sum of the surface integrals over the faces

$$V_i\frac{\partial \bar{U}_i}{\partial t} = \sum_k^{N_f} \oint_{S_k} (\mathbf{F_v} - \mathbf{F}).\mathbf{n}\, dS_k \tag{3.5}$$

and averaging the flux in the k-surface

$$\hat{F_k} = \frac{1}{\Delta S_k}\int_{S_k} (\mathbf{F_v} - \mathbf{F}).\mathbf{n}\, dS_k \tag{3.6}$$

By collating the viscous and inviscid contributions, the governing equations written in a semi-discrete form are

$$\frac{\partial \bar{U}_i}{\partial t} = \sum_k^{N_f} \frac{\hat{F}_k \Delta S_k}{V_i} \tag{3.7}$$

The equation is averaged in space, but not in time. A further average of the above expression between the time levels (n) and $(n+1)$ gives the following equation in conservative form

$$\bar{U}_i^{n+1} = \bar{U}_i^n + \Delta t \sum_k^{N_f} \frac{\tilde{F}_k \Delta S_k}{V_i} \tag{3.8}$$

where $\left(\Delta t = t^{n+1} - t^n\right)$ is the time step and $\left(\tilde{F}_k^n\right)$ is the space and time average of the flux over the k-surface at the (n) time level

$$\tilde{F}_k^n = \frac{1}{\Delta t}\int_{t^n}^{t^{n+1}} \hat{F}_k(t) dt \tag{3.9}$$

Following a couple of numerical steps, the time averaged explicit backward Euler finite volume scheme is defined as

$$\bar{U}_i^{n+1} = \bar{U}_i^n + \Delta t \sum_k^{N_f} \frac{\hat{F}_k^n \Delta S_k}{V_i} \tag{3.10}$$

Linear stability conditions, like the von Neumann method, impose restrictions on the allowable time step (Δt). This time step is strongly dependent on the wave speed propagation of hyperbolic conservation laws and grid size. Diffusion and source terms usually have smaller time scales and they can further reduce the allowable time step. The most famous condition, the Courant-Friedrich-Levy (CFL) restriction which comes out of the stability analysis, is the idea that the "numerical" domain of dependence of the solution should contain the "physical" domain of convergence. For an ordinary one-dimensional conservative method, this condition may be expressed as

$$\Delta t_{CFL} = CFL \left| \frac{\Delta x_i}{Max(S_{i-\frac{1}{2}}, S_{i+\frac{1}{2}})} \right| \tag{3.11}$$

where CFL is called the Courant number (or simply the CFL number) and is implemented as a user-given security factor. In steady situations, the desired results are obtained in the limiting state when ($t \to \infty$), thus small time steps are a big restriction in marching schemes, consuming an excess of computational effort. In order to circumvent the CFL restriction and speed up the solution process we introduce the "implicit" method.

3.2.2 Implicit Method

Explicit schemes as expressed above have very limiting constraints on the allowable time step (Δt) used by the viscous solver (see Batten *et al* [6]). An estimate for the viscous time step (Δt_C) was quoted by Turkel [59] as being

$$\Delta t_C \leq \frac{\rho P_r \Delta \xi^2}{4\gamma\mu} \tag{3.12}$$

where $(\Delta\xi)$ is a characteristic dimension of the cell. In addition, the CFL condition in Eqn 3.11 also restricts the time step (Δt_{CFL}), due to the inviscid part of the equations. Usually for highly viscous flux $(\Delta t_c << \Delta t_{CFL})$. To bypass such restrictions an implicit approach is adopted, where the time-averaged flux $\left(\tilde{F}^n\right)$ of Eqn 3.8 is replaced by the space-averaged flux at time level $(n+1)$ - $\left(\hat{F}^{n+1}\right)$, thus giving a new conservative scheme

$$\bar{U}_i^{n+1} = \bar{U}_i^n + \Delta t \sum_k^{N_f} \frac{\hat{F}_k^{n+1} \Delta S_k}{V_i} \tag{3.13}$$

The inviscid and viscous average fluxes are approximated at the new time level by a truncated Taylor expansion [6] as

$$\hat{F}^{n+1} \approx \hat{F}^n + \left(\frac{\partial \hat{F}}{\partial U}\right)^n \delta U \tag{3.14}$$

where (δU) states for the difference between the vector of conserved variables at time levels (n) and $(n+1)$: $\left(\delta U = \bar{U}^{n+1} - \bar{U}^n\right)$. Throughout the remainder of this work, the average variable $(\bar{U})$ will be referred as (U), in the same manner the space average flux $(\hat{F})$ will be replaced by (F). Substituting Eqn 3.14 in Eqn 3.13 eventually results in an Implicit semi-discretisation of the mass-averaged Navier-Stokes equations as

$$\left[\frac{V_i}{\Delta t}\mathbf{I} - \sum_k^{N_f} \left(\frac{\partial F}{\partial U}\right)_k \Delta S_k\right] \delta U = \sum_k^{N_f} F_k^n \Delta S_k \tag{3.15}$$

Further detail on the intermediate numerical steps in the above analysis can be found in the works of Batten *et al* [6].

The implicit scheme presented above does not have the CFL restrictions on time step as compared to the explicit scheme, this is because the numerical domain of dependence is much larger and therefore it is possible to use a time step (Δt) which is larger than in the explicit scheme. However, because of the iterative methods used to solve for the linear system of equations in the implicit method as described in Section 3.6, there is an associated overall computational cost increase per time step. Therefore in all cases the implicit method is more expensive per time step than the explicit method, but this

drawback is overcome by being able to use much larger time steps and hence be more efficient in finding a steady state solution.

3.2.3 B2 scheme

The B2 scheme, proposed by Batten *et al* [6], was developed to dampen or dissipate the oscillatory effects between alternative time steps, of using slope limiters, which are described in Section 3.3.3, in the Godunov method. This oscillation had the effect of preventing convergence of the numerical scheme to machine zero, and the phenomenon is associated with the artificial non-linearity introduced through the slope limiter in the discretisation scheme. Batten *et al* [6] proposed a temporal first order two-step integration implicit model, denoted B2:

$$U^{n+1} = U^n + \frac{\Delta t}{2V_i}\left(\sum_k^{N_f} F_k^{n+\frac{1}{2}} + \sum_k^{N_f} F_k^{n+\frac{3}{2}}\right) \tag{3.16}$$

The use of this scheme can be easily implemented by two successive backward Euler steps.

$$\delta U = B1(U^n, \Delta t) \tag{3.17}$$

$$U^{n+1} = U^n + \delta U \tag{3.18}$$

there after the B2 scheme is implemented as follows

$$\delta U^* = B1(U^n, \Delta t/2) \tag{3.19}$$

$$U^* = U^n + \delta U^* \tag{3.20}$$

$$\delta U^{**} = B1(U^*, \Delta t) \tag{3.21}$$

$$U^{n+1} = U^* + \delta U^{**}/2 \tag{3.22}$$

3.3 Inviscid Compressible Flow

The inviscid contribution of the Navier-Stokes equations are governed by the Euler equations

$$\frac{\delta U}{\delta t} + \frac{\delta F}{\delta x} + \frac{\delta G}{\delta y} + \frac{\delta H}{\delta z} = 0 \tag{3.23}$$

where (F), (G) and (H) are defined in Appendix A. To compute the inviscid contribution to the flux a Godunov method is used, which involves the solution of a local Riemann problem.

3.3.1 Godunov Method

In the Godunov method, the average inviscid flux of Eqn 3.6 is defined by

$$\hat{F}_k = \frac{1}{\Delta S_k} \int_{S_k} \mathbf{F}.\mathbf{n}\, dS_k \tag{3.24}$$

where each face of the cell (S_k) is obtained as a solution to a one-dimensional Riemann problem between two states, (U_L) and (U_R). These states are approximated by cell values in the first order extrapolation or by interpolated values in higher order extensions. The average flux may be redefined as

$$\hat{F}_k = F_{RP} = \mathbf{F}(U_{RP}).\mathbf{n} \tag{3.25}$$

where (U_{RP}) is the solution obtained with the Riemann solver which is a function of (U_L) and (U_R).

The Riemann solver used in the present study is the HLLC type. The choice of solver is based primarily on the following points: the HLLC type does not require artificial correction parameters compared to other Riemann solvers and its demonstrated successful implementation in compressible flows. In addition this solver incorporates the most

detailed physics while there is no need for artificial entropy correction and, due to its robustness, allows the use of implicit schemes.

3.3.2 HLLC Rieman solver

The value of (U) at the interface $(i+\frac{1}{2})$ is defined by

$$U_{i+\frac{1}{2}}^{HLLC} = \begin{cases} U_L & \text{if} \quad a_L > 0 \\ U_L^* & \text{if} \quad a_L \leq 0 < a_M \\ U_R^* & \text{if} \quad a_M \leq 0 \leq a_R \\ U_R & \text{if} \quad a_R < 0 \end{cases} \tag{3.26}$$

and the corresponding interface normal numerical flux (F) at $(i+\frac{1}{2})$, for Eqn 3.26, is defined as

$$F_{RP}^{HLLC} = \begin{cases} F_L & \text{if} \quad a_L > 0 \\ F_L^* = F_L + a_L(U_L^* - U_L) & \text{if} \quad a_L \leq 0 < a_M \\ F_R^* = F_R + a_R(U_R^* - U_R) & \text{if} \quad a_M \leq 0 \leq a_R \\ F_R & \text{if} \quad a_R < 0 \end{cases} \tag{3.27}$$

where $\big(F* = F(U*)\big)$. For more details on estimating the average state (U^*) see Appendix B.

To implement the HLLC Riemann solver in the Godunov method the following steps are performed :

Step I: Compute the wave speeds a_L, $a*$ and a_R

Step II: Compute the states for U_L^* and U_R^*

Step III: Compute the HLLC flux according to Eqn 3.27 and use it in the conservative formula $u_i^{n+1} = u_i^n + \frac{\Delta t}{\Delta x}\Big[f_{i-\frac{1}{2}}^n - f_{i+\frac{1}{2}}^n\Big]$.

The Average State Jacobians

For the implementation of implicit method Eqn 3.15, the jacobians for the inviscid and viscous fluxes have to determined. Batten *et al* [7] defined the average-state inviscid Jacobians for the flux at level $(n+1)$ on the Riemann problem as

$$F_{RP}^{n+1} = \begin{cases} F_L + \frac{\partial F_L}{\partial U_L}\delta U_L & \text{if} \quad a_L > 0 \\ F_L^* + \frac{\partial F_L^*}{\partial U_L}\delta U_L + \frac{\partial F_L^*}{\partial U_R}\delta U_R & \text{if} \quad a_L \leq 0 < a_M \\ F_R^* + \frac{\partial F_R^*}{\partial U_L}\delta U_L + \frac{\partial F_R^*}{\partial U_R}\delta U_R & \text{if} \quad a_M \leq 0 \leq a_R \\ F_R + \frac{\partial F_R}{\partial U_R}\delta U_R & \text{if} \quad a_R < 0 \end{cases} \tag{3.28}$$

where $\left(\frac{\partial F^*}{\partial U_R}\right)$ and $\left(\frac{\partial F^*}{\partial U_L}\right)$ are the average state Jacobians. A complete description of how these jacobians are calculated is found in Appendix B.

3.3.3 MUSCL Slope Limiting

A MUSCL linear reconstruction scheme is used to obtain formal second order accuracy. As a second order extension to the Godunov method the Minmod scheme given by Amaratunga [1] is used. Defining the following, $\left(\Delta U_{i+\frac{1}{2}} = U_{i+1} - U_i\right)$, $\left(\Delta U_{i-\frac{1}{2}} = U_i - U_{i-1}\right)$, and $\left(\Delta_{i,j} = x_i - x_j\right)$ as the right and left derivatives with the respective slopes defined as $\left(\phi_l = \frac{\Delta U_{i-\frac{1}{2}}}{\Delta_{i,j-1}}\right)$ and $\left(\phi_l = \frac{\Delta U_{i+\frac{1}{2}}}{\Delta_{i+1,j}}\right)$.

The Minmod Slope limiter states the slope in the i-th cell, (ϕ_i) as

$$\phi_i = \begin{cases} 0 & \text{if } \phi_l\phi_r \leq 0 \\ min\left\{k\left|\frac{\Delta U_{i+\frac{1}{2}}}{2\Delta_{i+\frac{1}{2},i}}\right|,\ k\left|\frac{\Delta U_{i-\frac{1}{2}}}{2\Delta_{i,i-\frac{1}{2}}}\right|\right\} sgn(\phi_l) & otherwise \end{cases} \tag{3.29}$$

Where the control parameter (k) offers the possibility to use slope limiters more or less "diffusive". For $(k = 0)$ the slope limiting process switch off and recover the first order scheme.

Multi-dimensional *MUSCL*

To take into account the conservation of the variables across the whole volume of an arbitrary cell, the equation $\left(u_i = \frac{1}{\Delta x}\int_{x_{i-\frac{1}{2}}}^{x_{i+\frac{1}{2}}} \tilde{u}_i(x,t)dx\right)$ is transformed to

$$U_i = \frac{1}{V_i}\int \tilde{U}(x,y,z,t^n)dV \tag{3.30}$$

where (V_i) is the volume of the cell. For a tri-dimensional centered grid, the *MUSCL* distribution can be expressed as

$$U_{i+\frac{1}{2}} = U_i + \frac{\Delta\xi_{min}}{2}\sqrt{\frac{V^-}{V^+}}\phi_i \tag{3.31}$$

$$U_{i-\frac{1}{2}} = U_i - \frac{\Delta\xi_{min}}{2}\sqrt{\frac{V^+}{V^-}}\phi_i \tag{3.32}$$

where (ϕ_i) is again the slope limiter function, $(\Delta\xi_{min})$ is the minimum distance in the (ξ) directions from the cell centre to either $(i+\frac{1}{2})$ or $(i-\frac{1}{2})$ interface. The tetrahedra volume balances in Eqns 3.31and 3.32 are required to preserve conservativity with the slope limiting process. This is evident by the fact that the new distribution of (U) satisfies

$$(U_{i+\frac{1}{2}} - U_i)V^- - (U_i - U_{i-\frac{1}{2}})V^+ = 0 \tag{3.33}$$

and therefore reaverages to the original cell averaged value (see Figure 3.1).

As a result the new interpolation values used in the HLLC Riemann solver are

$$\begin{aligned} U_l &= U_i + \delta U_i \\ U_r &= U_{i+1} + \delta U_{i+1} \end{aligned} \tag{3.34}$$

where (δU_i) and (δU_{i+1}) are slope corrections in the cell (i) and $(i+1)$, respectively, obtained from Eqns 3.31and 3.32.

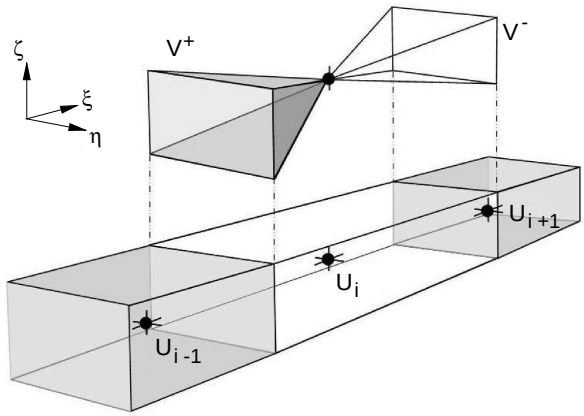

Figure 3.1: *MUSCL* slope limiting reconstruction in a three dimensional arbitrary cell, with V^+ and V^- the corresponding volumes in the ξ direction

Three-dimensional Metric Calculations

Calculating the volume balance, (V^+) or (V^-) respectively in each arbitrarily cell is an important pre-requisite to using the *MUSCL* method. One of the attractive features of the finite-volume approach is its ability to be used on any generalized orientated coordinate system. The only information about the mesh that we transmit to the method is the three curvilinear coordinates of the eight vertices of every cell in the mesh, as shown in Figure 3.2. With this information, we can calculate the metric coefficients strictly by the principles of geometry.

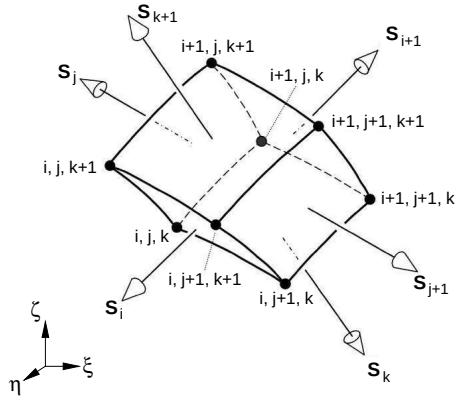

Figure 3.2: A typical computational cell i, j, k

With information on the four vertices the surface area is given exactly by one half the cross product of its diagonal line segments (see [40, 42]). With reference to Figure 3.3.

$$S_{5678} = 0.5(r_{75}\times r_{85} + r_{65}\times r_{75}) = 0.5(r_{75}\times r_{86}) \tag{3.35}$$

The volume $(V_i^{+,-})$ is computed in the following way. Without restriction a general hexahedron is composed of five tetrahedra (see Figure 3.3) each of whose volume is determined exactly by

$$V_{T_{1236}} = \frac{1}{6}\begin{vmatrix} x_1 & y_1 & z_1 & 1 \\ x_2 & y_2 & z_2 & 1 \\ x_3 & y_3 & z_3 & 1 \\ x_6 & y_6 & z_6 & 1 \end{vmatrix} \tag{3.36}$$

where the integer subscripts on $(V_{T_{1236}})$ refer to the four vertices that define the tetrahedron. The volume of the hexahedron then is the sum of the volumes of these five tetrahedra.

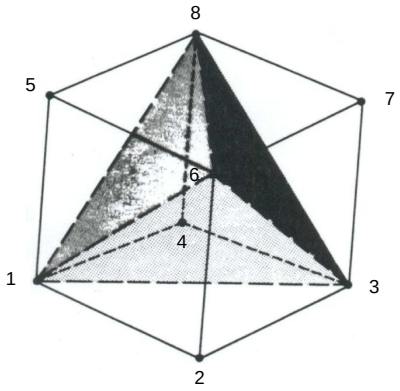

Figure 3.3: The volume of a hexahedronal cell is the sum of the five constituent tetrahedra: $V_{T_{1236}} + V_{T_{3867}} + V_{T_{1685}} + V_{T_{1348}} + V_{T_{3816}}$ [24]

The existing multi-dimensional *MUSCL* method takes advantage of the symmetry in (ζ) to equate the tetrahedra volume balance to an area weighting. However to account for a truer three-dimensional curvilinear grid, as used in the current study, the tetrahedra volume balance for the (i^{th}) cell is considered.

3.4 Viscous Compressible Flow

The discretisation of the viscous fluxes requires the evaluation of derivatives in each coordinate direction. This makes the viscous fluxes quite laborious to compute and therefore various assumptions are often made to eliminate the less significant viscous terms. For high Reynolds number flows with which we are primarily concerned, the viscous effects are generally confined to the near wall region and are dominated by the viscous strain rates normal to the wall; the viscous terms associated with the strain rates along the body are comparatively small and negligible. This was first realised by Prandtl in the development of boundary-layer theory, and later let to the thin layer approximation of Baldwin and Lomax [4], which neglects the cross derivative terms in the unsteady viscous fluxes and retains only those terms which are dominant for a general coordinate system.

The thin layer terms are often applied only to the coordinate direction normal to the body surface (see Yee [69]). Hung & Kuraski [35] successfully implemented an extension of this approximation in two directions, (ζ) and (ξ), where they considered the dominant normal diffusive terms and also the major streamwise diffusive terms and used it to solve for a supersonic flow over an axial corner. The present code has been designed to allow these terms to be switched on in all three directions simultaneously, normal, streamwise, and spanwise enabling the code to deal easily with general geometries. This amounts to an implementation of the full Navier-Stokes equations without the viscous cross derivatives terms. In some instances the neglected cross-derivatives can be of the same order of magnitude as the retained normal derivatives very near the junction of two walls, but in the present scenario the flow contains comparatively very low momentum hence the these viscous terms will be of negligible magnitude in comparison to the dominant terms, as a result neglecting the cross derivatives will not significantly affect the general solution.

Accordingly, the viscous flux for a generic direction (ξ) is given by

$$\bar{F}_v = J \begin{bmatrix} 0 \\ \xi_x\tau_{xx} + \xi_y\tau_{xy} + \xi_z\tau_{xz} \\ \xi_x\tau_{yx} + \xi_y\tau_{yy} + \xi_z\tau_{yz} \\ \xi_x\tau_{zx} + \xi_y\tau_{zy} + \xi_z\tau_{zz} \\ u\tau_{xx} + v\tau_{xy} + w\tau_{xz} + q_x \end{bmatrix} \tag{3.37}$$

where (J) is the transformation Jacobian (which corresponds to the volume of the cell in physical space). The vectors $(\bar{G}_v)$ and $(\bar{H}_v)$ follow from $(\bar{F}_v)$ using the substitution $(\xi \rightarrow \eta)$ and $(\xi \rightarrow \zeta)$. respectively.

The viscous flux terms are obtained in the general curvilinear coordinate system by splitting the flux $(\bar{F}_v)$ into subfluxes, $\left(\bar{F}_v^{(\xi)}\right)$, $\left(\bar{F}_v^{(\eta)}\right)$ and $\left(\bar{F}_v^{(\zeta)}\right)$ such that

$$\bar{F}_v = \bar{F}_v^{(\xi)} + \bar{F}_v^{(\eta)} + \bar{F}_v^{(\zeta)} \tag{3.38}$$

where $\left(\bar{F}_v^{(\xi)}\right)$, $\left(\bar{F}_v^{(\eta)}\right)$ and $\left(\bar{F}_v^{(\zeta)}\right)$ involve only derivatives of (ξ), (η) and (ζ) respectively. When computing fluxes normal to the (ξ) coordinate line, only terms in the subflux $\left(\bar{F}_v^{(\xi)}\right)$ are retained in the approximation.

After some manipulation eliminating the non essential terms, leaves us with the following revised viscous flux vector for $\left(\bar{F}_v^{(\xi)}\right)$

$$\bar{F}_v^{(\xi)} = \mu J \begin{bmatrix} 0 \\ \alpha_1 u_\xi + \beta_1 v_\xi + \beta_3 w_\xi \\ \beta_1 u_\xi + \alpha_2 v_\xi + \beta_2 w_\xi \\ \beta_3 u_\xi + \beta_2 v_\xi + \alpha_3 w_\xi \\ \tau_5^\xi \end{bmatrix} \tag{3.39}$$

the corresponding (α) and (β) coefficients are given by

$$
\begin{aligned}
\alpha_1 &= \tfrac{4}{3}n_x^2 + n_y^2 + n_z^2 \\
\alpha_2 &= n_x^2 + \tfrac{4}{3}n_y^2 + n_z^2 \\
\alpha_3 &= n_x^2 + n_y^2 + \tfrac{4}{3}n_z^2 \\
\beta_1 &= \tfrac{1}{3}n_x n_y \\
\beta_2 &= \tfrac{1}{3}n_y n_z \\
\beta_3 &= \tfrac{1}{3}n_z n_x \\
\alpha_4 &= \tfrac{Cp}{Pr}(n_x^2 + n_y^2 + n_z^2)
\end{aligned}
\tag{3.40}
$$

$$
\tau_E = \alpha_1(\tfrac{u^2}{2})_\eta + \alpha_2(\tfrac{u^2}{2})_\eta + \alpha_3(\tfrac{w^2}{2})_\eta + \beta_1(uv)_\eta + \beta_2(vw)_\eta + \beta_3(wu)_\eta + \alpha_4 T_\eta
$$

Similarly, the viscous flux vector $\left(\bar{F}_v^{(\eta)}\right)$ and $\left(\bar{F}_v^{(\zeta)}\right)$ can be obtained by replacing (ξ) with (η) or (ζ) and taking the projections of (n_x), (n_y) and (n_z) unit vectors in the (η) and (ζ) directions.

The method outlined above greatly simplifies the computation of the viscous fluxes and means that a dimensional operator split code need only carry one level of storage, even for time accurate calculations. In addition to the method described above, another variant of the viscous solver was also tried. The secondary method included some additional cross derivative terms in the viscous flux of Eqns 3.37 to mimic a solution which matched a more complete Navier-Stokes solution. These additional terms were mainly computed for the (ζ) direction, which is normal to flow direction and hence the most dominant. A listing of the explicit viscous fluxes solved in the second explicit method can be found in Appendix B.

All the above derivatives have been discretised in a centred scheme over the cell interface

$$
\left.\frac{\partial u}{\partial \xi}\right|_{i+\frac{1}{2}} \approx \frac{u_{i+1} - u_i}{\xi_{i+1} - \xi_i} \tag{3.41}
$$

This also applies to the primitive variables $(v,\ w,\ T)$. The viscous contribution is computed with an error $\left(\ \mathcal{O}(\Delta\xi^2/Re_{/l})\ \right)$ which is much smaller than the inviscid one which

determines the overall accuracy of the scheme. Once the viscous terms are determined, they can be incorporated into the scheme Eqn3.10.

3.4.1 The Viscous Jacobians

In a similar fashion to the way the inviscid Jacobians were implemented in the implicit scheme the corresponding viscous Jacobians also have to be calculated, and as instructed by Batten *et al* [7] this is done in the following way

$$F_v^{n+1} = F_v^n + \frac{\partial F_v}{\partial U_i}\delta U_i + \frac{\partial F_v}{\partial U_{i+1}}\delta U_{i+1} \tag{3.42}$$

where $\left(\frac{\partial F_v}{\partial U_i}\right)$ and $\left(\frac{\partial F_v}{\partial U_{i+1}}\right)$ are the viscous Jacobians, a complete listing is obtained in Appendix B.

3.5 Boundary Conditions

In general, all boundary conditions are imposed by controlling the flux through boundary interfaces. For this purpose, an extra row of dummy grid points is required at each boundary to store information which is used in the flux calculation. The conserved variables assigned to these dummy grid points are then manipulated to mimic the true interface boundary conditions.

For the Implicit scheme it is possible to find a relation between (∂U_{BC}), the ghost cell conserved variable vector, and (∂U_i) the conserved variable vector for the flow. These two variables can be expressed through a matrix $(\mathcal{C}_{BC})$ as

$$\partial U_{BC} = \mathcal{C}_{BC}\partial U_i \tag{3.43}$$

The way of evaluating of $(\mathcal{C}_{BC})$ will depend on the boundary itself. A listing of the boundary conditions appropriate to this study can be found in Appendix B.

3.6 Implicit Numerical Implementation

Batten *et al.* [6] developed a series of implicit Godunov methods, based on the linearization in time of the fluxes obtained from the solution of the local Riemann problems. The implicit method applied in this study is based on the work done by Batten *et al.* [6] and the resultant implicit scheme is built around the HLLC Riemann solver described in section 3.3.2, which uses frozen acoustic speeds to construct average state Jacobians. Moreover the way of constructing the Jacobians allows a simpler introduction of further contributions, as turbulence models or chemical species. One of the attractive features of this method over the explicit scheme is vastly reduced number of iterations required to achieve a converged solution.

However the current implicit method does have certain limitations. One important point is the need to increase the time step gradually, which allows the wave speeds to settle down and also the positivity of preservation condition is not guaranteed for the implicit method operating at extremely large *CFL* numbers. This produces an upper limit for the maximum allowable Courant number in the implicit method (however this limit should be much greater than one).

The resultant implicit scheme in Eqn 3.15 can be regarded in the differential form as a linear system of equations which can be expressed as:

$$A_{ij}\delta U_j = b_i \tag{3.44}$$

where (A_{ij}) is a $(N * N)$ matrix, (N) being the number of unknowns that creates the influence of the time level $(n+1)$ over the previous one (n) and is derived from the implicit discretisation to keep the scheme stable and (b_i) is the vector sum of fluxes over a time step. The total number of unknowns (N_T) for a three-dimensional system is $(N_T = 5 \times N_{cells})$. As a result (N_T) is very large in three-dimensional calculations, around $\sim 10^7$ in the present study with (A_{ij}) reaching $\sim 10^{14}$ elements, too large to be handled by any computer at present.

For the specialist case when $(A = \mathbf{I})$ the method is reduced to the explicit scheme. To

advance the solution in time the implicit method needs to solve the system of equations expressed in Eqn 3.44. In the case of multi-dimensional problems, where matrix (A_{ij}) is a very large sparse non-symmetric linear system, it is impossible to solve Eqn 3.44 exactly. As a consequence the use of iterative methods is the only alternative to achieve a solution. The methodology used in the current scheme is through implementation of the Bi-CGSTAB($l = 1, 2$) method. A complete description of the Bi-CGSTAB($l = 1, 2$) algorithm can be found in the works of Navarro-Martinez [47]. In the present code the matrix solver is the most CPU consuming process as a result the use of iterative methods has an increased overall cost penalty per time step.

Once the vector of variation of the conserved variables (δU_j) has been computed, the variables are updated in a simple manner as follows

$$U_j^{n+1} = U_j^n + \delta U_j \tag{3.45}$$

The system of equations in Eqn 3.44 is solved at every time step, until a stopping criteria is met. The density is usually the variable with the slowest convergence, therefore the density residual at the (n) time level (Res_ρ^n) defined with the (L_1) norm as

$$Res_\rho^n = \sum_{i=1}^{N_{cells}} \frac{\mid \rho_i^n - \rho_i^{n-1} \mid}{N_{cells}} \tag{3.46}$$

is used to monitor convergence. A steady solution is found when (Res_ρ^n) drops below 10^{-7} in the implicit calculations.

3.7 Parallel Processing

The use of multiple processors for running three-dimensional codes considerably reduces the computational time consumed to achieve a converged solution. This time saving occurs because the tasks are split between processors which in turn reduces the RAM memory load per node. Therefore an additional benefit of using parallel codes is the ability to use more densely packed grids, which has great benefits because this increases the overall accuracy

of the final solution. Flow structures and features are more clearly defined as a result and it also allows the smaller flow structures to be captured. Using multiple processors is necessary in three dimensional cases, because the large number of cells makes the use of single processor machines impractical at present.

The parallel version of the three-dimensional C-code uses MPI subroutines to permit communication between nodes. It is important to minimise the exchange of information between processors to increase the overall speed of the code. Correct management of these subroutines is compulsory to fulfil the memory requirements. Moreover, an excess of packages passed between nodes produce delays when running the program due to communication processes.

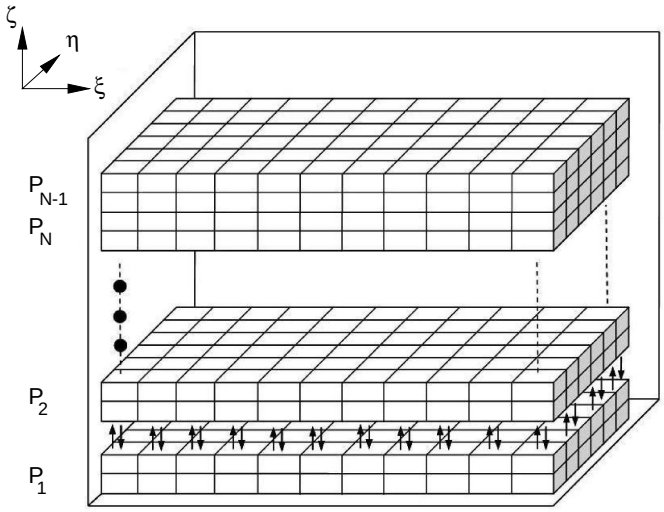

Figure 3.4: Distribution of computer nodes over the three-dimensional space (ξ, η, ζ) [47]

For the present three-dimensional problem the computational block (ξ, η, ζ) is equally split in the (ζ)-spanwise direction (see Figure 3.4). Every node interacts with its neighboring processors by updating the dummy cells after each iteration. For a first order scheme only one row of cells is required in each boundary for the communication process however, in a second order case like the *MUSCL* scheme, two rows are required to reconstruct the solution properly across processors.

The numerical simulations were carried out using a *Beowulf* type *Linux* cluster at the University of Southampton. The code was run using *Pentium III 800 MHz* processors,

each with *512 MB RAM* or *P4 1500 MHz* processors, each with *1 GB RAM.*

Parallelization efficiency is measured as the optimum number of processors required to give a steady state solution in the least amount of time. For the coarse and intermediate grids studied, for the average explicit three-dimensional run, it was found that using 12 processors was the optimum setup and a steady state solution was achieved in ~ 300 hours of CPU time. For the fine grid studies however, it turned out that using 20 processors was the optimum, with a steady state solution achieved in around ~ 720 hours of CPU time. The jobs were submitted to the computer cluster via a job queue, which was often quite long. This resulted in the actual run times *(real time)* of the simulations being very long. The *(real time)* required to run a three-dimensional simulation for a grid $232 \times 204 \times 180$ to convergence was approximately 50 days.

3.8 Numerical Grid Generation

In *CFD* simulations the computational grid plays a decisive role in determining the accuracy of the numerically generated solution. Broadly there are two types of meshes, "structured" and "unstructured". Unstructured girds are composed of non-ordered distributions of irregular polyhedra cells that cover the domain, and adapt well to complex geometries. Despite the good performance of these grids, they are affected by spurious errors associated with the viscous terms [57] and are difficult to handle because they need a complex connectivity matrix to locate each cell and its interacting neighbours. Structured grids consist of completely ordered cells, preferably orthogonal, that fill the domain and are usually indexed (i,j,k). The referencing system is much simpler when compared to unstructured grids, and furthermore the method is computationally inexpensive to implement. In addition, this type of grid produces less instabilities and deals better with viscous contributions.

Taking advantage of the robustness and stability of the current numerical scheme, the numerical code solves the discretised equations on a structured computational grid. Part of the grid generation procedure is undertaken using a commercial grid generation package called *GRIDGEN.V.14* [38]. Throughout this work *GRIDGEN.V.14* is used initially to

generate two-dimensional grids in the (ξ, η) plane. These grids are later extended to the third dimension (ζ) by simple stretching functions. For the unswept grids, the function assumes $\big(\ \zeta = \zeta(z)\ \big)$ only, and for the swept-fin example assumes $\big(\ \zeta = \zeta(x, y, z)\ \big)$.

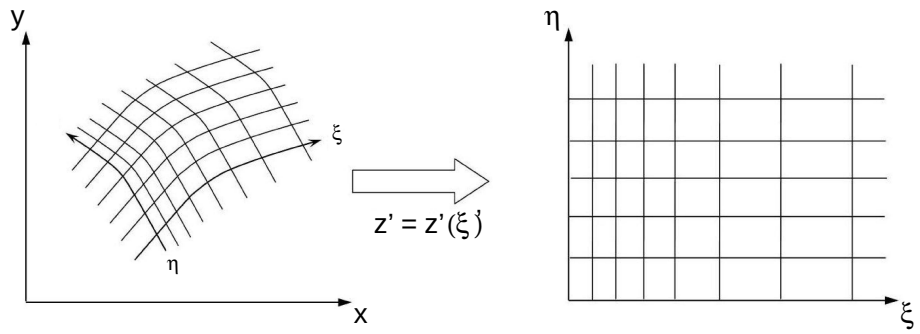

Figure 3.5: Sketch of the physical (x,y) and computational (ξ, η) space

To study the effect the grid type has on the numerical solution; two types of grid were generated using an algebraic method, the H-type and C-type. For both grid types the physical space (x,y,z) is mapped into the computational space (ξ, η, ζ), retaining the ordered structure and the orthogonal properties (see Figure 3.5).

3.8.1 Grid clustering

Grid stretching is the ratio of distances between adjacent grid points along a grid line.

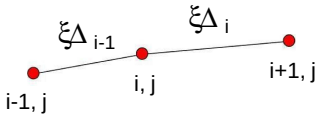

Figure 3.6: Illustration of grid stretching

$$S = \frac{max(\triangle\xi_i, \triangle\xi_{i-1})}{min(\triangle\xi_i, \triangle\xi_{i-1})} \tag{3.47}$$

Stretching is defined so that $(S \geq 1)$, this parameter can also be expressed as a percentage $(S\% = (S-1) * 100\%)$.

One-dimensional hyperbolic tangent stretching [38] is used in all regions to distribute the cells along the grid connectors. This type of stretching has been used in several numerical works, since it provides an effective way to smoothly vary the cell spacing along a line. On the current series of grids, grid clustering is implemented in all three spatial directions of the computational domain (ξ, η, ζ). In the (ξ, ζ) plane, points are clustered towards the plate surface in order to resolve the laminar boundary layer and to get an accurate measurement of heat flux on the plate. In the (η, ζ) plane, points are clustered near the leading edge in order to accurately resolve the leading edge shock, and also clustered towards the fin edge so the flow is accurately resolved in the separated region. Points in the (ξ, η) plane are clustered towards the plane of symmetry so that features close to the centerline of the fin are accurately captured. Taking advantage of the symmetry that exists on the fin/plate, only half of the configuration is used to construct a computational domain.

Grid stretching during the clustering process can lead to the presence of skewed cells in various quadrants in the computational domain. This can subsequently lead to the generation of perturbations during the simulation that may partially or completely destroy the numerical solution. A general rule is to keep stretching below $15 - 20\%$ to keep numerical errors within bounds. This is especially important in regions with strong flow gradients [48]. As a result of using individual explicit and implicit numerical algorithms independently to attain the final converged solution, considerable care is taken when implementing the clustering criteria. This is mainly because the implicit algorithm is particularly sensitive to instabilities due to large time steps.

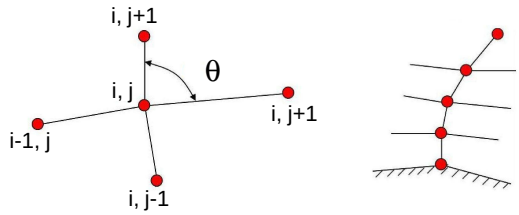

Figure 3.7: Illustration of grid Orthogonality

An elliptic solver is run on the (ξ, η) plane of the grid block in the physical domain. The elliptic solver improves the orthogonality of the mesh, especially in those regions where

the cells intersect with sharp or convex corners. Grid orthogonality (see Figure 3.7) is the angle that a grid line makes with the other grid lines intersecting at a grid point.

Orthogonality is defined so that ($\theta \leq 90°$). General rule is to keep orthogonality as close to 90° as possible, especially normal to solid surfaces to provide accurate estimates of the normal to the walls for wall boundary conditions. A minimum angle is probably 45°. Orthogonality is also very important on the plane of symmetry since skewing will create a strong grid dependence on this plane.

3.8.2 Three-Dimensional Extension

For the unswept-fin computational grid, the third dimensional variable of the computational grid (ζ) has been chosen to be a function of (z) only. A simple compression technique through a control function (ψ) is performed [57].

$$z = \psi(\zeta, C^{'}) \tag{3.48}$$

(ψ) stretches the grid towards the (z)-edge or the flat plate. ($C^{'}$) is a user given constant that increases or decreases the degree of stretching. In the present work, (ψ) is a function in the form

$$\psi = \frac{e^{C^{'}\bar{\zeta}} - 1}{e^{C^{'}} - 1}\zeta \tag{3.49}$$

where ($\bar{\zeta}$) is the coordinate (ζ) normalized to have values between 0 and 1.

The following figures illustrate the type of grids generated using the methods outlined in this section. Figure 3.8:(**top**) is an example of a *H-type* grid with Figure 3.8:(**middle**) illustrating a *C-type* grid. A modified version of the *C-type* grid is shown in Figure 3.8:(**bottom**) [1].

[1]- The (x,y,z) physical coordinate system shown is transformed to (ξ, η, ζ) in the computational coordinate system

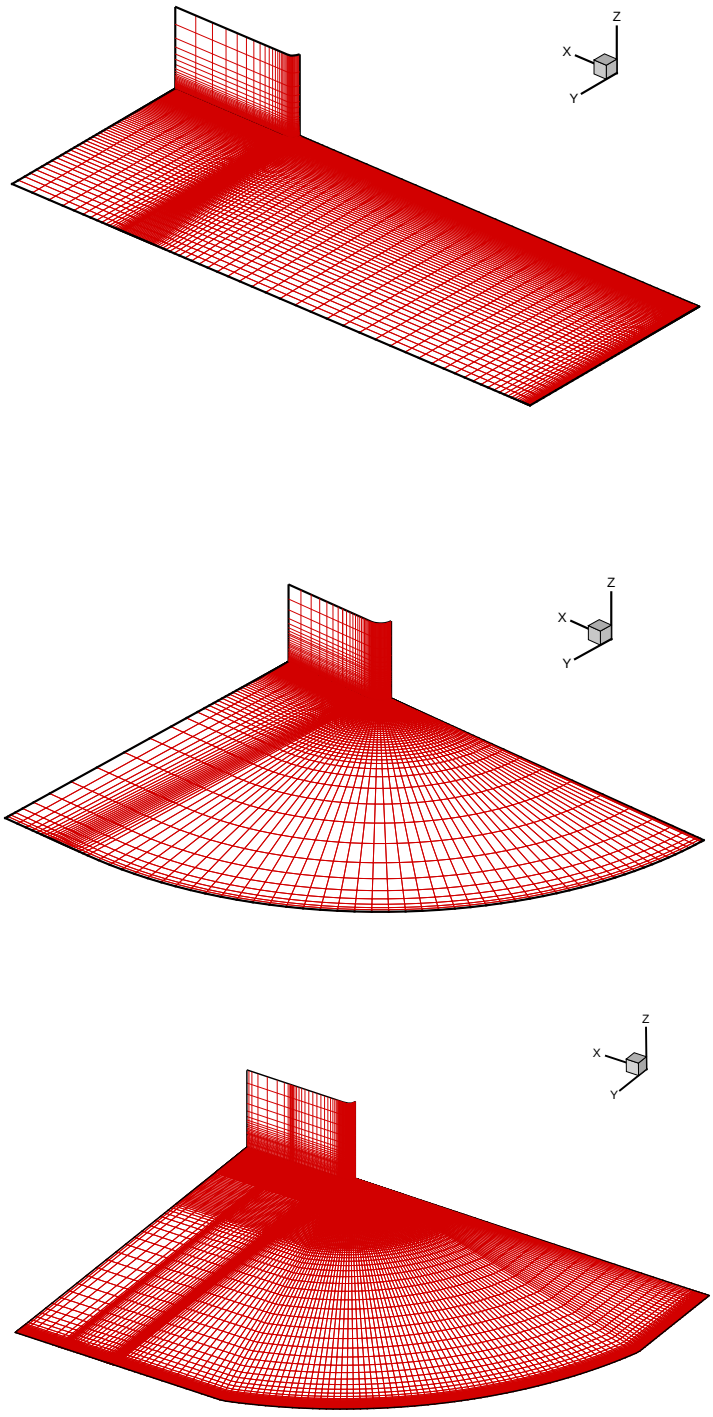

Figure 3.8: (**top**)*H-type* grid (**middle**) *C-type* grid (**bottom**) *C-type Hybrid* grid

3.8.3 Grid Properties

When computing flows which have boundary layers growing over walls or flat surfaces, require the grid to be clustered normal to the wall or flat surface in order to resolve the large gradients present through the boundary layer. As a consequence, it is important to define a set of variables that can used to quantify grid "quality" so that it is possible to measure the ability of a selected grid in being able to give an accurate solution to the flow problem.

One such factor is the "Reynolds number per cell", (Re_h) defined as,

$$Re_h = \frac{\rho_\infty U_\infty h}{\mu_\infty} \tag{3.50}$$

where (h) is the height of the cell and (∞) denote free stream conditions. The (Re_h) coefficient is a measure of the number of grid points across the boundary layer, and is representative of the grids ability to capture the inner deck of the "triple deck theory" [2]. Generally, the smaller the (Re_h) coefficient, the better the grid is in being able to capture the low deck of the boundary layer. The minimum (Re_h) is located in cells next to the blunt-fin and the leading edge.

Another important parameter is the cell dimension ratio ($\triangle x/\triangle y$), which due to mesh stretching reaches its maximum next to the plate. Very large or small ratios increase the oscillatory effects in second order schemes. Best results are obtained with values close to unity. Unfortunately, there are no analytic forms to determine the optimum ratios and empirical tests should be done. The coefficients for different grids evaluated at the leading edge are shown in Table 3.1.

The recommended grid parameters of Katzer [41] for Shock-Boundary Layer Interactions, near separation, ($\triangle x/\triangle y \leq 20$) and ($Re_h << 100$) are followed to accurately capture the low deck displacement.

[2]- Triple deck theory states that there are three decks within the boundary layer: the outer deck is largely potential flow, the middle deck covers most of the boundary layer profile and is comprised of rotational, inviscid, disturbance flow, and finally the inner deck close to the surface contains viscous disturbance flow.

The quality of the grid is also assessed against an additional set of criteria usually used on flows with turbulent boundary layers. The parameter $(y+)$ is a non-dimensional distance measured normal to the wall measured across the turbulent boundary layer. This variable is defined as:

$$y+ = y\frac{\sqrt{\rho_w \tau_w}}{\mu_w} \tag{3.51}$$

where the variables with the (w) subscript represent the values at the wall. The general rule is that the first grid point off the wall should have $(y+ < 1)$ to accurately define a turbulent velocity profile. It can go up to $(y+ = 5)$ for less accuracy. Resolution of heat fluxes requires $(y+)$ to be about 0.1 [48].

The grids used in the following simulations will use all three parameters defined to measure grid quality, therefore assuring that the grids are effective in determining the most accurate solution.

H-Type vs C-Type

To assess the merits or shortcomings of both the grid types to yield an accurate solution to the problem in terms of numerical accuracy and time dependency, two test grids with identical grid densities $(43 \times 40 \times 36)$ were run, and the solutions compared.

From the resulting simulations the following observations were made. When using the explicit method under a first-order scheme, it was observed that when using the *H-type* grid it was possible to run the scheme using higher explicit *CFL* numbers when compared to using the *C-type* grid. As a direct consequence the *H-type* grid gave a faster converged solution to the flowfield. However, due to the grid mapping technique the grid cells near the curved blunt section of the fin were highly skewed, even though an elliptic solver was used to smooth out these regions. This had a direct adverse affect on the numerical solution. This was expressed as numerical irregularities in the final solution. These irregularities were localised near the line of symmetry close to the blunt fin section, and manifested as "kinks" in the contour results of the solution parameters. In contrast the *C-type* grid did

not appear to suffer from this problem.

As a result of these observations, and taking into account the competing factors; it was decided that all subsequent numerical simulations of the blunt-fin were to use the *C-type* grid.

To better mimic the leading edge properties of the flat plate a modified *C-type Hybrid* was also tested. It was found that the new grid gave improved resolutions in the leading edge shock and the subsequent boundary layer.

Grid Studies

For this case two baseline grids (labelled $A1$ and $A2$) were generated, $(43 \times 40 \times 36)$ and $(58 \times 51 \times 45)$ respectively. To obtain finer grids these two grids were doubled and redoubled to obtain grids type B and C. Properties of these grids are shown in Table 3.1:

Grid	Type	$\Delta x/\Delta y$	Δx of smallest cell ($\times fin\ diameter$)	Re_h	y+
$43 \times 40 \times 36$	A1	15	0.008D	88	6.61
$58 \times 51 \times 45$	A2	15	0.008D	82	5.35
$86 \times 80 \times 72$	B1	10	0.004D	65	3.67
$116 \times 102 \times 90$	B2	8	0.004D	44	1.16
$172 \times 160 \times 144$	C1	6	0.002D	17	0.92
$232 \times 204 \times 180$	C2	4	0.002D	8	0.73

Table 3.1: Grid properties for $5mm$ diameter blunt-fin

From preliminary tests, it was found that a higher resolution of grid points was necessary in the boundary layer region in order to obtain a suitably well converged surface heat transfer rate solution. As a result of the grid clustering process, the shorter cell lengths close to the surface necessitate a shorter time step hence requiring a significantly higher number of time steps to reach a prescribed time level. Therefore using very fine grids for all three-dimensional simulations was not practical due to excessive computational and

time demands. As a result of these restrictions very fine grid-dependent studies were only undertaken for the unswept $5mm$ diameter fin case.

It was found that grid type $B2$ was the minimum requirement as a standard to give reasonably well defined surface heat transfer profiles. Hence from Table 3.1 it is clear that grid types $B2$, $C1$ and $C2$ would give the best solutions to the flow problem.

In a similar fashion, for the $10mm$ diameter fin two baseline grids were generated, $(58 \times 51 \times 45)$ and $(78 \times 72 \times 60)$. To obtain finer grids these two grids were doubled to obtain grid type B. Properties of these grids are shown in Table 3.2:

Grid	Type	$\Delta x/\Delta y$	Δx of smallest cell ($\times fin\ diameter$)	Re_h	y+
$58 \times 51 \times 45$	A1	15	0.008D	82	5.35
$78 \times 72 \times 60$	A2	10	0.004D	71	3.89
$116 \times 102 \times 90$	B1	8	0.004D	44	1.16
$156 \times 144 \times 1204$	B2	5	0.002D	22	0.98

Table 3.2: Grid properties for $10mm$ diameter blunt-fin

The simulations carried out for the $5mm$ diameter fin with $30°$ sweep are mainly for comparison purposes, hence fine grid studies were not necessary. The properties of this grid are shown in Table 3.3:

Grid	Type	$\Delta x/\Delta y$	Δx of smallest cell ($\times fin\ diameter$)	Re_h	y+
$58 \times 51 \times 45$	A1	15	0.008D	82	5.35
$116 \times 102 \times 90$	B1	8	0.004D	44	1.16

Table 3.3: Grid properties for $5mm$ diameter blunt-fin with $30°$sweep

3.9 Three-Dimensional Linear Interpolation

When using very fine three-dimensional grids to simulate complex flowfields like the present blunt-fin/plate example, starting the simulation from the beginning to achieve a steady state solution takes a considerable length of time. For an explicit scheme, this is primarily due to the small time step as a result of small grid cells in fine meshes. Experience has taught that for a complex flow like the blunt-fin/plate, the time taken to establish the inviscid flow structure could account for 50% of the total time taken to achieve a converged solution [47]. As a result, cutting out the time taken to reach this inviscid flow state could save considerable CPU time, and computational resources when attempting to attain a steady state solution for a fine grid simulation.

To solve this problem a pre-established flowfield result from a coarse grid is interpolated to the finer grid using a linear interpolation scheme. The interpolated result is then used as a starting point solution for the fine grid to start the final simulation.

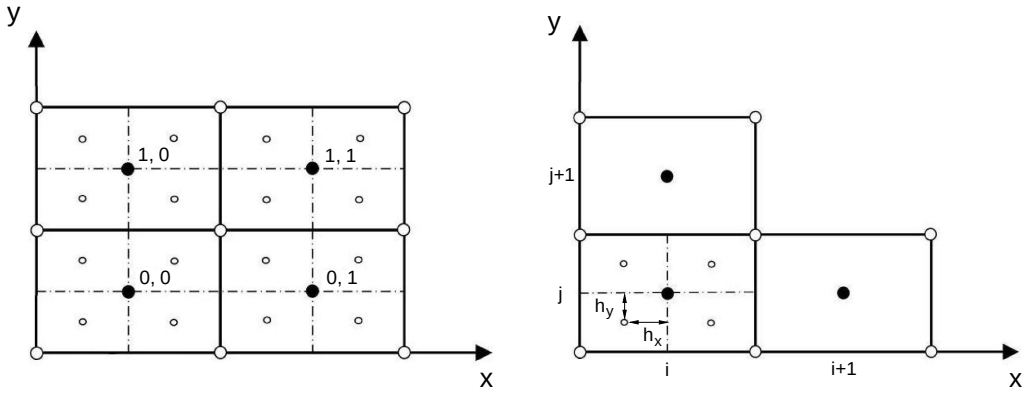

Figure 3.9: (**left**) Reference system (**right**) illustration of interpolation scheme

From Figure 3.9, the reference system for the large grid shows that points $(0, 0)$ and $(0, 1)$ correspond to cell centres (i, j) and $(i + 1, j)$ for the coarse grid, similarly $(1, 0)$ and $(1, 1)$ correspond to cell centres $(i, j + 1)$ and $(i + 1, j + 1)$.

We define the finer grid cell centre locations with the lower case (x_p, y_p) coordinates. Next we define parameters (h_x) and (h_y) for a generic cell as

$$h_x = x_p - X[0][0][k] \tag{3.52}$$

$$h_y = y_p - Y[0][0][k] \tag{3.53}$$

where (x_p, y_p) are the coordinates for a generic cell on the finer grid and $\big(X[0][0][k],\ Y[0][0][k]\big)$ represents the cell centre for a generic cell on the coarser grid, in accordance with the reference system shown in Figure 3.9.

If we define points $\big(\ (x1, y1);\ (x2, y2);\ (x3, y3);\ (x4, y4)\ \big)$ as the locations of the cell centres according to the reference system shown in Figure 3.9 and the variables $(f1;\ f2;\ f3;\ f4)$ which can represent anyone of solution variables (e.g. ρ, *p, u, v, w, T, Mach number*), at the corresponding cell centre locations.

$$x1 = X[0][0][k];\ x2 = X[1][0][k]; x3 = X[0][1][k];\ x4 = X[1][1][k] \tag{3.54}$$

$$y1 = Y[0][0][k];\ y2 = Y[1][0][k]; y3 = Y[0][1][k];\ y4 = Y[1][1][k] \tag{3.55}$$

$$f1 = f[0][0][k];\ f2 = f[1][0][k]; f3 = f[0][1][k];\ f4 = f[1][1][k] \tag{3.56}$$

defining the variable gradients as

$$\frac{\Delta f}{\Delta x} = \frac{f2 - f1}{x2 - x1} \tag{3.57}$$

$$\frac{\Delta f}{\Delta y} = \frac{f3 - f1}{y3 - y1} \tag{3.58}$$

The interpolated solution variable for the finer grid is given as $\big(F[i][j][k]\big)$, where it represents any one of the solution variables like (ρ, *p, u, v, w, T, Mach number*).

$$F[i][j][k] = f1 + \frac{\Delta f}{\Delta x} h_x + \frac{\Delta f}{\Delta y} h_y \tag{3.59}$$

The benefits of using the interpolation scheme can be seen when comparing the residual convergence histories in Figure 3.10 with Figure 3.11.

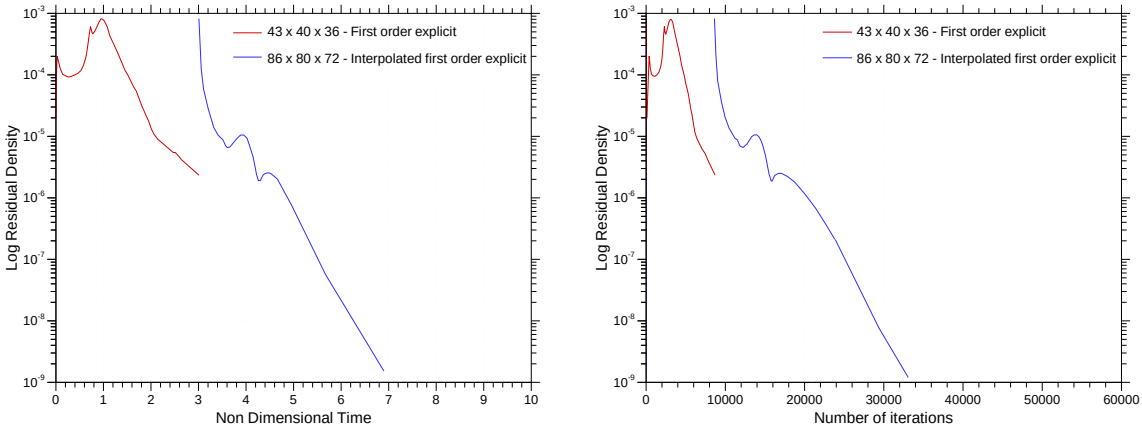

Figure 3.10: Convergence history for the density residual using an interpolated solution (**left**) with respect to non-dimensional time units (**right**) number of iterations

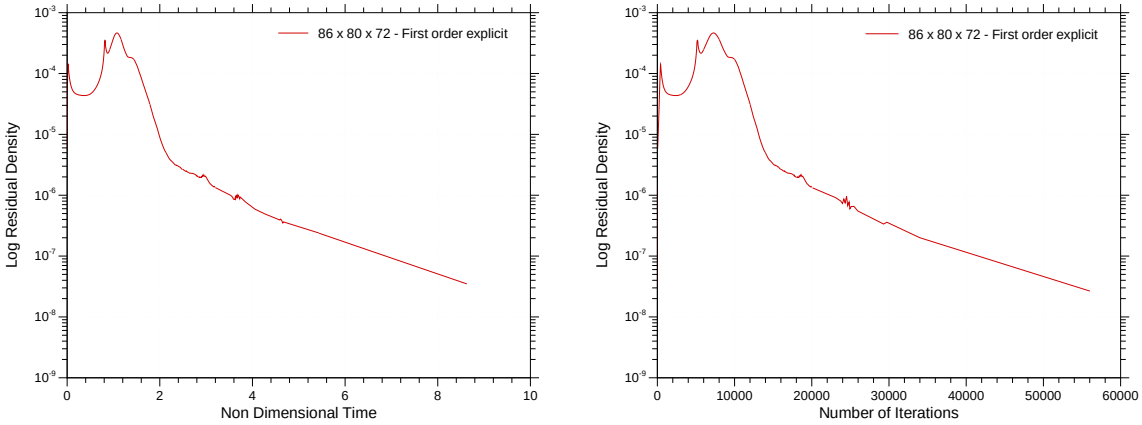

Figure 3.11: Convergence history for the density residual using a standard solution(**left**) with respect to non-dimensional time units (**right**) number of iterations

Figure 3.10 shows the convergence history for a grid of $(86 \times 80 \times 72)$ which was run with a first-order scheme, using an interpolated solution from grid $(43 \times 40 \times 36)$. Figure 3.11 shows the convergence history for the same grid of $(86 \times 80 \times 72)$ run using a first order scheme, however this example was started from the beginning, and run till convergence was achieved. The time it took to reach a pre-defined converged separation length of (x_S/D = -7.229) was compared for both grids. The interpolated $(86 \times 80 \times 72)$ grid took ∼30,000 iterations to achieve the desired separation length, whilst the normal $(86 \times 80 \times 72)$ grid took ∼60,000 iterations to attain the same separation length. Therefore it is quite clear to

see the potential benefits in using the interpolation method to give considerable savings in CPU time. As a result, grids $B1$, $B2$, $C1$ and $C2$ were all simulated using interpolated solutions.

3.10 Three-Dimensional Grid Convergence Studies

In the present study, the numerical solution was assumed to be convergent when the separation length (x_S), defined as the length from the base of the blunt-fin to the point of boundary layer separation, did not appear to change with time. One unit of time is characterized as the ratio of the reference length to free stream speed (L_{ref}/U_∞). The reduction of the density residual to a predefined value of 10^{-12} in the explicit calculations and 10^{-7} in the implicit scheme was also considered to be an additional condition for a converged solution. The residual is a comparison of density with the iteration number, and is defined in Eqn 3.46

3.10.1 General Criteria

In the present study we are only interested in the final steady state solution. The following convergence criteria is found to be generic to all the test cases.

Extensive test case simulations showed that the numerical scheme was very sensitive to the initial time step. Although it might be expected that the implicit approach would circumvent such restrictions, in practice starting the simulation using an initial implicit time step resulted in the numerical solution becoming unstable and eventually collapsing with the code exiting prematurely with an error. The problem manifests itself when the wavespeeds in the Riemann solver grew exponentially until they could not be handled by the inviscid solver. It is important to note that physically inconsistent initial conditions lead to problems in the implicit boundary conditions even for small initial time steps. The explicit scheme is less sensitive to the initial conditions.

In this case, the viscous and inviscid time constraints are of the same magnitude and a pure explicit scheme with a ($CFL = 0.6$) was found to be convergent. Shown in Figure 3.12

is the convergence history for grid $B1$ ($86 \times 80 \times 72$) for a converged solution in first and second-order.

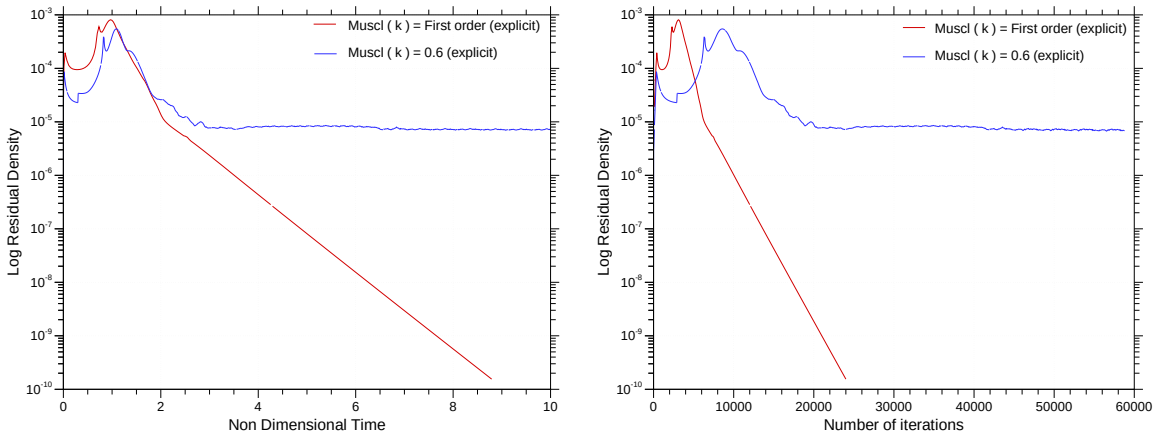

Figure 3.12: Density residual convergence history for grid $86 \times 80 \times 72$ using different *MUSCL* (k) factors (**left**) with respect to non-dimensional time units (**right**) number of iterations

As shown in Figure 3.12 the first-order solution required the least number of iterations and expense in time to achieve convergence according to the residual criteria. Although the residual in the second order method appears to flatten out, this does not imply that the solution has converged or that the solution is wrong. This point is considered in more detail later in this section. An important observation to make is the large number of iterations required under the explicit scheme to achieve convergence, as a result it is clear that using the explicit method on the higher density grids, grid types $B2$, $C1$ and $C2$ is impractical primarily due to time restrictions.

To navigate this problem a mixed explicit/implicit method is used. For the three grid types mentioned earlier, after obtaining a linear interpolated solution from its respective lower grid density counterpart, the flowfield solution is used as a starting point in the explicit scheme, using an initial explicit ($CFL = 0.4$). Once the explicit flowfield solution neared a state where the flow features had established themselves, usually after 1$\sim$2 units of time, the explicit solution was used as re-start solution under the implicit method starting with an initial ($CFL = 0.4$), progressively increasing at a ratio of 1.1 to a ($CFL = 14$) until the solution converged, as shown in Figure 3.13. The *MUSCL* factor used is ($k = 0.6$).

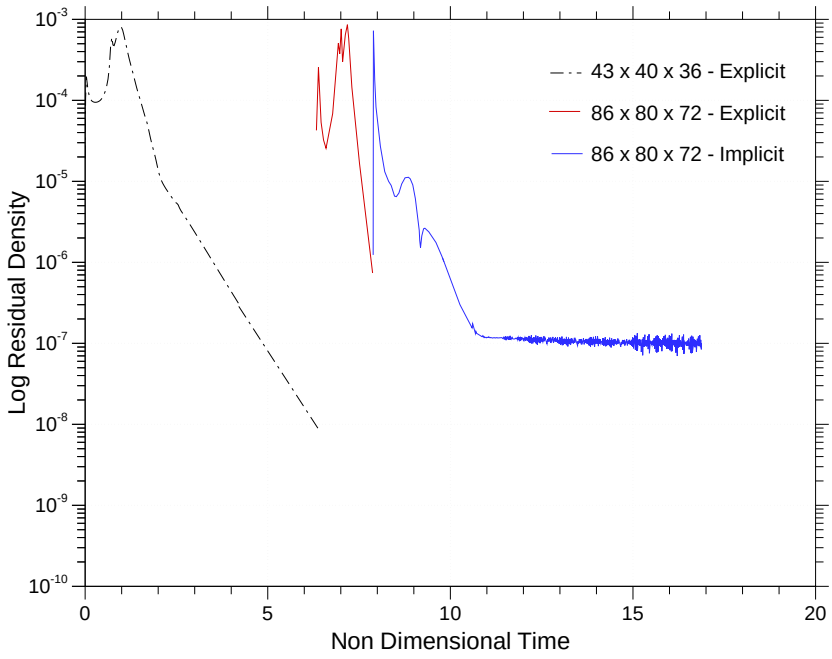

Figure 3.13: Convergence history for mixed a explicit/implicit scheme for grid $86 \times 80 \times 72$

3.10.2 Criteria for 5mm diameter blunt-fin

To accurately resolve the inviscid and viscous flow features, the *MUSCL minmod* slope limiter is used. Table 3.4 gives an indication of the maximum allowable *MUSCL* factor (k) that would give a converged result for each of the grids used, and Table 3.5 gives the resulting impact of various *MUSCL* factors on separation length.

Relative oscillation-free results were obtainable using a *MUSCL* factor ($k \simeq 0.5$) for all the grids. However it was discovered that considerably more detail of the flowfield could be captured at the higher *MUSCL* factors. For grid types *B1, B2* and *C1* using a *MUSCL*, ($k \simeq 0.7$), the residual convergence was observed to be unsteady and oscillates at a value of $\sim 10^{-5}$, much higher than the pre-set convergence limit. However, the primary marker stipulated for convergence - the separation point upstream of the fin on the plane symmetry - was observed to reach a stationary value. Using *MUSCL* factor values of ($k > 0.7$) was found to give highly unstable oscillations in the residuals and produced features which were deemed non-physical. These were numerical effects and not necessarily a measure of the instability of the flowfield.

Grid	Type	Maximum MUSCL (k)
$43 \times 40 \times 36$	A1	0.7 - 0.8
$58 \times 51 \times 45$	A2	0.7 - 0.8
$86 \times 80 \times 72$	B1	0.6 - 0.7
$116 \times 102 \times 90$	B2	0.6 - 0.7
$172 \times 160 \times 144$	C1	0.6 - 0.7
$232 \times 204 \times 180$	C2	0.5 - 0.6

Table 3.4: Various grids with maximum $MUSCL(k)$ factor

Grid	Type	First Order	MUSCL (k)= 0.5	MUSCL (k)= 0.7
$43 \times 40 \times 36$	A1	-6.887	-6.851	-6.823
$58 \times 51 \times 45$	A2	-6.978	-6.927	-6.907
$86 \times 80 \times 72$	B1	-7.229	-7.157	-7.117
$116 \times 102 \times 90$	B2	-7.461	-7.389	-7.345
$172 \times 160 \times 144$	C1	-7.664	-7.574	-7.531
$232 \times 204 \times 180$	C2	-7.648	-7.582	-7.533

Table 3.5: Various grids with the maximum $MUSCL(k)$ factor possible, and variation of final separation length (x_S/D)

Another competing factor that appeared while running the simulations was that, as the grid densities increased, the maximum allowable *MUSCL* factor to give a converged solution decreased. As a result of the above observation, the maximum value of (k) which can be applied to give a converged solution is somewhere between 0.6 and 0.7 for grid types *A1, A2, B1, B2* and *C1* apart from grid *C2*. For grid *C2* the maximum *MUSCL*, ($k = 0.6$) to give a converged solution. The results between grid *C1* and *C2* were found to be nearly indistinguishable because it was found for these two grid types the *MUSCL* step had a negligible effect on the surface heat transfer rate solution. This is due to the boundary layer solution being sufficiently resolved by the grid clustering alone. This also

suggests that, in this case, the sharpening of flow features away from the surface has little effect on the boundary layer flow. After consideration for the sake of consistency, a value of ($k = 0.6$) is used throughout the set.

The code was run using a number of individual runs "sub-runs" before convergence was achieved, (this was because of the time and processor limitations associated with running the code on the computer cluster). The residual plot in Figure 3.14 - which represents the residual convergence for an unswept $5mm$ diameter blunt-fin on a flat plate, simulated under a ($M_\infty = 6.7$) flow with a unit Reynolds number of ($Re/l = 7.6 \times 10^6 m^{-1}$) - was started using a preliminary converged solution, at the end of each run the separation point is noted and indicated on the convergence plot. Convergence was attained when the location of the separation point remained unchanged between runs. As can be seen in the case illustrated, the separation point stays constant at a value of 7.117 diameters (see Figure 3.14).

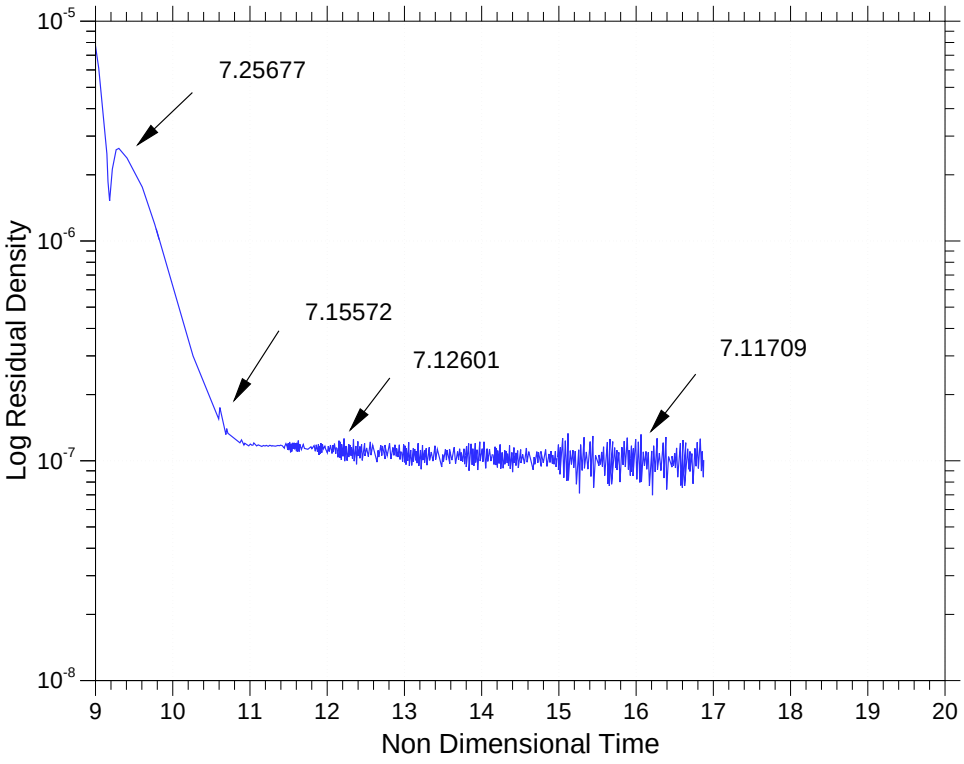

Figure 3.14: Convergence history for $86 \times 80 \times 72$ and tracking the separation point

3.10.3 Criteria for 10mm diameter blunt-fin

The 10mm diameter blunt-fin was plagued with serious convergence difficulties when using *MUSCL* factors ($k > 0.6$), primarily due to the increased interaction zone - separated region - present due to the larger fin diameter. As a result, for these simulations the maximum allowable *MUSCL* was limited to ($k = 0.6$). Although the residuals oscillated a lot at values of (10^{-4} - 10^{-5}), convergence was achieved through an eventual constant separation length.

The convergence plot for a grid ($156 \times 144 \times 120$) is shown in Figure 3.15

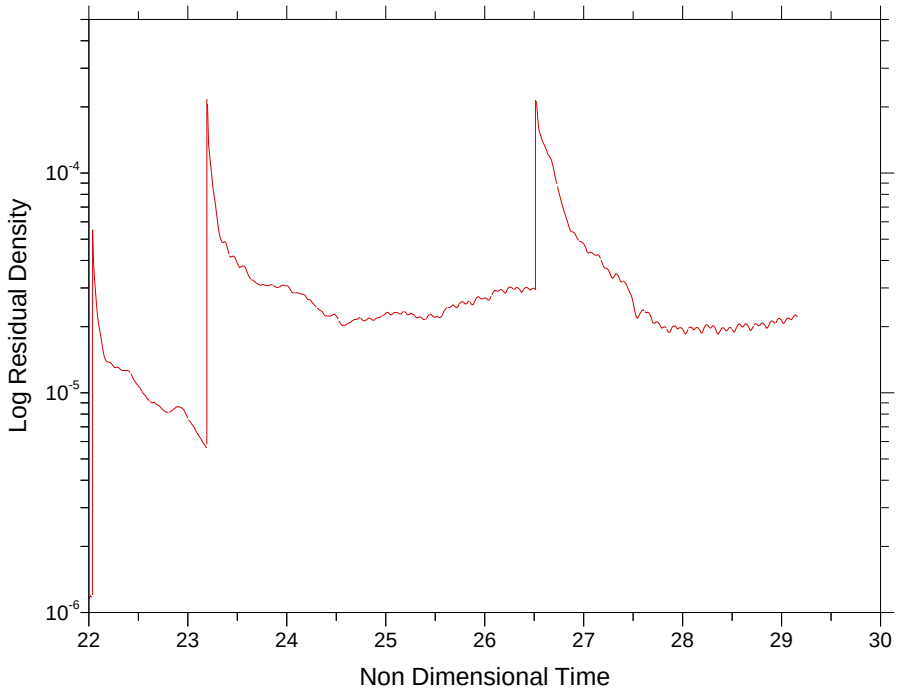

Figure 3.15: Convergence history for $156 \times 144 \times 120$ and tracking the separation point

The residual plot in Figure 3.15 was started using a preliminary converged solution. As was mentioned in the earlier 5mm case, the discontinuities or "spikes" in the convergence plot are a result of either changing the *MUSCL* (k) factor, or the *CFL* number for that particular run.

3.10.4 Criteria for 5mm diameter blunt-fin with 30°sweep

The 5mm diameter blunt-fin with 30°sweep had no difficulty in achieving a converged solution when using *MUSCL* factors, ($k > 0.6$), however to maintain consistency in the results the maximum *MUSCL* was limited to a ($k = 0.6$). The residual convergence for a grid ($58 \times 51 \times 45$) using the explicit method is shown in Figure 3.16. The data in the Figure is for a first order scheme, after 8 units of time the simulation was restarted with a *MUSCL* factor ($k = 0.6$) till convergence was achieved.

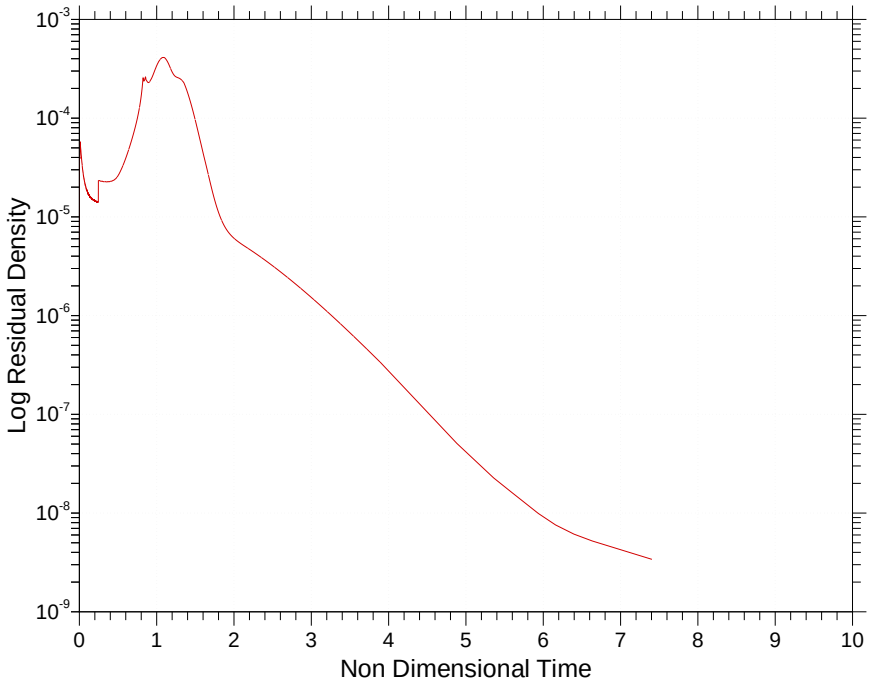

Figure 3.16: Convergence history for $58 \times 51 \times 55$

3.11 Three-Dimensional Grid Convergence Error

The most widespread and reliable methods to asses the grid convergence for complex numerical problems are based on the Richardson extrapolation [51]. The starting point is a grid refinement study with at least a converged solution on two grid sequences, the ratio

between the number of cells on the two sequences being variable. In its general form, the Richardson extrapolation uses the solution on the two grid sequences and the knowledge of the nominal order of accuracy of the numerical scheme to produce an error estimate in the numerical solution. However, this approach can be misleading in that the nominal order of accuracy can be quite different from the real or observed order of accuracy. This discrepancy between the nominal and observed order of accuracy is particularly large for high-speed compressible flows that have shocks. In most numerical codes, the numerical methods used to tackle high-speed compressible flows are second order, upwind schemes, mainly due to their accuracy and stability properties. However, in order to avoid non-physical oscillations around shocks, limiters are used. Limiters reduce the order of accuracy of the scheme to first-order in the regions across the shock (see Chapter 3, Section 3.3.3). As a result, it is necessary to use a generalised Richardson extrapolation by Roache [51] that employs the discrete solutions on three different grid sequences called the "Mixed 1^{st} + 2^{nd} Order Extrapolation".

3.11.1 Mixed 1^{st} + 2^{nd} Order Extrapolation

The Richardson extrapolation procedure is based on a series expansion of the discretization error, (DE), on the grid level (i):

$$DE_i = f_i - f_{exact} \tag{3.60}$$

where (f_{exact}) is the exact solution to a predicted value of some function and (f_i) is the solution on grid level (i). On a uniform grid the series expansion for the solution may be written as,

$$f_i = f_{exact} + \mathcal{O}(a^b) \tag{3.61}$$

where ($\mathcal{O}(a^b)$) represents higher order terms (similar to the Richardson extrapolation [51]). Here

$$a \simeq \sqrt{(dxdy)} \tag{3.62}$$

where (dx) and (dy) is the cell spacing in the (x) and (y)-directions respectively. Eqn 3.61 can also be written as,

$$f_i = f_{exact} + \mathbf{C}(a^b) \tag{3.63}$$

where $(\boldsymbol{C})$ and (b) are constants. If this expression is used on three successive grids with the assumption that the finest grid would have the closet solution to an exact solution, an estimate of the error may be obtained. The value of (b) is the formal order of accuracy of the algorithm and is given by:

$$b = \frac{(ln(f_{i_3} - f_{i_2}) - ln(f_{i_2} - f_{i_1})}{ln(\mathbf{r})} \tag{3.64}$$

where $(f_{i_1},\ f_{i_2},\ f_{i_3})$ are the results for a solution parameter at a location (i) from three successive grids, and $(\boldsymbol{r})$ is the refinement factor. In the grid sequencing performed in this study, $(\boldsymbol{r})$ is theoretically constant since the number of grid points is halved/doubled in each spatial direction between two consecutive grid levels. Thus, the overall refinement factor is 8 $(2 \times 2 \times 2)$ between two grid levels.

According to Viti [62] the "Mixed 1^{st} + 2^{nd} Order Extrapolation" produces the best error estimation for non-monotonic solutions by best implying it is the most conservative and that it is the closest to the true error. Therefore the discretization error given by Roache [51] for a predicted solution variable (f) between the fine grid$_1$ compared to a coarser grid$_2$ is given by:

$$DE_{fine} = \frac{f_{i_3} - f_{i_2}}{1 - \mathbf{r}^b} \tag{3.65}$$

Note (f_i) can be the solution of any flow parameter at a point in the domain. In the present study, this error analysis is conducted for the (St) number and (C_f) coefficient for successive grids in the grid refinement section.

Chapter 4

Numerical Test Cases

4.1 Introduction

The stability and accuracy of the original three-dimensional numerical scheme was throughly tested and validated against several three dimensional [1] test cases by Navarro-Martinez [47]. However, to test the stability and accuracy of the current code after the new modifications, two fully three-dimensional test problems are computed.

In the primary test the code is validated for a three-dimensional flat plate exposed to a hypersonic flow with the Reynolds number controlled to ensure the formation of a laminar boundary layer over the flat plate.

The primary objective of the second test was to check the accuracy and functionality of the new method implemented to calculate the three-dimensional metrics. For this purpose the code is used to solve for a supersonic flow over a cylinder/flat-plate configuration. The numerical results are compared against the experimental results of Özcan & Holt [11] for the same configuration.

[1]- Orthogonal in the (z) direction of the physical domain, or (ζ) the direction in the computational domain

4.2 Three-Dimensional Laminar Flow over a Flat Plate

4.2.1 Introduction

The primary test aims at simulating a hypersonic flow over a three-dimensional sharp flat plate, paying close attention to the formation of the leading edge shock and the growth of the viscous boundary layer. The current analysis will only focus on aspects of the three-dimensional flow along the plane of symmetry on the centerline of the plate. Effects of the three-dimensional flow structure due to the side edge of the plate are ignored.

The flat plate used to model the computational grid is based on the dimensions of the blunt-fin attached flat plate used by Schuricht [53]. The plate has a total length (L_{total}= $205mm$), with a reference length (L_{ref}) of $145mm$, and a width (L_{width}) of $102mm$. The length scale on the computational grid is non-dimensionalized with respect to the reference length (L_{ref}). The computational grid will only simulate half of the plate taking advantage of the symmetry that exists. The grid used for the flat plate simulation is a *C-type Hybrid* grid, and is identical to the grid used to study the blunt-fin.

Selecting the *C-type Hybrid* grid for this simulation will serve two purposes. For the primary case, it will a give an indication of how well the *C-type Hybrid* grid is able to accurately solve the flat plate problem, secondly the heat transfer results obtained from the current simulation will represent a heat transfer solution from an undisturbed flat plate and will be used to normalize the heat transfer data obtained from the blunt-fin/plate simulations, as done by Schuricht [53] in his experimental results.

It is noteworthy that, while all fluid problems are governed by the same equations, namely the full Navier-Stokes equations, what distinguishes one flow from another are the boundary conditions and the Mach number. Therefore although the current *C-type Hybrid* grid is generated using the geometric dimensions of the blunt-fin on a flat plate, the definition of the flat plate boundary conditions in three-dimensions for the *C-type Hybrid* grid are modified accordingly so that the presence of the blunt-fin is effectively erased to the incoming flow. An example of the flat plate *C-type Hybrid* grid is shown in Figure 4.1.

The plate configuration is exposed to freestream Mach number of 6.7 with a unit Reynolds

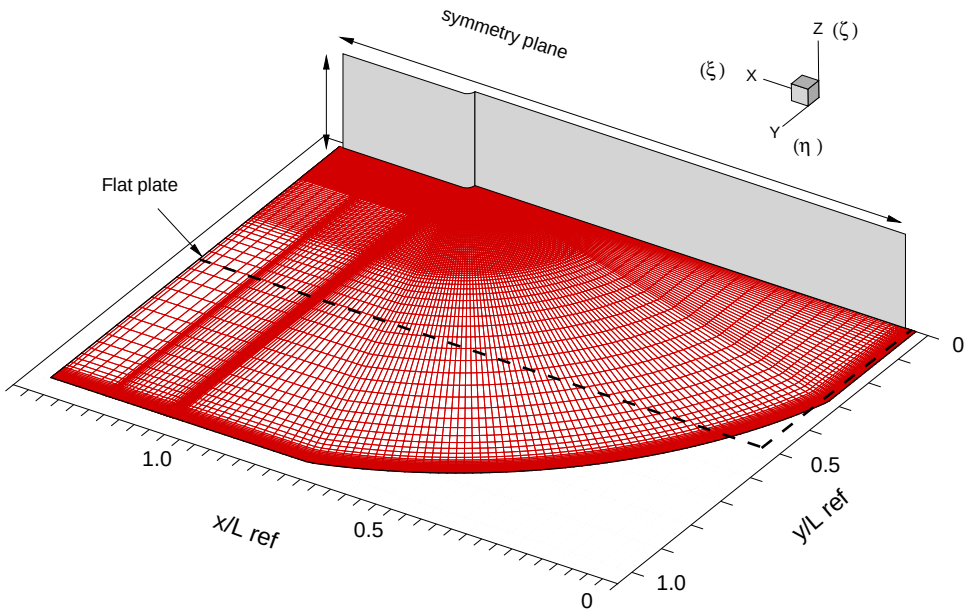

Figure 4.1: three-dimensional flat plate grid

number of ($Re/l = 7.6 \times 10^6 m^{-1}$). The initial conditions for the three-dimensional test simulation are a gas at rest in thermal equilibrium with the the plate surface. To allow for quick propagation of the incoming shock wave, the initial density was chosen to be 5% of the freestream density. In the present study we are only interested in the final steady state solution.

4.2.2 Numerical Results

The leading edge of the flat plate is the initial source of disturbance to the freestream and the grid resolution in this area could have a significant effect on the solution at the leading edge and, therefore, the flow downstream. Similarly, the grid resolution in the boundary layer region could be critical to the accuracy of the boundary layer solution and affect the prediction of surface quantities.

To demonstrate that the grid clustering implemented on the *C-type Hybrid* grid near the

leading edge and near the plate surface is optimized to capture the leading edge shock and laminar boundary layer, a comparison is made with the empirical correlations of Eckert [19] for skin friction coefficient and Stanton number. The definition of both these parameters can be found in (Chapter 2, Section 2.2). The resultant comparison is shown in Figure 4.2. It is important to stress however, that the grid clustering in the blunt-fin grid is dictated by features associated with separation well downstream of the leading edge. As a result this will account for some of the discrepancies observed near the leading edge in the numerical results, however this should be quite minimal. The numerical results are obtained with a first order scheme using a $(172 \times 160 \times 144)$ grid. Five grid cells are allowed between the inflow and the leading edge of the flat plate to allow the freestream flow to establish and to avoid boundary influence.

The Stanton number and skin friction coefficient profiles shown in Figure 4.2 display an initial decay in the downstream direction away from the leading edge which follows the $(x^{-\frac{1}{2}})$ curve associated with laminar flat plate flow. Theoretically, the heat transfer rate is infinite at the leading edge, although this is not actually determined as the leading edge lies between two grid points. As the boundary layer growth rate eases and the boundary layer thickness increases at a more moderate pace, a slowly decaying distribution can be observed. All correlations produce an excellent agreement for $(x/L_{ref} > 0.2)$. However, slight differences appear in the calculated values for skin friction coefficient and Stanton number in the region $(x/L_{ref} < 0.2)$, near the leading edge of the flat plate. This discrepancy in the calculated values in this region is most likely the result of strong viscous interaction, as discussed in (Chapter 2, Section 2.2). The reference temperature method of Eckert does not take into account viscous interaction [47, 19].

In (Chapter 2, Section 2.2) it was discussed that a region of strong interaction is assumed to exist for $(\bar{\chi} > 3)$ [2], $(\bar{\chi})$ is defined in Eqn 2.15. A distance (x_v) may be associated with the threshold from strong to weak interaction, given by:

$$x_v = \frac{M_\infty^6}{9Re_{/l}} C \tag{4.1}$$

where $\left(Re/l = \frac{\rho_\infty U_\infty}{\mu_\infty}\right)$ is the Reynolds number per unit length. In the present case this

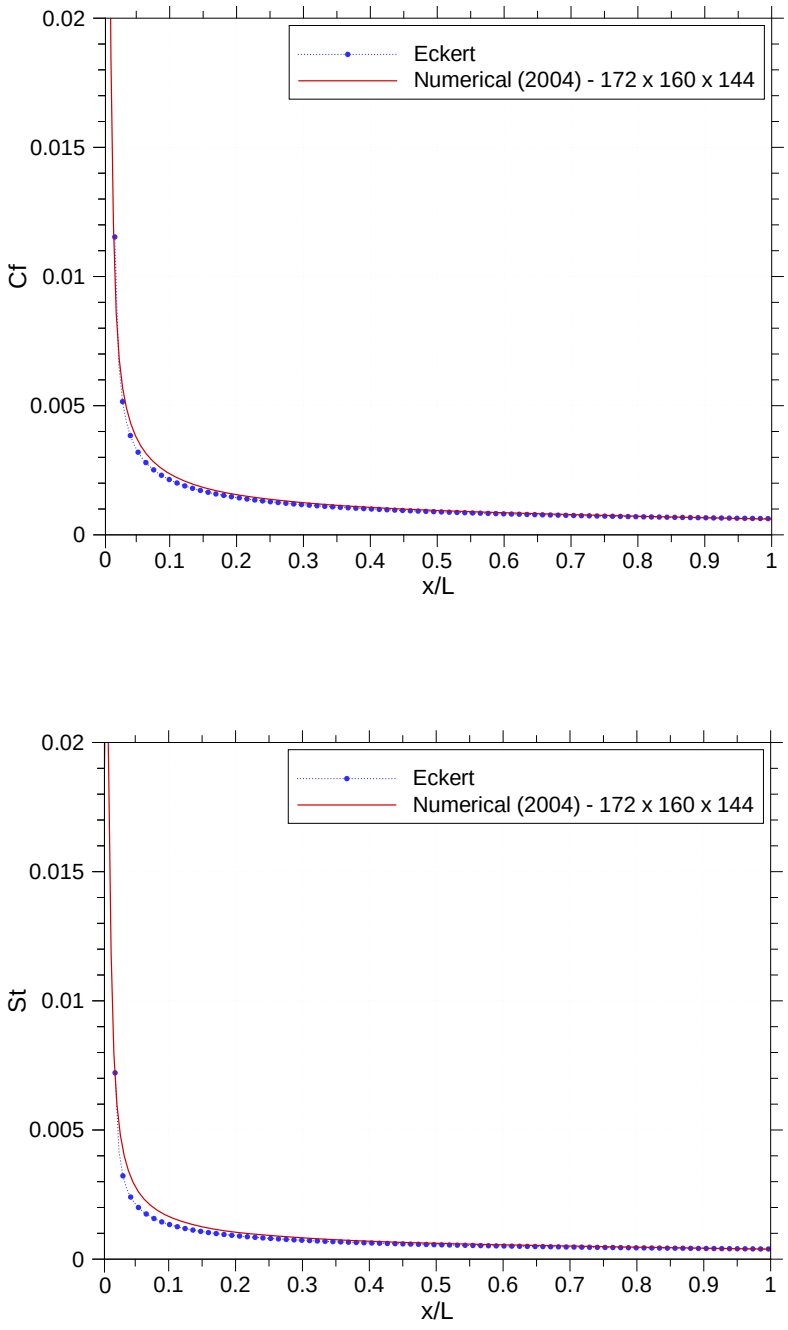

Figure 4.2: (**top**) Comparison of skin friction coefficient between flat-plate grid of $172 \times 160 \times 144$ and Eckert [19] (**bottom**) Comparison of Stanton number between flat-plate grid of $172 \times 160 \times 144$ and Eckert [19]

distance is estimated to be ($x_v/L_{ref} = 0.05$). As a result Eckert's empirical predictions for Skin friction coefficient and Stanton number are unlikely to produce accurate results in the strong interaction region where ($x < x_v$), which is where the major discrepancies are observed in Figure 4.2.

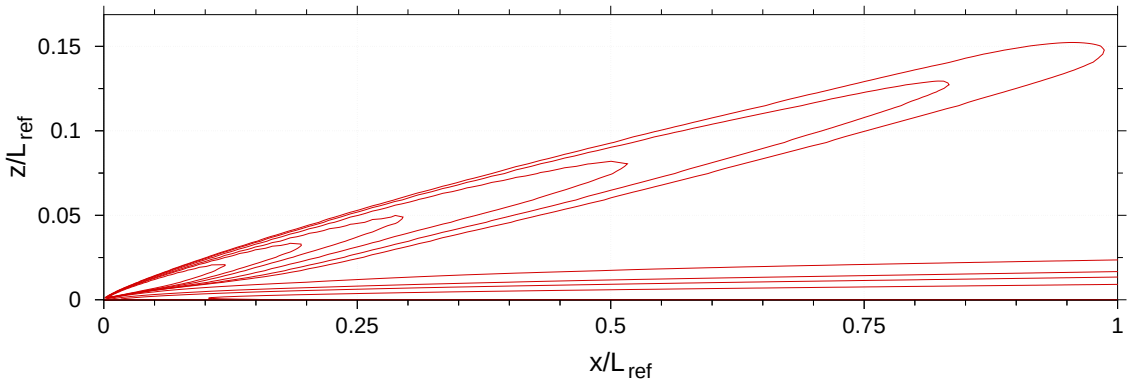

Figure 4.3: Density contours from symmetry plane

The density contours in the symmetry plane are shown in Figure 4.3. The weak leading edge shock and laminar boundary layer on the flat plate appear to be clearly resolved by the grid, and this profile is very similar to density profiles obtained by Navarro-Martinez [47] and Amaratunga [1] for equivalent flat plate simulations using two-dimensional grids with the same grid density. For a means of comparison, the leading edge shock angle measured by Navarro-Martinez [47] for a flat plate using the same freestream conditions, and using a *H-type* grid is ~ 10 degrees. The same angle measured from the current simulation using the *C-type Hybrid* is ~ 11 degrees. The comparison appears to be reasonably good.

4.3 Cylinder Test Case

4.3.1 Introduction

The three-dimensional test scenario used to validate the new methodology for calculating the three-dimensional metrics in the new code, is a supersonic flow over a cylinder/plate configuration.

Experimental data from tests undertaken by Özcan & Holt [11] for this configuration will be used to compare the numerical results obtained from the simulation. Also available for comparison is additional independent numerical data from tests carried out by Lakshmanam & Tiwari [45] on the same configuration. The numerical algorithm used by Lakshmanam & Tiwari was the MacCormack explicit predictor corrector, time split, finite volume method.

4.3.2 Experimental Conditions

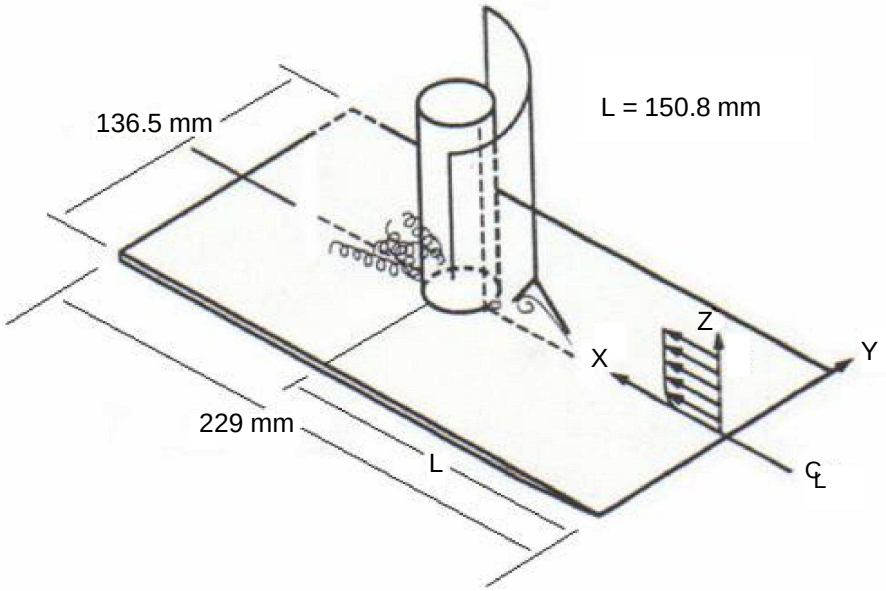

Figure 4.4: experimental rig [45]

The experiments undertaken by Özcan & Holt were carried out in 15×15 cm supersonic wind tunnel at the University of California Berkeley [11]. The overall dimensions of the flat plate on which the cylinder is mounted is given in Figure 4.4, which also shows the coordinate system chosen for data presentation.

The wind tunnel was operated nominally at a Mach number of 2.36. Laminar flow test conditions were obtained by controlling the tunnel stagnation pressure. The tunnel stagnation values for pressure and temperature were ($p_0 = 24{,}000 N/m^2$) and ($T_0 = 294K$) respectively.

4.3.3 Numerical Modelling

The freestream velocity, temperature and pressure used in this numerical investigation are ($U_\infty = 567.3ms^{-1}$, $T_\infty = 139.1K$) and ($p_\infty = 1747.4Pa$) respectively. These conditions correspond to a freestream Mach number of 2.36 and a freestream unit Reynolds number of the order $2.7 \times 10^5 m^{-1}$. The constant used for the ratio of specific heat (γ) is 1.4. The Sutherland model for viscosity is used for this simulation.

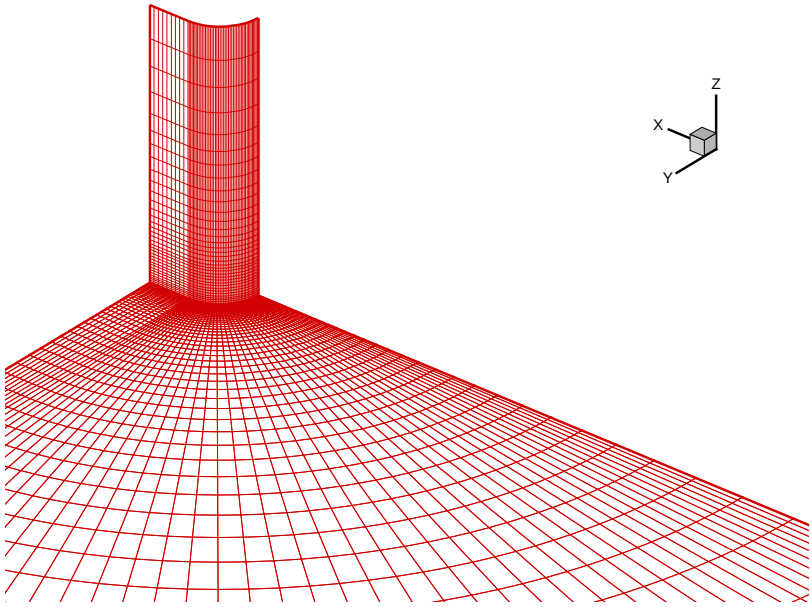

Figure 4.5: Numerical grid

The mesh was generated using *GRIDGEN.V.14* as described in (Chapter 3, Section 3.8). The grid is a standard *C-type* grid with the grid clustered near the flat plate and in the region surrounding the cylinder/flat plate junction. The geometric dimensions for the mesh were taken from Figure 4.4. An example of the grid ($58 \times 56 \times 50$) is shown in Figure 4.5.

The grid generated only models the front section of the cylinder, primarily because our interests are only concerned with what is happening to the flow in front of the leading edge of the cylinder, and its assumed that information concerning downstream effects do not affect the flow upstream. The grid is based on a reference length (L_{ref}) of $150.8mm$, a fin diameter ($D = 6.35mm$) and a fin height of $50mm$. Table 4.1 gives some grid properties.

Grid	Type	$\Delta x/\Delta y$	x_S/D	Δx of smallest cell ($\times fin\ diameter$)
$58 \times 56 \times 50$	A	15	7.4	0.006D
$116 \times 112 \times 100$	B	8	8.1	0.004D

Table 4.1: Grid properties for 6.35mm cylinder

The grids used for this study was an initial ($58 \times 56 \times 50$) coarse grid (Type-A), and a doubled ($116 \times 112 \times 100$) fine grid (Type-B), (see Table 4.1). For the initial simulation the coarser mesh was used to generate a quick solution for the flow field, once a near converged solution was established the flow properties were interpolated to the doubled grid and allowed to converge to yield a more accurate solution. The size of the first and last (ξ) mesh cells are the smallest cells used in the domain, and are non-dimensionalized with reference to the cylinder diameter (D), and is set to ensure sufficient resolution of the viscous effects near the plate surface. For this test, grid properties similar to the ones defined by Lakshmanam & Tiwari [45] are used. According to them the first mesh cell off the wall is equal to $0.005D$ and was found to be sufficient to ensure resolution of the viscous effects. Only two grid studies were undertaken mainly because the objective was to check the three dimensional metrics and not the accuracy of solver.

Taking advantage of the symmetry that exits for the configuration at the symmetry plane ($j = 1$), only half of the cylinder is solved. The boundary conditions imposed are: zero-gradients exist for all primary variables at the outer boundaries in the ($j = max$) and ($k = max$) directions. The cylinder has zero incidence, and a symmetry condition is imposed at the plane of symmetry. The wall is also assumed impermeable, and no-slip boundary conditions are applied. The wall is also assumed to be adiabatic, and the pressure gradient normal to the wall is set to zero. The grid block has five cells ahead of the inflow boundary to allow the freestream flow to establish and avoid boundary influence on the flow at the leading edge. Freestream conditions are used to initialise the flow domain. The simulation was run using 5 *Pentium III 800 MHz* processors on the *Beowulf* type *Linux* cluster, and took one week to achieve a converged result.

For comparative studies, streamline contours, pressure profiles and velocity profiles in the

symmetry plane and at several (x/D) locations are presented against the experimental results of Özcan & Holt [11] and the numerical results from a $(40 \times 100 \times 50)$ grid by Lakshmanam & Tiwari [45]. Additional results will show plate surface skin patterns.

4.3.4 Numerical Results

The salient inviscid features observed for this type of configuration exhibit all the characteristics of a blunt-fin/plate type interaction. This type of interaction is described in considerable detail in (Chapter 2, Section 2.5.2). The presence of shocks are indicated by steep gradients in the density contours above the surface boundary layer, which in Figure 4.6 is highlighted by contour lines compressed together. Clearly seen is a weak plate leading edge shock, a shock induced boundary layer separation shock, a bow shock formed infront of the cylinder and a point where a shock/shock interaction occurs as a result of the separation shock and bow shock intersecting. The ripple like characteristics as seen on the leading edge shock further downstream of the leading edge is caused as a result of poor grid resolution due to large coarse cells in the affected region.

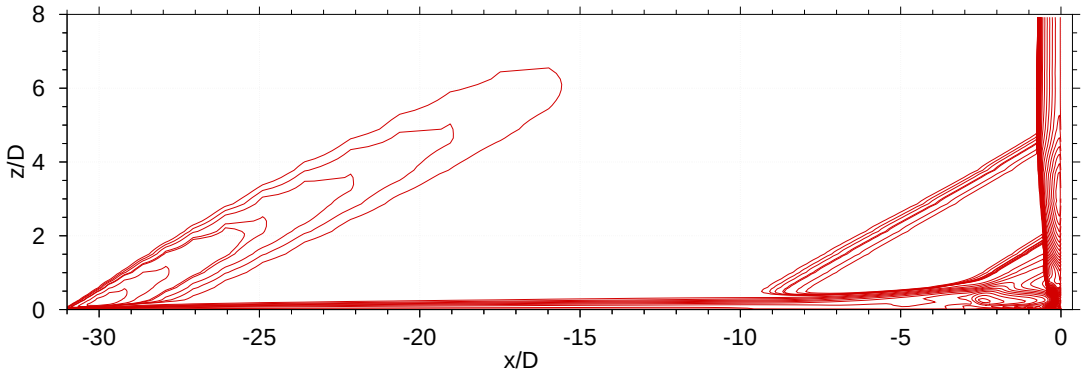

Figure 4.6: Density contours from the plane of symmetry, indicating the structure of the interference interaction

This phenomenon is common to structured grids that are not always orientated in the direction of an incoming shock, where grid oblique shock are modelled by pairs of grid-aligned shocks. As a result, shock resolution would suffer in areas where the grid density is low. A similar observation was made by Navarro-Martinez [47].

Underneath the separation shock the separated flow turns into a vortex system which develops downstream and in the span direction to produce a horseshoe vortex system (refer to Chapter 2, Section 2.5.2).

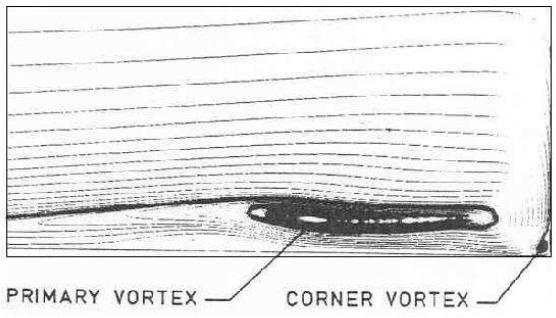

Figure 4.7: Streamline contours in symmetry plane by Lakshmanam & Tiwari [45]

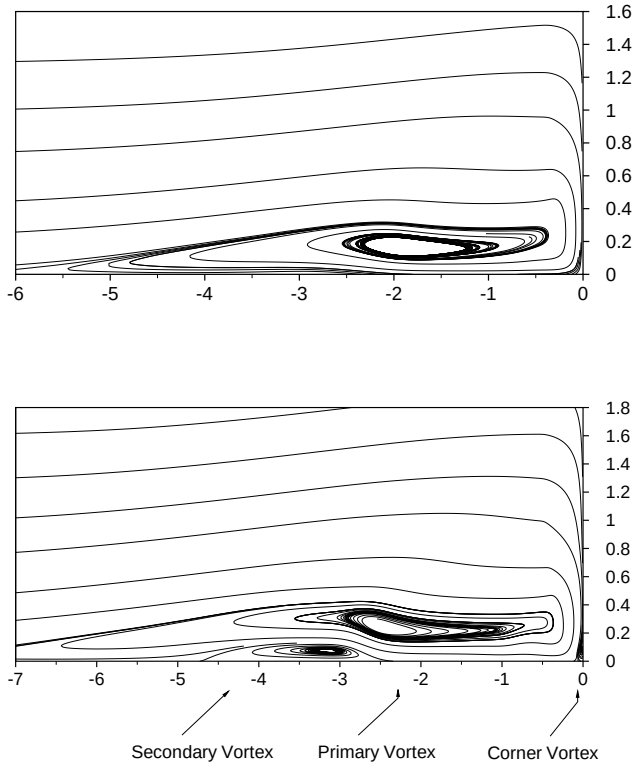

Figure 4.8: (**top**) Computed streamline contours in symmetry plane grid $58 \times 56 \times 50$ (**bottom**) Computed streamline contours in symmetry plane grid $116 \times 112 \times 100$

This vortex structure is clearly illustrated in the computed velocity streamlines shown in Figures 4.7 and 4.8. The streamlines obtained by Lakshmanam & Tiwari [45] in Figure 4.7, taken from the plane of symmetry along the centerline, show a two vortex structure, with a primary core vortex and a smaller corner vortex. The present numerical results identify a very similar structure as seen in Figure 4.8 with the main vortex core and the corner vortex well captured. However, the results from the higher density grid (see Figure 4.8:(**bottom**)) also indicates a second vortex localised at the plate surface. This feature does not appear in the numerical results of Lakshmanam & Tiwari. However, a closer observation of Figure 4.7 indicates a region just underneath the main vortex core where there is a large deviation in the streamline paths close to the plate surface. This could be indicative of a localised vortex, but as a result of poor grid resolution in this region of Lakshmanam & Tiwari's grid, this feature does not appear to be captured by the numerical scheme.

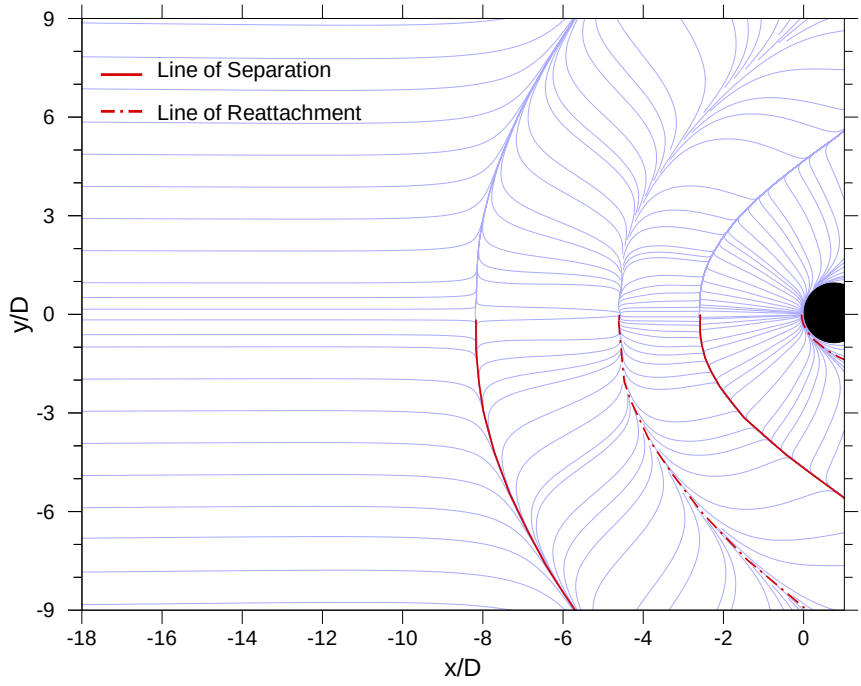

Figure 4.9: Computed skin friction streamline on plate surface of grid $116 \times 112 \times 100$

The study of separation phenomena requires the visualization of the near-wall flow field. A representation of the flow near the wall may be obtained from the numerical flow field

by use of skin friction lines as shown in Figure 4.9.

The extent of the separation is characterized by the separation distance (x_S), which is measured from the primary separation line to the cylinder leading edge along the symmetry axis. For laminar flow past long protuberances the extent of the separation correlates with Reynolds number based on (L_{ref}), which is the distance between the flat plate leading edge and the cylinder leading edge. This relationship was reported in (Chapter 2, Section 2.5.2).

Based on surface measurements by Özcan & Holt [11] for the Reynolds number reported in this study of $2.7 \times 10^5 m^{-1}$, they observed two distinct separation lines as shown in Figure 4.9. In addition the observed streamline pattern in Figure 4.8 is consistent with the presence of two separation lines ahead of the cylinder.

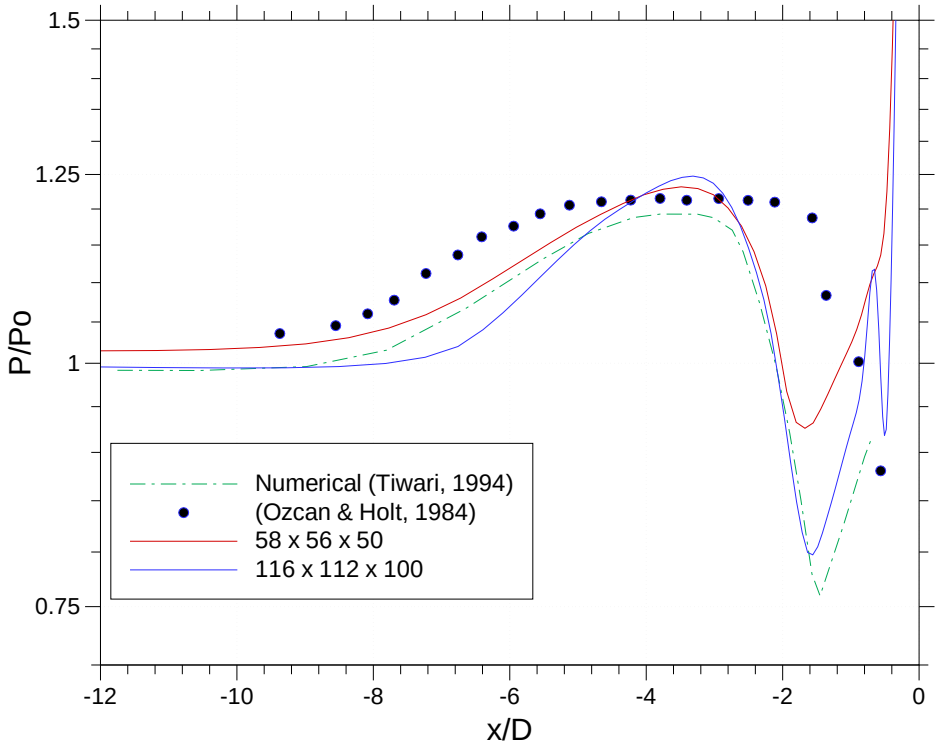

Figure 4.10: pressure profile in symmetry plane [45]

The pressure distribution along the axis of symmetry is shown in Figure 4.10. It is apparent that, in the experiment, the pressure begins to rise at about (x/D = -9) upstream of the fin

leading edge. The pressure reaches a valley downstream of the plateau and then increases across the detached bow shock.

There appears to be considerable differences in the computed pressure profiles when compared with the experimental results of Özcan & Holt; however there appears to be a good agreement with the numerical pressure profile obtained by Lakshmanam & Tiwari [45]. The peak pressure point is accurately estimated, experimental values indicate a peak of around 1.24, whereas computed values reach around 1.25, similarly the experimental pressure peak appears to be $\simeq$ 3 diameters from the cylinder, this is well matched by both computed results.

The computed results using the fine mesh, slightly underpredict the extent of separation. Experimentally initial separation was observed to be at (x_S/D = -8.5), the computed separation point was at (x_S/D = -8.1), which is a equal to the separation length calculated by Lakshmanam & Tiwari [45]. The reasons given by Lakshmanam & Tiwari [45] for the failure to match the experimental results, (e.g. like the predicted the length of the pressure plateau region observed in the experimental data) is due to the flow going through transition to turbulence in this region.

The computed and experimentally measured streamwise velocity profiles along the line of symmetry are shown in Figure 4.11. The streamwise velocity component is nondimensionalized with reference to the velocity (u_e) at the edge of the boundary layer. In general, the agreement between the computation and the experiment is quite good, except the location and height of the separated flow region at (x/D = -2.4) are slightly underpredicted by the numerical code. In the experiments, streamwise and vertical velocities (u and (w) were measured by a single-component, forward scatter, differential (dual) beam laser-velocimeter [11].

4.3.5 Viscous Cross-Derivatives

To physically quantify the impact on the numerical solution, by way of including the viscous cross derivatives , two cases of the cylinder on a plate flate was simulated. The first case just took into account the normal derivatives in all three spatial directions (ξ,

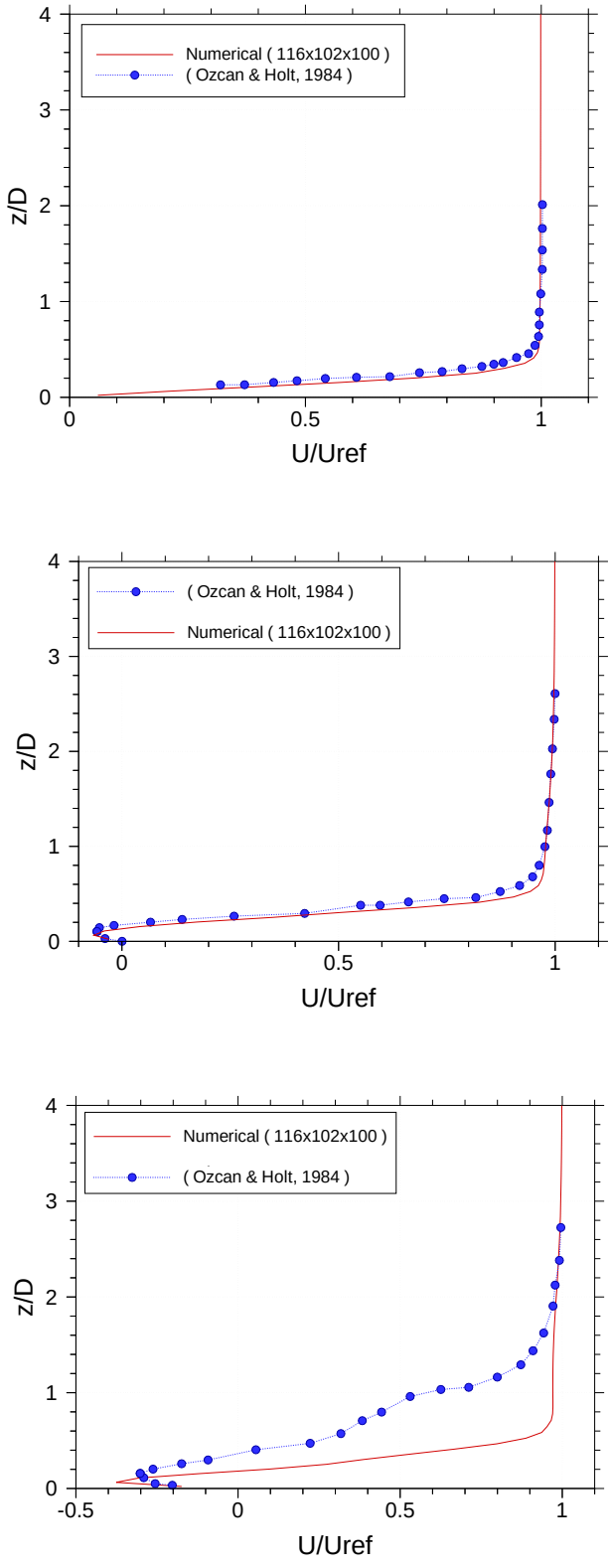

Figure 4.11: (**top**) Streamwise velocity profile at x/D=-8 (**middle**) Streamwise velocity profile at x/D=-4 (**bottom**) Streamwise velocity profile at x/D=-2.4

η and ζ). The second test looked at incorporating the additional cross derivatives mainly the (ζ) related derivatives, normal to the flow direction.

From the results it is revealed that the computation of the additional cross derivative terms took about 4% more CPU -time/cycle than when computing just the same thin layer terms. The effect this has on the numerical convergence is illustrated in Figure 4.12, where it can be observed that the extra terms considerable increase the time required to achieve a converged solution.

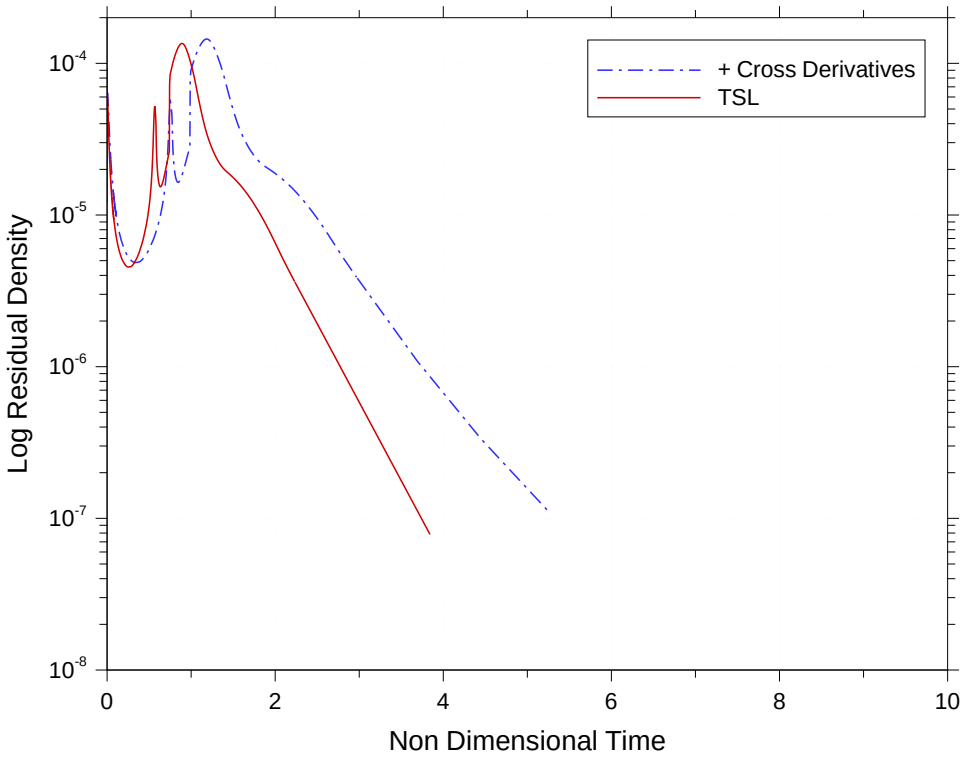

Figure 4.12: Convergence history for cylinder with and without including the cross derivatives in the viscous fluxes

Viscous Method	C_f at (x/D = -0.5)	C_f at (x/D = -1.0)
TSL	-0.02216	-0.01428
Cross derivatives	-0.02211	-0.01425

Table 4.2: Skin friction coefficient at various x/D locations for different viscous solvers

Table 4.2 gives the calculated skin friction coefficients at two locations near the cylinder/flat plate junction, (x/D = -0.5) and (x/D = -1.0), the corner of two surfaces is where the cross derivative terms might affect the numerical solution.

As the results indicate, inclusion of the viscous cross derivative terms has no appreciable impact on the skin friction coefficient, and hence on the final numerical solution.

4.4 Summary of Test Results

The numerical results from the test simulations has shown that the numerical scheme using a *C-type* grid is capable of accurately simulating a flat plate flow and the more complex cyclinder/plate flow.

The flat plate results indicate that the *C-type* grid is able to accurately resolve the laminar boundary layer and leading edge shock, thus making it suitable for use in blunt-fin simulations. The numerical code has demonstrated that the accuracy achieved in the simulations is quite sufficient and the results are comparable to those found by Navarro-Martinez [47] and Amaratunga [1].

The results from the cylinder/plate flow show that the three-dimensional metrics are working and are capable of solving a generic three-dimensional flowfield. The numerical results show favourable comparisons with the experimental results and with further grid refinement studies more accurate results could be obtained however, this was not the primary aim of these initial tests. In addition, a comparison of the computed results between Lakshmanam & Tiwari [45] and the current simulation show superior comparisons to the experimental results and more detail about the flow field using the current numerical method for the same grid densities.

Inclusion of the viscous cross derivatives in the cylinder simulations did not appear to change the final result drastically, coupled with the additional increase in CPU time per time step, does not warrant its inclusion in the viscous solver. As a result all subsequent simulations will only compute the full thin layer terms in all three spatial directions.

Chapter 5

Three-Dimensional Numerical Results

5.1 Introduction

This chapter will present and discuss the results obtained from numerically modelling several types of blunt-fin attached to a flat plate, exposed to a hypersonic freestream of nitrogen gas. Experimental data obtained by Schuricht [53] for blunt-fins, particularly from the unswept $5mm$ diameter blunt-fin on a flat plate, will be used as a reference in the present study. The experiments carried out by Schuricht were conducted in the Southampton University Light Piston Isentopic Compression (SULPICT) hypersonic wind tunnel facility.

5.2 Experimental Details

The (SULPICT) wind tunnel facility uses nitrogen as the test gas. The running time is approximately 0.5 *secs*, long enough to consider to the flow to be steady. In the experiments performed by Schuricht [53] the freestream Mach number in the working section was 6.7 with a unit Reynolds number of $7.6 \times 10^6 m^{-1}$. Schuricht believed that the subsequent flow

in the interference region surrounding the fin remained laminar, however that turbulent transition cannot be completely ruled out.

The stagnation temperature is approximately $600K$, and results in local absolute temperatures which remain sufficiently low for the assumption of perfect gas flow to remain valid throughout the domain of interest. The experimental run time is sufficiently short for changes in the surface temperature to be considered as negligible, (typically $\Delta T_w/T_w \leq 0.03$).

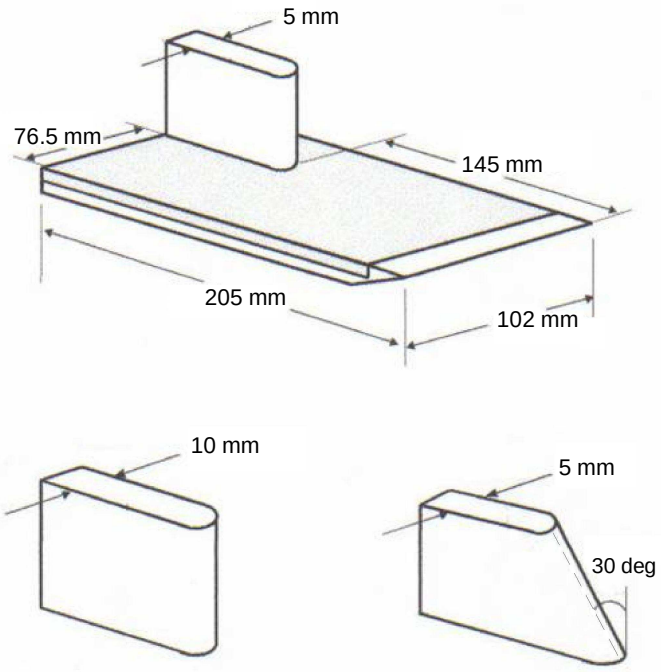

Figure 5.1: A schematic of the experimental rig used by Schuricht [53]

The experimental model consisted of a flat plate section $205mm$ in length and $102mm$ in width. The width of the plate was limited by the core of the test section; this is $150mm$ in diameter. A single blunt-fin, $60mm$ in length, was attached approximately $145mm$ from the leading edge of the plate (to allow a substantial boundary layer to develop ahead of the fin) and offset from the centerline by approximately $25.5mm$ (to allow a large heating footprint to be observed. The fin had a height of $25mm$ and for a 0° sweep angle two fin diameters are considered, $(D = 5mm)$ and $(D = 10mm)$. Additionally a fin with a diameter $(D = 5mm)$ with a sweep angle of 30° is also considered. A schematic of the various blunt-fin configurations considered is illustrated in Figure 5.1.

The transitional Reynolds number for this flow is assumed to be $\left(Re_{trans} = 1.3 \times 10^6\right)$, as a result transition should occur approximately $171mm$ from the leading edge of the flat plate. This would appear to lie within the domain interest looked at in this study. However it is clear that this region is well behind the blunt-fin leading edge and the separated region of interest ahead of the fin. While transition might affect the heat transfer results from $171mm$ onwards the flow in the separated region ahead of the blunt-fin and the flow up to $(x/D = +5)$ would appear to be laminar. Therefore in conclusion the Reynolds number is sufficiently low for the attached flow ahead of the blunt-fin to remain laminar as well as the flow in the separated region ahead of the blunt-fin.

The surface measurements recorded by Schuricht consisted of heat transfer maps obtained by liquid crystal thermography, surface oil flow visualization and schlieren photography. Apart from full heat transfer maps of the plate surface, heat transfer measurements were also taken along the plate which coincided with the fin centerline or symmetry line and at several points normal to the fin surface, coinciding at $(x/D = +1)$, $(x/D = +5)$ and $(x/D = +10)$ downstream of the fin leading edge. Oil flow and schlieren photographs allowed estimates of the separation and reattachment lengths to be made. Schuricht estimated that in regions where the liquid crystals have responded correctly the overall uncertainty in the deduced value of the heat transfer coefficient to be in the region of $(\pm 10\%)$. For more detail on the experimental heat transfer measurement technique and the related equipment refer to Schuricht [53].

5.3 Numerical Modelling

Numerical simulations of the three basic blunt-fin configurations described above are performed using a constant specific heat ratio ($\gamma = 1.4$) and a constant Prandtl number of ($Pr = 0.704$). The transport properties "viscosity" and "thermal conductivity" are based on the Lennard-Jones model [47]. A length scale based on the diameter of the blunt-fin ($D = 5mm$) is used as a characteristic length for non-dimensionalising distances. The resultant coordinate system is centered with $\left((x, y) = 0 \right)$ set at the base of fin leading edge. As a result distances upstream of fin leading edge are negative; downstream are positive.

Freestream quantities are calculated based on a Mach number of ($M_\infty = 6.7$), a unit Reynolds number of $\left(Re/l = 7.6\times10^6 m^{-1}\right)$ and a stagnation temperature of ($T_o = 600K$). The freestream temperature is obtained via the adiabatic relationship for temperature given by

$$T_\infty = T_0\left(1 + \frac{\gamma-1}{2}M_\infty^2\right)^{-1} \tag{5.1}$$

The freestream velocity is given by

$$U_\infty = M_\infty\sqrt{\gamma R T_\infty} = M_\infty\sqrt{\frac{\gamma R_N T_\infty}{m_{N_2}}} \tag{5.2}$$

where (R) is the universal gas constant, (R_N) is the gas constant for nitrogen and (m_{N_2}) is the molecular mass of nitrogen. The freestream density is obtained from the unit Reynolds number:

$$\rho_\infty = \frac{Re/l\mu_\infty}{U_\infty} \tag{5.3}$$

with (μ_∞) obtained from the Lennard-Jones model [47]. The freestream pressure is determined through the equation of state for an ideal gas. The calculated freestream temperature, velocity and pressure are ($T_\infty = 56.6K$, $U_\infty = 1050ms^{-1}$) and ($p_\infty = 430Pa$). Due to the small time scales involved, the plate is considered to be isothermal at a temperature of $300K$, similar to the mean wall temperature in the experiments performed by Schuricht [53].

An example of the *C-type Hybrid* grid of type $B1$ described in Table 3.1 for the $5mm$ unswept blunt-fin is shown in Figure 5.3, with an additional view of the symmetry plane in Figure 5.2. The dimensions of the grid shown are based on the $5mm$ unswept blunt-fin, in the upstream streamise direction from the base of the fin, the grid extends the length of the plate surface, 29 diameters. A minimum of five grid points are placed ahead of the leading edge to avoid inflow boundary influence on the leading edge of the flow, and to properly resolve the leading edge shock. In the downstream streamwise direction the grid

extends to 8.5 diameters. Spanwise, the grid stretches to 29 diameters.

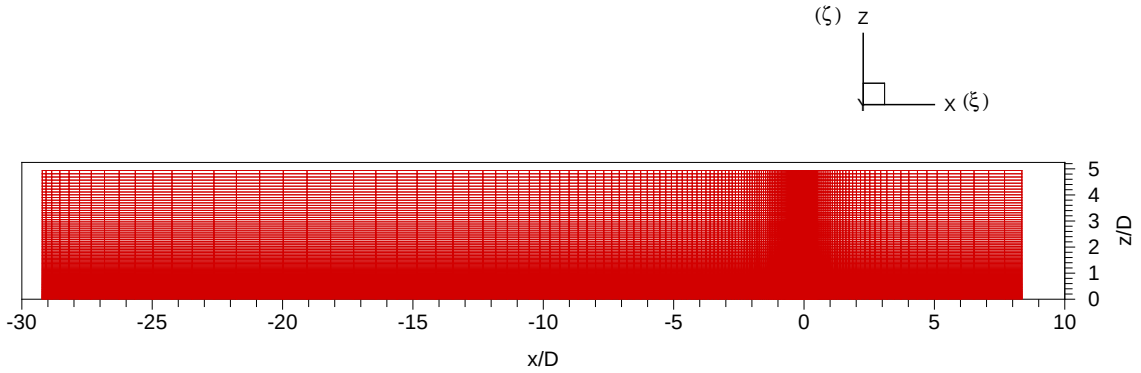

Figure 5.2: View of symmetry plane

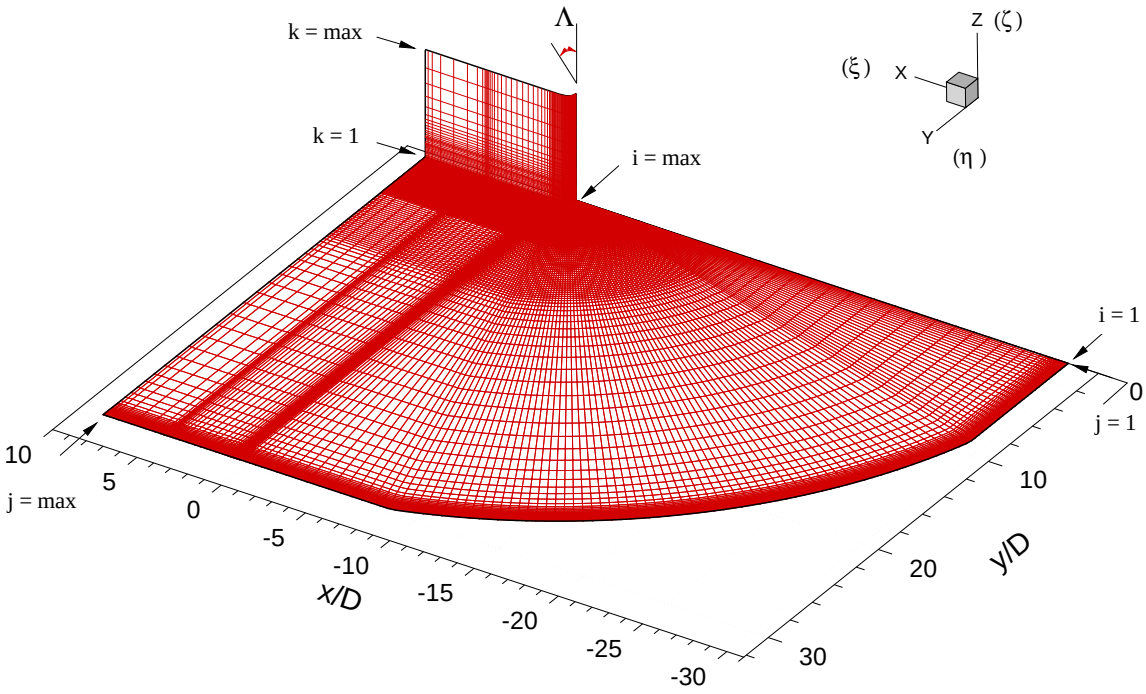

Figure 5.3: A three-dimensional view of a *C-type Hybrid* grid used in the computations, example grid $B1$, $172 \times 160 \times 144$

5.3.1 Boundary Conditions

Fixed, hypersonic, inflow boundary conditions are imposed along the outer ($i = 1$) boundary, and fin sweep (Λ) is varied depending on the model simulated, going from 0 for the $5mm$ and $10mm$ fins to 30° for the $5mm$ swept fin. A symmetry condition is imposed on the plane which is along the fin centerline at ($j = 1$).

The flat plate and blunt-fin wall surfaces are assumed to be impermeable, and no-slip boundary conditions are applied. The flat plate and blunt-fin walls are assumed to be isothermal with the pressure gradient normal to the walls set to zero.

The outer outflow boundaries at ($j = max$) and ($k = max$) are assumed to be distant enough from the blunt-fin not to interfere with the flowfield of interest. Therefore, a first-order extrapolation boundary condition was applied to these surfaces, where the ghost cells at the boundary interface mimic the boundary cells inside the computational domain. This way the gradients are always zero.

A listing of the boundary conditions appropriate to this study can be found in Appendix B.

The height of the blunt-fin is small enough to avoid impingement of the flat plate leading edge shock, while still being large enough to lead to an asymptotic behaviour, which means that any further increase of its height does not change the interaction extent. In particular, once the asymptotic height ($z/D = h_a$) is reached, then the upstream influence length, the primary separation distance and location of the triple point are independent of (z/D). Dolling & Bogdonoff [15] stated that for the asymptotic behaviour condition to be fulfilled, ($z/D > 2.5$). The current ratio of ($z/D = 5$), would appear to fulfil the asymptotic criterion set by Dolling & Bogdonoff [15].

5.4 5mm blunt-fin simulations

This section will present the results from the numerical simulations of the unswept 5mm blunt-fin. Experimental data obtained by Schuricht [53] for the same fin configuration will be used for referencing wherever needed.

5.4.1 Grid Refinement Study

To determine a means of quantifying the effect the grid has on the numerical solution, a series of different size grids are studied and their effect on specific variables examined. Table 5.1 shows the grids used in this grid dependency study. To ensure consistency the parameters used to define grid clustering on all the grids studied are kept the same, with only the number of grid cells in the (ξ, η, ζ) directions being varied. The primary aim of the mesh dependency study is to determine whether a grid independent solution could be obtained given the limitations of the available computational resources; which are described in Chapter 3, Section.

Grid	Type
$43 \times 40 \times 36$	A1
$58 \times 51 \times 45$	A2
$86 \times 80 \times 72$	B1
$116 \times 102 \times 90$	B2
$172 \times 160 \times 144$	C1
$232 \times 204 \times 180$	C2

Table 5.1: The grids used in the mesh dependency tests

A quantitative analysis is made on the variation of numerical separation length, plate skin friction coefficient, Stanton number and pressure ratio on the plate surface. All variables are measured along the line of symmetry or fin centerline on the grid. In addition to the quantitative analysis, a qualitative study is made of the effect grid refinement has on the structure of the general flowfield. This is achieved by examining the density contours and

particle streamlines taken from the plane of symmetry.

For the purpose of easily identifying clear differences in the simulated results, the plots for skin friction coefficient, Stanton number and pressure ratio will only show variation in properties from (x/D = -25) to (x/D = 0). In a similar manner, only the salient features in the contour profiles are noted and compared with in this grid dependency study. A detailed analysis of the flow structure is made later in this chapter, but for the current grid refinement study only the effects the grid has on these features is noted.

The various density contour profiles in Figure 5.4 clearly show the inviscid characteristics described in Chapter 2, Section 2.5.2 specific to blunt-fin/plate type interactions. Features like the plate leading edge shock, shock induced boundary-layer separation shock and detached fin bow shock are clearly visible in Figures 5.4:(**B**)- 5.4:(**D**). Although the features of the interaction flowfield appear in all the grids studied, their locations within the flowfield and resolution varies considerably in all but the finest grids. This is clearly illustrated when comparing the shock positions/angles between Figure 5.4:(**B**) & 5.4:(**D**). The shock structure in the coarse grid shown in Figure 5.4:(**B**) is poorly resolved and the angle of the leading edge shock is comparatively smaller when compared with Figure 5.4:(**D**), which represents the solution from the fine grid. Poor shock resolution is directly related to the number of grid points and the grid clustering criteria imposed on the grid. The stipulated requirement of accurately capturing and resolving the laminar boundary layer results in stretching the grid towards the plate surface. This in turn leads to a poor distribution of cells near the upper boundary with small ($\Delta x/\Delta z$) ratios. A direct consequence is the subsequent loss in resolution of the shock which has to be spread across several cells in this region. This loss in shock resolution is notably present in only the coarsest grids, such as grids A1 and A2.

Grid resolution also affects the flow structures captured in the separated region as seen in the particle streamline plots in Figure 5.5. The coarsest grid in the set shown in Figure 5.5:(**A**) appears to lack a considerable amount of detail about the vortical flow structure when compared to the other grid solutions. The root recirculation region and the recirculation regions on the plate surface upstream of the fin root are not captured at all in grid ($43\times40\times36$). However, systematic improvement in grid density appears to yield

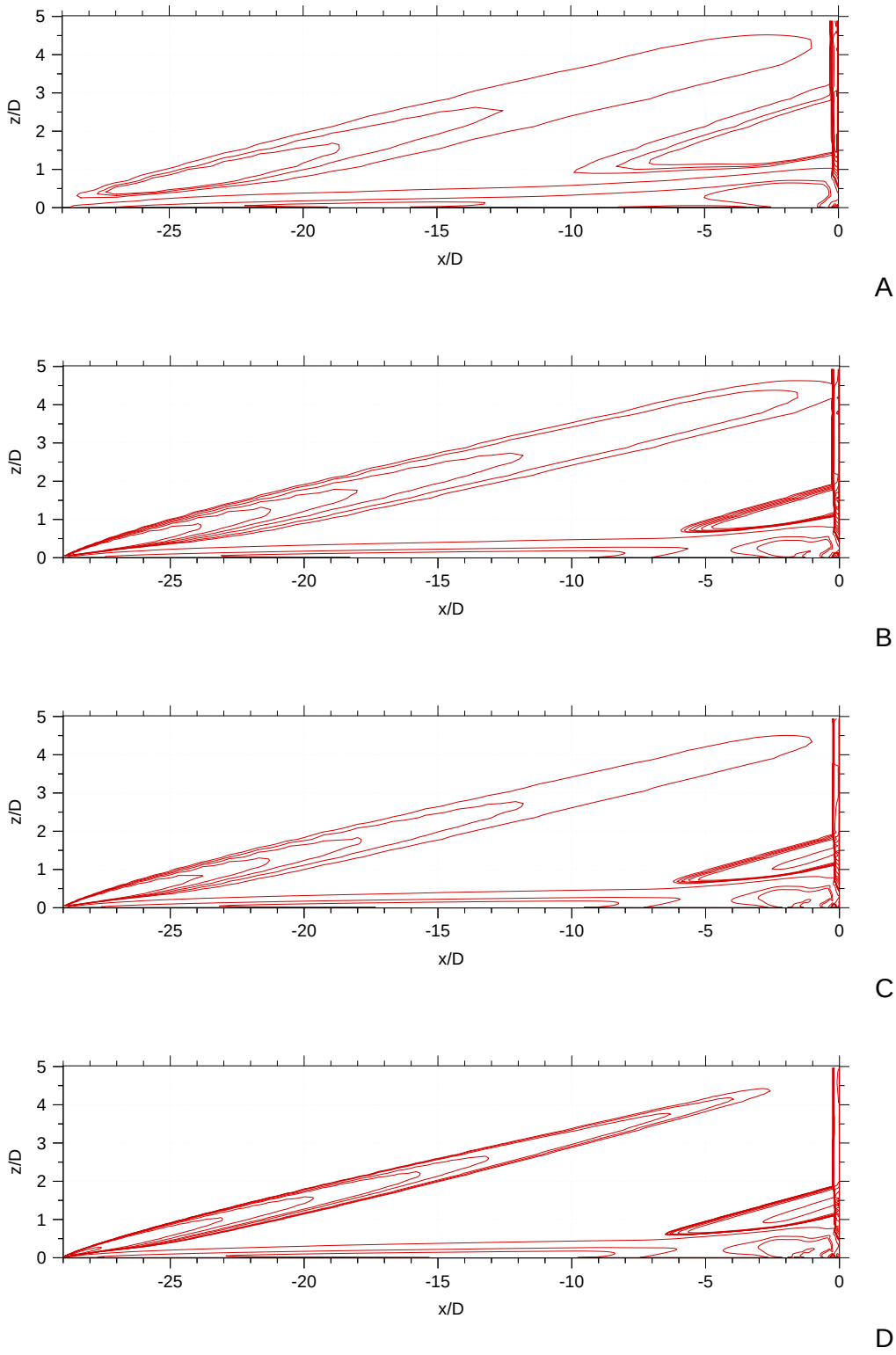

Figure 5.4: Density contours in the plane of symmetry for a range of (ρ) values: 0.0056 - 0.023 in increments of 0.001 (**A**) $43 \times 40 \times 36$ (**B**) $86 \times 80 \times 72$ (**C**) $116 \times 102 \times 90$ (**D**) $172 \times 160 \times 144$

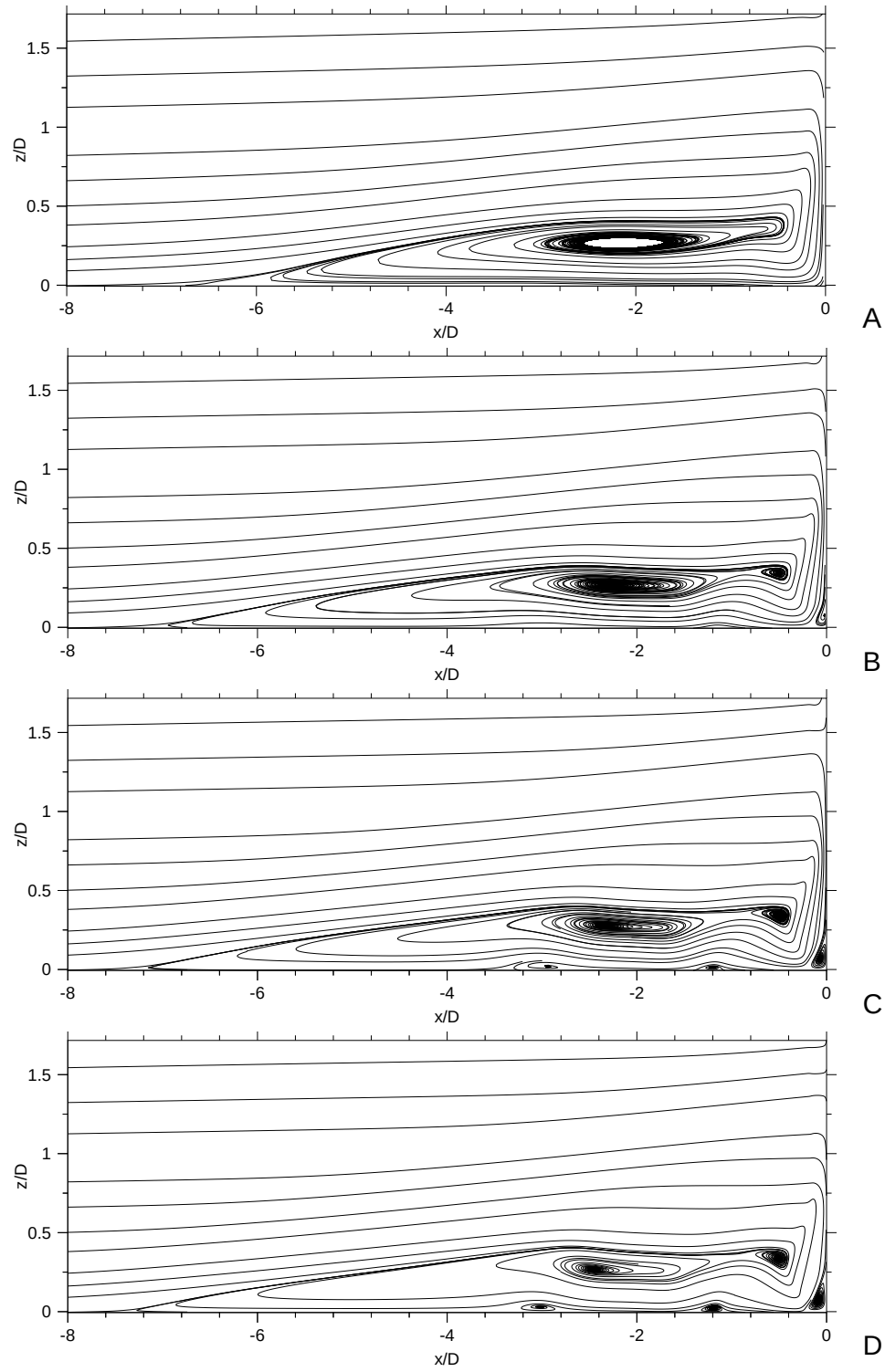

Figure 5.5: (**A**) Velocity streamlines $43 \times 40 \times 36$ (**B**) Velocity streamlines $86 \times 80 \times 72$ (**C**) Velocity streamlines $116 \times 102 \times 90$ (**D**) Velocity streamlines $172 \times 160 \times 144$

more detail of the vortical flow structure, with greater detail present in each increment. Overall mesh refinement clearly gives sharper more resolved inviscid features, like shocks and clearer definition of flow structures therefore giving a more accurate description of the flowfield. The most significant feature is the capture of further "secondary" vortices near the plate surface.

The variation in Stanton number along the line of symmetry for the various grid densities is shown in Figure 5.6, along with a comparison with Eckert's correlation for an undisturbed flat plate. The profiles initially show a strong decay away from the leading edge, similar to the ($x^{-\frac{1}{2}}$) decay observed on the flat plate, (see Figure 4.2). Further downstream of the leading edge there is a decrease relative to the Eckert comparison consistent with laminar separation, followed by an increase in Stanton number as the fin base is approached with a succession of peaks and valleys downstream of separation. It is evident that any discrepancies in the profiles are highlighted near the leading edge where, as described in Chapter 2, Section 2.2, there is a region of strong viscous interaction and where the rate of change in the Stanton number is greatest.

Table 5.2 gives the values for Stanton number at discrete points on the centerline for the three grids outlined.

Grid	Location, x/D	$C_f \times 10^{-3}$	$St \times 10^{-3}$
$58 \times 51 \times 45$	-27	4.7	4.0
	-25	2.3	1.6
	-20	1.7	0.9
$116 \times 102 \times 90$	-27	2.9	2.4
	-25	2.07	1.34
	-20	1.55	0.78
$232 \times 204 \times 180$	-27	2.8	2.25
	-25	2.0	1.28
	-20	1.52	0.757

Table 5.2: Measured quantities, location and grid density

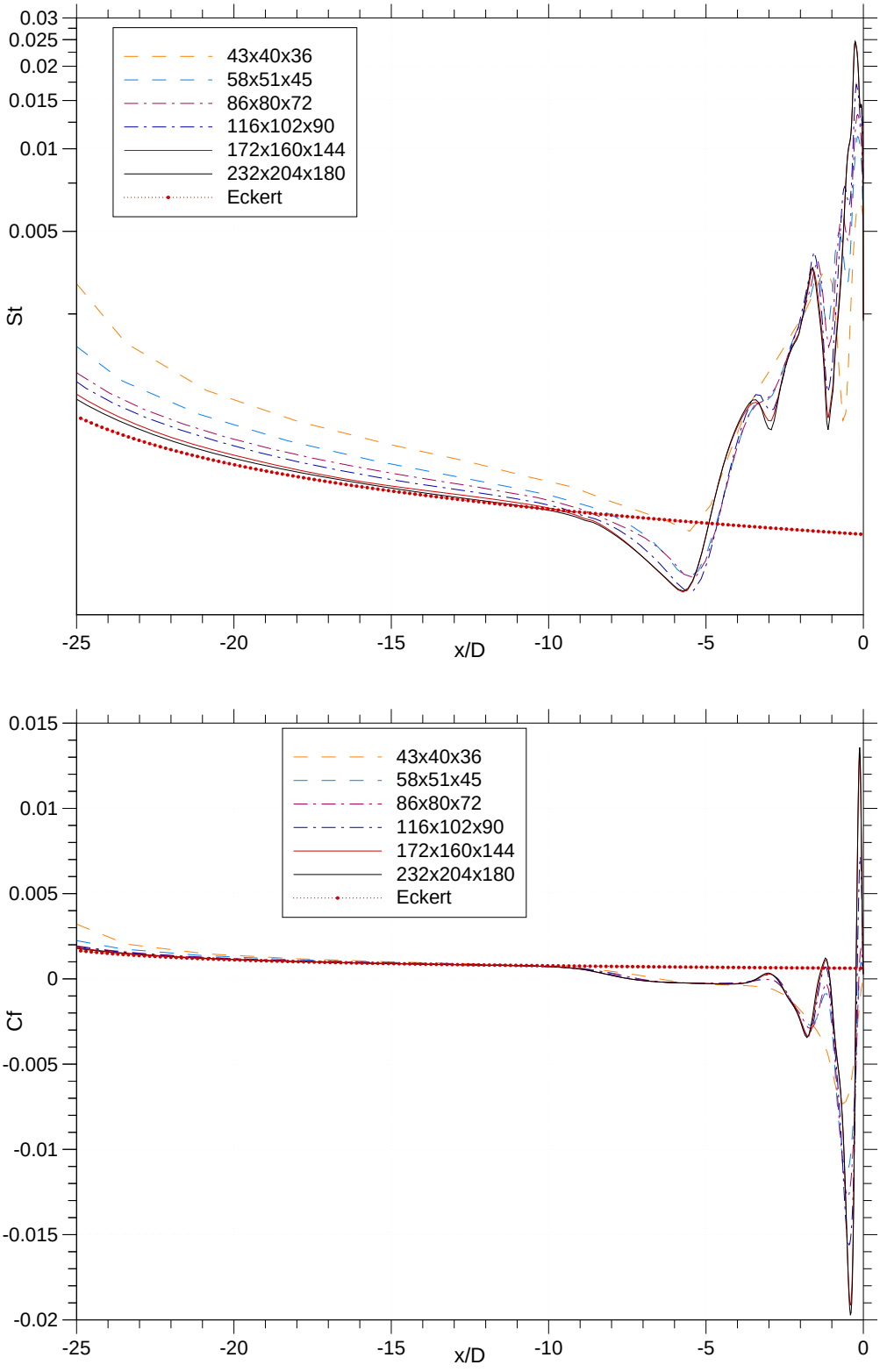

Figure 5.6: (**top**) Stanton number comparison for different grid densitites (**bottom**) Skin friction coefficient comparison for different grid densitites

The three stations are just downstream of the plate leading edge (in the region of high viscous interaction). Using these values as input parameters in the equations for evaluating the numerical convergence error (see Chapter 3, Section 3.11), generates the error results found in Table 5.3.

Location, x/D	-27D	-25D	-20D
Error in $C_f \times 10^{-3}$	0.0333	0.0233	0.01
% Error in C_f	3.57	3.50	1.97
Error in $St \times 10^{-3}$	0.05	0.02	0.0077
% Error in St	6.67	4.69	3.04

Table 5.3: Error analysis between grid $232 \times 204 \times 180$ and $116 \times 102 \times 90$ using method by Roache [51]

The results in Table 5.3 represent a comparison for Stanton number made between grid *B2* ($116 \times 102 \times 90$) and *C2* ($232 \times 204 \times 180$), because as assumed earlier it is taken that the results from the finest grid, in this case *C2*, represent the "true" value for Stanton number and skin friction coefficient. At station (x/D = -27) the value for Stanton number in grid *B2* is approximately +6.67% higher than the corresponding value for grid *C2*. Further downstream, at station (x/D = -20) this drops to +3.04%. Figure 5.6 clearly indicates that for ($x/D >$ -20) from the leading edge, all the profiles produce nearly equivalent results apart from the baseline grids of ($43 \times 40 \times 36$) and ($58 \times 51 \times 45$). All the error percentages in Table 5.3 are within the standard limits of experimental error ($\pm$10%). The general trend observed in the results in Table 5.3 verifies the statements made earlier, that the greatest difference occurs at the leading edge. The process of grid refinement indicates that the Stanton number profile tends toward the Eckert solution upstream of separation, and within the separated region the number and absolute value of the successive peaks in the Stanton number profile increase with increasing grid resolution. The coarser grids clearly overpredict the Stanton number values near the leading edge, indicating that there is a significant impact of the cell size on the calculated Stanton number. In addition, the plot indicates that apart from the final peak, grid refinement has the effect of decreasing the magnitude of the minor peaks. As a rule of thumb for an accurate calculation of

the Stanton number on the plate surface, the grid cells on the surface must satisfy the following condition: ($\Delta x/\Delta z \leq 8$).

A comparison of the skin friction coefficient on the plate $\left(C_f = \tau_w/\frac{1}{2}\rho_\infty U_\infty^2 \right)$ measured along the centerline also illustrated in Figure 5.6, appears to show similarities to the patterns observed in the Stanton number profile. The profiles show a strong decay away from the leading edge, again similar to the decay observed on a flat plate, (see Figure 4.2). Further downstream of the leading edge there is a decrease relative to the Eckert comparison, which is consistent with laminar separation; this is followed by a succession of peaks and valleys in the profile as the fin base is approached. The coarser grids clearly overpredict the (C_f) values near the leading edge, indicating a similar relationship to cell size as found with the Stanton number comparison in Figure 5.6. Table 5.3 also shows the grid convergence error for the calculated skin friction coefficient, and even though the skin friction coefficient wasnt measured experimentally by Schuricht the associated errors are within the ($\pm 10\%$) limit of standard experimental error. It is also apparent from Table 5.3 that the skin friction coefficient is less sensitive to grid convergence compared to the Stanton number. In general it is shown that as the number of grid points increase along the centerline, the improvement in the results and tendency for the skin friction profile to match the Eckert solution upstream of separation is clearly observed.

Grid	Type	x_S/D
$43 \times 40 \times 36$	A1	-6.821
$58 \times 51 \times 45$	A2	-7.118
$86 \times 80 \times 72$	B1	-7.236
$116 \times 102 \times 90$	B2	-7.487
$172 \times 160 \times 144$	C1	-7.533
$232 \times 204 \times 180$	C2	-7.534

Table 5.4: Separation lengths for different 5mm diameter blunt-fin grids

The separation point on the current skin friction profile, which is measured along a two-dimensional plane taken along the line of symmetry, is determined by the location at which

a zero wall shear stress solution is obtained ($\tau_w = 0$), however it is important to note that this is not true for three-dimensional separation as explained in Chapter 2, Section 2.3.1. The skin friction profile shows that ($\tau_w = 0$) occurs at six distinct points, as a result the flow separates and reattaches at three points along the line of symmetry. The variation in the primary non-dimensionalized separation length for the different grids is shown in Table 5.4. The results indicate that the primary separation point moves upstream as the grid is made finer. This compares favourably with Navarro-Martinez's [47] experiences with ramp simulations. A pattern of upstream scaling in the numerical separation length with successive grid refinement was observed in the three-dimensional compression ramp simulations by Navarro-Martinez [47], and three-dimensional circular jet simulations by Dixon [12].

Schuricht [53] estimated using the limited available experimental results, that separation would occur around $\simeq -7D$, measured from the root of the blunt-fin. The experimental separation length appears to correlate well with the value obtained from the numerical results.

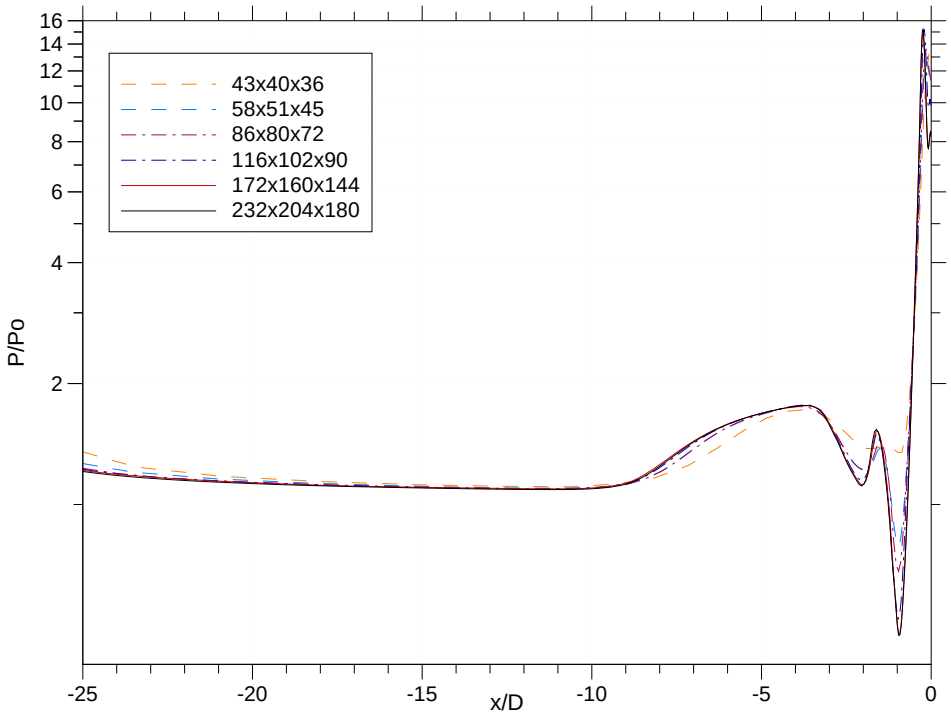

Figure 5.7: Detail of Pressure comparison for different grid densitites

The pressure distribution along the line of symmetry is shown in Figure 5.7 for the six grids. The profile shows a rapid rise in pressure just prior to separation, this rise in pressure is followed by a pressure plateau, which then exhibits a series of peaks and valleys attributed to regions of flow separation and reattachment, with the maximum peak occurring near the base of the fin. Similar to the previous observations for Stanton number and skin friction coefficient, the process of grid refinement produces a sharper profile with a relative decrease in the overall pressure ratio upstream of separation as the grid is refined, with the values at the peaks increasing in magnitude.

In conclusion, the grid refinement study indicates that the process of grid refinement yields a more accurate solution to the flowfield with each increment. Although the general structure of the flowfield appears to remain constant in the finest grids the separation length, Stanton number and skin friction coefficient still appear to be changing, albeit at a much slower rate. It has to be concluded that although the results are tending towards a grid independent solution the present set of grids studied will not yield a totally grid independent solution.

Further grid refinement is beyond the limits of the available computational resources. It is unlikely that further grid refinement will change the flowfield structure significantly.

5.4.2 General Flow Features of 5mm blunt-fin

The general structure of the computed fin interference flowfield, which includes the inviscid outer flowfield and the inviscid/viscous features associated with the fin interference interaction, can be obtained by examining the contour profiles for density, static pressure and temperature.

These indicate that the flowfield is dominated by the region of separated flow ahead of the fin. Bearing this in mind the contour profiles are taken from a two-dimensional plane located on the fin centerline or grid symmetry line upstream of the fin. A detailed analysis of the features present in this region can be made by examining the various density, temperature, and pressure contours.

The contour profiles shown in Figures 5.8- 5.10 are results obtained from grid type *C2* ($232 \times 204 \times 180$).

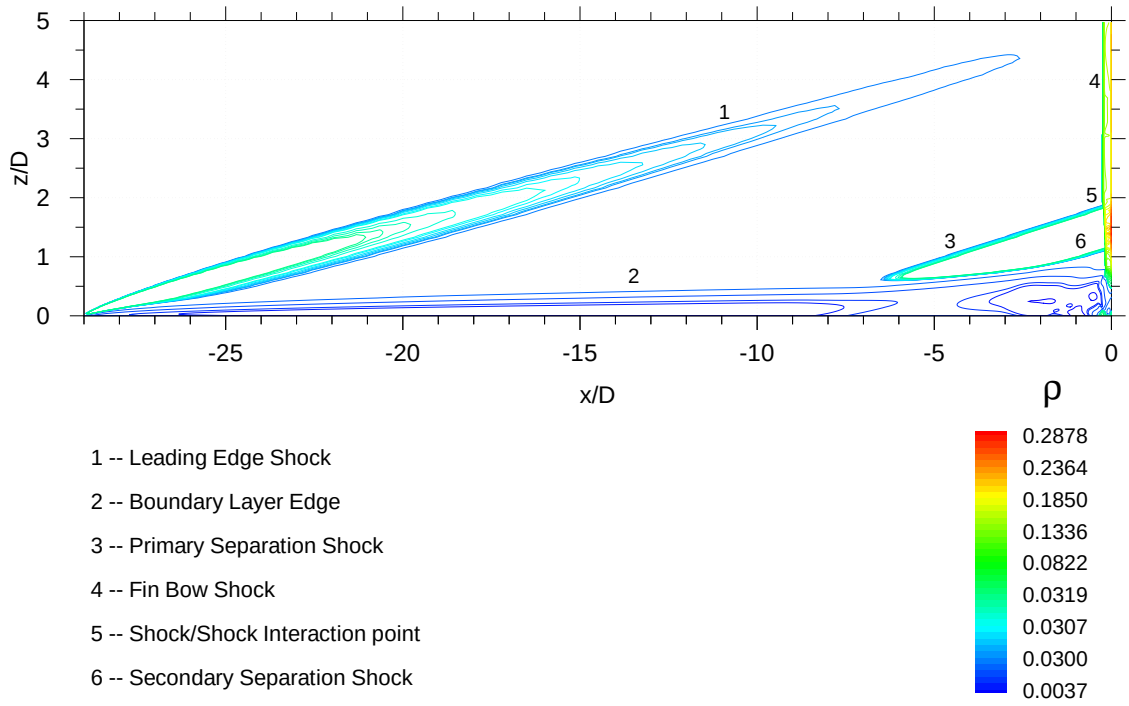

Figure 5.8: Density contours from the plane of symmetry, indicating the structure of the interference interaction

The density contours indicate a wave pattern generally consistent with the features observed in the schlieren photographs taken by Schuricht [53] for the same configuration, (see Figure 2.14). A complex shock pattern is clearly observed with a well defined leading edge shock, shock induced boundary layer separation shock, fin bow shock and a shock/shock interaction point as a result of the separation shock intersecting the fin bow shock. Steep gradients in density can be seen at the edge of the boundary layer where the density decreases due to a rise in temperature with an approximately constant pressure across the boundary layer. Steep density gradients are also present very close to the plate surface, which are the result of increases in density caused by the low surface temperature on the plate in comparison to the peak temperature within the boundary layer.

The flow in the separated region appears to indicate further complexities in its structure. Straddled between top of the separation bubble and primary separation shock is band of

high density changes. This appears to be caused by the formation of a second oblique shock, which is confirmed later by observing the boundary layer profile taken at this location. Interestingly this feature does not appear to be captured in the schlieren image in Figure 2.14. A region of flow just behind the shock/shock interaction point appears to indicate a zone where there is large variation in density values; this pattern of clustering in the density contours is also observed when an Edney type IV interaction with a localised supersonic jet [67] is seen to occur. A similar region with a large variation in the density gradients appears very close to the root of the fin/plate attachment location.

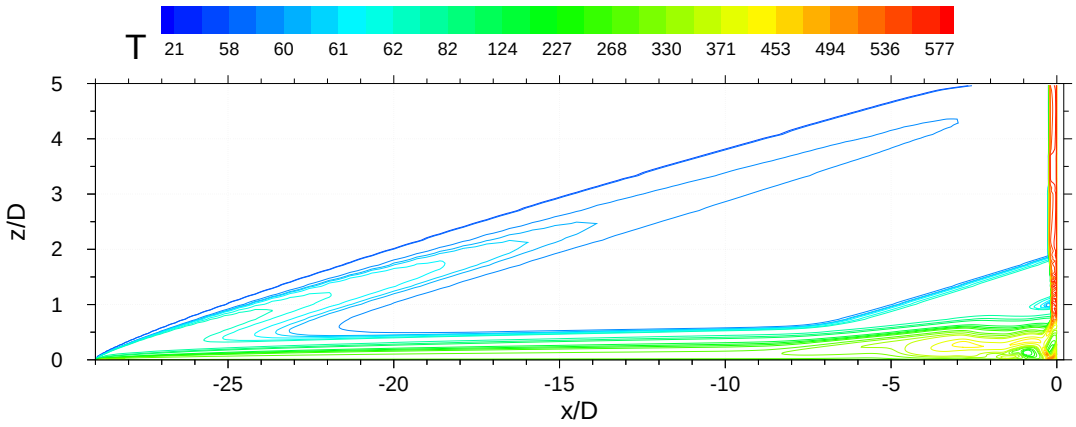

Figure 5.9: Temperature contours from the plane of symmetry

The temperature contours shown in Figure 5.9 clearly outline the extent of the thermal boundary layer and shear layers. The contours indicate that most of the changes in temperature occur close to the wall and in the separated region with comparatively smaller changes occurring across the shock wave. The largest changes in temperature appears to occur within the boundary layer where the kinetic energy is dissipated and very close to the surface where the temperature drops to the value at the plate surface. Also indicated in the temperature contours, embedded within the hot shear layer are two bubbles of relatively cooler gas, close to the leading edge of the blunt-fin. The presence of the second oblique shock is weakly outlined in the temperature contours. The temperature gradients in the shock layer (region between the bow shock and the blunt-fin) are relatively small except in the thin boundary layer where the temperature drops sharply to the blunt-fin surface temperature of $300K$.

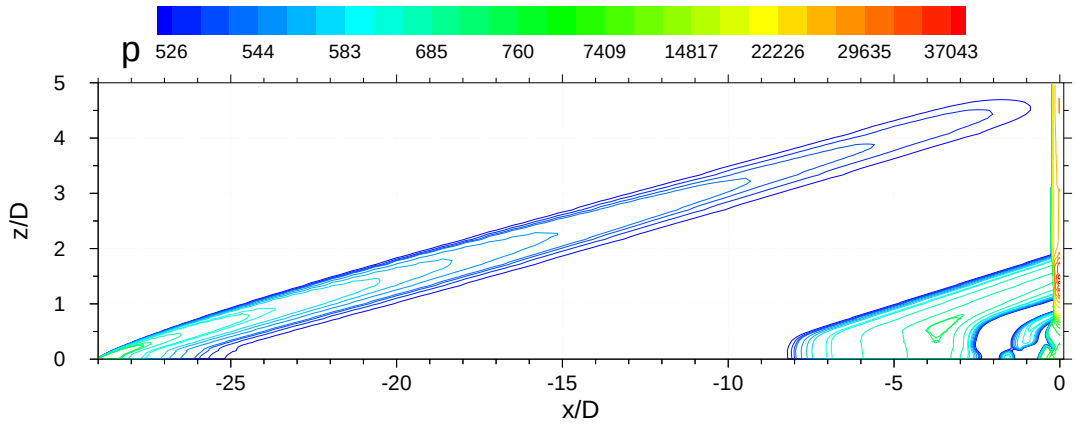

Figure 5.10: Pressure contours from the plane of symmetry

The contours for pressure in Figure 5.10 clearly show the three main shock structures, leading edge, separation and detached bow shock. Also indicated by the clustered contour lines is the suspected second oblique shock, just below the primary separation shock. The almost orthogonal contour lines near the wall show the constant pressure in the boundary layer. The pressure profile also indicates a region of high pressure behind the shock interaction point, this is consistent with observations made earlier which cited the presence of a supersonic jet as a result of Edney type IV interaction.

The image sets in Figure 5.11 show a selection of Mach number contours in the separated region for the (x/D) range indicated. For the purpose of identifying the relevant features the Mach contours plotted in Figure 5.11 have filtered out the higher Mach numbers and only show Mach numbers within a defined range. In Figure 5.11:(**A**), Mach numbers ($M > 1$) are filtered out and appear as blue regions in the image. From Figure 5.11:(**B**), Mach numbers ($M > 2$) are filtered out and again appear as blue regions in the image.

What is revealed as a result of filtering regions greater than Mach 1 is the appearance of two supersonic bubbles embedded within the predominantly subsonic shear layer. These feature also appear in the temperature contour profile in Figure 5.9 which highlighted the existence of two bubbles of low temperature surrounded by higher temperature gas, one within the shear layer, and a second just behind the bow shock.

Hung & Buning [33] tried to elucidate a possible mechanism for the presence of similar

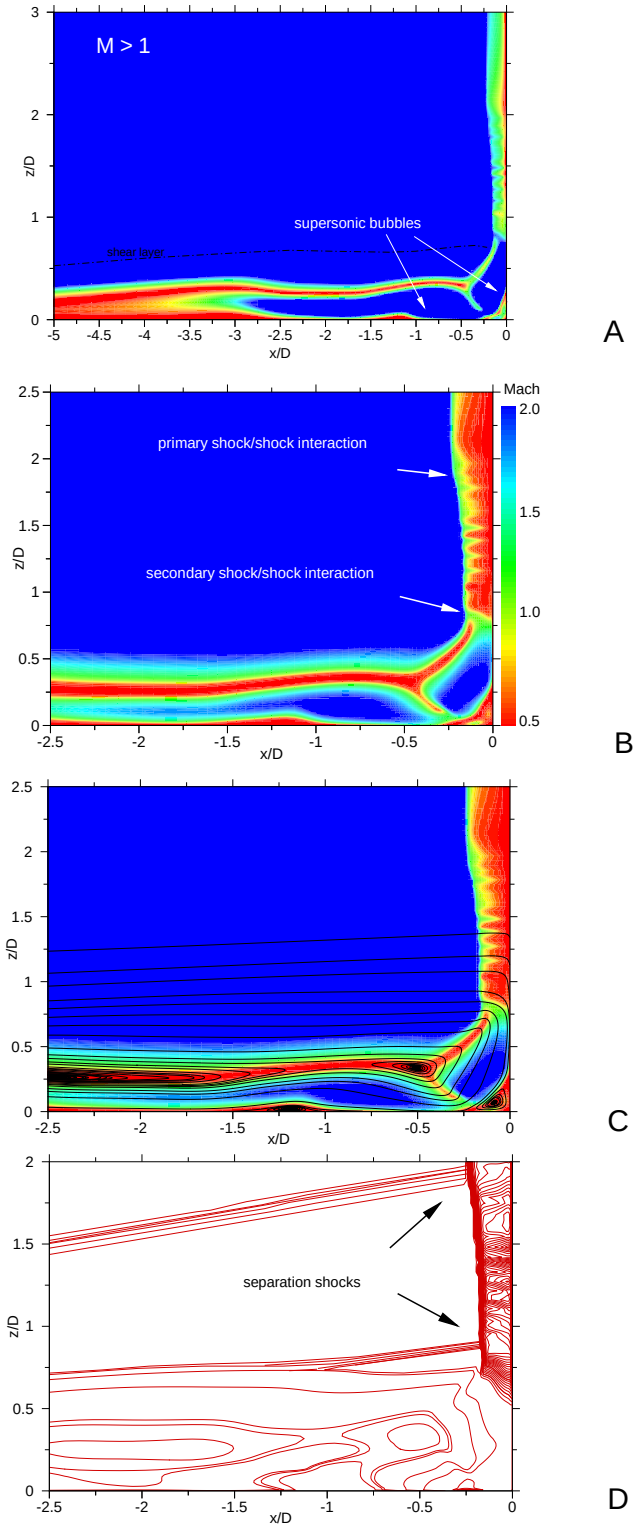

Figure 5.11: (**A**) Mach contours in symmetry plane highlighting supersonic zones (**B**) Mach contours highlighting supersonic jets caused by a Type *IV* interaction (**C**) Velocity streamlines superimposed on Mach contours in symmetry plane (**D**) Density contours highlighting separation shocks

embedded supersonic zones in turbulent separated flow they discovered in their numerical simulations. They concluded that the horseshoe vortex brings an abundance of fresh high-momentum fluid into the separation region. As this high-momentum fluid accelerates, it results in two reversed-flow supersonic zones; one on the fin, and another on the plate. Since then several other theories have been put forward for the existence of these supersonic bubbles, one school of thought suggested by Yamamoto [68] appears to correlate well with the evidence present in the current simulation.

Yamamoto suggested that between the primary separation shock and the surface of the shear layer a second oblique shock is formed. This is indicated in Figure 5.11:(**right**) and it originates from the separated region. This oblique shock intersects the bow shock, and as a result a second *Edney* Type IV shock/shock interaction occurs. This point is marked in Figure 5.11:(**B**) by the second arrow near the plate; the first arrow indicates the first *Edney* Type IV shock-shock interaction. As a result of the second *Edney* Type IV interaction, a jet of very high speed fluid bounded by a shear layer is produced; as described in Chapter 2, Section 2.4.1. This feature can be seen in the Mach contour plot in Figure 5.11:(**B**), where a jet of high speed fluid appears to form at the shock interaction point. This jet of fluid is accelerated further by the presence of the vortices as indicated by looking at the subsequent particle velocity vectors in Figure 5.11:(**C**). This leads to pockets of supersonic flow below the subsonic shear layer in the separated region. There is strong evidence to support the second separation shock theory by looking at the density contours in one of the images in Figure 5.11:(**D**), where there appears to be a second oblique shock produced in the separated region, and there is a pronounced deflection in the bow shock at the point of interaction, indicative of a shock/shock interaction.

The existence of two reversed-flow supersonic zones was also observed by Voitenko et al. [63] in their experiments, when they studied a ($M = 3.11$) turbulent flow over a cylinder. It was argued that a similar shock/shock interaction leading to a supersonic jet was the cause of the supersonic zones observed; however, both Voitenko's experiments and Yamamoto's simulations were undertaken with turbulent boundary layers. The results from the present simulations seems to indicate a similar phenomenon occurs with laminar boundary layers.

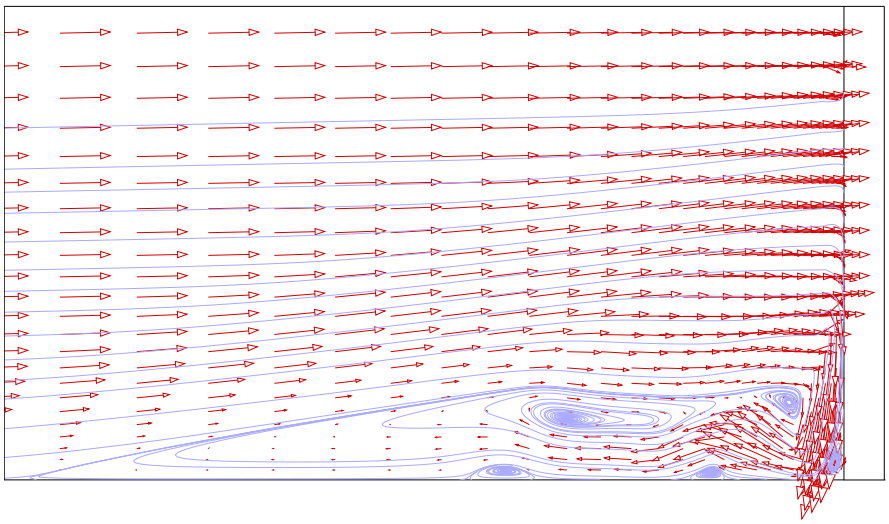

Figure 5.12: Velocity vectors in region of separated flow in the axis of symmetry

In Chapter2, Section 2.5.2 we introduced several physical parameters that could be measured from the blunt-fin flowfield which can be used for comparing experimental observations with similar numerical predictions. The contour profiles in Figure 5.8 - 5.10 give us an opportunity to quantify the numerical results by being able to compare these parameters to the experimental observations. The first comparison that can be made is for the leading edge shock angle. The leading edge shock angle measured from the schlieren photo in Figure 2.14 is $\sim$ 11 degrees. The numerical shock angle can be measured from the density contours in Figure 5.8, and the resultant numerical shock angle appears to be in the range of 10 to 13 degrees. The coarseness of the grid near the upper boundary, and numerical diffusion causes the shock solution to be spread over a wide area which makes it difficult to obtain more accurate measurement of the numerical shock angle. However, the comparison indicates that the numerical shock angle appears to be within the same range as the experimental result. A further form of comparison can be made for the calculated pressure ratio across the oblique shock. Using the expression for (p_2/p_1) from oblique shock theory [3],

$$\frac{p_2}{p_1} = \frac{2\gamma}{\gamma+1}\Big(M_1^2 sin^2\beta_1 - 1\Big) + 1 \tag{5.4}$$

Using the experimental value for ($\beta_1 = 10.5°$) and ($M_1 = 6.7$), using Eqn 5.4 gives an experimental ($p_2/p_1 = 1.508$). The equivalent numerical pressure ratio calculated from the pressure profile in Figure 5.10 is ($p_2/p_1 = 1.52$). Once again the comparison appears to be very good.

From the schlieren images Schuricht [53] estimated certain geometrical non-dimensional constants for the flow; these parameters were also calculated from the numerical data, and the comparisons are shown in Table 5.5. From analysing the velocity profile on the flat plate and the density contours in Figure 4.3, the height of the flat plate boundary layer at 145mm, which represents the location of the blunt-fin root is ($\delta = 3.48mm$), ($z/D = 0.696$).

$Type$	D/δ	K/δ	K/D	K/K_{tp}
5mm - Schuricht	1.5	7.6	5	3.4
5mm - Numerical	1.44	7.18	5	3.24

Table 5.5: Fin dimension relationships

Under the classification of Hung and Clauss [36], the current blunt-fin would be classed as a "short" protuberance (see Chapter 2, Section 2.5.2) because ($D/\delta < 6$). As a result the heating distribution will be primarily dictated by the ratio (K/δ).

The most important parameter to note in Table 5.5 is the ratio (K/K_{tp}), which is defined as the ratio of fin height (K) to the height of the triple point (K_{tp}). This result is important because it controls and gives an indication of the level of interaction in the separated region. Large discrepancies in (K_{tp}) will alter the size and scale of the separated region thus affecting the vortical structures within the separated region. This, in turn will, affect the heating solution on the flat plate.

The numerical value obtained from the density profile in Figure 5.8 is ($K_{tp} = 7.35mm$). The value Schuricht [53] measured for (K_{tp}) was $\simeq 7.7mm$. Taking into consideration that the experimental value for (K_{tp}) was measured from a Schlieren photo, accounting for a measurement error of around ($\pm 5\%$), the numerical prediction appears to be well within the error range therefore showing good agreement with the experimental prediction.

Boundary Layer Profiles

To get more detail about the variation in density, temperature and velocity within the separated region, profiles of these following variables across the boundary layer normal to the flat plate are taken at the following points along the plate centerline, (x/D = -7), (x/D = -3) and (x/D = -1). To clearly differentiate any differences observed within the separated layer the profiles in Figures 5.13- 5.15 only extend to (z/D = +3), above the plate surface.

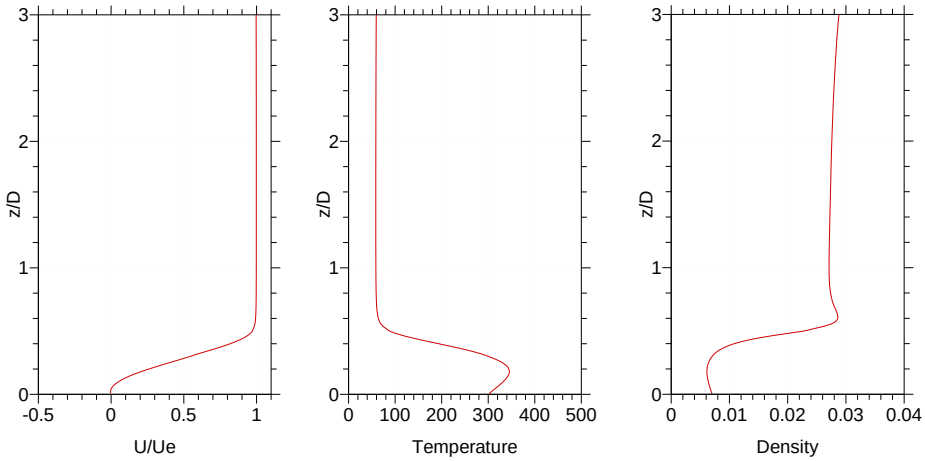

Figure 5.13: (**left**) Velocity profile at x/D = -7 (**middle**) Temperature profile at x/D = -7 (**right**) Density profile at x/D = -7

Analysing the velocity profiles within the boundary layer in Figures 5.13- 5.15, indicate that the boundary layer has just separated at ($x_S/D \simeq$-7) - (see Table 5.4) - as indicated by the regions of reverse flow in the near-wall region.

The velocity profile at (x/D = -3), Figure 5.14, indicates a very small region of positive flow velocity very near the plate surface within the reverse flow region. However the flow direction changes back to reverse flow further away from the plate ($z/D > 0.05$). This is clearly indicative of the presence of a small secondary recirculation region, and this is shown to be case by inspecting the particles paths in Figures 5.5, where a separation bubble vortex is present at (x/D = -3).

The observed peak in the temperature profiles in Figures 5.13- 5.14 at ($z/D \sim 0.2 - 0.4$)

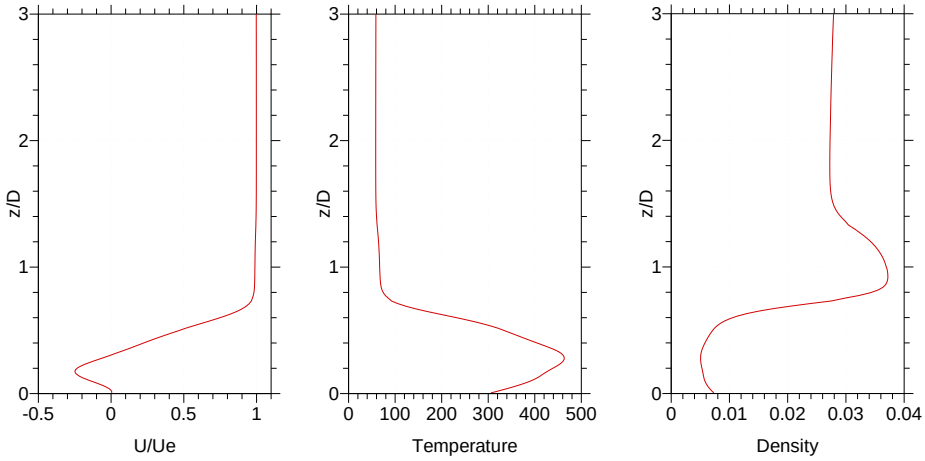

Figure 5.14: (**left**) Velocity profile at x/D = -3 (**middle**) Temperature profile at x/D = -3 (**right**) Density profile at x/D = -3

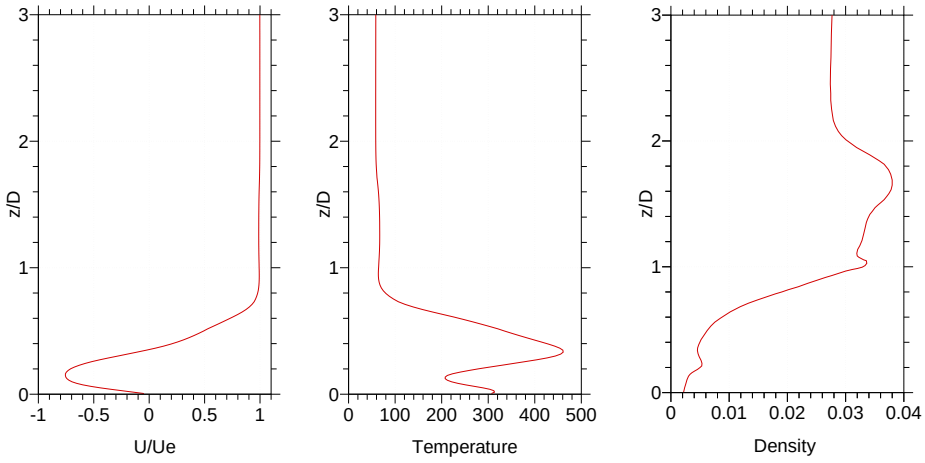

Figure 5.15: (**left**) Velocity profile at x/D = -1 (**middle**) Temperature profile at x/D = -1 (**right**) Density profile at x/D = -1

is caused by the dissipation of kinetic energy into thermal energy within the shear layer and this peak is close to the stagnation temperature of the flow which is $600K$. Since the pressure is approximately constant across the boundary layer, the rise in temperature from the edge of the boundary layer towards the surface gives a corresponding decrease in density as seen in the density profiles in Figures 5.13- 5.14. The peak is followed by a decrease in temperature closer towards the plate surface which is comparatively cooler, being kept at $300K$. A corresponding increase in density can be seen as the temperature

decreases from the peak value to the cooler surface value. The temperature increase due to the dissipation of kinetic energy and the corresponding decrease because of the cooler plate surface temperature can be seen in the equivalent temperature contours in Figure 5.9. However, the rapid changes in density at the minimum mask the variation across the boundary layer in the density contours shown in Figure 5.8.

The pocket of low temperature as seen in Figure 5.15 at (x/D = -1) near the plate surface at ($z/D \sim 0.1$), when compared to the surface plate temperature of $300K$, is due to the embedded supersonic zone seen and described in Figure 5.11. The region of flow below ($z/D \sim 0.05$) is hotter because it appears to be within a small separation bubble as indicated in the particle streamlines in Figure 5.5.

The density variation at (x/D = -1) in Figure 5.15 clearly shows the presence of the second oblique shock, indicated by the double peak in the density profile in the region ($z/D \simeq 1$). Correlating this with the density contours in Figure 5.8 clearly shows the region where the second separation shock occurs.

Station, x/D	N_{BL}	N_{TBL}
-28.5	35	42
-26	39	45
-7	42	47

Table 5.6: Number of points in velocity and thermal boundary at several x/D locations

The edges of the velocity and temperature boundary layers is usually taken to be the point where the flow achieves 0.99 of the respective free stream value. Table 5.6 shows the number of grid points in the velocity boundary layer (N_{BL}) and the thermal boundary layer (N_{TBL}) at several station (x/D) locations along the line of symmetry.

Upon careful analysis of the temperature and velocity profiles it is clear that the thermal boundary layer is slightly thicker than the velocity boundary layer at the same location. This is expected since ($Pr < 1$), the Prandtl number can be considered to be a measure of the ratio of the velocity boundary layer thickness to the thermal boundary layer thickness

[2]. Additionally for good simulation of laminar boundary layers it is recommended that there are (≥ 25) points in the boundary layer [48], and from Table 5.6 it is clear that this criterion is satisfied.

Vorticity Contours

In Chapter2, Section 2.5.2 it was indicated that the separated flow in front of the fin was a region that contained a high level of vorticity. As a result the streamwise vorticity distribution can be used to investigate the presence of vortices and other structures within this region of flow. In addition to the vorticity present in the separated flow the presence of highly curved shocks produce a considerable amount of vorticity as a result of large entropy gradients [3], according to *Crocco's theorem*. The present interference flowfield has several curved shocks like the fin bow shock and the reflected shock from the separation shock/bow shock interaction.

The transport equation for vorticity in compressible flow is given as:

$$\frac{\partial \omega}{\partial t} + (v.\nabla)\omega = (\omega.\nabla)v - \omega(\nabla.v) - \nabla\times\frac{\overrightarrow{\nabla}p}{\rho} - \overrightarrow{VD} \tag{5.5}$$

where the vorticity vector is defined by ($\omega = \nabla\times v$), the velocity vector $\left(v = (u, v, w) \right)$ and $\left(\overrightarrow{VD}\right)$ represents terms associated with viscous dissipation forces with $\left(\nabla\times\frac{\overrightarrow{\nabla}p}{\rho}\right)$ representing baroclinic terms. Usually the vortex stretching term $\left((\omega.\nabla)v \right)$ is the most dominant factor in vorticity generation.

To observe any vortices in the separated flow region, the vorticity field is projected along the separation region into a plane defined by its normal ($\mathbf{n}$) as

$$\omega_n = \omega.\mathbf{n} \tag{5.6}$$

The distribution of (ω_y) in a plane perpendicular to the flat plate along the line of symmetry as shown in Figure 5.16 outlines the iso-vorticity contours. For clarity, the iso-contour legend in Figure 5.16 will only indicate the maxima and minima of vorticity, and the plot

area will be restricted to show the region (x/D = -4 to 0) and (y/D = 3 to 0) [1].

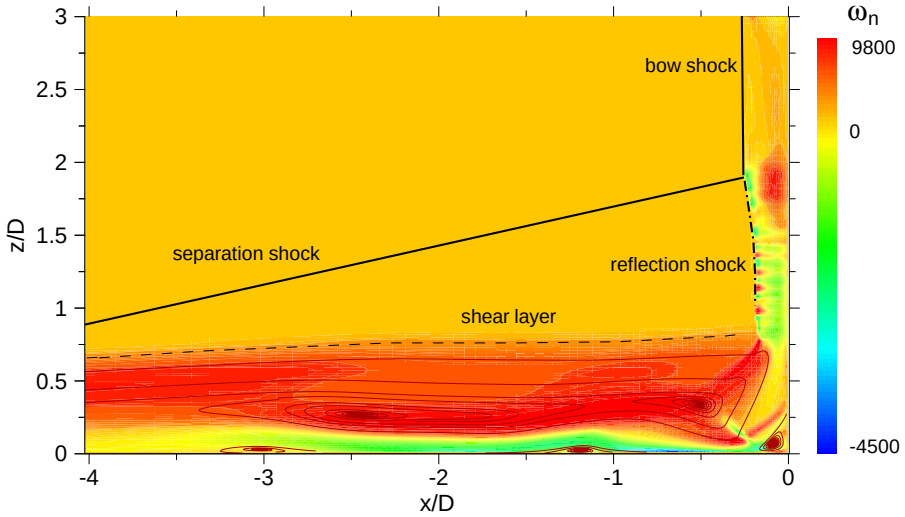

Figure 5.16: Detail of Iso-vorticity contours of (ω_n) in symmetry plane with the separated region highlighted

Figure 5.16 indicates that a majority of the flow in the separated region is of positive vorticty, much higher than the corresponding vorticity of the outer flowfield, with the maxima occuring in regions where there are horseshoe vortices which are rotating in a positive direction in line with the freestream flow. The peak vorticity appears to occur in a region of flow just behind the fin bow shock at the location where the fin bow shock and boundary layer separation shock intersect. A region on the plate surface near the base of the blunt-fin ($-1 \leq x/D \leq -0.4$) exhibits an area of negative vorticity, and features associated with this negative vorticity are counter-rotating horseshoe vortices on the plate surface.

The detached curved bow shock of the fin shows a region of varying positive and negative vorticity. In particular, the maximum in positive vorticity occurs near the point where the separation shock intersects the fin bow shock, as illustrated in Figure 5.16. This region is characterized by a vortex as seen in Figure 5.17. The concentrated vorticity just above the point of interaction as shown in Figure 5.16 results in the formation of vortex as shown in

[1]- In the current projection the plane is pointing in the negative y-direction which puts the rotation in Figure 5.16 in the opposite sense to the usual sigh convention ie. positive is clockwise as you look into the plane and negative anticlocwise.

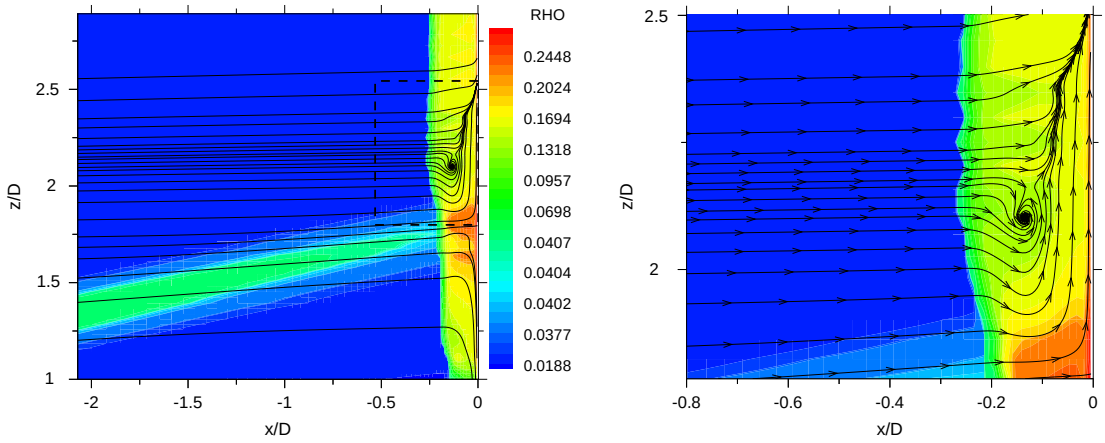

Figure 5.17: (**left**) Vortex structure formed from Type IV interaction (**right**) Enlargement of vortex structure

Figure 5.17. For clarity and to observe the location of the vortex, density contours have been superimposed so that the location of the vortex can be seen in relation to the point of shock/shock interaction. The presence of such a vortex system was shown to exist in Chapter 2, Section 2.1.1.

The initial analysis of the separated region from the observations made from examining the iso-contour profiles for density, pressure and temperature in addition to looking at the boundary layer profiles and iso-vorticity contours in the symmetry plane indicate that the flow in the separated region is more complicated than initially revealed from reviewing past experimental and numerical work on laminar fin/plate interactions. The existence of a second oblique shock within the primary separated flow and the presence of vortices behind the bow shock has not been reported in previous laminar experimental and numerical studies.

Flow and Shear Stress Topology

The previous section has shown that as a result of the complex shock/boundary layer and shock/shock interactions the flow within the separated region reorganizes itself into vortical structures which dominate the separated region. These are fully three-dimensional

structures that develop downstream and spread out in the spanwise direction to produce a horseshoe vortex system which wraps around the blunt-fin. Along the paths of these vortices the most outstanding consequence is an important increase in heat flux, skin friction coefficient and pressure at the plate surface in correspondence with the reattachment of the separated flow (see Chapter 2, Section 2.5.2). It is well established that flow reattachment points and regions of high shear result in local increases in heat transfer due to the local thinning of the boundary layer [18]. The latter creates steeper velocity and temperature gradients at the plate surface, resulting in increased skin friction and enhanced heat transfer. Although Schuricht's experimental work has provided a great deal of information about various aspects of laminar blunt-fin interactions, questions still remain regarding the precise flow topology and the horseshoe vortex phenomena. For instance, discrepancies in the horseshoe vortex system topology upstream of the blunt-fin/plate junction are apparent when comparing the inferred streamline patterns of Schuricht [53] and Hung [36]. Both studies were conducted using very similar unit Reynolds number, which is an important dimensional parameter that controls the number of vortices in the separated shear layer, (see chapter 2, section 2.5.2) for more detail.

It has been reported that insufficient spatial resolution and numerical or experimental errors may easily lead to misinterpretation of the vortex patterns or even to the impossibility of a unique identification of the topological structures [5]. Ballio [5] reported that the use of experimental oil-flow visualization as a tool to map flow structures from interpreting the surface shear stress lines is subject to considerable debate. As a result, obtaining an accurate description of the flow in the three-dimensional separated region via numerical simulation and deducing the resulting impact on surface flow topology is very important in understanding the true extent of thermal heating on the surface of the plate.

In order to compare the numerical flowfield with the corresponding experimental solution, one has to visualize the near-wall flowfield. The direction of a flow velocity is visualized using particle streamlines. In simulations with viscous continuous flows the velocity of the flow at a solid wall is zero by definition, as a result this prevents the calculation of steamlines directly on the walls. The aim would be to find the limiting streamline at locations where the velocity goes to zero while the direction of the velocity vector is determined by the direction of the velocity near the wall. Consequently skin friction lines

on the plate surface are used instead of near-wall particle traces. The skin friction lines as described in Chapter 2, Section 2.3.1 use the wall shear stress vector for visualization purposes. The wall shear stress vector ($\overrightarrow{\tau_w}$) is the derivative normal to the wall of the velocity vector ($\overrightarrow{v}$). In general it is nonzero and points in the direction of the near-wall velocity vectors when projected normal to the wall. The skin friction lines provide global information about the near-wall flowfield and show the location of separation and reattachment of the flow at the wall.

To build a three dimensional picture of the flowfield structure planar sections normal to the plate surface are taken at the illustrated locations as shown in Figure 5.18. The table in Figure 5.18 shows the locations of the different profiles on the plate surface, where (ϕ) is measured on the plate surface in a clockwise direction.

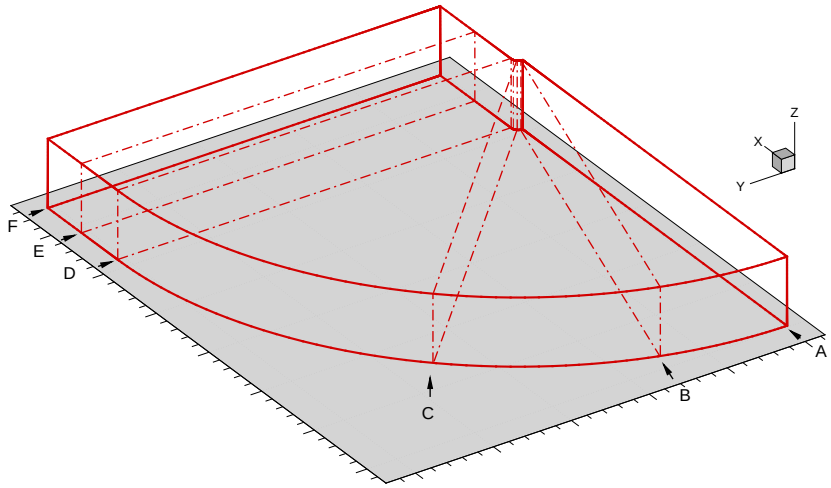

PROFILE	x/D	ϕ
A	0 → -29	0
B	0 → -27	20°
C	0 → -15	45°
D	+1	90°
E	+4	90°
F	+8	90°

Figure 5.18: Schematic of section profiles and their locations

The particle streamline pattern in the symmetry plane and skin friction lines on the flat plate surface are significant two-dimensional "footprints" of the complex three-dimensional flow around the blunt-fin. The skin friction line pattern over the plate surface for the 5mm

blunt-fin is shown in Figure 5.19, for clarity the plot area is restricted to (x/D = -15 to +8) and ($y/D = \pm$ 7).

Because of their definition, the no-slip singularities of the velocity flowfield are also singular points for the wall shear stress or skin friction field, but of course the nature of the singularities is not the same for the two fields; nodes, saddles and foci will be identified with capital letters (N,S,F) for the velocity field in the symmetry plane and with small letters (n,s,f) for the shear stress field on the solid surface with (**R**) denoting a reattachment line and (**S**) a separation line.

A saddle of separation exists on the centreline well upstream of the blunt-fin. The saddle, (s_A), is highlighted as the point furthest outward from the root of the blunt-fin in Figure 5.19. Through (s_A) goes the separation line ($\mathbf{S_A}$) towards which the skin friction lines converge. The separation line is strongly deflected when it encounters the freestream as shown in Figure 5.19 along with the resultant horseshoe vortex as shown in Figure 2.8 in Chapter 2, Section 2.3.2. There is a node of reattachment right at the base of the blunt-fin (n_1). Through (n_1) goes the attachment line ($\mathbf{R_1}$) from which the skin friction lines diverge. In addition there are two other distinct pairs of separation saddles and reattachment nodes (s_2), (s_3) and (n_2), (n_3), originating from the centreline. Also present is a nodal point of separation and reattachment (s_2'), (n_2') that originate close to the reattachment line ($\mathbf{R_1}$). In addition there is another nodal point of separation (s_4) near the side surface of the fin. The number of saddles and nodes follows the topology suggested by Tobak [58] for a flat plate with an attached normal plate, and agree with eqn 2.22 - 3 saddles and 3 nodes.

The particle streamlines in the symmetry plane of the computed flowfield (Profile **A** in Figure 5.18), show that the streamwise vorticity of the incoming separated boundary layer is organised into several vortices. Two primary vortices with (foci F_1 and F_2) concentrate positive vorticity (see Figure 5.20) into 3 cores. Secondary vortices with (foci F_1a, F_2a and F_3a) separate from the plate surface and concentrate the vorticity of opposite sign which is generated on the plate surface by the reverse flow.

The streamline profile in Figure 5.20 exhibit features which are consistent with a three-dimensional separated flow as shown in Figure 2.6 in Chapter 2, Section 2.1.1. The flow

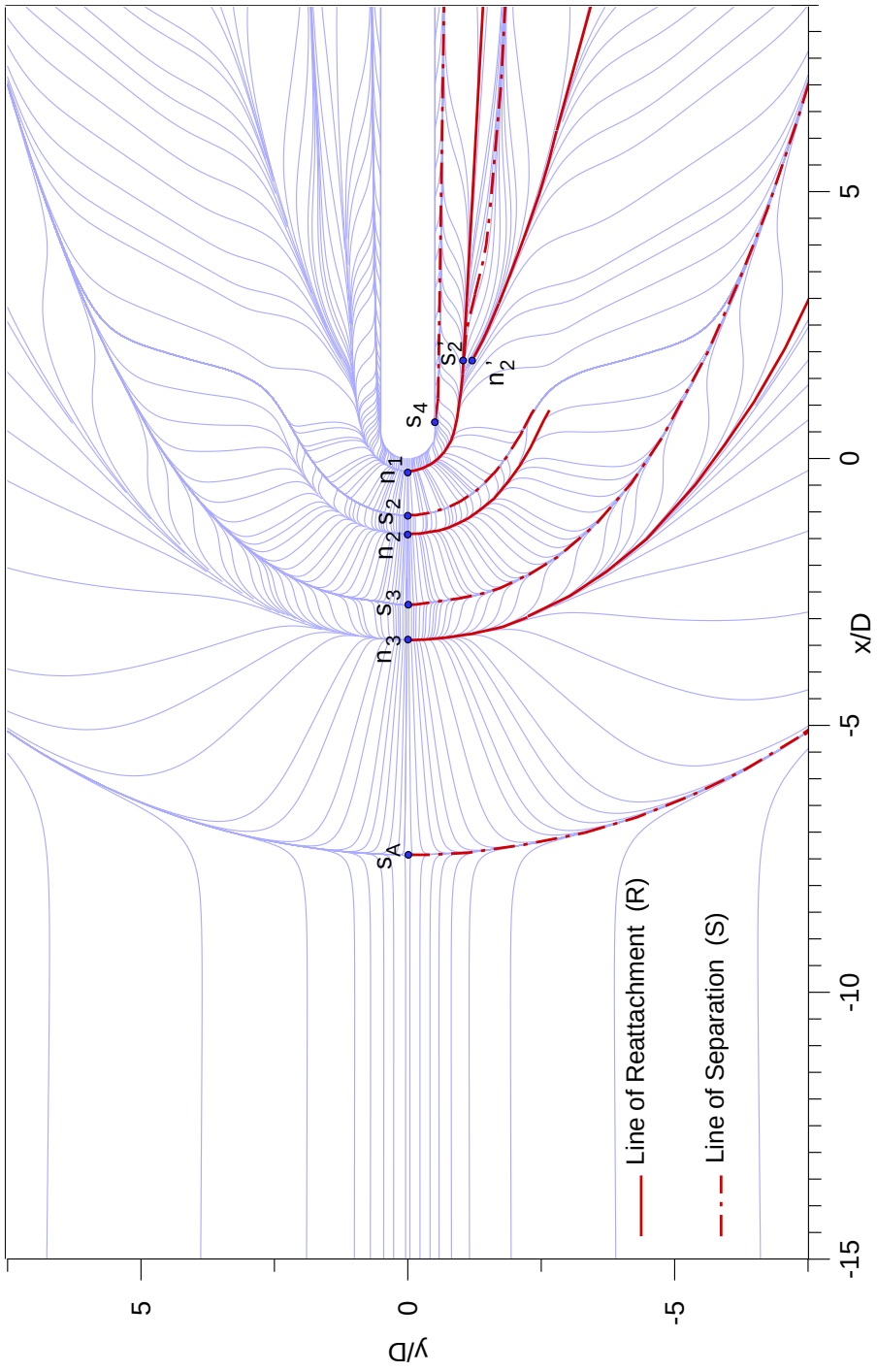

Figure 5.19: Surface skin friction streamlines on flat plate, with lines of separation and reattachment highlighted. A separation saddle is denoted by *(s)* and a reattachment node by *(n)*

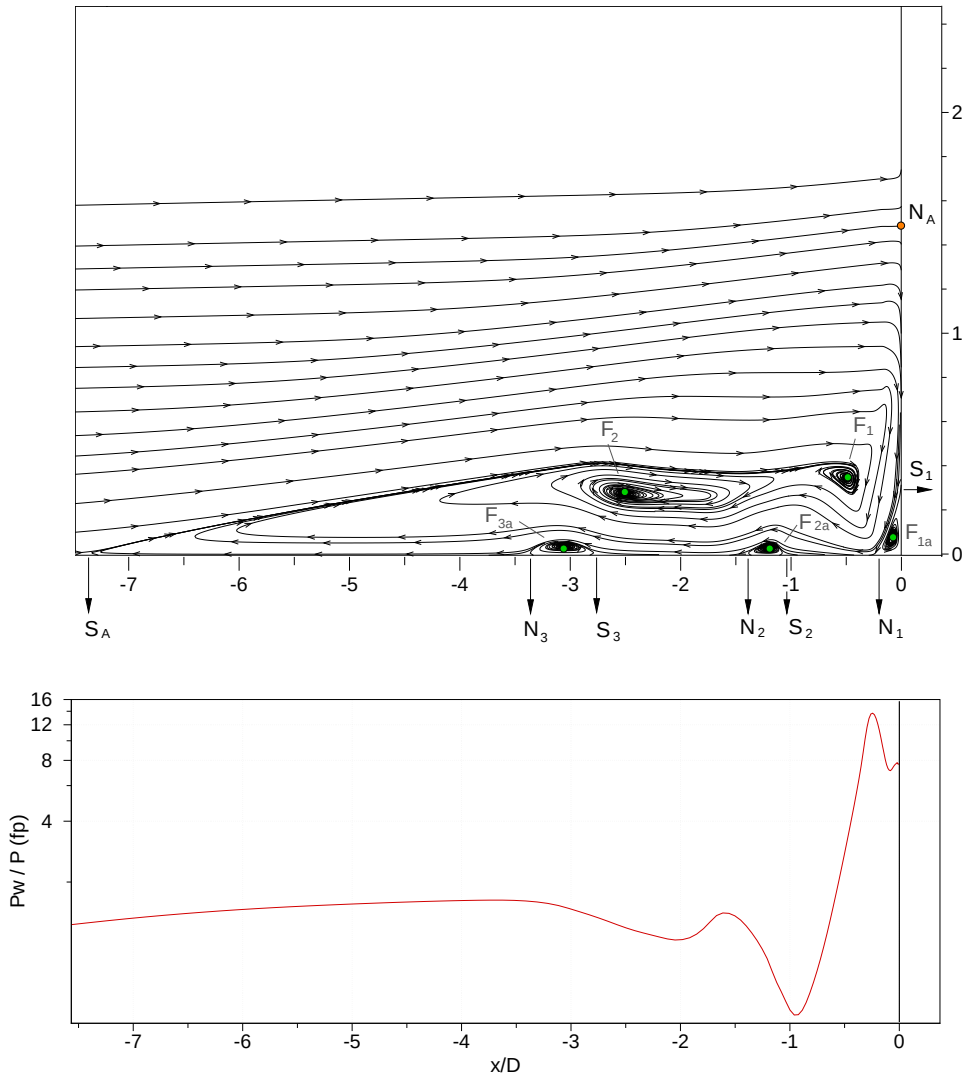

Figure 5.20: (**top**) Particle streamlines in profile plane at location A (**bottom**) Plate surface pressure

topology can be explained using the pressure distribution along the line of symmetry, as shown in Figure 5.20. Upstream flow separation (S_A) is caused by the strong adverse pressure gradient generated by impingement of the strong fin bow shock on the flat plate boundary layer, resulting in the formation of a single vortex along the centreline. Reattachment (N_A) of the primary separated flow (S_A) occurs at around ($z/D = +1.5$) on the blunt-fin, measured from the base. The formation of the root vortex with foci (F_1a) is the result of separation at (S_1) with a strong reattachment occurring near the foot of

the fin. This reattachment (N_1) is responsible for the final peak heating observed on the centreline at the foot of the fin. This phenomenon shall be discussed in more detail later in this chapter. The reverse flow at the plate surface within this large separated region initially encounters a favorable pressure gradient but, upon encountering the upstream flow is forced to undergo a second separation, (S_2). As a result of this secondary separation, it induces the primary vortex to bifurcate to form two separate cores, (F_1) and (F_2) as seen in Figure 5.20. From the resultant bifurcation process the separated flow near the surface encounters a favorable pressure gradient and as a consequence reattaches at node (N_2), this is clearly shown in the pressure profile in Figure 5.20. Upon reattachment, as discussed above, the flow undergoes tertiary separation at (S_3) similar to the process that caused secondary separation. The flow reattaches itself further upstream at node (N_3). These secondary and tertiary separations and reattachments leads to the formation of two additional secondary vortices with foci (F_2a) and (F_3a). The pressure distribution profile in Figure 5.20 indicates that the location of the vortices appear to correspond to minima in the pressure profile as discussed in Chapter 2, Section 2.5.2.

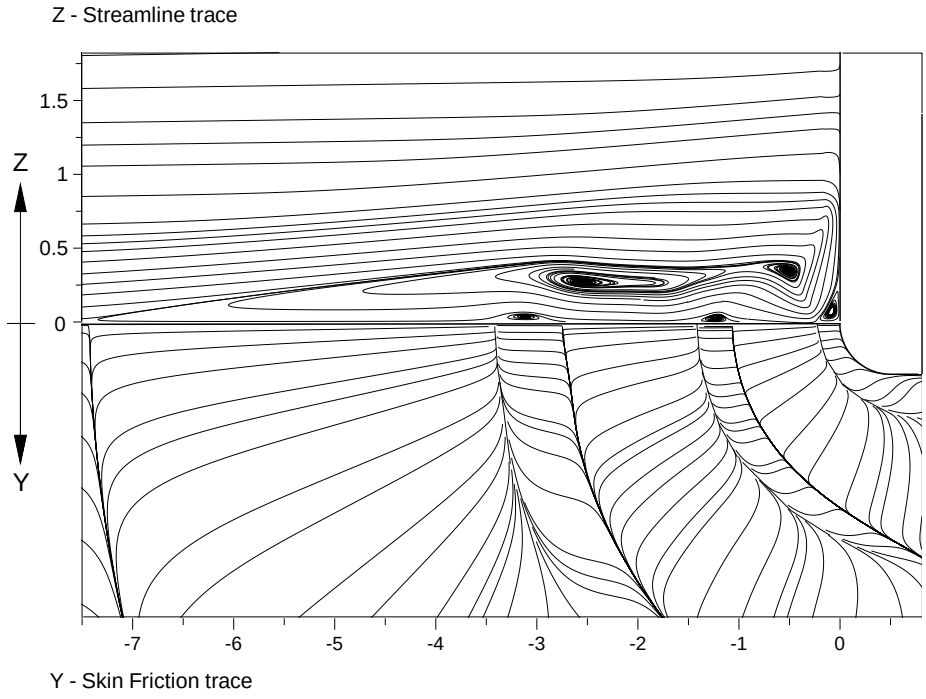

Figure 5.21: Superimposed streamlines and shear stress lines

Superimposing the symmetry plane streamline profile in Figure 5.20 with the surface skin friction profile in Figure 5.19 clearly shows that the locations of the vortices agree with their respective separation and reattachment points as seen in Figure 5.21.

Comparing the flow features found in the planar section profiles taken at ($\phi = 0°$) with ($\phi = 20°$) in Figure 5.22, appears to show that the structure of the inviscid flowfield is maintained in the region that is bounded by the two profiles.

The two main vortices which are embedded in the separated region appear to spiral around the fin as would be expected, and the same applies to the two smaller vortices localised on the plate surface and the root vortex at the base of the fin. The shock structure also appears to duplicate itself, with little change to the leading edge, separation, bow shocks and the shock interaction point. It is interesting to note how small in size the vortical structure is in relation to the height of the blunt-fin

Analysing the profiles taken at locations ($\phi = 45°$) to ($\phi = 90°, x/D = 8$) show several differences in the shock and particle streamline structure when compared to those observed in profiles taken at locations ($\phi = 0°$) and ($\phi = 20°$).

The flow structure observed from analysing the Mach and density contours in Figure 5.23 appear to share a lot in common with features observed for a sharp-fin flow configuration as described by D*é*lery [13]. These features are best explained by studying a schematic representation of this type of interaction as shown in Figure 2.12 from Chapter 2, Section 2.5.2. The main dominant features of the flowfield consist of a near normal shock that intersects an oblique separation shock, and the resulting reflected shock all meet at a defined triple point. The shock/shock interaction leads to the formation of a slip line which forms at the triple point, and bounds several reflected shocklets ending in a near normal shock. The separated region contained within the separation shock contains a conical vortex, with one or two more separation saddles.

The features described above can be readily identified in the density and Mach contours in Figure 5.23. The interaction between the separation shock and the bow shock is present throughout the profiles, however the resulting triple point is poorly resolved at each of the locations where profiles **D**,**E** and **F** are taken, this is partially due to the grid becoming

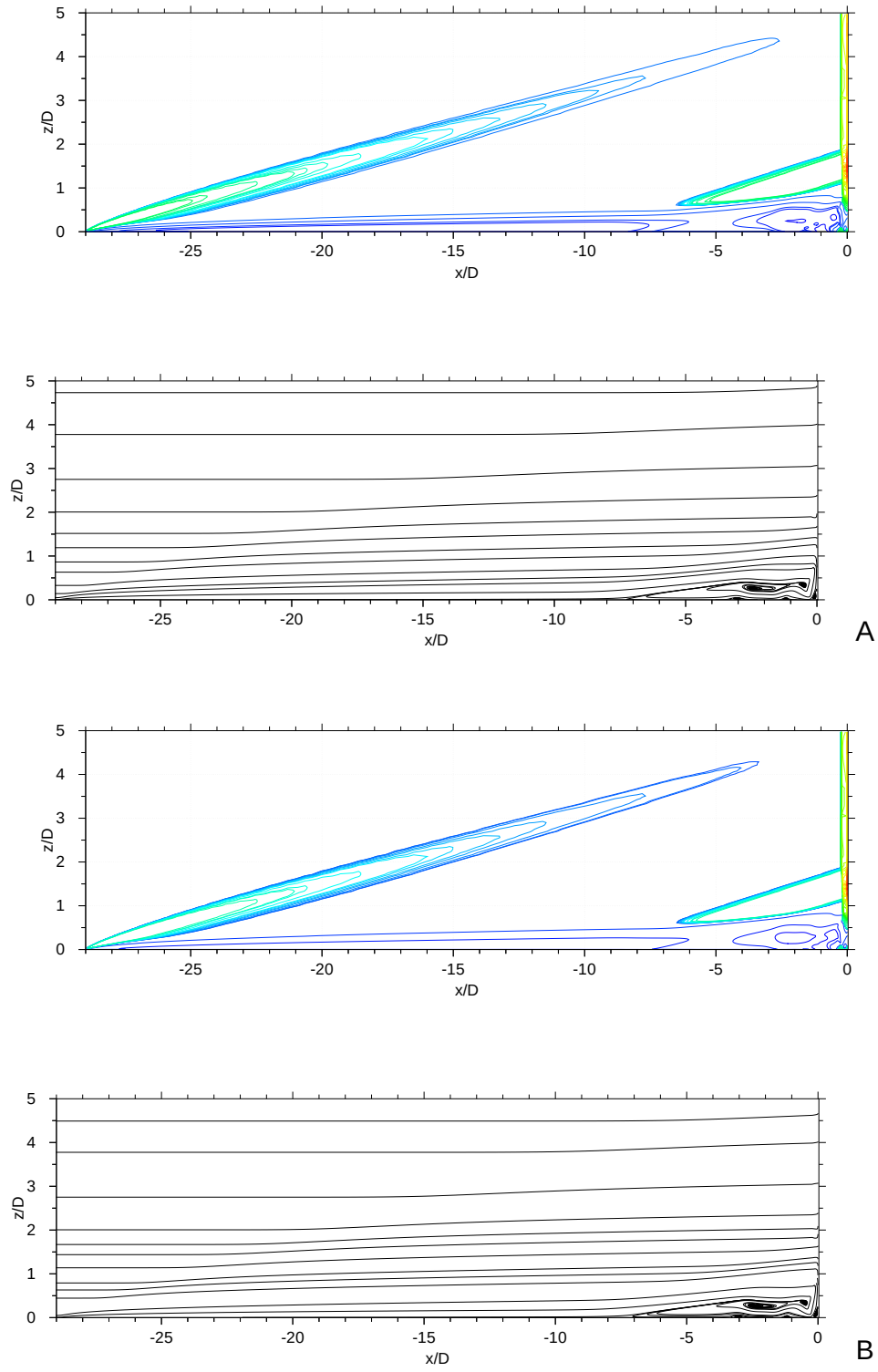

Figure 5.22: (**A**) Density contours and Velocity streamlines in profile at point A (**B**) Density contours and Velocity streamlines in profile at point B

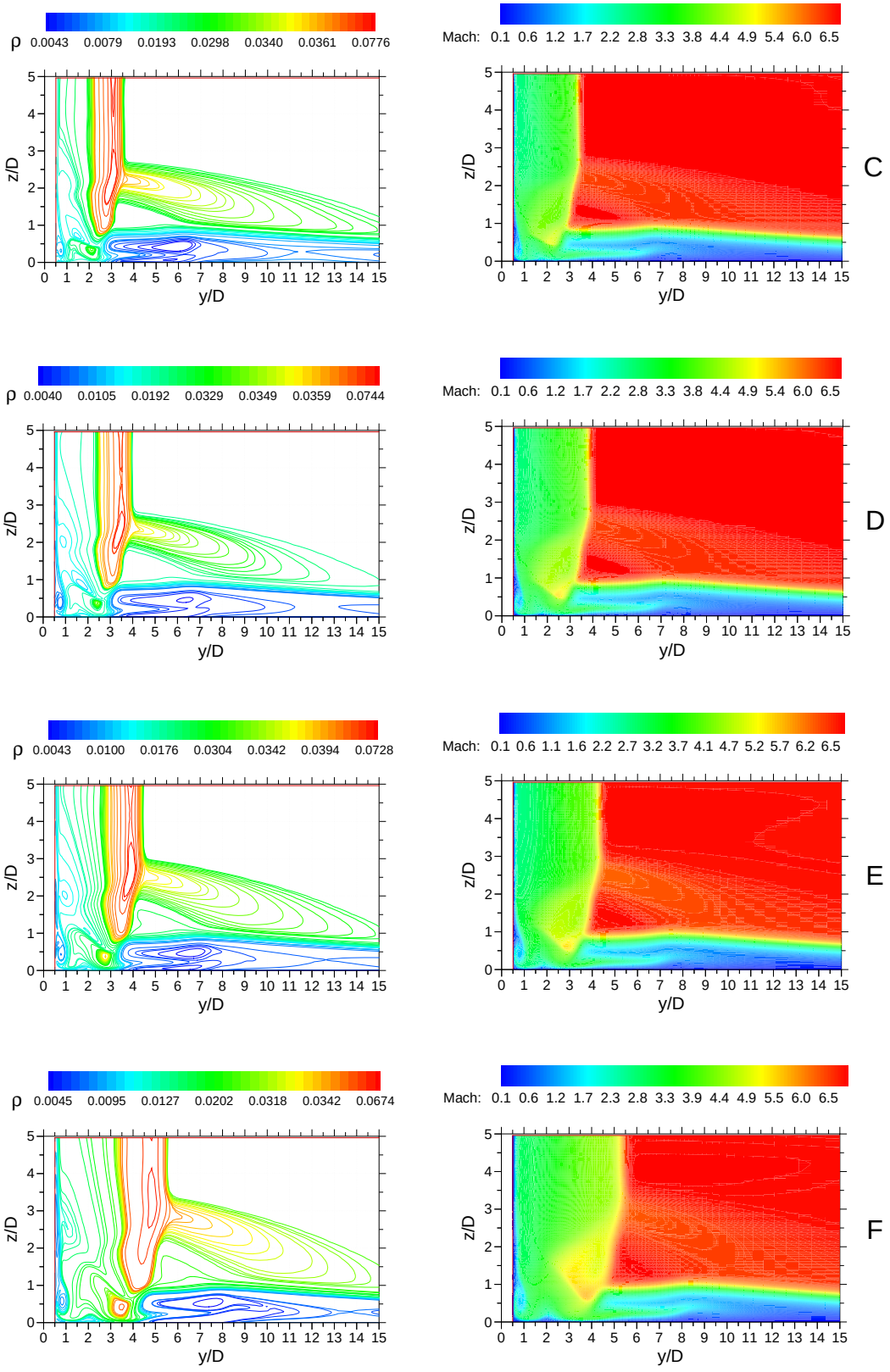

Figure 5.23: Cross plane density (left) and Mach number (right) contours at locations $C - F$

increasingly coarser at each of these locations. This fact is clearly illustrated in profile **F** where the captured bow and separation shocks are quite thick. The presence of a supersonic shear layer, slip line and normal shock can be seen in the Mach contour profiles taken at locations (**C** → **F**) in Figure 5.23, however the reflected shocklets within the bounded slip line are not evident from the Mach or density contours. A schematic of the flow structure in profile **F** is illustrated in Figure 5.24 and the comparison looks strikingly similar to the schematic in Figure 2.12 in Chapter 2, Section 2.5.2 which represents the interaction for a sharp-fin.

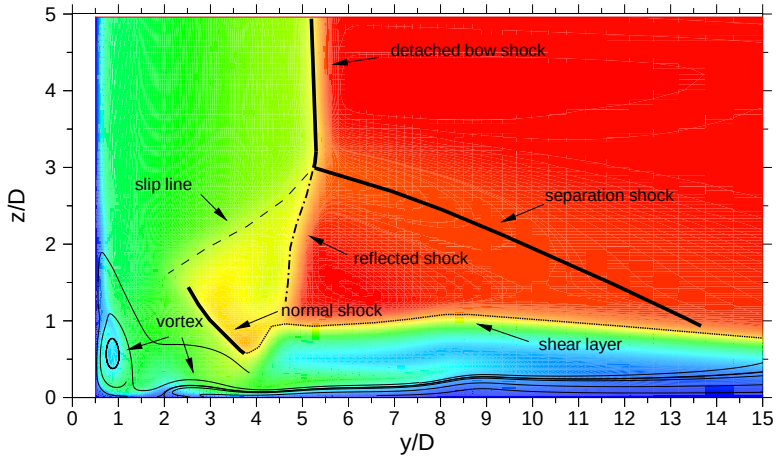

Figure 5.24: A schematic of the features observed in profile at location F

Analyzing the streamline traces in the various profiles in Figure 5.25 clearly indicates that the vortex structures formed in front of the blunt-fin leading edge spread out laterally away from the fin as they flow around it downstream of the blunt-fin leading edge. This is clearly seen when comparing profiles taken at locations **C** and **F**. The vortex with focus (F_2) observed in profile **C** approximately at ($y/D \simeq 6.5$), has spread out to around ($y/D \simeq 8.0$) from the fin edge by the time this feature is observed at profile **F**. The vortices with foci (F_1a) and (F_3a) in Figure 5.20 are clearly seen in Figure 5.25 profile **F**. The vortices with foci (F_1) and (F_2) as seen in Figure 5.20 appear to merge into one single vortex with foci (F_2) further downstream as seen in Figure 5.25 profile **F**. The vortex with foci (F_2a) is a notable absentee in all of the profiles.

The root vortex at the base of the blunt-fin, foci (F_1a) in Figure 5.20, grows in size as it evolves and flows downstream of the fin root as shown in Figure 5.25. The growth of this

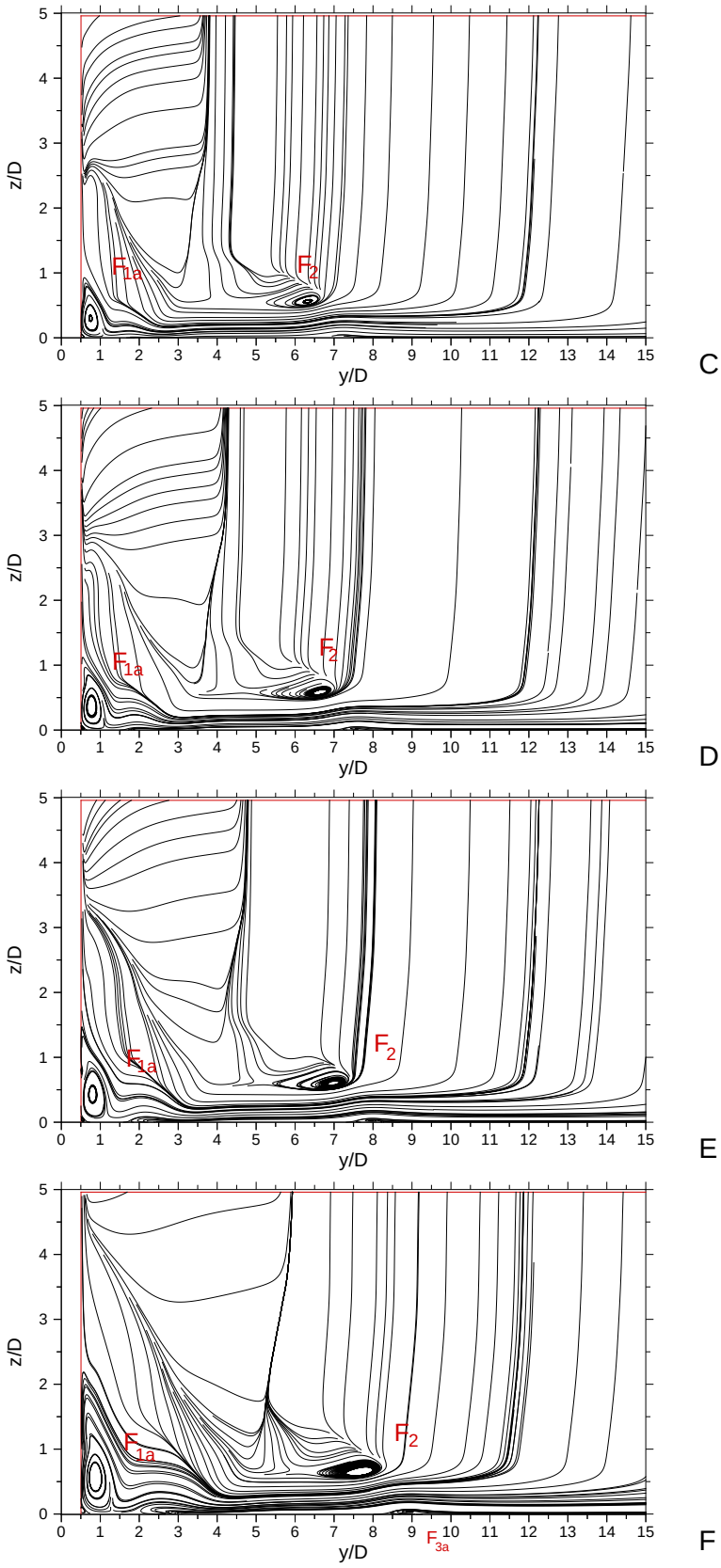

Figure 5.25: Cross plane particle streamlines from profiles at locations $C - F$

feature can be clearly seen by examining the skin friction lines on the unwrapped fin-side surface in Figure 5.26. The root vortex originates from a separation saddle at (s_1) which occurs at ($z/D \simeq 0.3$) on the fin. The subsequent separation line ($\mathbf{S_1}$) which forms the separated surface, grows downstream on the fin surface until it reaches the end of the fin at ($x/D = 8.5$). The separated region at the end of the fin surface has eventually grown to ($z/D \simeq 2$) on the fin. What is also apparent within this large separated region on the fin-side surface is the presence of secondary separation and reattachment lines. There appears to be three other singularities on the fin-side surface: a separation saddle (s_5) and reattachment node (n_5) pair and a reattachment node (n_4) associated with the separation saddle (s_4) that occurs on the plate surface as seen in Figure 5.19. The reattachment line ($\mathbf{R_5}$) which runs through the node (n_5) is quite smeared although its existence can be seen; the second reattachment line ($\mathbf{R_4}$) which runs through node (n_4) is more distinct and its path is quite clear. The vortices associated with the separated surfaces on the fin-side surface can be clearly identified from the streamlines shown in Figure 5.27. From Figure 5.26 it appears the small root vortex at the fin/plate junction is first formed at ($x/D \sim 0.5$) which is at the shoulder of the fin, and the second vortex on the fin-side surface first originates at ($x/D \sim 3$).

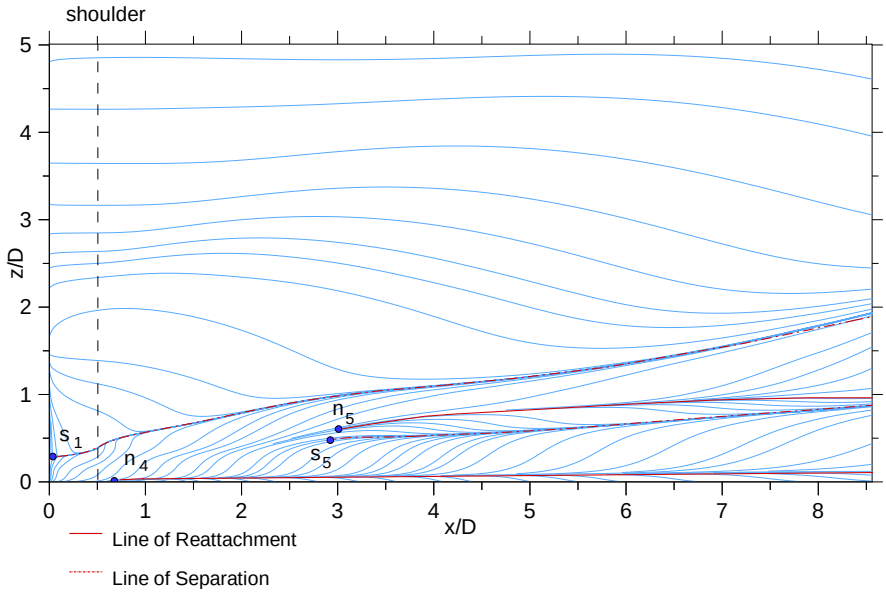

Figure 5.26: Skin friction lines on unwrapped fin-side surface

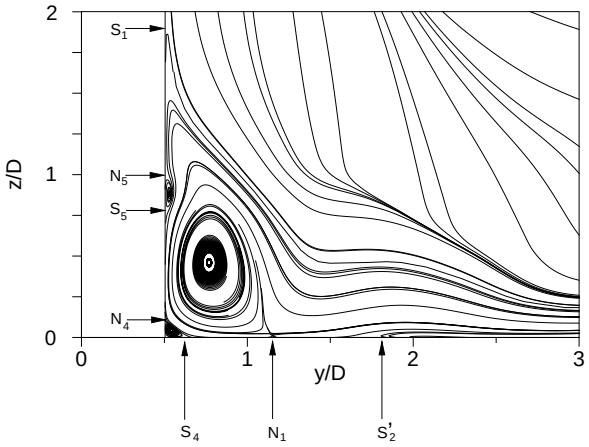

Figure 5.27: Enlargement of Streamlines near fin edge in profile plane at location F

Analyzing the different profiles (**D** $\rightarrow$ **F**), presented in Figures 5.23 and 5.25, coupled with the enlarged view of the corner of profile **F** in Figure 5.27, it is possible to suggest a mechanism that will lead to the formation of separation line (**S'$_2$**), and its paired reattachment line (**R'$_2$**) shown in Figure 5.19. The separation saddle first appears in the profile taken at location **D**, in Figure 5.25. It appears to be formed near the vicinity of the large re-circulation region of the root vortex, foci (F_1a). This region is bounded with low momentum flow which contains large positive density and pressure gradients, and it appears that the flow separates as a result of the adverse pressure gradients. However the flow reattaches further out as a result of a more favourable pressure gradient due to a drop in pressure which is a result of the flow accelerating. In addition, the separated surface as a result of (**S'$_2$**), and (**R'$_2$**) does not appear to show a distinct vortex core judging by analysing the particle streamline traces in Figure 5.25.

The impingement point of the supersonic jet on the blunt-fin surface as a result of the *Edney* Type *IV* interaction, can be seen in the pressure and skin friction coefficient contours on the fin-side surface in Figure 5.28 and Figure 5.29.

This impingement point correlates well with the indicated position of the jet as seen in Figure 5.11 at ($z/D \sim 2$). This region is characterised by very high coefficients of friction ($C_f \sim 0.01$), the result of high shear stresses and large pressure gradients as indicated in Figure 5.28. The magnitude of the (C_f) values in this region of the fin-side are comparable

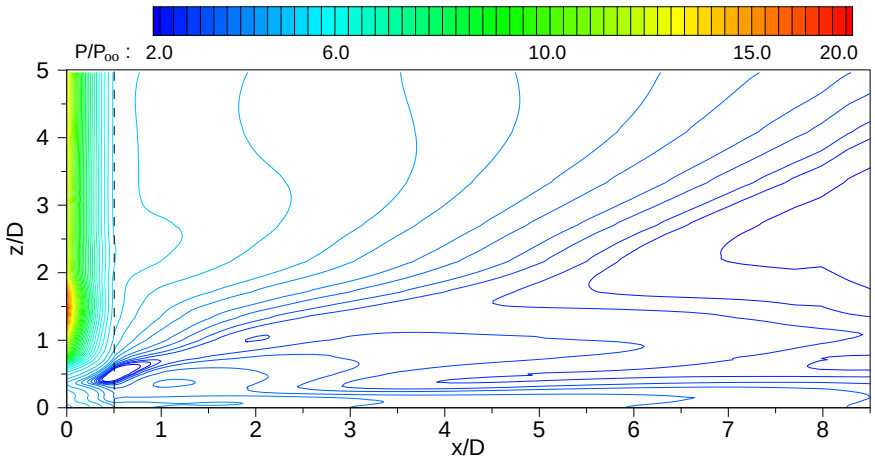

Figure 5.28: Normalized pressure contours on fin-side surface

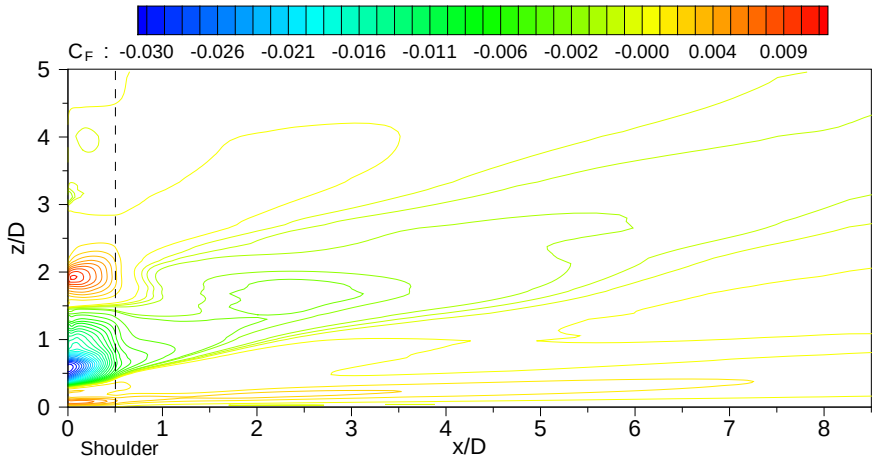

Figure 5.29: Skin friction coefficient on fin-side surface

to the (C_f) values recorded at the base of the blunt-fin/plate junction (see Figure 5.6). The primary reattachment of the upstream separation point is also indicated on the surface of the blunt-fin, this area at ($z/D \sim 1.5$) is highlighted by large pressure values and positive values of skin friction coefficient. The pressure contours reveal that the impacting jet on the leading edge of the blunt-fin surface fans higher pressure fluid generally over the upper surface of the fin, with the leading edge region recording some of the highest values. A bubble of low pressure occurs near the lower part of the fin this is due to the fluid expanding as it flows over the shoulder of the fin.

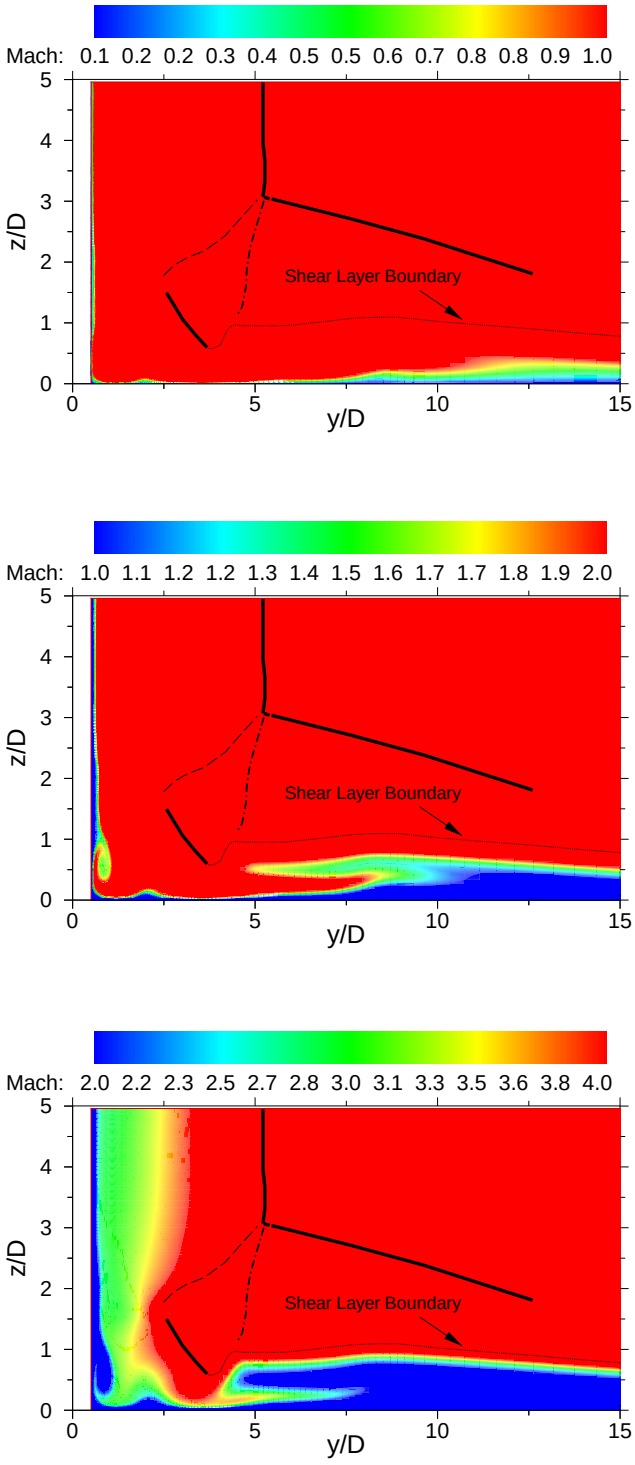

Figure 5.30: Mach contours taken at profile F for three different Mach number ranges (**top left**) Mach no. 0.1 - 1.0 (**top right**) Mach no. 1.0 - 2.0 (**bottom**) Mach no. 2.0 - 4.0

Studying the section profiles for Mach number, density and particle stream traces in Figures 5.23 and 5.25 highlight several salient features worth mentioning.

A closer examination of the Mach contours and the subsequent shear layer in Figure 5.30 reveals that a large portion of this shear layer is inherently supersonic. This is in contrast quite different to what was observed earlier in Figure 5.11, where the flow within the shear layer in the symmetry plane was observed to be mainly subsonic. As a result, it appears that most of the vortical structures observed in profile **F** lie within this supersonic region. Foci (F_1), (F_1a), (F_2) in Figure 5.11 are embedded in a region of subsonic flow, whereas in Figure 5.30 the flow within these foci are clearly supersonic. This clearly indicates that the flow within the vortical structures accelerates as they form and flow around the blunt-fin structure.

The density contours in the section profiles indicate a complex topology of varying pockets of high and low density. Embedded in this flow region is the presence of a normal shock straddled between two pockets of varying density which occur at ($y/D \simeq 3$ - 4). In addition, it appears the conical vortices in the separated flow are embedded in regions of low density, this fact is similar to what is observed in profile **A**.

What appears to emerge from analysing the section profiles is that upstream of the root of the blunt-fin the flow is dictated by the presence of the fin, therefore the flow exhibits the characteristics of a protuberance type flow, however downstream of the fin root the effects of the fin-side/plate junction become more dominant and the flow is dictated by this structure which can be characterised as a corner type flow.

Up to now, only results from planar sections have been presented, but nothing has been shown to give a general idea of the three-dimensional evolution of the flow over the blunt-fin. Collating all the information about the flow from various section profiles, it is possible to construct a three-dimensional picture of the flow structure surrounding the blunt-fin, and this is illustrated in Figures 5.31- 5.37.

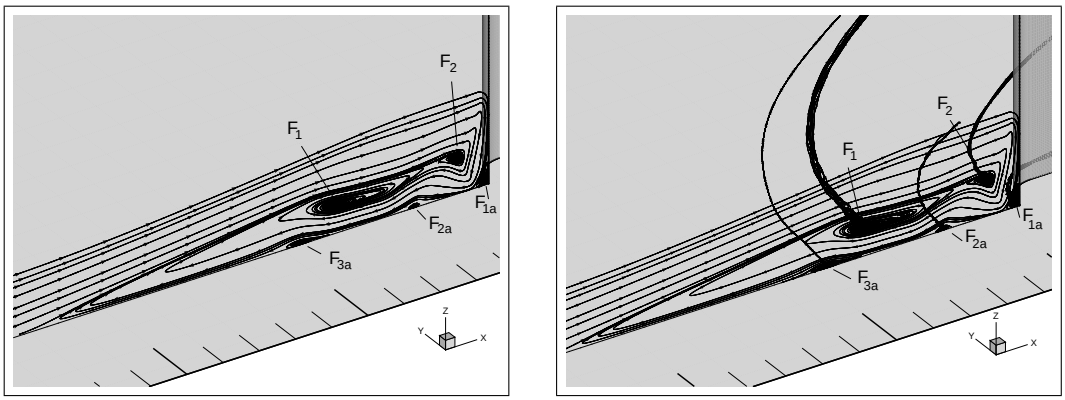

Figure 5.31: (**left**) Streamline traces taken along the symmetry plane (**right**) Streamline traces and three-dimensional vortex formation

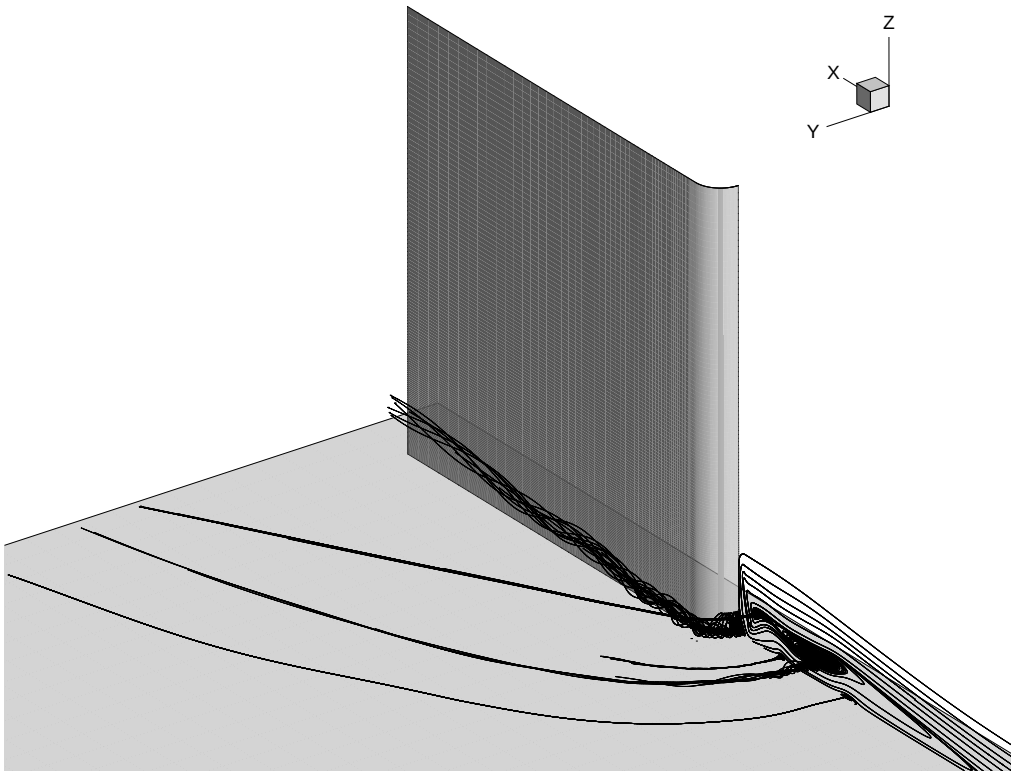

Figure 5.32: Three-dimensional vortex structure around blunt-fin

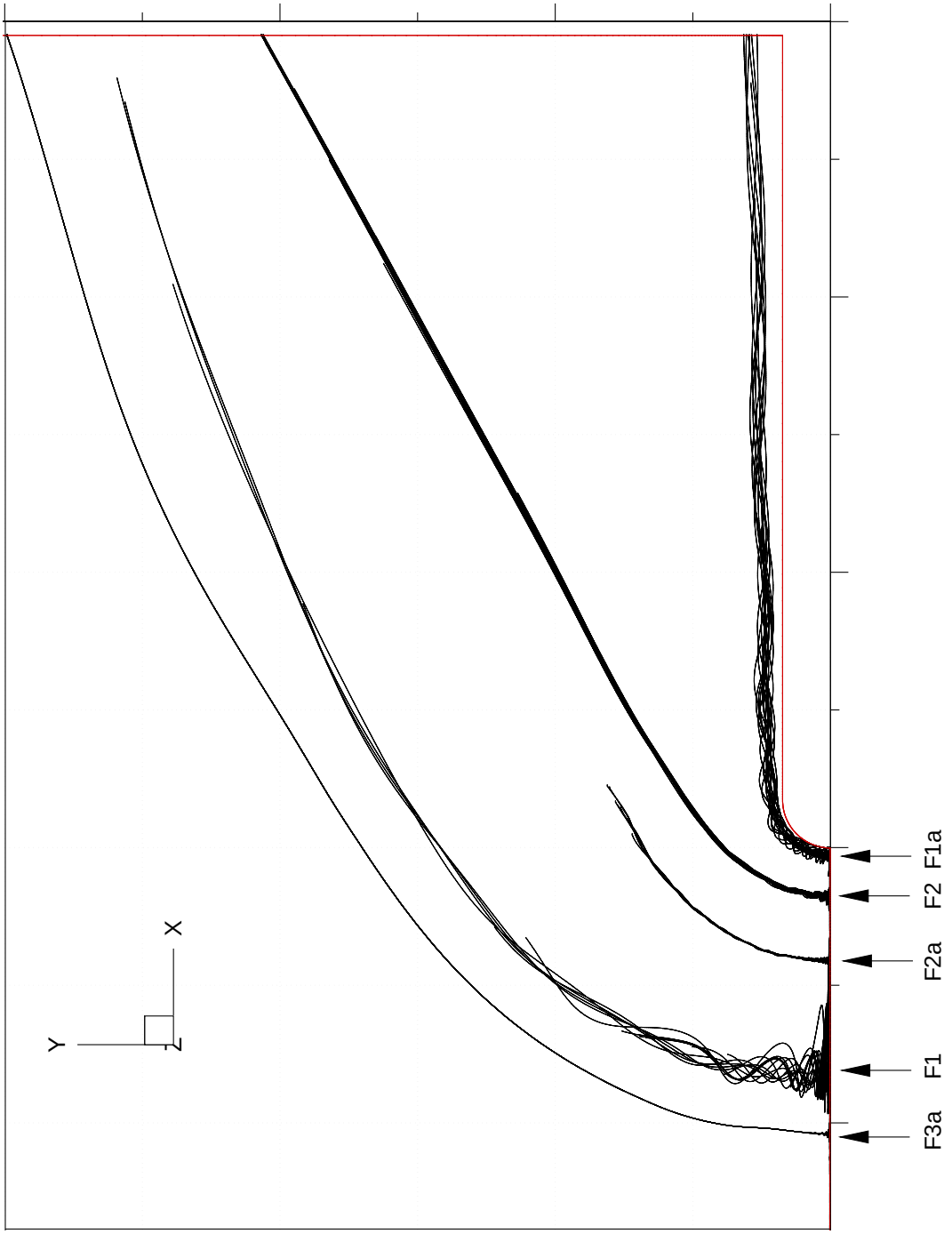

Figure 5.33: Plan view of streamline trace

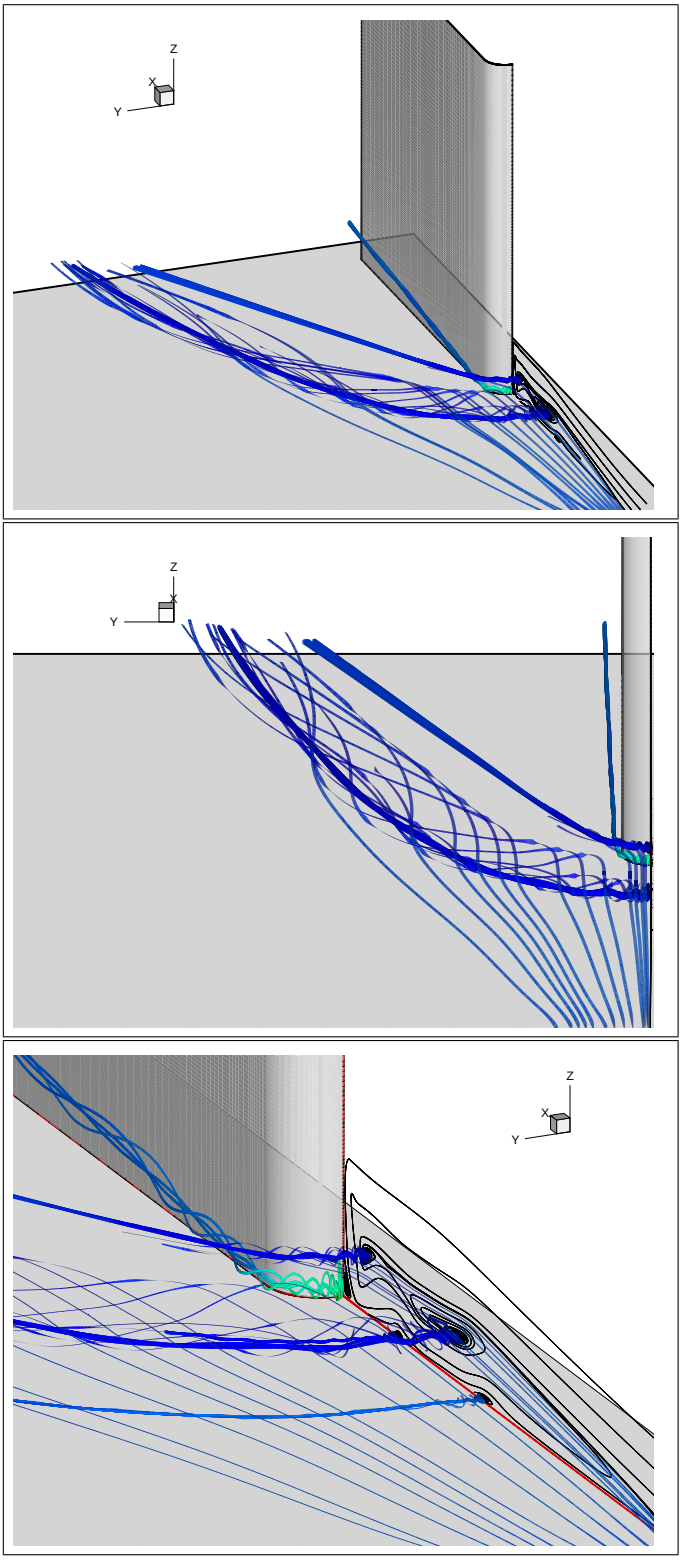

Figure 5.34: (**top**) three-dimensional stream ribbon trace, view 1 (**middle**) three-dimensional stream ribbon trace, view 2 (**bottom**) three-dimensional stream ribbon trace, view 3

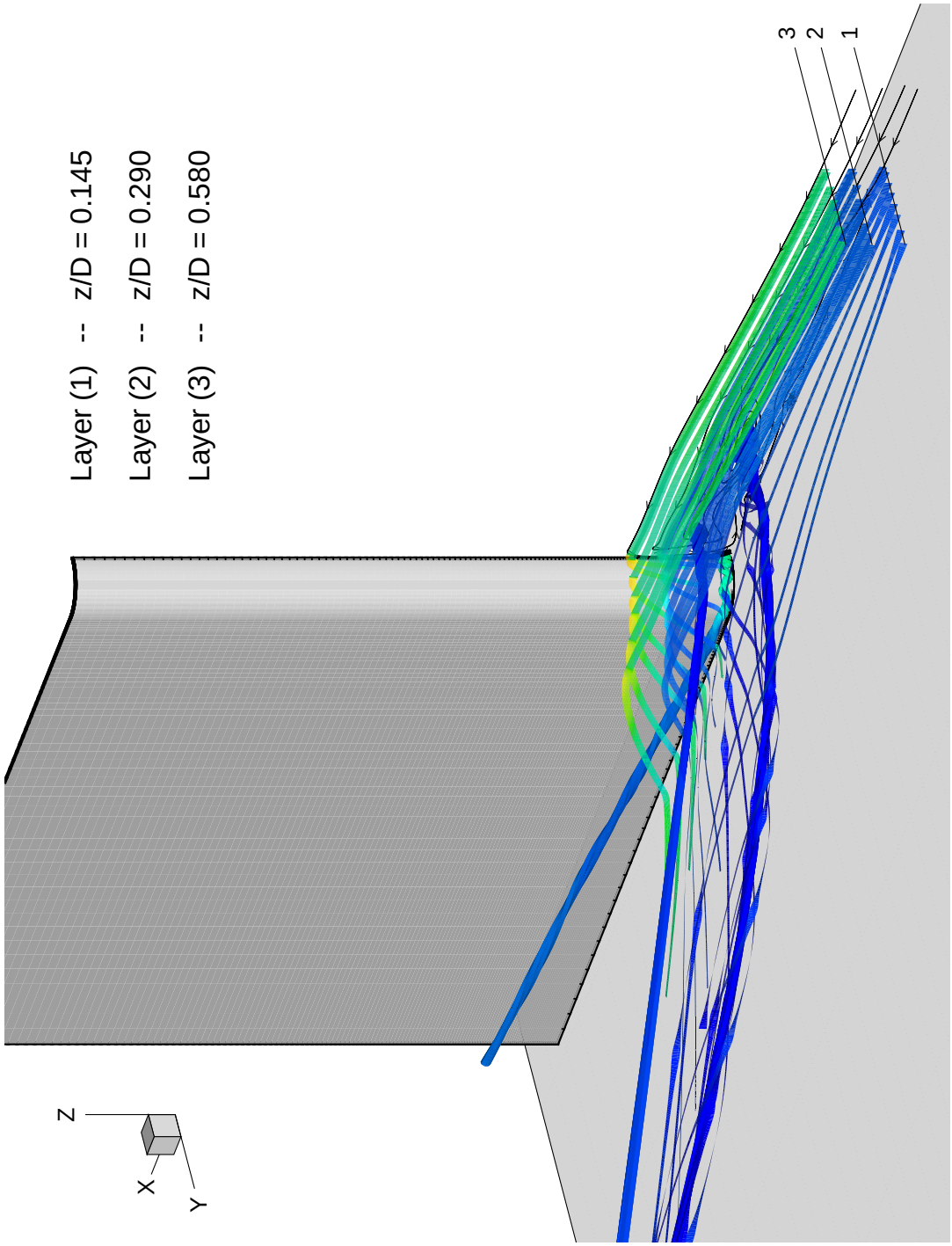

Figure 5.35: Three-dimensional stream ribbon trace, at three different z/D layers

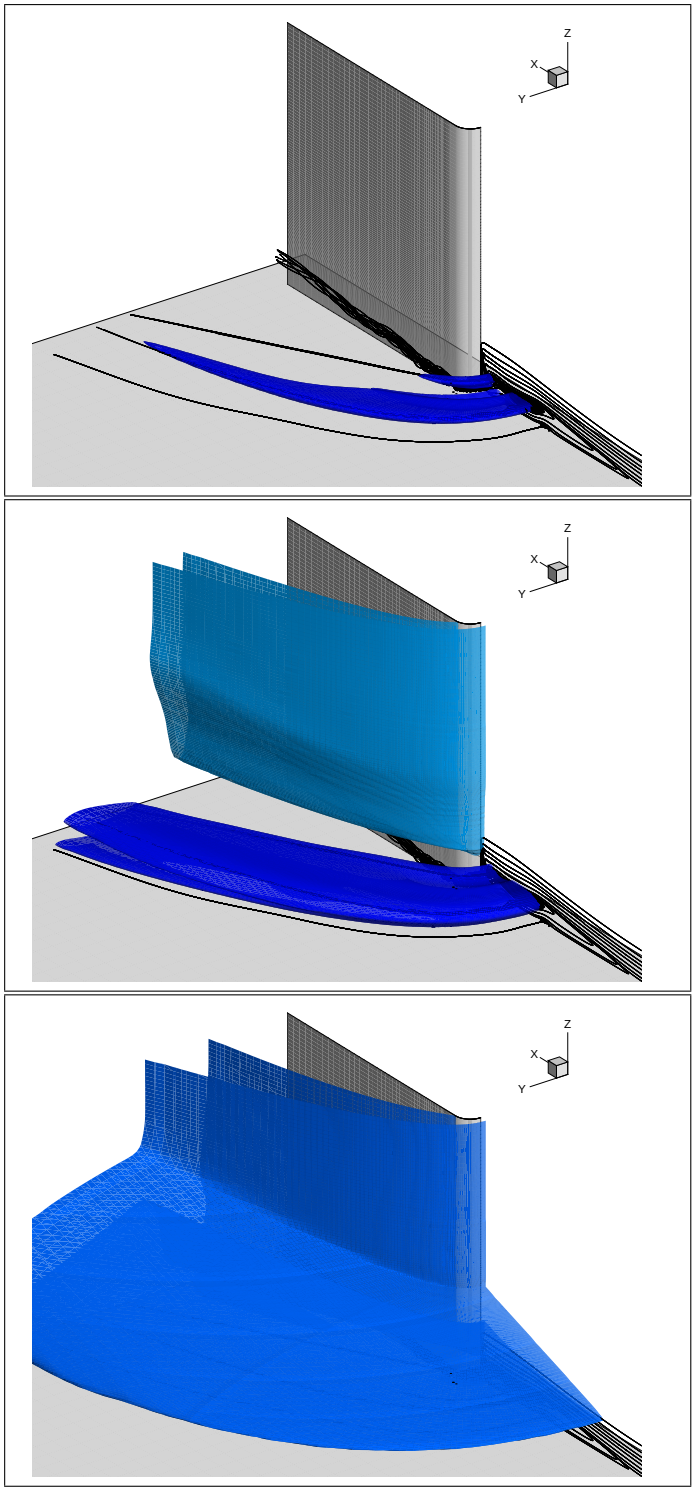

Figure 5.36: (**top**) isometric surface of constant density within horseshoe vortex system (ρ = 0.004) (**middle**) isometric surface of constant density depicting bow shock ($\rho = 0.05$) and density band within horseshoe vortex system (ρ = 0.005) (**bottom**) Three-dimensional shock structure, showing bow shock and separation shock surfaces using constant isometric density surface (ρ = 0.032)

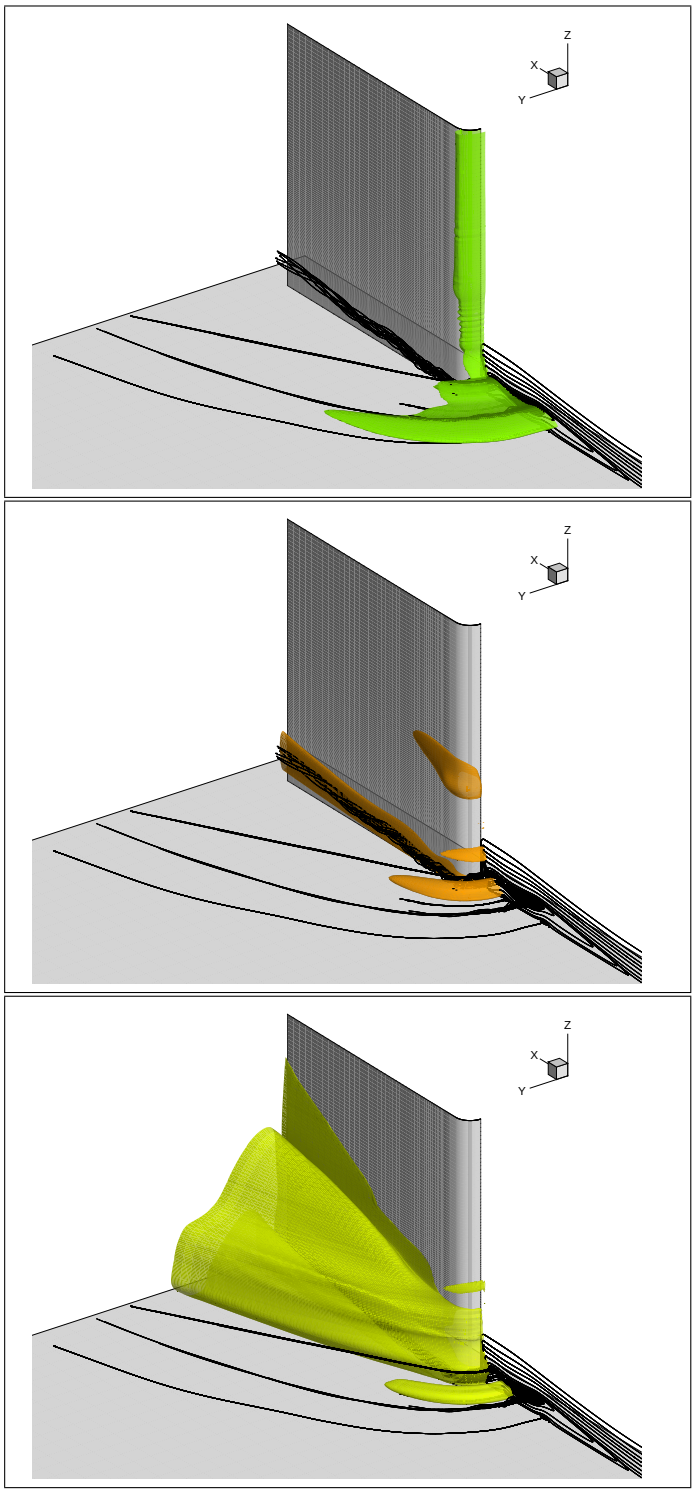

Figure 5.37: (**top**) isometric surface of constant Mach number, M = 0.9 (**middle**) isometric surface of constant velocity, w = 200 m/s (**bottom**) isometric surface of constant velocity, w = 50 m/s

Figure 5.31 shows how the streamlines in the two-dimensional symmetry plane evolve into three-dimensional vortex features as indicated in Figure 5.32. From Figure 5.31 it appears that most of the rotational velocity in the particles in the vortices (F_1), (F_1a), (F_2), (F_2a) and (F_3a) is concentrated in the central core, and it is this core feature that appears to evolve around the fin scavenging flow from the surrounding area. Clearly indicated in Figure 5.33 is the subsequent paths taken by the horseshoe vortex patterns around the blunt-fin. Figure 5.33 appears to show that the vortices associated with foci (F_1), (F_2a), (F_2) and (F_3a) evolve almost in parallel with each other around the fin. Also clearly illustrated is the growth of the root vortex on the blunt-fin as it flows around the fin. It appears the root vortex further downstream has the biggest core when compared to the other vortices and as indicated the high energy fluid in the little vortex scavenges and draws into itself the surrounding flow, increasing in size as it flows downstream.

A closer examination of Figure 5.33 appears to show that the vortex with foci (F_2a) disappears shortly after it evolves from the symmetry plane when compared to the other vortices that can be clearly traced back downstream to the edge of plate boundary. This is significant because it indicates that this vortex has substantially lower rotational velocity in its core compared to the other vortices, and as a result it is unable to entrain enough flow from the outer flowfield to evolve further downstream. As a result the vortex diffuses into the surrounding flowfield further downstream. This observation is unique because, as shown in the plot it highlights the fact that this vortex is actually absorbed into the surrounding flow and disappears hence its associated heat transfer footprint also disappears and this is not attributed to vortex lifting as was suggested by Schuricht [53].

This theory is further supported by examining the particle stream traces in Figures 5.34-5.35. The images indicate that most of the flow in the separated region is swallowed by the primary vortex cores of (F_1) and (F_2). It appears most of the spanwise flow in '*layer 1*' is entrained into vortex (F_2), with flow near the symmetry plane being entrained into vortex (F_1). In '*layer 2*' the flow is entrained into the the combined recirculation region that contains vortex cores (F_1) and (F_2). '*layer 3*' indicates that the flow passes over the combined core of (F_1) and (F_2), and flows down towards the plate surface. What this implies is that because (F_2a) and (F_3a) are localised on the plate surface, rotating in counter clockwise direction to the primary vortex cores (F_1) and (F_2), it appears there is a

considerably smaller volume of fluid available to scavenge and entrain into these vortices. The stream trace ribbons in Figure 5.34:(**bottom**) clearly highlights the reduced level of flow entrainment into vortex cores (F_3a) and (F_2a). In addition, an analysis of the velocity vector plot in Figure 5.12 highlights another point, the flow directly above vortex (F_2a) is travelling considerably faster than the flow in the vortex core, as a result is unlikely to be drawn into it. However the flow surrounding vortex core (F_3a) is travelling at a much reduced speed, thus is more able to be drawn into its core. More importantly, because vortex (F_2a) is considerably smaller than vortex (F_3a), it is plausible that even less fluid is consumed by it. Therefore the evidence clearly indicates why vortex (F_2a) is unable to evolve the complete length downstream.

Figure 5.36 and Figure 5.37 plots isometric surfaces of a selected constant variable. The isometric density surfaces in Figure 5.36 clearly show the bow shock and constant density surfaces within the separated flow. Figure 5.36:(**top**) indicates the primary vortex cores of (F_1) and (F_2) are embedded in a region of low density. Figure 5.36:(**middle**) gives the position of the bow shock and the low density band within the separated region containing the primary vortex cores. The deflection of the bow shock as a result of the interaction with the oblique separation shock is clearly seen. Figure 5.36:(**bottom**) indicates the extent of the separation shock/bow shock interaction. What is evident is the spreading of the separated region in a more spanwise direction further downstream of the fin root. This primarily impacts the triple point which travels further up the fin as the flow progresses downstream.

The isometric Mach and (w) [2] velocity surfaces in Figure 5.37 indicate regions of a constant value. The (Mach = 0.9) surface highlights the three-dimensional extent of the subsonic layer within the separated flow and behind the bow shock. The layer within the recirculation region is confined to the line of symmetry and the surrounding flow near it. The vortices that form at the centerline in the subsonic layer will become embedded in regions of supersonic flow further downstream as shown in Figure 5.37:(**top**). The constant (w)-vertical velocity surface depicted in Figure 5.37:(**middle**) and Figure 5.37:(**bottom**) highlights a isometric surface for two constant speeds. The higher velocity surface, ($w = 200ms^{-1}$), highlights a section of flow that is accelerated by the

[2]- Velocity components: (u)-streamwise; (v)-spanwise; (w)-vertical

impacting supersonic jet on the fin surface and the vortex core within vortex (F_1a). The lower velocity surface, ($w = 50ms^{-1}$), highlights the low velocity within vortex (F_2a), and the region of flow encased within the bow shock and fin surface.

5.4.3 Surface Heating on Plate

The surface heat transfer profiles give us the first real opportunity to compare quantitative data obtained from the experiments conducted by Schuricht [53] with results obtained from the numerical simulations undertaken in this study.

The surface heat flux from the numerical results is calculated using first order surface temperature gradients:

$$\dot{q}_w = \kappa \frac{\partial T}{\partial \zeta} \tag{5.7}$$

This is used to calculate the Stanton number defined by Eqn 2.9 in Chapter 2, the non-dimensional parameter usually used to define heat flux.

$$St = \frac{\dot{q}_w}{C_p \rho_\infty U_\infty (T_r - T_w)} \tag{5.8}$$

From this we can define the heat transfer coefficient (h) as

$$h = \frac{\dot{q}_w}{(T_r - T_w)} \tag{5.9}$$

where,

$$h = St \rho_\infty U_\infty c_p \tag{5.10}$$

For the remainder of this section, the surface heat fluxes will be compared using the respective heat transfer coefficients.

Following the procedure in Schuricht's work, the numerical heat transfer coefficient (h) has been normalized with respect to the undisturbed heat transfer coefficient (h_u) for a flat plate. The flat plate was simulated earlier, and the results are described in Chapter 4, Section 4.2. The resultant heat transfer coefficient (h/h_u) will be used to compare the heat transfer profiles. Therefore regions where the normalised value (h/h_u) is less than one represents a region of reduced heat flux while a region where ($h/h_u > 1$) represents a region of enhanced heat flux.

Figure 5.38 shows the spatial distribution of normalized heat transfer contours (h/h_u) obtained by Schuricht for the 5mm unswept blunt-fin; Figure 5.39 is the equivalent contour profile obtained from the numerical simulation. Comparing the distribution patterns of the two images show very strong similarities. Both heat transfer images indicate that regions of high heat transfer follow the shape of horseshoe bands around the blunt-fin. This observation is consistent with earlier suggestions that heating enhancements occur along the horseshoe shaped vortex paths.

From observation, the experimental heat transfer images in Figure 5.38 indicate four distinct regions of enhanced heating. The outer-most feature is a high heat flux band where ($h/h_u \simeq 4$); further inward, closer to the root of the blunt-fin shows a thicker band where (h/h_u) is between 4 to 5 times the undisturbed value. The region closest to the blunt-fin root has two distinct traces where the heat flux (h/h_u) is $\simeq$ 8 to 10 times the undisturbed value. The regions that appear white in Figure 5.38 are areas where no valid data were obtained. Schuricht [53] concluded that in these areas the liquid crystal layer had cleared, and the surface temperature is therefore in excess of the liquid crystal colourplay bandwidth. It was also suggested that close to the blunt-fin root at ($x/D \simeq$ -1) is region where the liquid crystals had ablated due to high shear and heat transfer locally. As a result, Schuricht had to estimate the heat transfer coefficient in these regions by knowing the approximate temperature rise that occurred within the time interval. Schuricht concluded that as a lower band estimate, ($h/h_u > 10$).

Comparing with Figure 5.39; the numerical profile also demonstrates four distinct regions of enhanced heating with the spatial location of each band a offering good correlation to the experimental data. The higher heat flux bands in the numerical contour profile

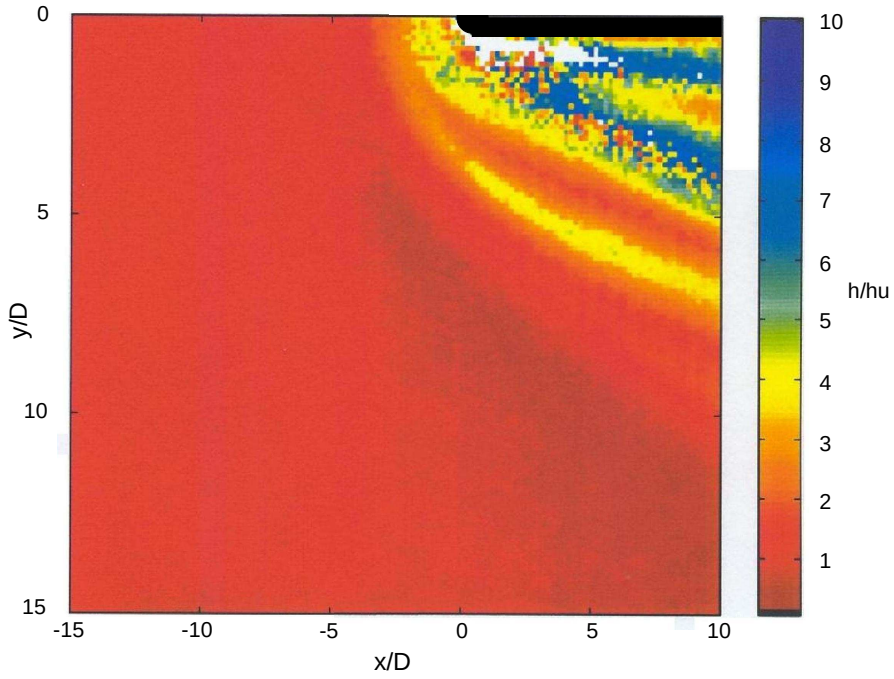

Figure 5.38: Experimental heat transfer contours on plate surface Schuricht [53]

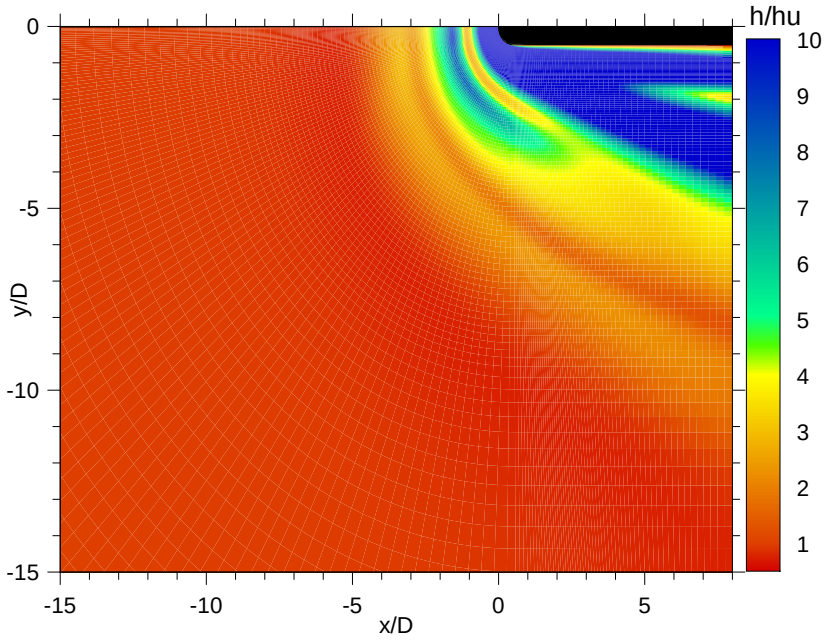

Figure 5.39: Numerical heat transfer contours on plate surface

are more clearly resolved than in the experimental results, and more significant as will be shown later, the root of the blunt-fin indicates considerably higher heat transfer rates, approximately 60 times the equivalent undisturbed flat plate value. As highlighted earlier, a direct comparison with the available experimental results in this region is not possible, because the liquid crystal technique employed by Schuricht could not provide reliable results at such high heat fluxes.

The numerical results indicate that the maximum heat transfer coefficient $(h/h_u)_{max}$, which occurs near the root of the blunt-fin, is around 5 times greater than the maximum value estimated by Schuricht from the experiments. The calculated numerical $(h/h_u)_{max}$ is also considerably larger than the value estimated from Eqn 2.28 in Chapter 2, Section 2.5.2, which is calculated to be around 7. However similar findings have been reported by Tutty $et.al$ [60] for turbulent blunt-fin interactions where there has been large discrepancies between the numerical and experimentally calculated $(h/h_u)_{max}$. In these simulations the available experimental data suffered from similar losses as a result of liquid crystal ablation, but when comparisons were made between the predicted values for heat transfer coefficient and the equivalent numerical values, differences with similar orders of magnitude were observed.

An important difference that has emerged between the experimental and numerical results concern the outer heating band: in the numerical results the heat flux associated with the outer band near the line of symmetry, is around $(h/h_u \simeq 3.5)$. However, as this feature wraps around the blunt-fin, (h/h_u) decreases to $\simeq 3$. This trend appears to occur in the opposite direction in the experimental results in Figure 5.38. The experimental heat flux associated with this feature near the line of symmetry is approximately $\simeq 2$, increasing to $(h/h_u \simeq 4)$ as the heating band wraps around the blunt-fin. A more detailed examination of this difference is made later by inspecting crossflow and centerline (h/h_u) profiles.

Figure 5.40:(**top**) shows the actual oil-flow and liquid crystal response obtained by Schuricht for the 5mm unswept blunt-fin. The regions on the liquid crystal response highlighted by a blue/black band represents an area of enhanced heating and, as indicated, there appear to be four distinct horseshoe shaped bands surrounding the blunt-fin. The enhanced heating band closest to the root appears to split in two as the feature evolves downstream of

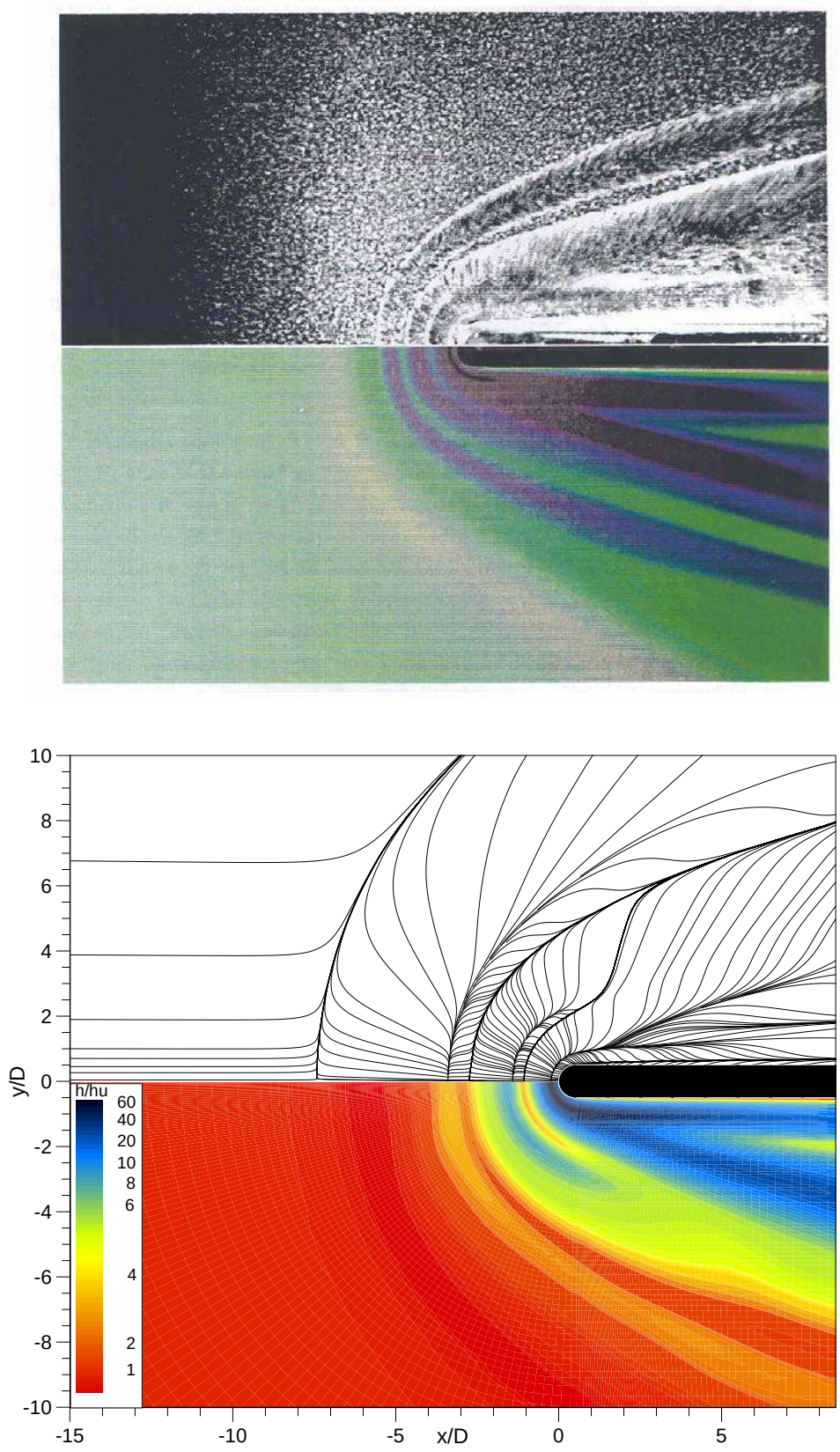

Figure 5.40: (**top**) Liquid crystal response and oil-flow over plate surface by Schuricht [53] (**bottom**) Heat transfer distribution and skin friction streamlines on plate surface

the fin root. The oil-flow image reveals the location of any separation or reattachment lines present on the surface. As discussed in Chapter 4, Section 5.1.5, regions of low shear signifies flow separation, and on the oil-flow in Figure 5.40:(**top**) is indicated by regions where the oil accumulates as streaky white lines. The areas on the plate where flow reattachment occurs, regions of high shear, are indicated by an absence of oil. It is clear that distinguishing unique separation and reattachment lines close to the fin root is quite difficult due to poor visual resolution and smearing. This highlights the difficulty in using oil-flow images alone to ascertain a separation topology for such configurations.

The equivalent numerical comparison, which shows the plate skin friction streamlines mirrored against the heat transfer contours for the plate, is illustrated in Figure 5.40:(**bottom**). The comparison shows similarities with the experimental results, and as indicated the four distinct enhanced heating bands correspond with four reattachment lines expressed by a divergent herringbone pattern. Regions where flow separation occurs is indicated by a convergent pattern in the streamlines and is highlighted by the cooler bands, which in Figure 5.40:(**bottom**) is shown to be areas that are either red/orange. A closer inspection of the region near the blunt-fin wall indicates a line of separation very tightly packed near the fin edge. This feature was noted earlier when examining the lateral section profiles, where a very small corner vortex is observed at the base of the fin, (see Figure 5.26). This result is similar to observations made for a sharp-fin in Chapter 2, Section 2.5.1.

One of the most pronounced features highlighted by the numerical results is the extremely large heat fluxes calculated at the flow reattachment node (n_1), (see Figure 5.40 and Figure 5.19). Studying the localised Mach number and density field near this reattachment node in Figure 5.41, it is possible to postulate a mechanism that could be responsible for the observed large heat flux associated at (n_1).

The Mach contours indicate that the reattachment node (n_1) is straddled between two supersonic zones, with one supersonic pocket located near the corner vortex with foci (F_1a). A closer inspection of Figure 5.41:(**left**) reveals that the flow at the reattachment node (n_1) is itself subsonic. The localised density contours in Figure 5.41:(**right**) reveal that the reattachment location is a region of higher density when compared to the flow regions neighbouring the reattachment location. Figure 5.12 highlights the most important

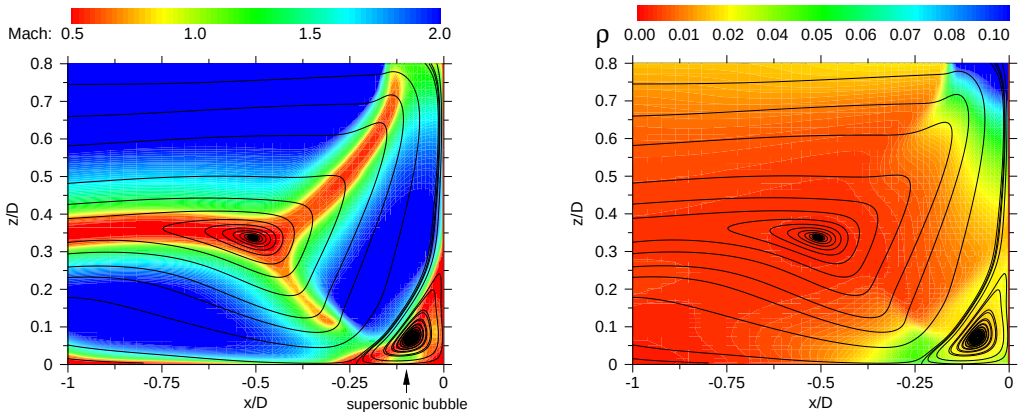

Figure 5.41: (**left**) Enlarged view of Mach contours near the root vortex (**right**) Enlarged view of Density contours near the root vortex

fact, as indicated by the velocity vectors, the flow is accelerated considerably down towards the plate surface by the surrounding supersonic regions to form a near vertical supersonic jet like feature. The boundary layer on the plate at (n_1) is extremely thin as a result of flow reattachment, the near vertical supersonic jet appears to be concentrated at the reattachment point. Sudden retardation of the flow because of the jet of high speed flow striking the plate surface causes a large transfer of kinetic energy to thermal energy. The increased density of particles and high pressures correspond to a greater mass of high speed particles striking the surface, and as a result gives a clear indication on why the heat transfer rate at the reattachment point (n_1) is so high.

Although Schuricht did not take any heat flux measurements on the fin-side surface of the blunt-fin, the numerical results obtained from the present simulation allows for a detailed analysis of the heat flux distribution on the blunt-fin side surface. The heat transfer coefficient distribution indicates three distinct regions of enhanced heating on the side surface of the fin as shown in Figure 5.42. The heat flux contour field on the fin-side surafce has been normalised with respect to the undisturbed (no fin) heat flux coefficient estimated from Eckerts reference enthalpy method at a position 145mm downstream of the plate leading edge (the fin/plate junction), this was estimated to be $2217 Wm^{-1}K^{-1}$.

The most distinct region occurs on the fin leading edge, ($x/D = 0$), and two secondary regions span the entire chord of the fin side surface. The region which records the most

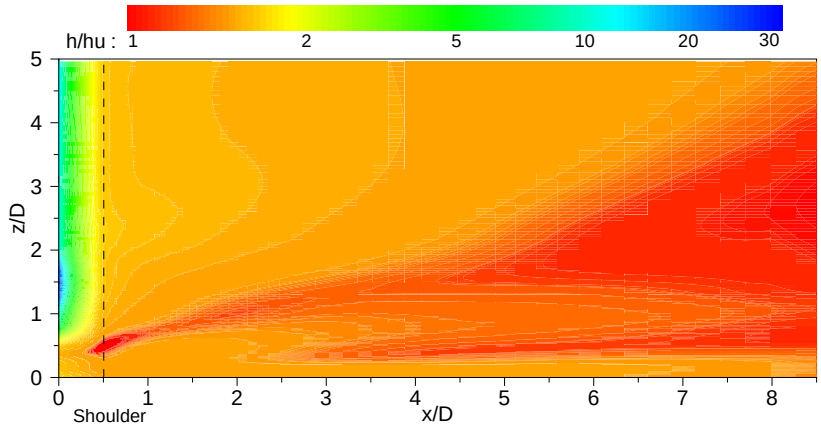

Figure 5.42: Heat transfer distribution on the side surface of blunt-fin

dramatic heating is likely caused by the impacting supersonic jet on the fin surface, which produces the most distinct impression on the surface heating profile as indicated in Figure 5.42. At the jet impingement point, ($h/h_u \simeq 30$), with the surrounding area around the jet also experiencing elevated levels of heating. The contour map reveals that the impacting supersonic jet appears to cause two distinct jet flow features. The first jet seems to follow a path initially upwards away from the triple point along the fin leading edge similar to findings of Fomison [21], and is the more distinct of the two, causing significant heating enhancement. The second jet, much weaker, passes on either side of the fin and traverses across the side surface of the fin causing a relatively minor heating increase, ($h/h_u \simeq 1.8$). The two regions on the fin side surface surface are localised near the base of the fin, and are the result of conical vortices that were highlighted in Figure 5.27, formed inside the large separated region of vortex (F_1a). The heating levels as a result of these vortices is relatively low by comparison ($h/h_u \simeq 1.8$).

Inspection of the heat transfer profiles along discrete lines on the plate surface is more beneficial and reveals more detail about the characteristics of the heating profile, and enable further comparisons to be made with the experimental data obtained by Schuricht. To simplify comparison with Schuricht's results the notation used in Figure 5.43 has been changed so that the nodal points (n) are replaced with ($\mathbf{R}$), signifying the reattachment line that flows through the reattachment nodes. For example ($\mathbf{R_1}$) is associated with node (n_1).

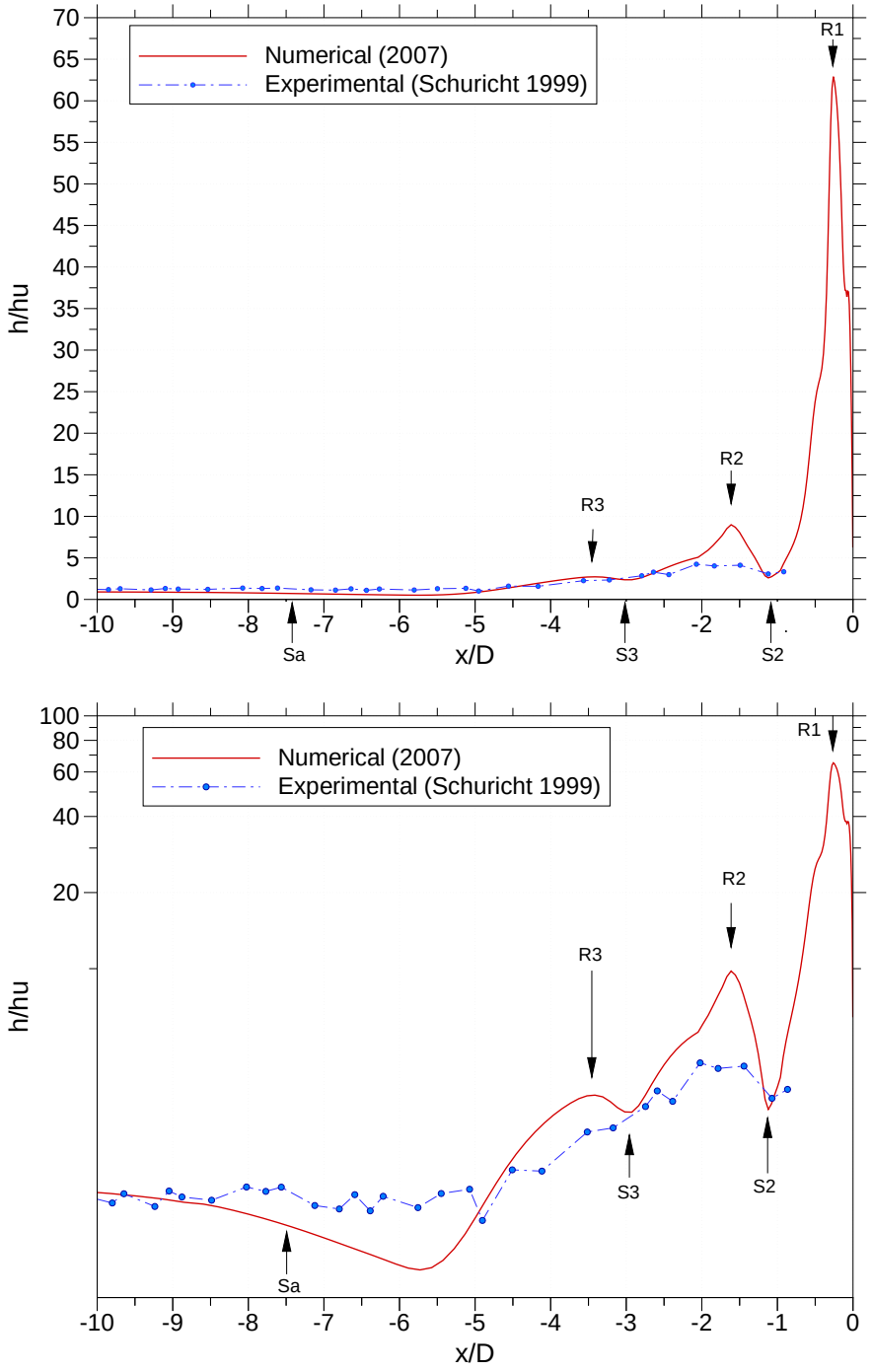

Figure 5.43: (**top**) Normalized linear heat transfer coefficient (h/h_u) along centerline (**bottom**) Normalized logarithmic heat transfer coefficient (h/h_u) along centerline

The numerical centerline heat transfer profile shown in Figure 5.43 in both linear and logarithmic form, reveals three distinct peaks associated with three reattachment points on the surface of the plate. The location of these peaks and valleys are consistent with the flow topology suggested by the surface skin friction streamlines in Figure 5.19, and symmetry plane velocity streamlines of Figure 5.20. The flow reattachment nodes in the skin friction topology map were labelled ($n_1 = \mathbf{R_1}$), ($n_2 = \mathbf{R_2}$) and ($n_3 = \mathbf{R_3}$) respectively, with (n_1) equating to the location where $(h/h_u)_{max}$ occurs, closest to the blunt-fin root. The magnitude of the peaks increase as the fin root is approached. The highest heating coefficient occurs at ($\mathbf{R_1}$), where $(h/h_u)_{max} \simeq 63$. This value is significantly higher than the value ($h/h_u > 10$) estimated by Schuricht from his experimental data, as highlighted earlier.

Comparing the two data sets in Figure 5.43, shows that the numerical results over predict the heat transfer coefficient at each reattachment point along the centerline. The difference between the numerical and experimental (h/h_u) increases as the root of the blunt-fin is approached. Starting upstream of the separation point; the numerical profile shows a more pronounced decrease in the heat transfer coefficient at primary separation which occurs at ($x_S/D \simeq$ -7.5), compared to the experimental results which show no appreciable change in (h/h_u). The heat transfer coefficient associated with ($\mathbf{R_3}$) is similar in both data sets, with ($h/h_u \simeq 3.5$). The coefficient associated with ($\mathbf{R_2}$) in the numerical profile increases to around ~ 2 times greater than the equivalent experimental value. The greatest difference occurs at ($\mathbf{R_1}$), where the associated heat transfer coefficient is approximately ~ 6 times greater than the equivalent experimental value at ($\mathbf{R_1}$).

The numerical results do however show a very favorable comparison with the experimental data in the undisturbed regions and in the general spatial distribution of the peaks and valleys. Clear points of similarity to observe between the numerical and experimental data concern the location of separation point ($\mathbf{S_2}$) and the reattachment points ($\mathbf{R_2}$) and ($\mathbf{R_1}$). According to the numerical results, separation point ($\mathbf{S_2}$) and reattachment node ($\mathbf{R_1}$) occur at around ($x/D \simeq$ -1.2) and ($x/D \simeq$ -0.2) respectively; these appear to agree well with the experimental data, where Schuricht estimated that the reattachment node ($\mathbf{R_1}$) would occur at ($x/D \simeq$ -0.15). Further similarities appear with the location of reattachment node ($\mathbf{R_2}$) which is around ($x/D \simeq$ -1.6) in both data sets. In addition both

data sets indicate that the heating rise begins to occur just over ($x/D \simeq$ -5) upstream of the blunt-fin root.

Schuricht reasoned that the centerline (h/h_u) profile contained four distinct peaks which, he concluded, corresponded to four reattachment points. In contrast the numerical centerline profile only indicates three distinct reattachment peaks. The missing peak appears to occur between ($\mathbf{R_1}$) and ($\mathbf{R_3}$) in Schuricht's terminology (see Figure 5.46), which in the numerical profile is between ($\mathbf{R_2}$) and ($\mathbf{R_3}$). The existence of a fourth peak, which implies the presence of a fourth reattachment node on the centerline is very difficult to distinguish from the experimental centerline heat transfer profile in Figure 5.43. As the evidence is not conclusive, its existence is questionable.

To analyse the spanwise distribution in the surface heating due to flow reattachment on the plate, lateral or crossflow plots of (h/h_u) are taken at ($x/D = +1$), ($x/D = +5$) and ($x/D = +8$) downstream of the fin root, and shown in Figures 5.44 (linear scale) and 5.45 (logarithmic scale). Initial observations clearly show the lateral spread in the heating footprint with increasing distance downstream as seen earlier in Section 5.1.5. A comparison with the experimental results in Figures 5.44 and 5.45 clearly show an excellent agreement in spatial distribution of the peaks and valleys, but significant discrepancies exist in the magnitudes of the peaks.

At ($x/D = +1$) and ($x/D = +5$) it has to be highlighted that from the available experimental data the high heat flux associated with peak ($\mathbf{R_1}$) was unable to be measured because of limitations in the measurement technique and, the peak associated with ($\mathbf{R_2}$) in Figure 5.44:(**top**) and ($\mathbf{R'_2}$) in Figure 5.44:(**middle**) is an approximation, due to corruption in the data gathered [53].

The lateral heating profile at ($x/D = +1$) appears to show a near identical pattern to that observed on the centerline upstream of the fin. The peaks associated with ($\mathbf{R_1}$), ($\mathbf{R_2}$) and ($\mathbf{R_3}$) are matched in magnitude with the centerline result; however the peaks have moved apart when compared with the same centerline peak locations. A comparison cannot be made at ($\mathbf{R_1}$) because the peak could not be measured experimentally. The peak at ($\mathbf{R_2}$) appears to be over predicted and the peak at ($\mathbf{R_3}$) is underpredicted. However, a realistic comparison cannot be made for ($\mathbf{R_2}$) because, as highlighted earlier, the experimental

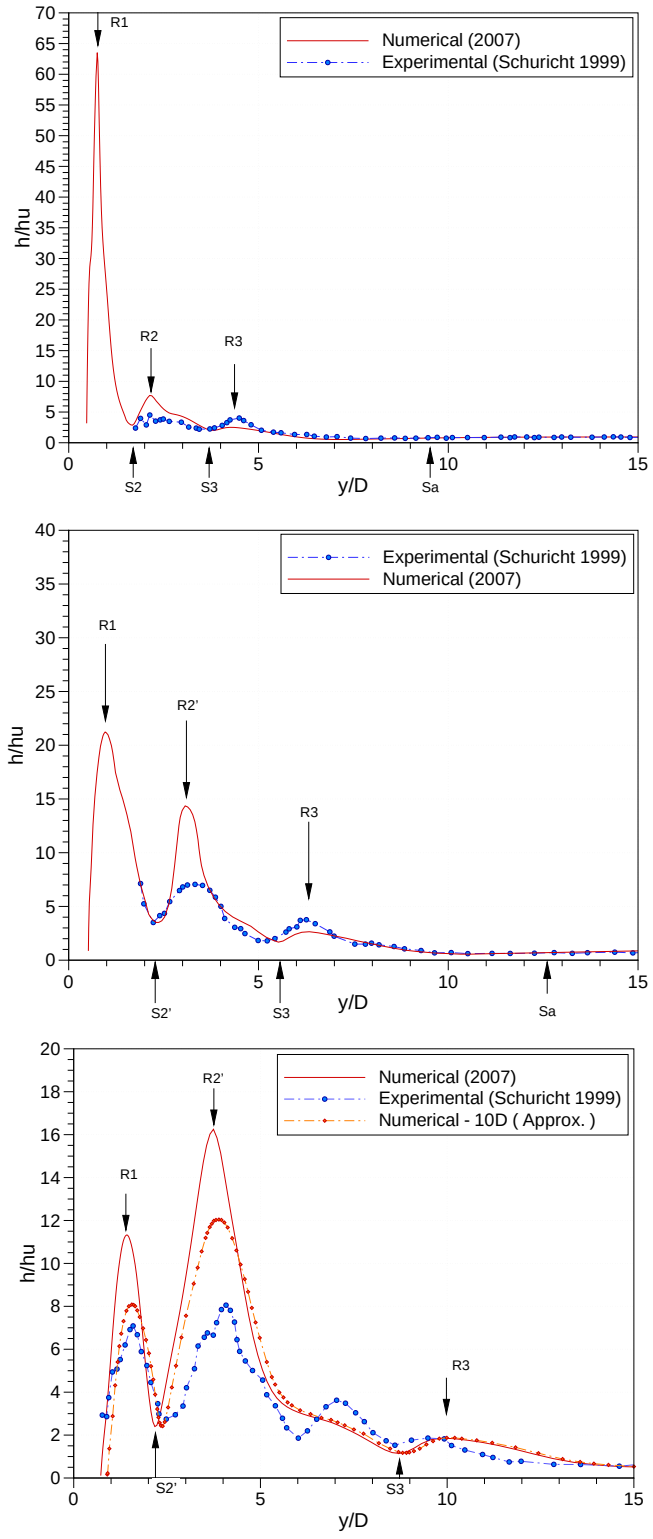

Figure 5.44: (**top**) Normalized linear heat transfer coefficient (h/h_u) laterally at $x/D = 1$ (**middle**) Normalized linear heat transfer coefficient (h/h_u) laterally at $x/D = 5$ (**bottom**) Normalized linear heat transfer coefficient (h/h_u) laterally at $x/D = 8$

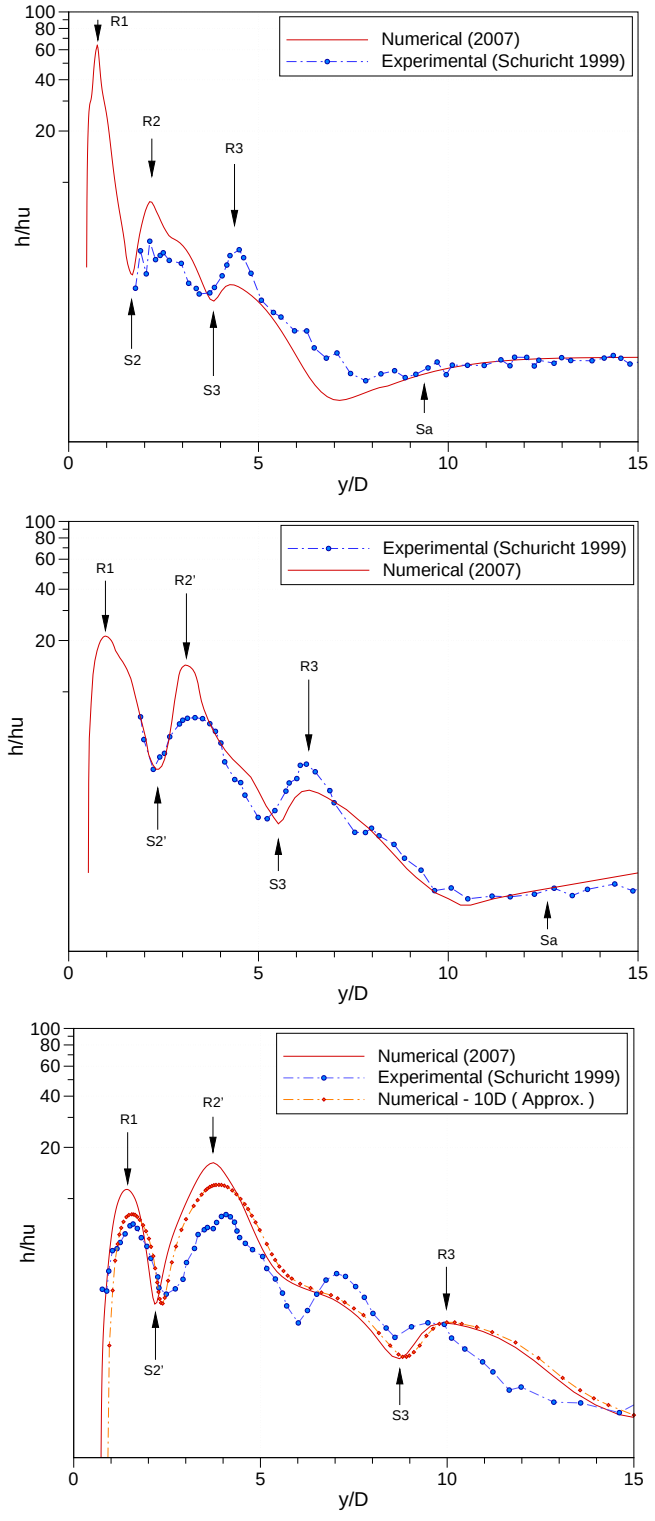

Figure 5.45: (**top**) Normalized logarithmic heat transfer coefficient (h/h_u) laterally at $x/D = 1$ (**middle**) Normalized logarithmic heat transfer coefficient (h/h_u) laterally at $x/D = 5$ (**bottom**) Normalized logarithmic heat transfer coefficient (h/h_u) laterally at $x/D = 8$

data associated with ($\mathbf{R_2}$) is an approximation.

A similar examination of the peaks at ($x/D = +5$) show a dramatic shift in the magnitude of the heat transfer coefficients. The most significant change is the decrease in surface heating at ($\mathbf{R_1}$), which records a 64% drop in magnitude whilst the second peak records a 75% increase. The peak at ($\mathbf{R_3}$) appears to be unchanged. The most severe surface heating due to ($\mathbf{R_1}$) is localised near the nose of the blunt-fin, after which further downstream, tends to decay considerably. This is most likely due to the strength of the supersonic jet impacting on the plate surface diminishing away from the blunt section of the fin. Secondly, the second peak at ($y/D = +3$) is no longer caused by the reattachment line ($\mathbf{R_2}$), because as discussed earlier in Section 5.4.2 this reattachment line disappears after ($x/D > +2$). This peak is now attributed to a new reattachment line ($\mathbf{R'_2}$) which was formed at ($x/D = +4$) as a result of flow separation due to a swept-shock interaction. Making a comparison with the experimental data at ($x/D = +5$) highlights similar differences to those observed at ($x/D = +1$). The peak at ($\mathbf{R_1}$) is still not captured experimentally, and the peak at ($\mathbf{R'_2}$) is again an approximation due to data corruption. However, as previously found, ($\mathbf{R'_2}$) is overestimated, and ($\mathbf{R_3}$) is still slightly underpredicted when compared to the experimental values. Experimentally the heat flux at ($\mathbf{R_3}$) was measured to be around ($h/h_u \simeq 3.5$), whilst the numerically calculated value for heat flux at ($\mathbf{R_3}$) is around ($h/h_u \simeq 2.5$). Similarly, at ($\mathbf{R'_2}$), the experimental heat flux was approximated to be around ($h/h_u \simeq 7$), and numerically the heat flux at ($\mathbf{R_3}$) is around ($h/h_u \simeq 14$).

Station ($x/D = +8$) represents the furthest point downstream of the blunt-fin leading edge modelled by the computational domain. The heating profile shows that the heat flux at ($\mathbf{R_1}$) has reduced considerably at ($x/D = +8$), when compared with ($\mathbf{R_1}$) at ($x/D = +5$) and ($x/D = +1$). In addition the heat flux at ($\mathbf{R'_2}$) appears to have increased in magnitude further downstream. The peak at ($\mathbf{R_3}$) appears to be the same as before. Comparing the heating profiles at ($x/D = +8$ and $+5$) indicate the existence of three distinct peaks associated with flow reattachment at ($\mathbf{R_1}$), ($\mathbf{R'_2}$) and ($\mathbf{R_3}$), very similar to the profile at ($x/D = +1$) in Figure 5.44:(**top**). A direct comparison cannot be made with the available experimental data since the experimental measurements were taken at ($x/D = +10$). However, to facilitate a comparison, extrapolating from the regression trend observed from previous heat flux profiles at other locations gives us an approximate

numerical profile at ($x/D = +10$) and this is indicated in Figure 5.44:(**bottom**).

The comparison at ($x/D = +10$), as shown in Figure 5.44:(**bottom**) appears to show the greatest variation in the heat flux between the measured experimental data and the calculated numerical results. However, as in the previous results at the centerline, ($x/D = +1$) and at ($x/D = +5$) the spatial distribution of the peaks and valleys is quite well matched. The numerical results at ($x/D = +10$) overpredicts the heat flux at (**R'$_2$**), but gives a closer match at peaks (**R$_1$**) and (**R$_3$**). The experimentally heat flux at (**R$_1$**) was measured to be around ($h/h_u \simeq 7$), whilst the numerical value for heat flux at (**R$_1$**) is around ($h/h_u \simeq 8$). Similarly, at (**R$_3$**), the experimental heat flux was approximated to be around ($h/h_u \simeq 2$), and numerically the heat flux at (**R$_3$**) is also around ($h/h_u \simeq 2$). The heat flux at (**R'$_2$**) from the experimental data is around (h/h_u) $\simeq 8$ and the same peak from the numerical results is around ($h/h_u \simeq 12$). This represents a 33% increase between the numerical and experimental heat flux measured at (**R'$_2$**). The experimental results in Figure 5.44:(**bottom**) appear to show a fourth peak in the heat flux profile at ($y/D \simeq 6.5$). In the numerical results there appears to be an observed rise in heat flux after (**S$_3$**) which occurs around ($y/D \simeq 8.5$), but its exact characteristics cannot be determined, and the profile is quite diffused.

A significant factor that could lead to overprediction of the heat flux at ($x/D = +10$), is the grid resolution at that location. A similar behaviour in the calculated heat flux is also observed in the grid dependency study in Section 5.1.4. It was shown that the cell size had a strong impact on the calculated Stanton number which was overpredicted near the leading edge and with most of the coarse grids studied. As a result it was concluded that the minimum grid cell ($\Delta x/\Delta y$) required for an accurate measurement of Stanton number, was (≤ 8). The current ratio of ($\Delta x/\Delta y$) is (≥ 11) in the grid cells at ($x/D = +10$) for distances of ($y/D > +5$). As a result an accurate comparison for the peak strength at (**R$_3$**) may not be possible and is the probable reason for the difference in magnitude.

Schuricht, after examining the centerline, lateral crossflow and plate surface heat transfer data along with the oil flow experiments, proposed a complex flowfield model containing eight horseshoe vortices, in four counter counter rotating pairs as shown in Figure 5.46:(**top**). The resultant separation and reattachment path of the flow on the plate

surface due to these vortices is shown in Figure 5.47:(**top**). The equivalent numerical models are also shown in Figure 5.46:(**bottom**) and Figure 5.47:(**bottom**) respectively. For the ease of comparison the notation used by Schuricht for labelling the vortices and subsequent separation and reattachment lines on the experimental results have been adopted on the numerical model. It is clear to see by comparing the two models that they share quite a significant amount of detail, however there also appear to have distinct differences.

The most significant difference between the two models is the presence of vortex pairs (SV_2) and (PV_2) as proposed by Schuricht. In the following analysis it was shown that the presence of this vortex pair could not be ascertained with any degree of certainty from the experimental centerline and ($y/D = +5$) heat transfer data. The possible existence of this vortex pair was indicated by the reattachment point seen in the ($y/D = +10$) lateral crossflow heating profile. However, this result is unique because Schuricht was unable to duplicate this finding with the 2.5mm diameter, and 7.5mm diameter blunt-fins that were also tested. This phenomenon could have come about as a result of subtle variations in flow (Re/l) in the tunnel, which causes the vortex arrangement in the separated flow to change from one structure to another; (see Chapter 2, Section 2.5.2). Variations in flow models put forward from conjecture through experimental data, and ones obtained through numerical analysis is common place. Further examples of conflicting models derived from experimental, and numerical methods can be seen in various other studies [45], [11], [60] and [5].

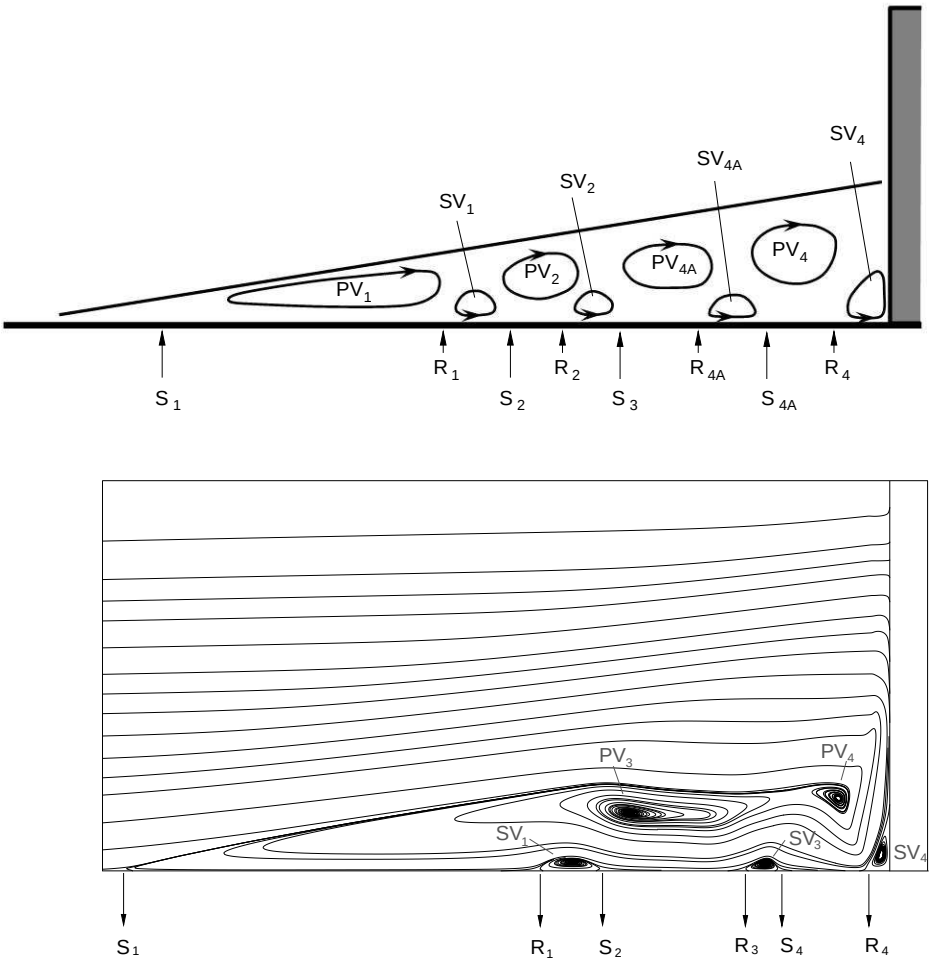

Figure 5.46: (**top**) Vortex profile suggested by Schuricht [53] on centerline (**bottom**) Numerically obtained Vortex profile along centerline

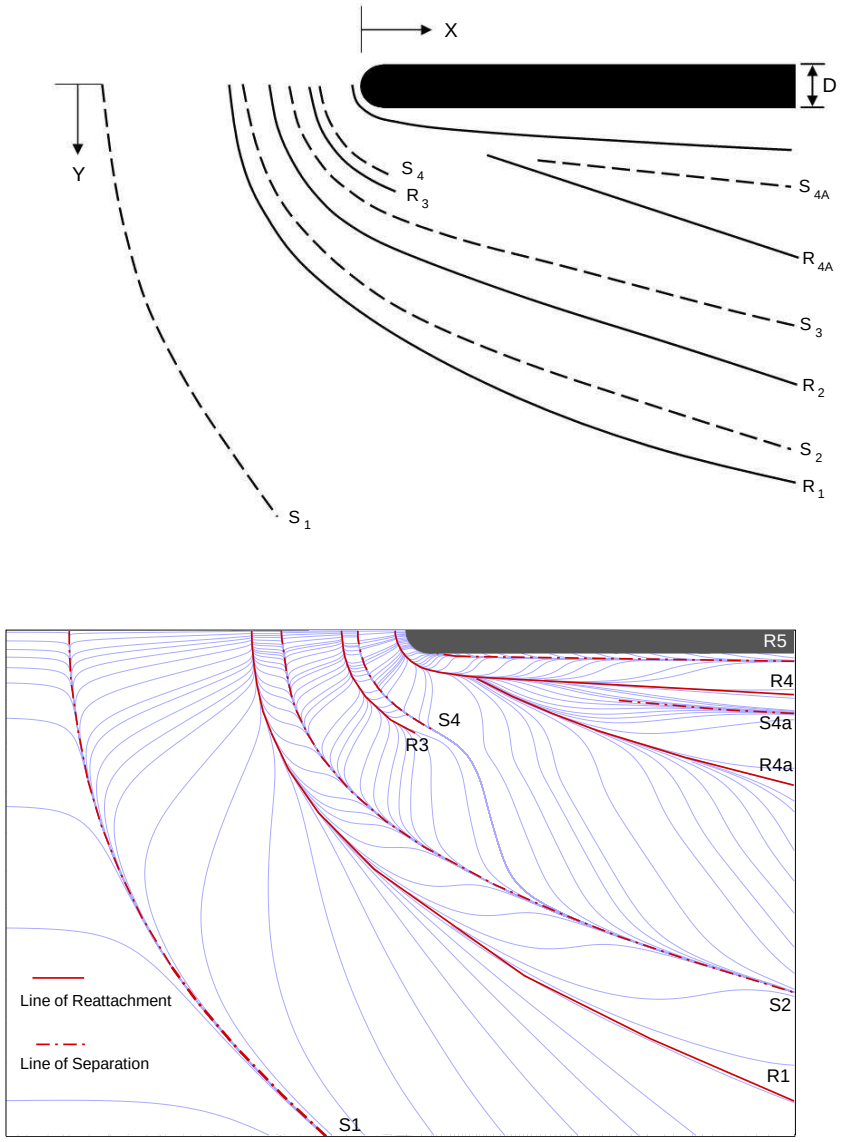

Figure 5.47: (**top**) Surface skin friction map suggested by Schuricht [53] on the flat plate (**bottom**) Numerically obtained Surface skin friction map on the flat plate

5.5 10mm blunt-fin simulations

The effect of fin leading edge diameter on the relative scale of the interference interaction for laminar as well as turbulent flows is well documented (see [17], [15]), with details of the salient effects described in Chapter 2 Section 2.5.2. However all the available data from previous parametric studies regarding effects of leading edge diameter are in the form of surface measurements, which can only indicate changes to surface variables and as a result only give an idea of changes to the relative size of the surface interaction footprint. These methods were unable to document the changes that would occur to the three-dimensional flow field structure, and as a result there is no available data describing such changes. Therefore, to investigate the impact doubling the leading edge diameter has on the three-dimensional interference flow field, simulations are carried out using an unswept 10mm diameter blunt-fin. The initial boundary conditions used for the numerical simulation are identical to that used for the 5mm diameter fin simulation. Length scales in the current set of simulations are non-dimensionalised with respect to ($D = 10mm$). Heat transfer coefficients are non-dimensionalised with respect to the undisturbed flat plate. With the fin height maintained at 25mm, the ratio of fin height to fin diameter is ($K/D = 2.5$). It was earlier stated that for the asymptotic behaviour condition to be fulfilled, ($K/D >$ 2.5). The current ratio is on this limit, and as a result there is a strong possibility the asymptotic condition might not be fulfilled for the 10mm diameter fin.

5.5.1 Grid Refinement Study

A grid dependency study similar to the one carried out for the 5mm diameter fin was undertaken for the 10mm diameter fin. The grids studied are shown in Table 5.7.

The effects on skin friction coefficient, Stanton number and pressure ratio on the plate surface along the line of symmetry for the different grids are presented. In addition, changes in the general flowfield structure as a result of grid refinement are also examined. For the purpose of easily identifying clear differences in the simulated results the plots for skin friction coefficient, Stanton number and Pressure ratio will only show variation in properties from (x/D = -25) to ($x/D = 0$).

Grid	Type
$58 \times 51 \times 45$	A1
$78 \times 72 \times 60$	A2
$116 \times 102 \times 90$	B1
$156 \times 144 \times 120$	B2

Table 5.7: The grids used in the mesh dependency tests

The density contours, and velocity streamlines from the plane of symmetry, for a selection of different grids are shown in Figures 5.48 & 5.49. As observed in the 5mm fin grid refinement study, successive grid refinement yields sharper inviscid and viscous features, such as shocks and boundary layer structures. The results indicate, as observed for the 5mm fin, a similar smearing in the leading edge shock as a result of the clustering criterion imposed. Primarily this loss in shock resolution is notably present in only the coarsest grids, A1 and A2, therefore accounting for the visibly lower leading edge shock angle in Figure 5.48:(**A**) compared to Figure 5.48:(**D**).

The variation in Stanton number along the line of symmetry, for the various grid densities is shown in Figure 5.50:(**top**). Also included in the plot is the theoretical Eckert solution for a flat plate. The dominant features of the profile are an ($x^{-\frac{1}{2}}$) decay away from the leading edge, followed by a pronounced dip at flow separation followed directly by a rapid rise with a range of peaks and troughs. This profile follows a similar pattern of variation to the one observed for the 5mm diameter fin. However, it is important to note distinctive differences between the 10mm and 5mm diameter fin result. In the 10mm results there appear to be 4 distinct peaks and troughs compared to 3 in the 5mm study. Furthermore, the drop in Stanton number at separation is far less pronounced in the 10mm result when compared to its 5mm counterpart. In addition, it is observed from the current set of simulations that there appears to be a larger difference between the finest 10mm grid results and the Eckert solution upstream of the separation point when compared with similar 5mm diameter fin results in the same range. For example, the Eckert value for Stanton number at a point (x/D = -20) is 0.0007, the value obtained from the finest 5mm grid at that location is 0.00074. This represents an approximately $\sim$5% increase. At the

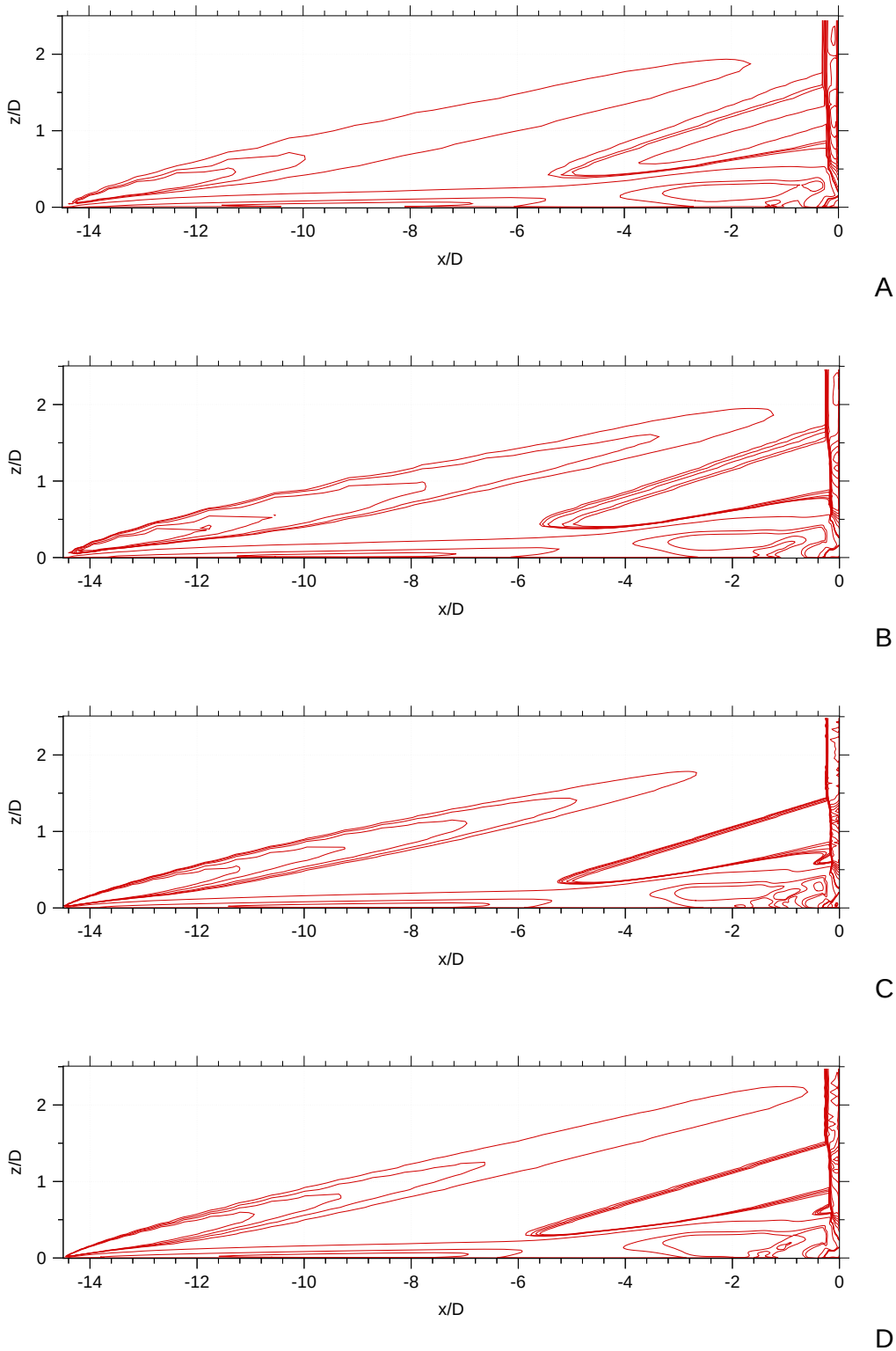

Figure 5.48: Density contours in the plane of symmetry for a range of (ρ) values: 0.0056 - 0.023 in increments of 0.001 (**A**) $58 \times 51 \times 45$ (**B**) $78 \times 72 \times 60$ (**C**) $116 \times 102 \times 90$ (**D**) $156 \times 144 \times 120$

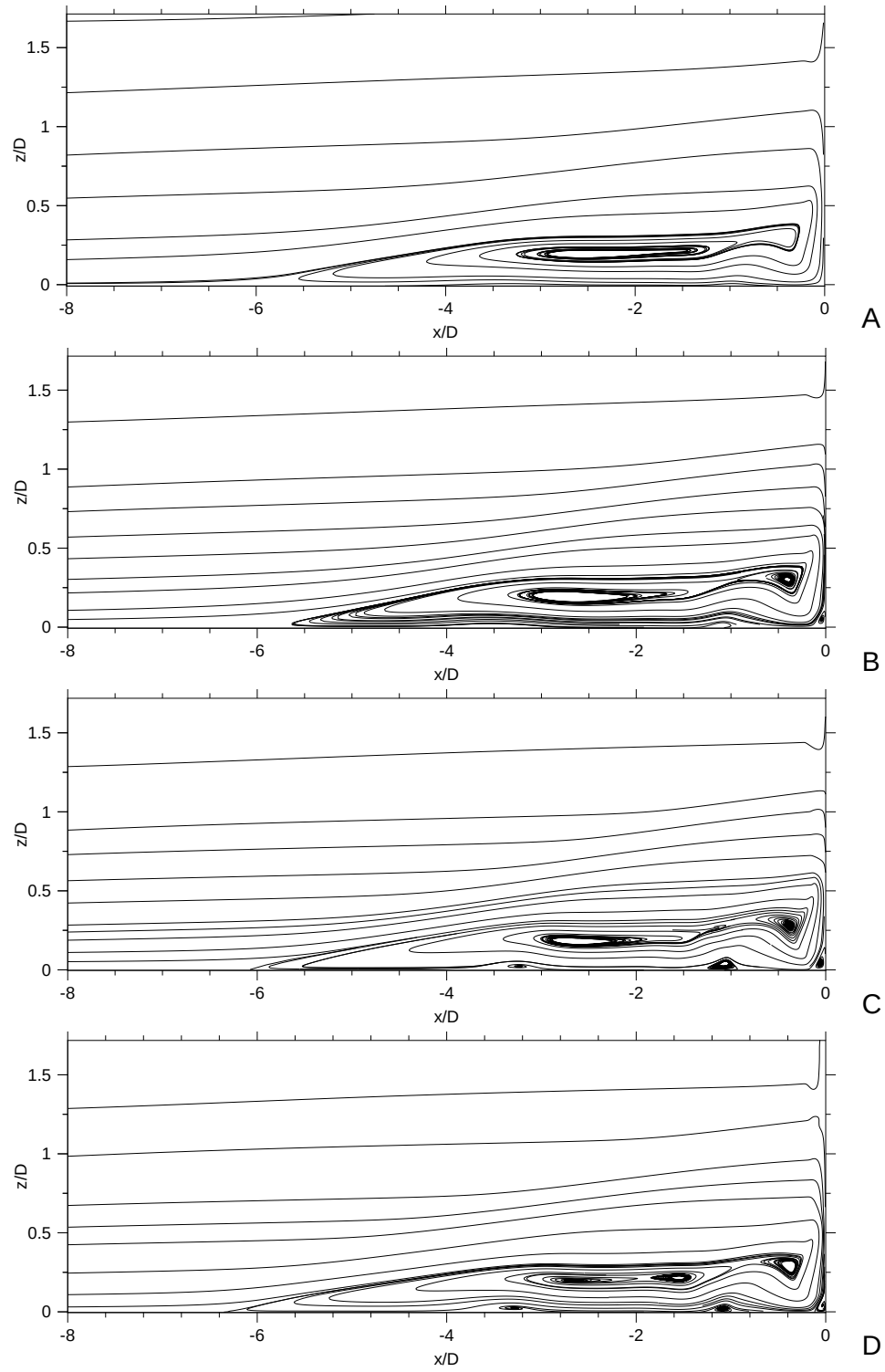

Figure 5.49: (**A**) Velocity streamlines $58 \times 51 \times 45$ (**B**) Velocity streamlines $78 \times 72 \times 60$ (**C**) Velocity streamlines $116 \times 102 \times 90$ (**D**) Velocity streamlines $156 \times 144 \times 120$

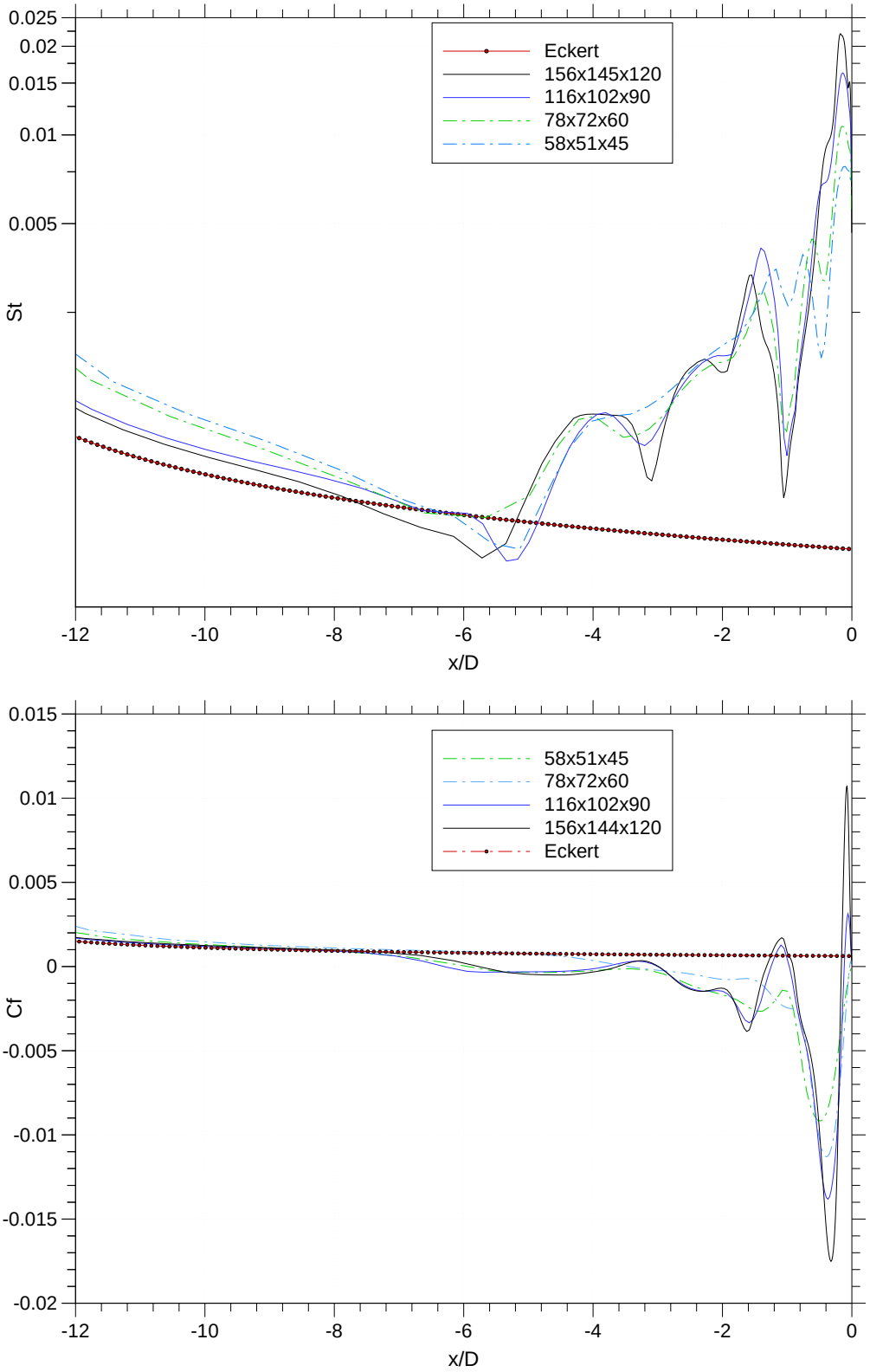

Figure 5.50: (**top**) Stanton number comparison for different grid densitites (**bottom**) Skin friction coefficient comparison for different grid densitites

same location, the value obtained from the 10mm grid is 0.0008, which represents a ∼13% increase. This would imply that the heat flux results obtained from the current crop of simulations will not be truly representative of the final state of the heat flux distribution on the flat plate for a 10mm diameter fin interaction. This is clearly visible from the Stanton number plot where they clearly overpredict the Stanton number near the leading edge, and at positions close to the fin root there still appears to be some variation in the magnitudes of the recorded peaks between the two finest grids studied, the $(116 \times 102 \times 90)$ and $(156 \times 144 \times 120)$. This clearly indicates the significant impact of the cell size on the calculated Stanton number as found in the 5mm diameter fin study.

A comparison of the skin friction coefficient along the line of symmetry Figure 5.50:(**bottom**), appears to show a similar variation to the pattern observed in the Stanton number profile and previous skin friction coefficient profiles for the 5mm diameter fin. The main differences in the current profile is the larger separation length and the lower values of skin friction in the peaks and troughs, specifically close to the fin root. Similar to the results of the 5mm fin, (C_{fw}) is overpredicted near the leading edge indicating a similar relationship to cell size as found with the Stanton number comparison in Figure 5.50:(**top**) and previous results. The skin friction profile only indicates three distinct separation and reattachment points when compared to the Stanton number profile in Figure 5.50:(**top**). The location of the fourth peak in Figure 5.50:(**top**) occurs at $(x/D$ = -4), looking at the equivalent point in Figure 5.50:(**bottom**) appears to indicate an increase in (C_{fw}), however since $(C_{fw} \neq 0)$ it cannot be definitively characterised as a further singularity. As a result it is not considered to be another separation/reattachment point.

Grid	Type	x_s/D
$58 \times 51 \times 45$	A1	-5.575
$78 \times 72 \times 60$	A2	-5.760
$116 \times 102 \times 90$	B1	-6.130
$156 \times 144 \times 120$	B2	-6.250

Table 5.8: Separation lengths for different 10mm diameter blunt-fin grids

The variation in the non-dimensionalized primary separation length for the different grids is shown in Table 5.8. The expected scaling in separation length with successive grid refinement is clearly visible from Table 5.8. The results from the table clearly show that the separation length has not converged with finest grid simulated.

A comparison of the non-dimensionalzied separation length (x_S/D), between the 10mm and 5mm fin interaction reveals some notable differences. Comparing the separation lengths from 10mm grid *B1* ($116 \times 102 \times 90$) and *B2* ($156 \times 144 \times 120$), with the respective separation lengths from 5mm grid *B2* ($116 \times 102 \times 90$) and *C1* ($172 \times 160 \times 144$), reveals a 18.1% and 17.04% decrease in (x_S/D). The result appears to indicate a decrease in the non-dimensionalized separation length with an increase in fin diameter. A similar decrease in the non-dimensionalzied separation lengths in the 5mm and 7.5mm diameter unswept fin interaction was observed by Schuricht [53] in his experiments.

However, it has to be noted that the final separation length from the current crop of 10mm grids have not yielded a converged value. Further complicating the matter is the possibility that the asymptotic criterion might not have been met in the current simulation, and the final separation length could change with a change in fin height (K). To verify the theory of a decrease in the non-dimensionalized separation length with an increase in fin diameter, further investigation with a finer grid is recommended.

The pressure profile shown in Figure 5.51 is very similar to that observed in the 5mm case, the only difference being that the pressure rise appears to begin further upstream of the fin root at (x/D = -15), compared to (x/D = -10) in the 5mm case. This observation is consistent with the earlier finding of an increased separation distance. Also highlighted in Figure 5.51 is the additional localised but small pressure peak at (x/D = -4).

The grid dependency study has shown that the present set of grids used will not produce a grid independent solution for the 10mm blunt-fin. It is clear that with further grid refinement there is the potential to get a more accurate solution. It would appear that the following sets of type B grids, might have to be doubled to get a set of type C grids to really offer the chance of achieving a grid independent solution.

However for the purpose of qualitatively comparing surface heat transfer distribution and

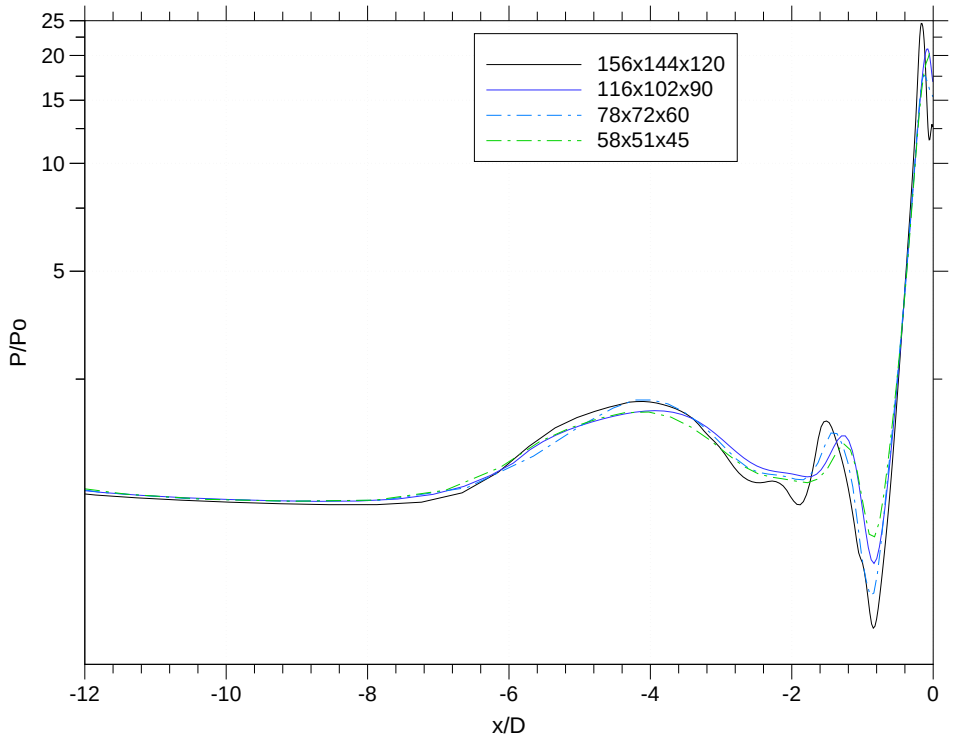

Figure 5.51: Detail of Pressure comparison for different grid densitites

any differences attributed to fin diameter in the scale of the interaction between the 5mm and 10mm diameter fins, the numerical results from grid $(156 \times 144 \times 120)$ will be able to provide a reasonably accurate comparison.

5.5.2 General Flow Features of 10mm blunt-fin

The structure of the flowfield in the axis of symmetry for the 10mm blunt-fin interaction bears remarkable similarity to the flow structure observed in the 5mm study.

The shock structure from analysing the density contours (see Figure 5.52), clearly capture the leading edge shock, shock induced boundary layer separation shock, and fin bow shock. The magnitude of the non-dimesionalized bow shock stand-off distance (Δ/D) for the 10mm interaction is very similar to what is observed in the 5mm fin interaction, $(\Delta/D \simeq 0.3)$.

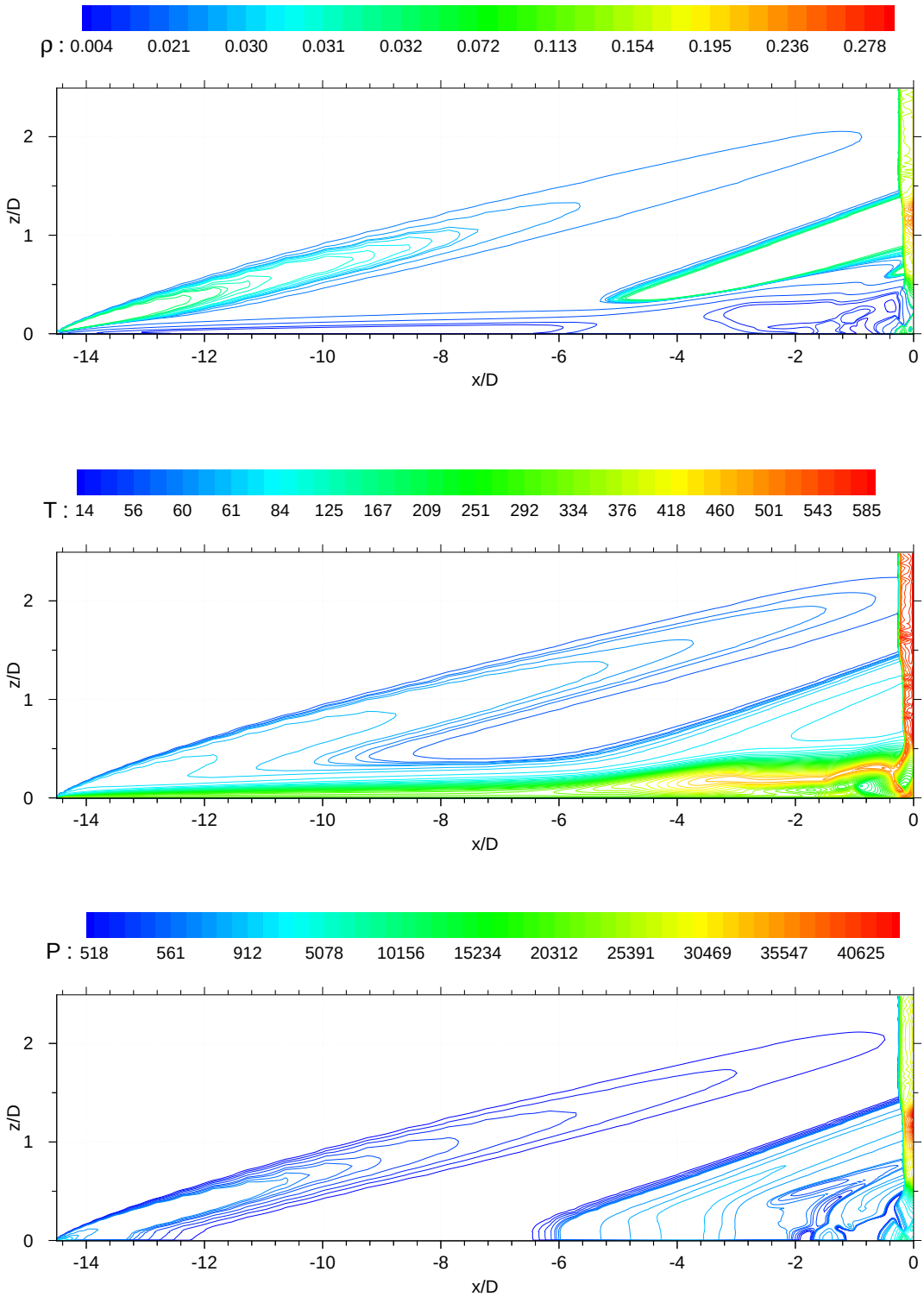

Figure 5.52: (**top**) Density contours (**middle**) Temperature contours (**bottom**) Pressure contours

The kinks in the bow shock are a good indicator of shock/shock interaction points, and from Figure 5.52 it is clear to see two distinct points of interaction at ($z/D \simeq 2.75$) and ($z/D \simeq 1.25$). The flow in the separated region appears to indicate further complexities in its structure with large density gradients visible throughout the separation bubble. A region of flow just behind the primary shock/shock interaction point at ($z/D \simeq 2.75$) appears to indicate an area where there is large variation in density. This is very similar to what was observed for the 5mm fin where it was discovered that these large density gradients were caused by an impacting supersonic jet, the result of an Edney type IV interaction. A similar region of large density gradients exist very close to the root of the fin/plate attachment location.

The temperature contours in Figure 5.52 clearly outline the extent of the thermal boundary and shear layers. The two bubbles of relatively cooler gas, close to the leading edge of the blunt-fin highlight the the embedded supersonic zones similar to the 5mm fin study. The presence of the second separation shock is barely visible in the temperature contours. The pressure contours clearly show the three main shock structures, leading edge, separation and detached bow shock. Also indicated by the clustered contour lines is the second separation shock, just below the primary separation shock. The pressure profile also indicates a region of high pressure behind the primary shock separation/bow shock interaction point.

A table with some geometrical constants for the 10mm diameter fin flow field is shown in Table 5.9. The boundary layer height used for comparison in the table below is the undisturbed boundary layer height measured 145mm from the leading edge, ($\delta = 3.48mm$), ($z/D = 0.696$).

$Type$	D/δ	K/δ	K/D	K/K_{tp}
5mm - Numerical	1.44	7.18	5	3.24
10mm - Numerical	2.87	7.18	2.5	1.85

Table 5.9: Fin dimension relationships

Given the height of the fin remains constant at 25mm, the (K_{tp}) for the 10mm fin is

calculated to be ($K_{tp} = 13.51$). Comparing this with the 5mm fin which has a ($K_{tp} = 7.72$), reveals a 43% increase in the height of the triple point. This appears to show that although the non-dimensional separation length is smaller in the 10mm fin interaction, the physical size of the separated region in relation to the flat plate and model is larger than the 5mm fin. As highlighted earlier, the current (K/D) ratio is very close to the minimum value quoted for asymptotic behaviour. To verify the fact that the criterion holds for the current analysis, it is necessary to analyze the surface heat transfer rates; this is carried out later in this chapter. With a ($D/\delta = 2.87$) the 10mm fin would still be classed as a 'short' protuberance (see Chapter 2, Section 2.5.2), and the heating distribution dictated by the ratio (K/δ). Since the (K/δ) ratio in Table 5.9 is the same as the ratio for the 5mm fin, it is expected that both heating distributions would be very similar.

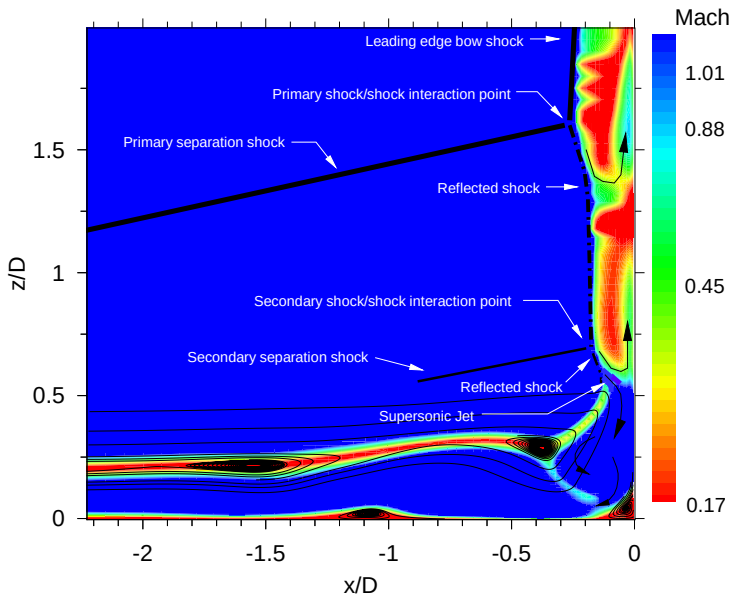

Figure 5.53: Embedded supersonic zones within the separated region in the 10mm interference flowfield

Figure 5.53 shows the Mach contours for the (x/D) range indicated. For the purpose of identifying the relevant features the Mach contours plotted in Figure 5.53 only show regions below ($M < 1$); regions where the Mach number is > 1 are highlighted in a dark blue colour. Clearly outlined are the two supersonic bubbles embedded within the

recirculation zone. The second supersonic jet from the second shock/shock interaction can be clearly seen, with the path of the high speed gas outlined by the black arrows. The primary supersonic jet does not appear to be well captured; however the path of the gas can be seen from analysing Figure 5.53, and is marked by the black arrow.

Pattern of Separated Flow

The plate surface skin friction lines for the 10mm fin interaction describe a field very similar to the surface skin friction field observed for the 5mm fin. The primary separation saddle, (s_A), is highlighted as the point furthest outward from the root of the blunt-fin in Figure 5.54. Through (s_A) goes the separation line towards which the skin friction lines converge. The separation line is strongly deflected when it encounters the freestream as shown in Figure 5.54. There is a node of reattachment right at the base of the blunt-fin (n_1). Through (n_1) goes the attachment line from which the skin friction lines diverge. In addition their are two other distinct pairs of separation saddles and reattachment nodes (s_2, s_3) and (n_2, n_3), originating from the centreline Figure 5.54. A nodal point of separation and reattachment (s_2', n_2') originates close to the reattachment line ($\mathbf{R_1}$). In addition there is another nodal point of separation (s_4) near the side surface of the fin. The number of saddles and nodes is identical to the 5mm fin *(3 saddles and 3 nodes)*.

The main difference between the two surface topologies is the relative spacing between the sets of separation and reattachment pairs. In the 5mm surface skin friction field in Figure 5.19 the primary separation point (s_A) is located considerably further upstream compared to separation points (s_2, s_3) which are relatively much closer together and nearer the fin. When a similar comparison is made in the 10mm surface skin friction field, it is clearly evident that all separation points are evenly spaced, in particular (s_3) which has moved further upstream.

The streamlines in the symmetry plane for the 10mm flowfield are shown in Figure 5.55: the diffused spanwise vorticity of the incoming boundary layer is organised in three primary vortices (foci F_1, F_2 and F_3); and secondary vortices (foci F_1a, F_2a and F_3a) separate from the bottom surface, and concentrate the vorticity of opposite sign generated on the bottom surface by the reverse flow.

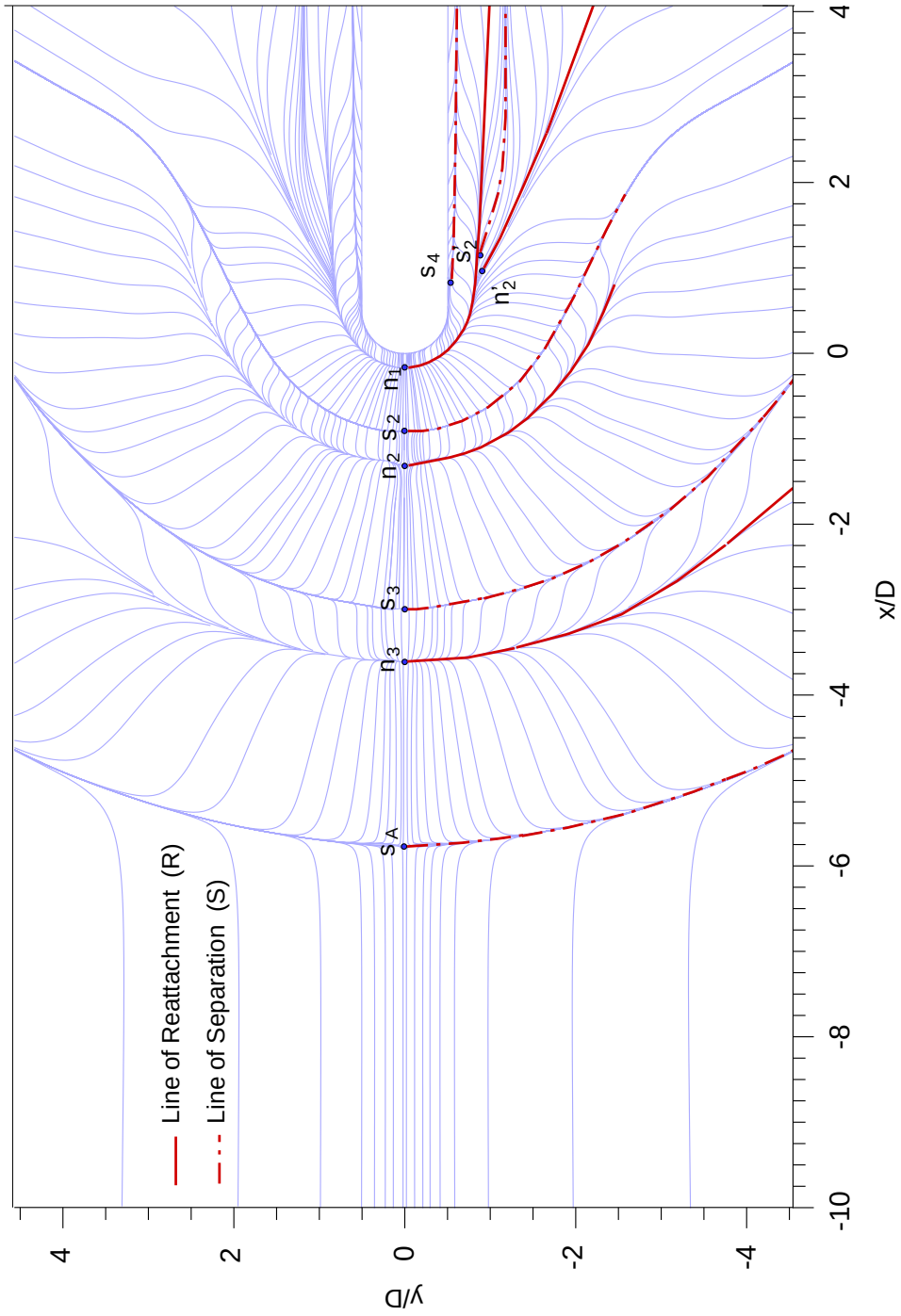

Figure 5.54: Surface skin friction streamlines on flat plate with highlighted separation and reattachment lines. A separation saddle is denoted by *(s)* and a reattachment node by *(n)*

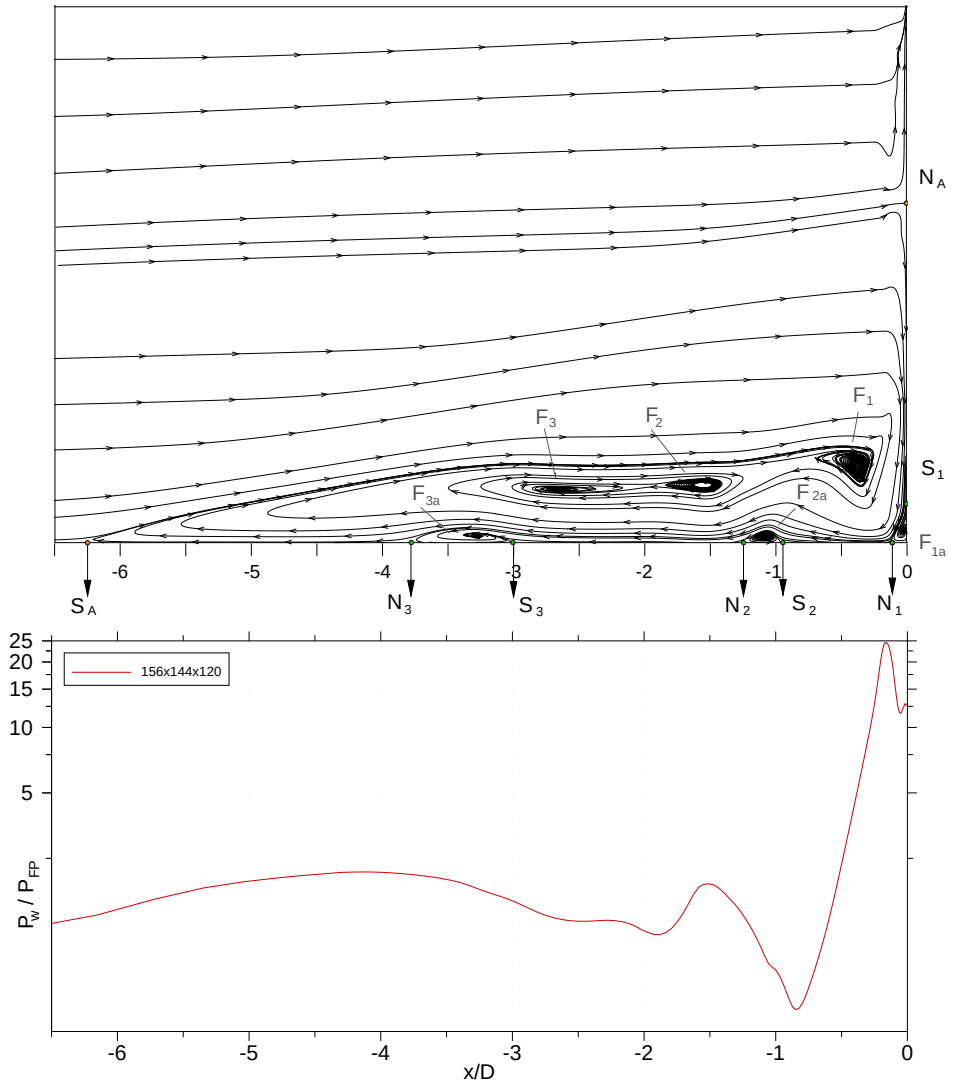

Figure 5.55: (**top**) Particle streamlines in profile plane at location A (**bottom**) Plate surface pressure

The vortex structure within the separation bubble is very similar to the structure observed in the 5mm fin study. The primary difference is the bifurication of vortex (F_2), found within the recirculation zone of the 5mm interaction (see Figure 5.20). This main vortex breaks into vortices (F_2) and (F_3) as observed in Figure 5.55. The main reason for this bifurication would appear to be the presence of a pressure rise at ($x/D \simeq$ -4) as shown in the wall pressure profile. The flow encountering this adverse pressure gradient induces the primary vortex to bifurcate to form two separate cores, as seen in Figure 5.55. As the pressure rise increases in the upstream direction, it results in tertiary separation at (S_3)

seen at ($x/D \simeq$ -6) similar to the process that caused secondary separation. The flow reattaches itself further upstream at node (N_3). These secondary and tertiary separation and reattachments leads to the formation of two secondary vortices.

Cross flow section profiles, (Profile **D** - **F**) taken at (x/D = +1, +2.5 and +4) shows the flow structure in the lateral extent of the 10mm interaction. Examining the Mach, density and streamline profiles in Figures 5.56- 5.57 indicate a very similar flow field structure to the one observed in the 5mm fin study. The main shock features which consist of the normal bow shock, separation shock and reflected shock are well captured. The normal shock which was clearly defined in the 5mm case at (x/D = +4) is poorly resolved in the 10mm fin at the same location. However its presence is indicated by the streamlines in Figure 5.57:(**F**). The most outstanding difference between the two different fin diameter interactions is the lateral extent of the separated region, and the separation shock/normal shock interaction point, which for the 10mm fin is larger than in the 5mm case. The flow within the separated region close to the flat plate exhibits similar characteristics to the features discovered in the 5mm case. The presence of a supersonic zone in an other wise subsonic flow is present in Figure 5.56.

The streamline profiles in sections (Profile **D** - **F**) indicate the growth of the corner root vortex as this feature evolves downstream from its inception point at the junction of the fin leading edge. A noticeable omission in the section streamlines is the presence of the vortices that originated from the fin centerline. The most probable cause for the loss of detail in the inviscid/viscous structures found in the regions ($y/D > 5$) is the lack of grid points, beyond ($y/D > 5$) the grid becomes very coarse with the cell size exceeding the size of some the features themselves, and since these structures are quite small, the grid clustering in that region will be unable to resolve such fine features.

Figures 5.59 and 5.58 give a good representation of the three-dimensional vortex structure surrounding the 10mm fin. The similarities in the vortex flow field between the present 10mm interaction and the 5mm interaction (see Figures 5.32 and 5.33) can clearly be seen in the following Figures. A close examination of Figure 5.58 appears to show that vortex with foci (F_2a) suffers a similar fate as its counterpart in the 5mm interaction, where this feature diffuses into the surrounding incoming flow due to its inability to entrap

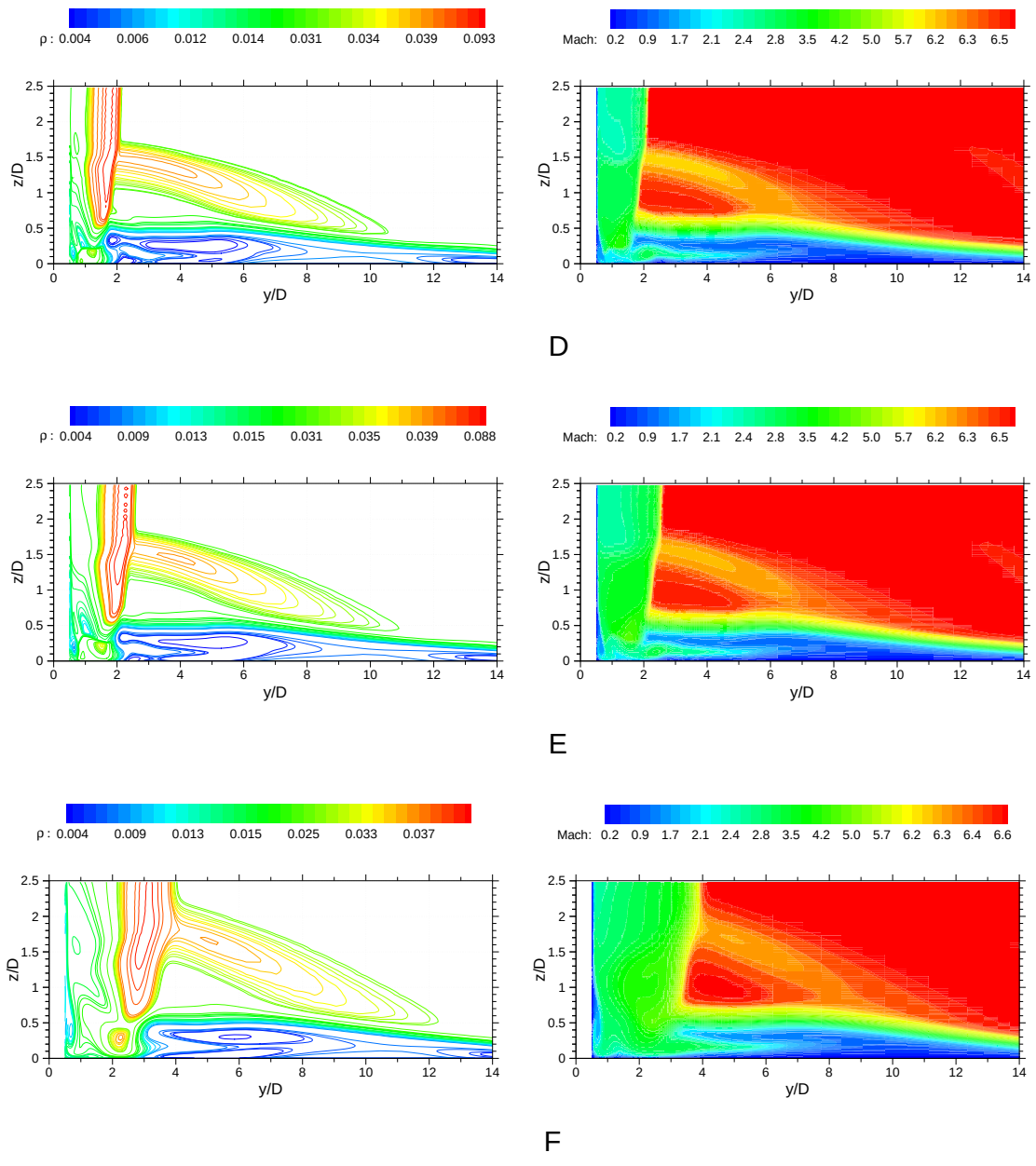

Figure 5.56: Cross plane density and Mach number contours in profile planes D - F

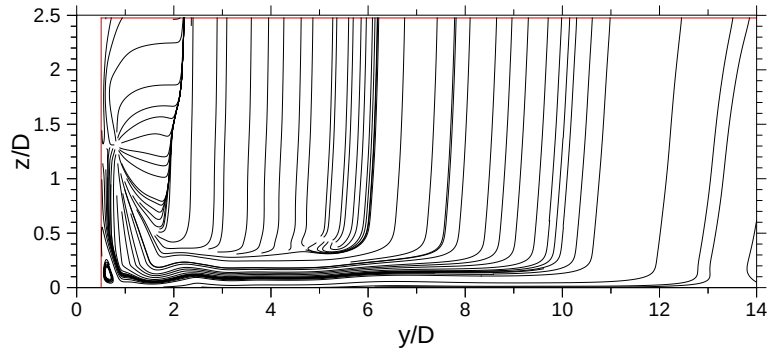

D

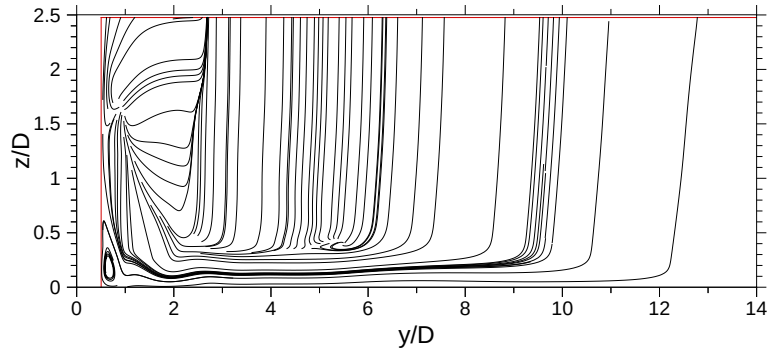

E

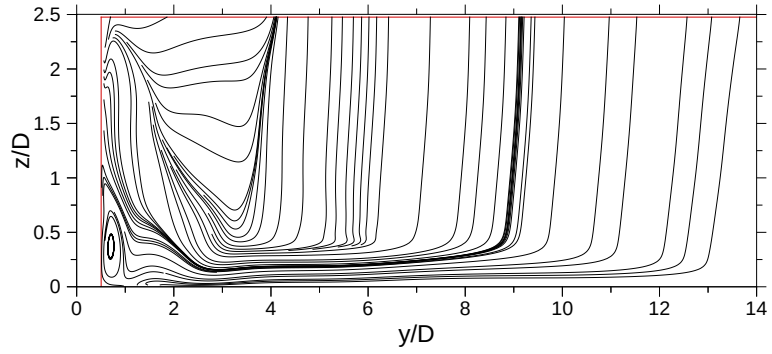

F

Figure 5.57: Cross plane particle streamline paths in profile planes D - F

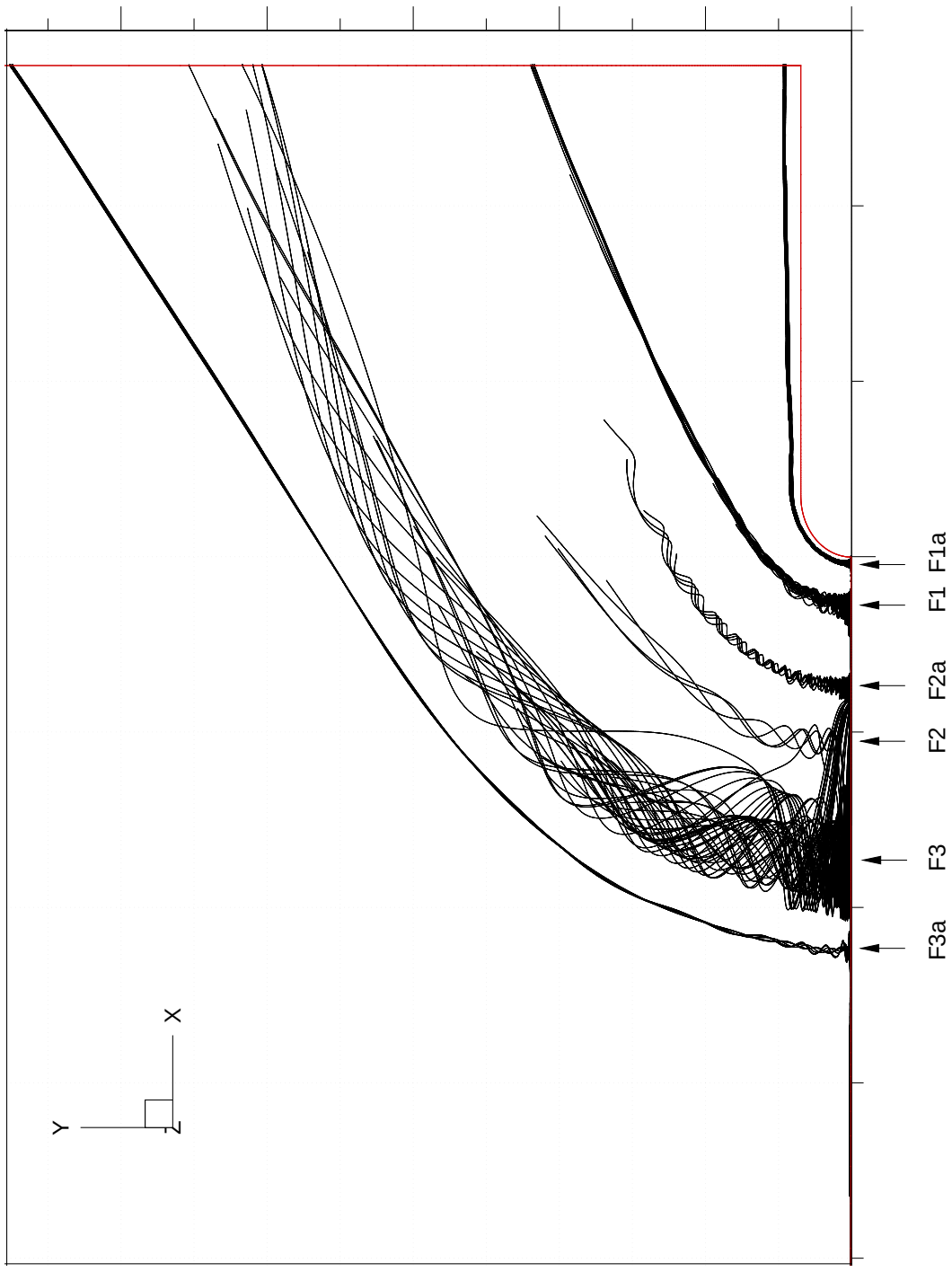

Figure 5.58: Top-plan view of horseshoe vortices

additional gas because of low rotational momentum. Another important observation that can be made from Figure 5.58 is that vortex (F_2) appears to merge with vortex (F_3) further away from the fin symmetry line, to form a single core, and does not appear to evolve around the fin as an independent vortex. In addition, it appears that the primary vortex core is considerably larger in the 10mm study when compared to its 5mm twin, this is an expected result given the fact that the separated region is considerably larger in the 10mm case.

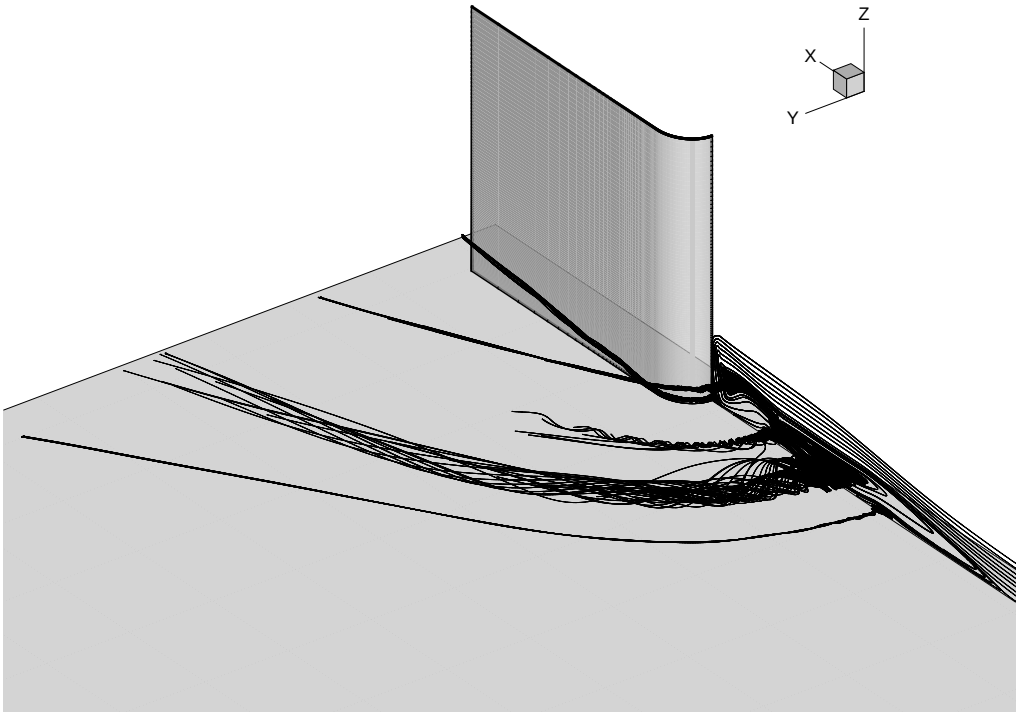

Figure 5.59: Three-dimensional horseshoe vortex paths around the fin

5.5.3 Surface Heating on Plate

In order to investigate the interaction scaling effects of fin diameter, the non-dimensionalised heat transfer coefficient maps for the 5mm, 10mm and 7.5mm fin interaction are compared in Figure 5.60. The 5mm and 10mm (h/h_u) maps in Figure 5.60 have been numerically generated whilst the 7.5mm (h/h_u) heat transfer coefficient map is obtained from the experimental results of Schuricht [53]. As with the (h/h_u) map of the 5mm interaction,

distances on the 10mm (h/h_u) map have been non-dimensionalised with respect to the 10mm fin.

A qualitative comparison of the surface heating distributions in Figure 5.60 confirms that all the unswept fin types generate a very similar heat flux profile. Clear similarities in the general shape and location of the increased heating bands are visible. The most dominant difference that appears between the 10mm, 7.5mm and 5mm fin diameter interactions is the increasing size of the thermal interaction footprint with increasing diameter. Figure 5.60:(**top**) which shows the 10mm fin displays the largest, broadest surface interaction.

The three profiles in Figure5.60 clearly show that the fin leading edge diameter is the major scaling factor for the blunt-fin interaction as the extent is approximately similar in each profile. This confirms the experimental observations of Schuricht [53] and, Hung and Clauss [36]. The heating profile from the 10mm interaction appears to indicate that the height of the 10mm fin is sufficient to produce an asymptotic result.

A quantitative analysis of the heat transfer coefficient field in Figures 5.60:(**top**) and 5.60:(**bottom**), appear to show considerable similarity in the range of values measured across the interference zone. Apart from the maximum recorded value for the 10mm case; which at the base of the fin plate junction is around $(h/h_u)_{max} \simeq 50$, the general magnitude of the enhanced heating bands surrounding the fin are generally similar to what was found in the 5mm interaction.

The maximum for the 10mm fin is somewhat lower than the $(h/h_u)_{max} \simeq 60$ recorded for the 5mm fin. Although the limitations of the current grid were highlighted in Section 5.1.1 in the current chapter, it is unlikely to be the reason for this discrepancy. It has to be noted that Schuricht [53] observed a similar difference between the 5mm and 7.5mm results in his experimental work. A possible reason could be that the supersonic jet impacting the plate surface, which is partly responsible for the extremely high values being recorded, could be weaker in the 10mm interaction.

An overall synopsis of the surface results in Figures 5.60 leads to the conclusion that, changes in fin leading edge diameter do not appear to significantly influence the magnitude of heat transfer within the interference zone. This agrees with the findings of Hung and

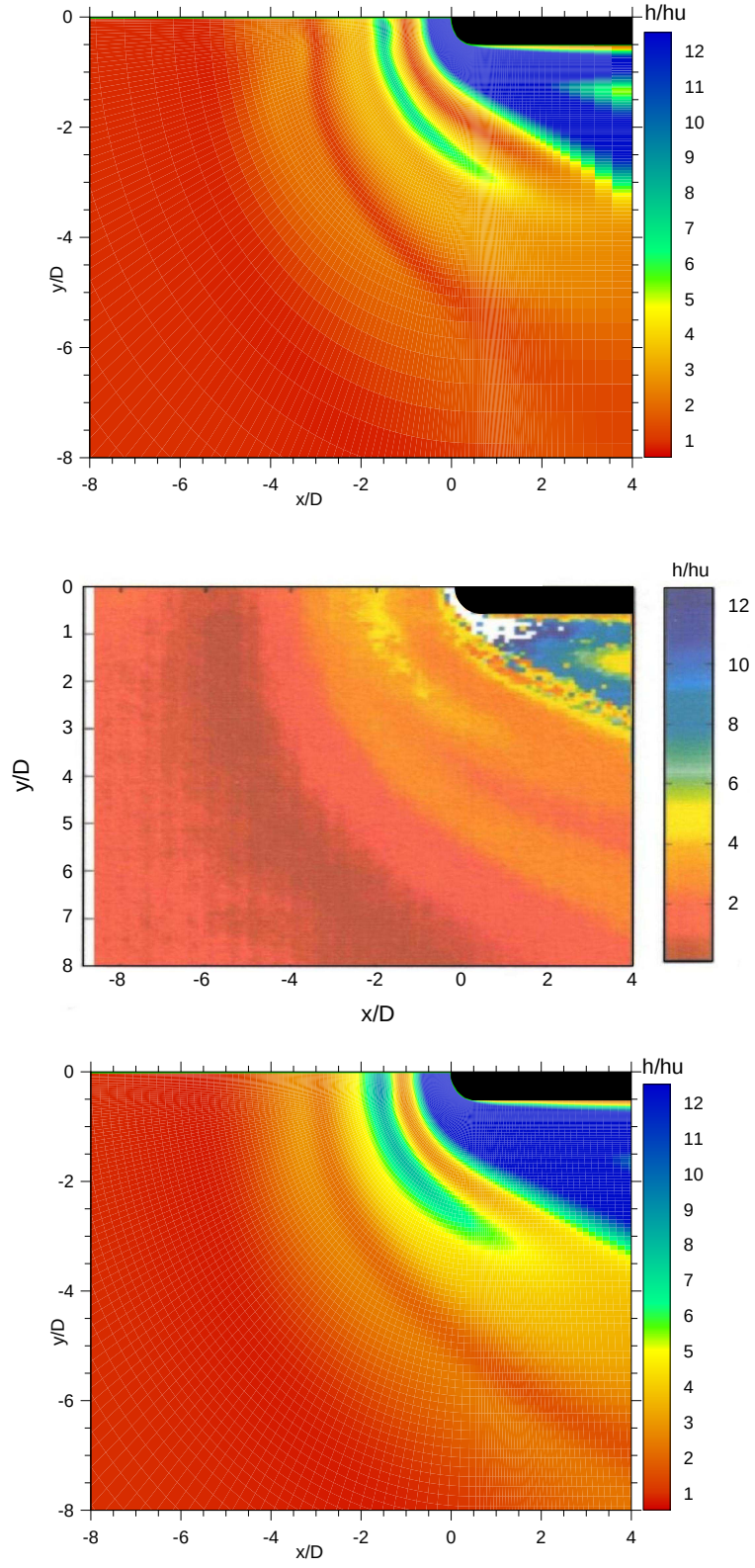

Figure 5.60: (**top**) Numerical normalised plate surface heat flux for 10mm fin (**middle**) Experimental normalised plate surface heat flux for 7.5mm fin (**bottom**) Numerical normalised plate surface heat flux for 5mm fin

Clauss [36], where the heating distribution will be primarily dictated by the ratio (K/δ), since this ratio is the same for both fin types it was expected that the heating rates too would be the same.

A closer examination of Figure 5.60:(**bottom**) also appears to show, straddled between the two outer enhanced heating bands, the presence of another possible increased heat flux band slightly upstream of the increased heat flux band attributed to $(\mathbf{R}_2)$. A better understanding about the origins of this feature can be found by examining the centerline and crossflow (h/h_u) profiles.

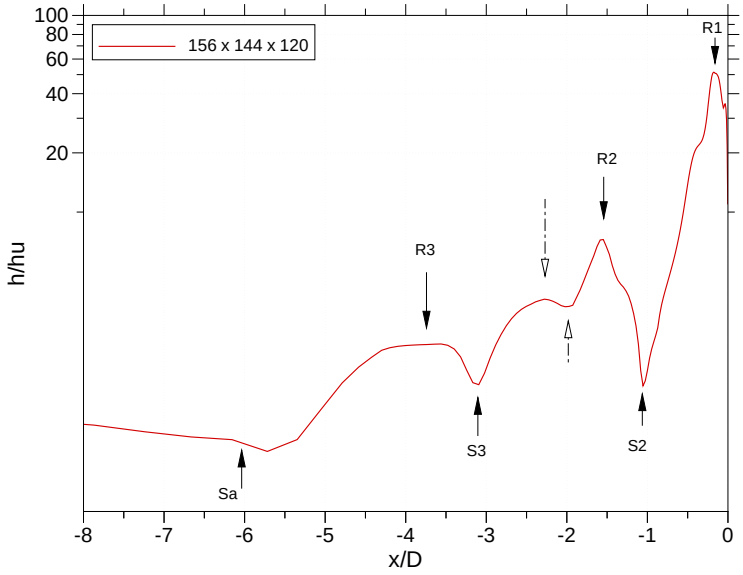

Figure 5.61: Normalized linear heat transfer coefficient (h/h_u) along the axis of symmetry

The numerical centerline (h/h_u) profile, shown here in Figure 5.61, reveals three distinct increased heating peaks associated with three flow reattachment points on the surface of the plate. The location of these peaks and valleys are consistent with the flow topology suggested by the surface skin friction streamlines in Figure 5.54, and symmetry plane velocity streamlines of Figure 5.55. The reattachment nodes in the skin friction topology map were labelled (n_1), (n_2) and (n_3) respectively, with (n_1) equating to the location where $(h/h_u)_{max}$ occurs, closest to the blunt-fin root. The magnitude of the peaks increase as the fin root is approached. The highest heating coefficient occurs at (n_1), where $(h/h_u)_{max}$ $\simeq 52$.

The crossflow spanwise distribution in surface heating at ($x/D = +1$) and ($x/D = +4$) for the 10mm interaction is shown in Figure 5.62. The profiles exhibit close similarities to what was observed on the 5mm interaction at ($x/D = +1$) and ($x/D = +5$) (see Figure 5.45).

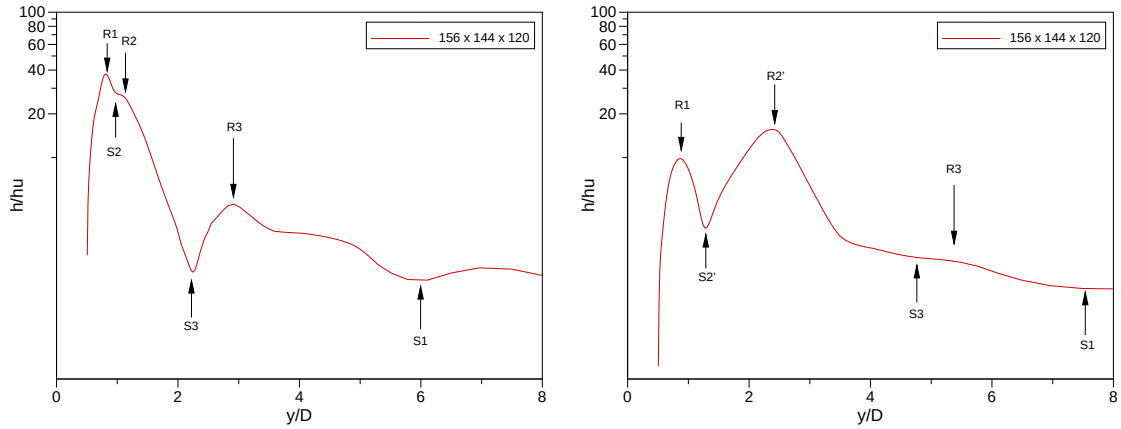

Figure 5.62: (**left**) Normalized linear heat transfer coefficient (h/h_u) laterally at $x/D = +1$ (**right**) Normalized linear heat transfer coefficient (h/h_u) laterally at $x/D = +4$

The lateral extent of the interaction does not appear to scale exactly with fin leading edge diameter. In particular, it can be observed that, at ($x/D = +1$), the peak in heat flux associated with the reattachment points ($\mathbf{R_2}$) and ($\mathbf{R_3}$) for the 10mm interaction appear at ($y/D \simeq 1$) and ($y/D \simeq 3$). The same reattachment points on the 5mm interaction appear at ($y/D \simeq 2$) and ($y/D \simeq 4$) respectively. Secondary factors which might influence the lateral scale of the interaction (which include the effect of boundary layer growth over the fin and asymptotic height of the fin) suggest that the lateral scale ought to be greatest for the small fin and least for the largest fin (turbulent-boundary layer fin flow by Haq [28] confirms this). It appears the crossflow numerical results between the 5mm and 10mm fins support this theory.

The centerline profile also suggests the existence of a fourth peak (indicated by the hollow arrows) at (x/D = -2.3). This location corresponds with the enhanced heating band seen earlier on Figure 5.60:(**top**). Although this feature is clearly visible on the centerline heating profile, its physical manifestation in the interference flowfield, primarily a separation and reattachment point, are missing in the surface skin friction streamlines in Figure 5.54,

and symmetry plane velocity streamlines of Figure 5.55. The absence of a separation bubble on the plate surface is further corroborated when the centreline skin friction profile is analysed in Figure 5.63.

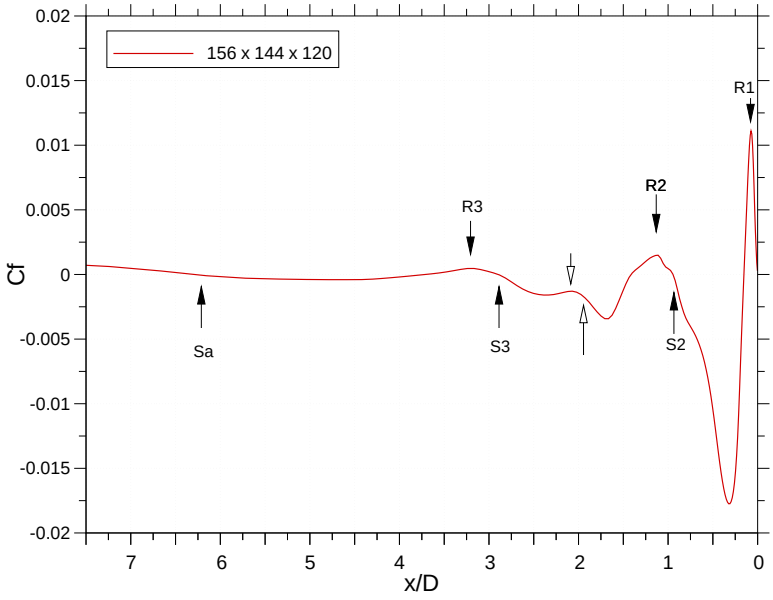

Figure 5.63: Skin friction coefficient along the axis of symmetry

Figure 5.63 clearly shows that the skin friction coefficient in the region of interest does not reach or equal zero at any point. A skin friction value of zero along the centerline is the usual indicator of a separation point. The absence of a separation point reveals the concurrent absence of a reattachment point in the localised region. As a result, it would be safe to assume that the enhanced heating bad localised round the region (x/D = -2.3) is not the result of a reattachment point.

An increase in heat transfer in the region of interest can only be caused by a deceleration in the flow at that location; loss of kinetic energy in the flow is transformed into thermal potential. The surface pressure profile along the centreline in Figure 5.55:(**bottom**) shows a gradual increase in pressure and temperature in the region (x/D = -2.3) as a result of the flow losing momentum. The adverse pressure gradient is however insufficiently severe to force separation as indicated in Figure 5.63. The loss of flow momentum with a corresponding increase in pressure and temperature appears to be the likely cause of the increase in heat transfer seen in Figure 5.61.

5.5.4 Comparison of 10mm and 5mm blunt-fin Flow

The heat transfer coefficient map in Figure 5.60 gives a good illustration of how the interaction foot print scale with fin diameter.

However, to fully appreciate the physical size of the interaction zone with respect to each diameter, the centerline (h/h_u) profile, and the centerline skin fiction profile have been plotted together with respect to distance from the leading edge of the plate. These plots are illustrated in Figure 5.64(**top**) and Figure 5.64(**bottom**).

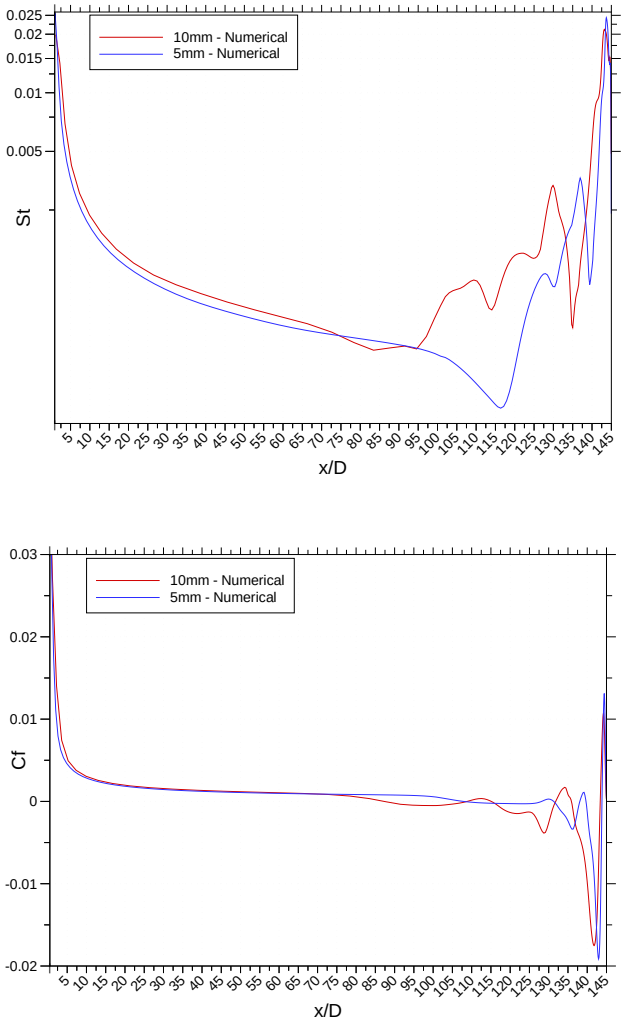

Figure 5.64: (**top**) Comparison of the centerline Stanton number profile for the 5mm and 10mm fin (**bottom**) Comparison of the centerline Skin friction coefficient profile for the 5mm and 10mm fin

A close examination of Figure 5.64:(**top**) clearly shows the increased size of the separated zone in the 10mm interaction with respect to the 5mm result. This is an expected result considering that the interference flowfield is largely governed by the fin bow shock interacting with the boundary layer growing over the flat plate. Physical reasoning suggests that, for a given flow Mach number, the bow shock shape and location will be primarily be determined by the leading edge diameter (see Chapter 2, Section 2.5.2). Clearly visible are the similarities in the heat flux values at each corresponding reattachment point.

A look at the Skin friction coefficient profile along the centerline in Figure 5.64:(**bottom**) paints a similar picture. The increased physical size of the separated region can be seen by the early onset of separation in the 10mm interaction compared to the 5mm interaction.

The two results also clearly show the increased heat flux and skin friction observed in the 5mm interaction at the ($\mathbf{R_1}$) reattachment point, when compared to the same point on the 10mm interaction.

5.6 5mm blunt-fin with 30° sweep simulations

To investigate the effects of fin leading edge sweep, a 5mm diameter blunt-fin with ($\Lambda = 30°$) sweep is simulated using the same flow conditions as the unswept 5mm diameter blunt-fin. The grid generated is an algebraically mapped C-type grid, shown here in Figure 5.65. The two grids studied are shown in Table 5.10.

Grid	Type
$58 \times 51 \times 45$	A1
$116 \times 102 \times 90$	B1

Table 5.10: The two grids studied for the swept fin

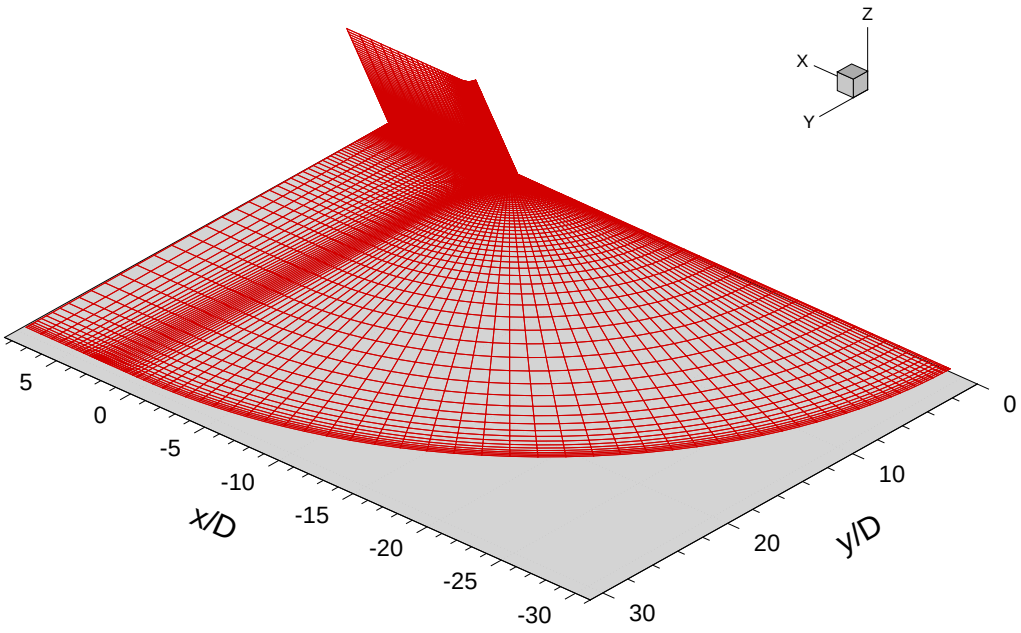

Figure 5.65: Swept fin grid, $116 \times 102 \times 90$

The primary purpose of this simulation was to observe the scaling effects on the interaction due to fin sweep, to analyze any distinct three-dimensional features that are present in swept fin interactions, and to compare the effects of sweep on the heat flux distribution

on the flat plate. The numerical heat flux results are also compared with experimental heat transfer data for a 30° swept fin conducted by Schuricht [53]

5.6.1 General Flow Features of blunt-fin with 30° sweep

The effect fin sweep has on the subsequent scale of interaction has been documented before by Schuricht [53] and Hiers and Loubsky [29] to name a few. However, all these were experimental results and no numerical simulations of the three-dimensional flow field were conducted.

The general trends observed were a dramatic decrease in the scale of the interaction, both in a streamwise and spanwise direction. Surface measurements indicate a reduction in the complexity of the interaction in the separated boundary layer. This is primarily caused by the reduction in the bow shock strength, and the reduced stand-off distance as a result of sweeping the fin. To observe these effects, density, temperature, pressure and Mach contour profiles are recorded from the plane of symmetry.

The density, temperature and pressure contours describe a flow structure within the separated region very similar to what was observed for the unswept 5mm diameter fin, but at a much reduced scale. The density contours indicate less complexities in the separated boundary layer, but clearly outlined is the shock structure with the bow shock, separation shock and reflected shock all well defined. Important observations to be made from the density plot is the reduced stand off distance between the bow shock and swept fin leading edge, and the lower separation shock angle compared to the unswept 5mm diameter fin interaction. The separation shock appears to originate at ($x/D \simeq$ -4), which appears to agree with the separation distance recorded by Schuricht [53].

From examining the temperature contours within the separated layer, it is evident that the supersonic recirculation regions seen in the unswept 5mm diameter fin also appear to occur in the swept fin. This is more clearly identifiable in the Mach contours in Figure 5.67. A table with some geometrical constants for the ($\Lambda = 30°$) swept fin flow field is shown in Table 5.11. The boundary layer height used for comparison in the table below is taken to be ($\delta = 3.48mm$), ($z/D = 0.696$).

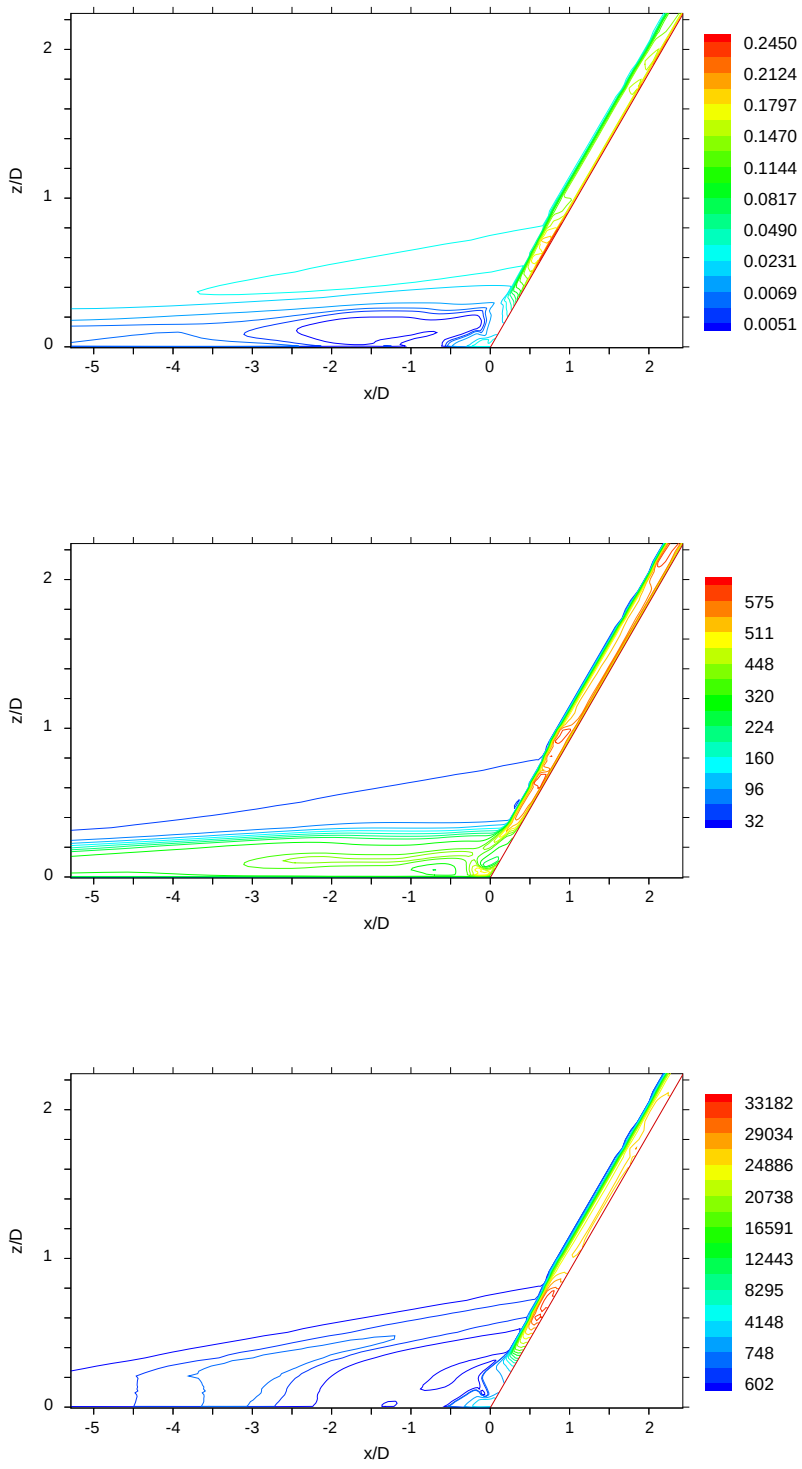

Figure 5.66: (**top**) Density contours (**middle**) Temperature contours (**bottom**) Pressure contours in the symmetry plane

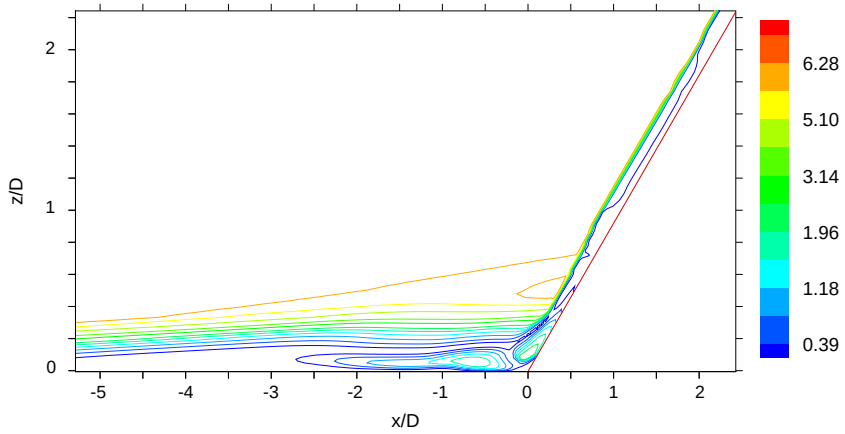

Figure 5.67: Mach contours in the symmetry plane

As Table 5.11 indicates, the decreased interaction zone is revealed by the (K/K_{tp}) ratio. For the swept fin, ($K_{tp} = 4$), comparing this with the unswept 5mm fin which has a ($K_{tp} = 7.72$), reveals a 48% reduction in the height of the triple point which would also translate to similar order of reduction in the separation length.

Type	D/δ	K/δ	K/D	K/K_{tp}
5mm - Numerical ($\Lambda = 30°$)	1.44	7.18	5	6.25

Table 5.11: Fin dimension relationships

Figure 5.68 presents the particle streamlines in the symmetry plane for the swept fin interaction. The plot indicates that separation occurs at (x_S/D = -4), and the separated flow rolls into one primary vortex, with an additional root vortex as expected at the junction of the fin/plate. The separated flow reattaches further up the swept fin at (z/D = +0.8). Comparing the relative sizes of the recirculation regions of the swept fin and upswept fin, confirms the reduced size of the swept fin interaction. For example the height of the separated layer for the swept fin is ($z/D \simeq +2.5$), whereas for the unswept fin it is

($z/D \simeq +4$). The size of the root vortex is also much smaller for the swept fin than the unswept fin.

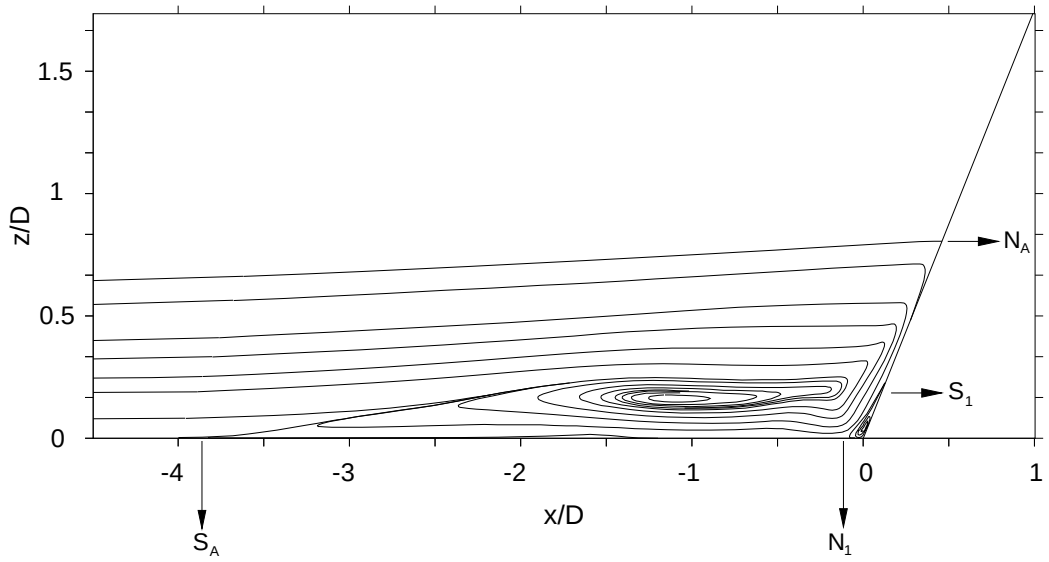

Figure 5.68: Particle streamlines in the symmetry plane

Following the particle streamline trace is a map of the skin friction lines on the flat plate surface as indicated in Figure 5.69. The skin friction streamline map clearly identifies the primary separation line, ($\mathbf{S}_A$), and the root vortex reattachment line ($\mathbf{R}_1$).

The primary separation line for the swept fin is more curved than the equivalent separation line on the unswept fin interaction. This clearly indicates that the spanwise extent of the interaction is also considerably smaller than the equivalent unswept example. The skin friction lines also indicate secondary separation and reattachment lines on the plate surface. Lines ($\mathbf{S'}_2$) and ($\mathbf{R'}_2$) look very similar to the secondary separation and reattachment lines observed for the unswept fin. This signifies that the strength of the bow shock is sufficient to initiate secondary separation on the fin side surface as a result of a swept shock interaction, is observed in unswept finside interactions.

The three-dimensional plot of the vortex paths in Figure 5.70 indicates that the primary

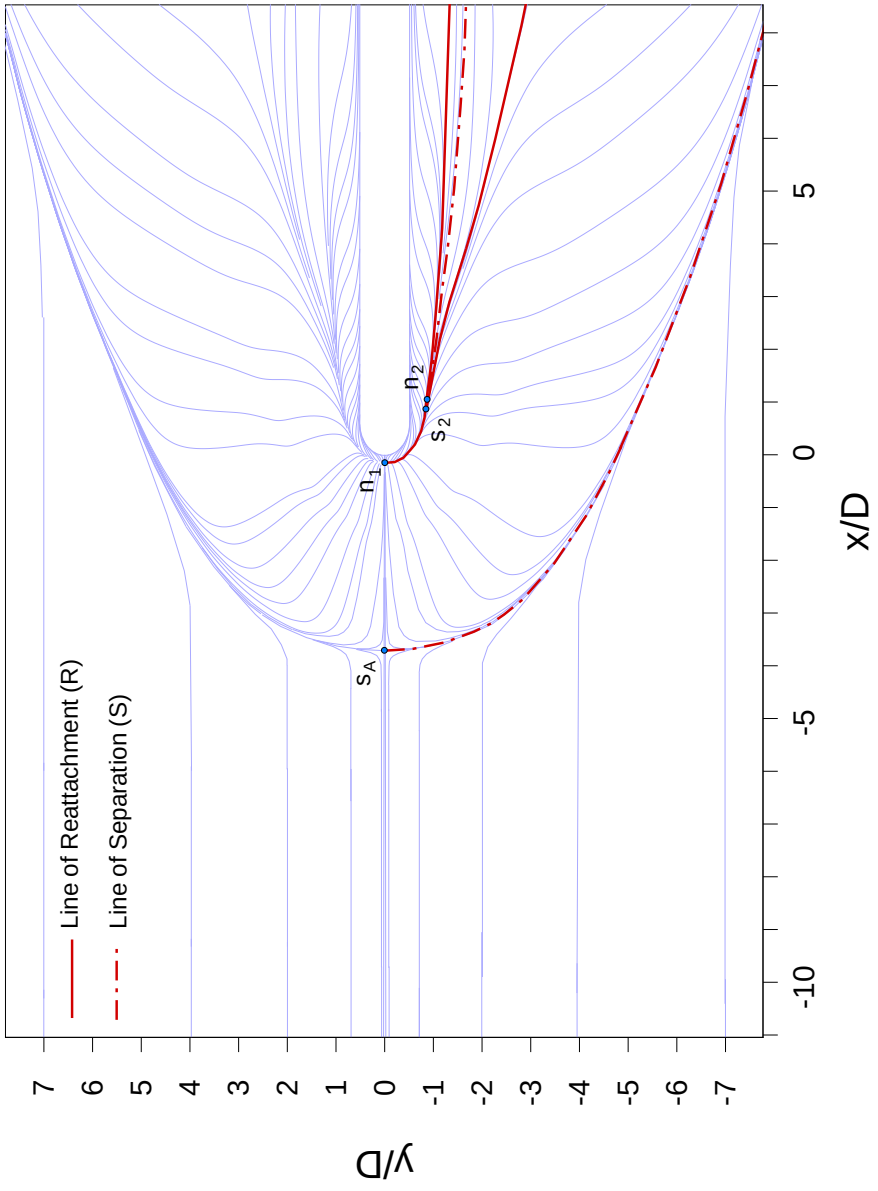

Figure 5.69: Surface skin friction streamlines on flat plate with highlighted separation and reattachment lines. A separation saddle is denoted by *(s)* and a reattachment node by *(n)*

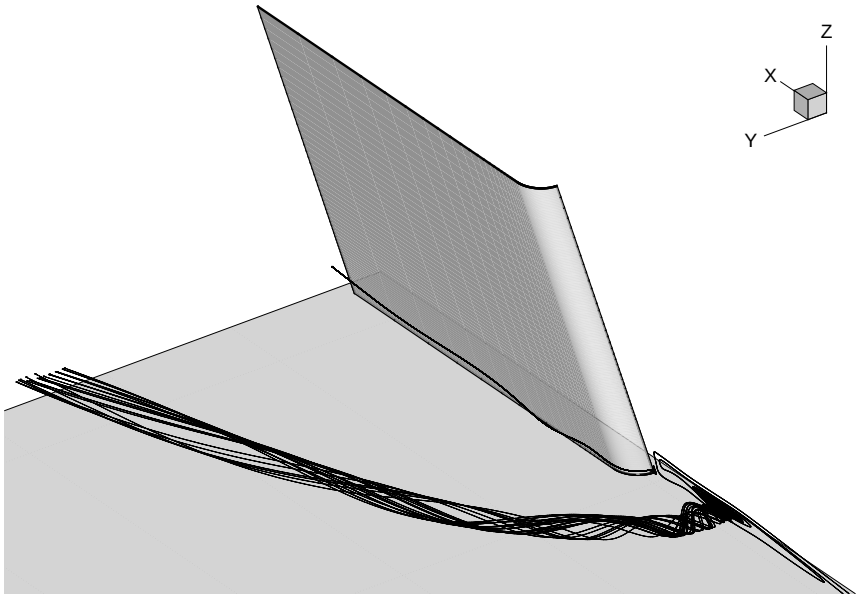

Figure 5.70: View of three-dimensional vortex paths around swept-fin

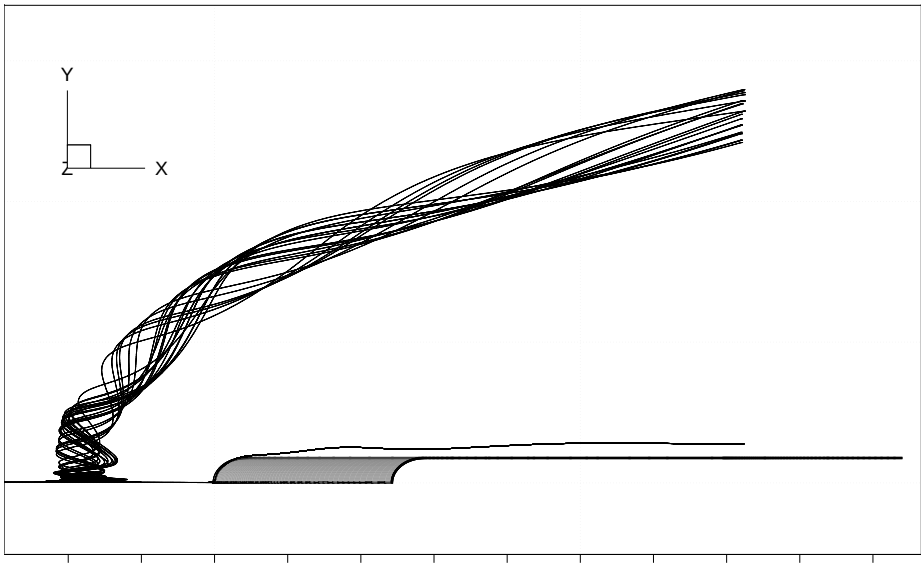

Figure 5.71: Plan view of vortices formed on a swept-fin

vortex entrains quite a considerable quantity of the surrounding flow into its core, however, unlike in the case of the unswept fin, the root vortex is considerably smaller and appears to entrain very little from the surrounding fluid. Figure 5.71 highlights how small the root vortex is in comparison to the primary vortex.

5.6.2 Surface Heating on Plate

The heat flux contour pattern on the flat plate, shown here in Figure 5.73, displays similarities to the unswept case, with the features seeming to be compressed together within the smaller disturbed flow region.

The numerical distribution shows the two distinct bands of increased heat flux surrounding the fin. The maximum heat transfer occurs along a thin band surrounding the leading edge, with $(h/h_u)_{max} \simeq 8$. This is a considerable reduction in $(h/h_u)_{max}$ when compared with the unswept fin for which peak values $\simeq 60$ times the equivalent undisturbed flat plate value were observed. The reduced bow shock strength leads to lower pressures and hence lower heating rates downstream of the shock. However, it appears the primary cause for the reduced heat transfer at ($\mathbf{R}_1$) is due to the reduced strength of the supersonic jet within the recirculation region striking the plate surface.

The comparison between the experimental heat flux contours in Figure 5.72 and the numerical set in Figure 5.73 appear to show reasonable agreement in general spatial distribution and the magnitudes of the contours; however, as with the unswept fin some differences exist. The experimental result does not appear to indicate a second heat flux band that borders the band closest to the fin as indicated in the numerical result in Figure 5.73. This result could be due to poor illumination of the crystals, an explanation put forward by Schuricht [53] for the poor resolution. As a result a comparison is made of the centerline and crossflow, at $(x/D = +1)$, heat flux profiles to get a better indication of the surface heating.

As Figure 5.74 indicates the comparison between the numerical and experimental results is quite favourable. Both data sets appear to indicate the same number of peaks and valleys, with a good correlation of spatial features. The numerical centerline profile shows

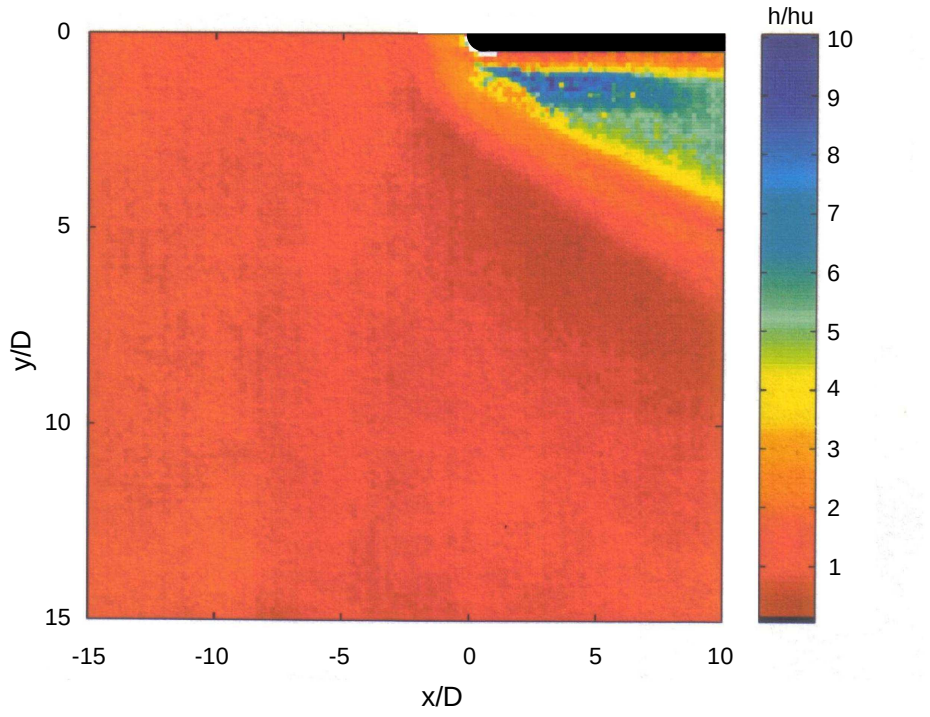

Figure 5.72: Experimental heat transfer contours on plate surface Schuricht [53]

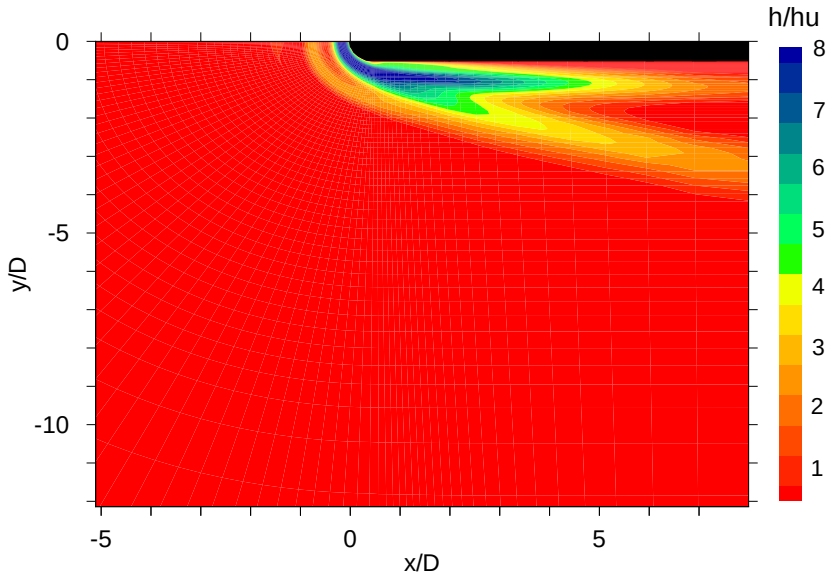

Figure 5.73: Normalized heat transfer contours on plate surface

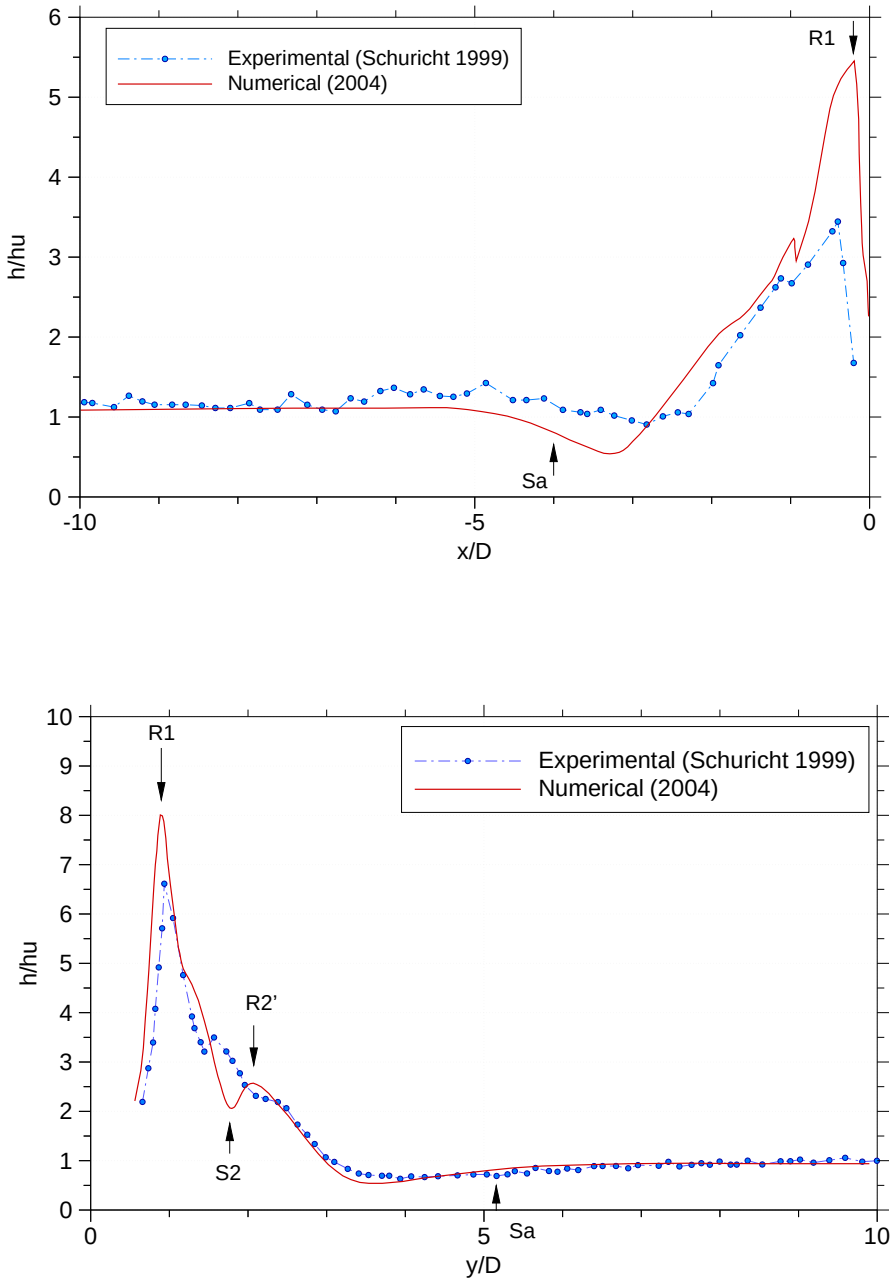

Figure 5.74: (**top**) Normalized linear heat transfer coefficient (h/h_u) along the axis of symmetry (**bottom**) Normalized linear heat transfer coefficient (h/h_u) laterally at $x/D = +1$

good agreement upto primary separation, whereupon the numerical data produce a more pronounced decrease in surface heating compared to the experimental data. The subsequent rise in heat flux appears to occur at similar points in both result sets, at around ($x/D \simeq$ -3). The numerical profile records a higher peak heating value at ($\mathbf{R}_1$), ($h/h_u \simeq$ 5.5), compared to the experimental value of ($h/h_u \simeq 3.5$). This appears to be a recurring theme thus far in the numerical results.

The crossflow profile at ($x/D = +1$) shows excellent agreement with the experimental results. The calculated numerical maximum heat flux is $(h/h_u)_{max} \simeq 8$, and the equivalent experimental maximum is $(h/h_u)_{max} \simeq 7$. The experimental results appear to show a plateau at the location of ($\mathbf{R'}_2$) which could be indicative of a reattachment point, thus it would appear that the numerical heat flux contour profile is correct.

Chapter 6

Conclusions and Recommendations for Future Work

6.1 Conclusion

The numerical simulation of a three-dimensional laminar hypersonic Mach 6.7, blunt-fin interference flowfield produced by several configurations of a fin attached to a flat plate were presented.

The numerical calculations solved the compressible Navier-Stokes equations using an Implicit and Explicit finite volume code developed at the University of Southampton. The numerical scheme has been adapted to accept any generic three-dimensional geometry, and has the ability to accommodate additional explict viscous cross-derivative terms to offer the potential of giving a full Navier-Stokes solution. In the present study the influence of these cross-derivatives terms was demonstrated to be negligible and were therefore omitted from the solution to speed up the calculation. Several three-dimensional configurations have been simulated, including an unswept blunt-fin, fins of various diameters and a circular cylinder.

6.1.1 Results

The three-dimensional results of the unswept $5mm$ diameter blunt-fin interaction show a rich, complex three-dimensional structure within the separated flow caused by the interaction of the bow shock with the advancing boundary layer. The horseshoe vortices formed inside the separation bubble appear to be stable, with no fluctuation in shape or location with the passage of time. The path of these vortices around the blunt-fin are clearly mapped, and the mechanism of flow entrapment into these vortices is clearly indicated. The results indicate that the side wall of the blunt-fin plays a dominant role in determining the flow structure beyond the leading edge dominated section of the blunt-fin. The result of this is additional separation and reattachment of the flow as a result of pressure gradients downstream of the fin root. The increased heat flux spikes are solely the result of flow reattachment caused by the vortices that originate from the fin centerline, upstream of the fin root. The exception to this is the additional separation and reattachment due effects of the fin side wall. The supersonic jet formed as a result of an Edney type IV shock-shock interaction due the oblique separation shock intersecting the fin bow shock is documented. The impact the jet has on the heat flux on the fin-side surface is described, with measured levels around ($h/h_u \simeq 30$).

The surface topological features, and surface heat flux profiles observed on the flat plate from the numerical simulation indicate good agreement with the experimental results obtained by Schuricht for the same blunt-fin configuration. The numerical simulation was able to obtain data in regions that were unable to be measured experimentally due to limitations in the liquid crystal thermography thermal mapping method used by Schuricht. The numerical results indicate vastly increased highly localised heat transfer rates when compared to predictions made from the experimental data. From the numerical results it was possible to elucidate a mechanism responsible for the extremely large heat transfer rates close to the blunt-fin root. It appeared that as a result of a shock/shock interaction inside the separated region, a supersonic jet is formed by another Edney type IV interaction. This jet is accelerated towards the plate surface by the rotating horseshoe vortices, and upon impacting the plate releases a considerable amount of energy which results in highly elevated levels of heat transfer, around 60 times the undisturbed flat plate value at that location.

Studies of fin sweep and variable fin diameter on the scale of the interaction reveal distinct changes to the flow structure, with the trends observed consistent with the findings of Schuricht and others. The results indicate that the leading edge diameter has a measurable impact on the extent of the interaction, the resulting change in the size of the separated region effects the vortex structure insider the separation bubble. The separation bubble in the $10mm$ diameter fin simulation indicates further bifurication of the primary vortex into two smaller vortices. This impacts on the relative placement of the secondary vortices which, in turn, affects the heat flux distribution on the flat plate. Fin diameter does appear to have an effect on the maximum heat flux on the flat plate. The maximum heat transfer rate appears to be lower than that observed for the 5mm diameter blunt-fin. However, apart from the localised maximum heat transfer rate, changes in fin leading edge diameter do not appear to significantly influence the magnitude of heat transfer within the interference zone.

The swept fin simulation indicates a dramatic reduction in the size of the separation bubble, with a simultaneous reduction in the peak surface heat transfer rate on the flat plate ($h/h_u \simeq 8$). The separation bubble only contains a large single primary vortex core, with an additional root vortex. This is compared with the $5mm$ unswept blunt-fin, which has four vortices excluding the root vortex in the separated region. Overall, the swept fin interference flowfield is considerably smaller than the same unswept fin. The impact of incorporating sweep in vehicle design is quite obvious. As the present study has shown sweeping the fin by 30° dramatically removes "hot spots" on the fin leading edge and plate surface. These "hot spots" are caused by shock/shock and shock/boundary layer interactions. They are extremely localised as seen in this study, and generally very difficult to insulate against efficiently. Incorporating fin sweep considerably reduces the heating distribution and the extent of the disturbed flow on the plate surface and could also possibly reduce the weight of any control surface.

6.2 Recommendations for Future Work

As a result of the work carried out in this thesis, the following topics are recommended for further study:

- The effects of variation in Reynolds number on the fin interaction should be studied in more detail, with the main emphasis on the effect it has on the vortex structure within the separation bubble, and the stability of resulting structure.

- An appropriate turbulence model should be incorporated into the code to allow for a comparison with past experimental results obtained by Haq [28] and others, and to enable a comparison of the surface heat transfer profiles between the turbulent and laminar flowfields.

- The grid dependence study has shown that the current solution is not fully grid independent: a higher number of grid points offers the possibility of capturing finer flow features and generating a more accurate surface heat transfer profile. In order to maximise the potential of the current computational platform it is possible to increase the parallelization efficiency of the parallel numerical scheme by parallelizing in all three spatial coordinates directions (ξ, η, and ζ) instead of the current single (ζ) direction.

- A future improvement to the current viscous solver would be to incorporate the additional jacobian terms of the cross derivative terms in the implicit method. This is purely for the benefit of having the option of a complete Navier-Stokes solver using the implicit method.

- For the benefit of future comparisons between experimental and numerical results a more comprehensive collection of experimental results of the flowfield away from the flat plate surface is required, in particular a description of the vortex flowfield in the separated region. The use of non-intrusive flowfield measurement techniques such as planar laser induced fluorescence [22] could offer the possibility of further detailed comparisons.

Bibliography

[1] S. R. Amaratunga. *A Numerical Study into Surface Catalytic Effects in Non-Equilibrium Reacting Viscous Laminar Hypersonic Flow.* PhD thesis, University of Southampton, Southampton, 1998.

[2] J. D. Anderson. *Hypersonic & High Temperature Gas Dynamics.* McGraw & Hall, NewYork, 1989.

[3] J. D. Anderson. *Modern Compressible Flow.* McGraw & Hall, NewYork, 1990.

[4] B. S. Baldwin and H. Lomax. Thin-layer approximation and algebraic model for separated turbulent flows. *AIAA Paper 78-0257*, 1978.

[5] F. Ballio and S. Franzetti. Topological analysis of a junction vortex flow. *Advances in Fluid Mechanics III*, 29, 2000.

[6] P. Batten, D. M. Ingram, R. Saunders, and D. M. Causon. An implicit viscous solver for the compressible navier-stokes equations. *Computers and Fluids*, 25(2):421–431, 1996.

[7] P. Batten, M. A. Leschiner, and U. C. Goldberg. Average-state jacobians and implicit methods for compressible viscous and turbulent flows. *J. Comput. Phy*, 134:38–78, 1997.

[8] J. J. Bertin. *Hypersonic Aerothermodynamics.* AIAA Educational series, NewYork, 1994.

[9] D. R. Chapman, D. M. Kuehn, and H. K. Larson. Investigation of separated flows in supersonic and subsonic streams with emphasis on the effect of transition. *NACA Report*, 1958.

[10] N. Clarke, P. Batten, C. Lambert, and D. M. Causon. On the choice of wavespeeds for the hllc riemann solver. *SIAM J. Sci. Comput*, 18(6):1553–1570, 1997.

[11] O. Özcan and M. Holt. Supersonic separated flow past a cylindrical obstacle on a flat plate. *AIAA Journal*, 22:611–617, 1984.

[12] F. C. Dixon. *Numerical Simulations of a Trasverse Sonic Jet in a Laminar Hypersonic Flow*. PhD thesis, University of Southampton, Southampton, 2003.

[13] J. M. Dlery. Toward the elucidation of three dimensional separation. *Annual Review of Fluid Mechanics*, 33:129–154, 2001.

[14] D. S. Dolling. Comparison of sharp and blunt fin-induced shock wave/turbulent boundary-layer interaction. *AIAA Journal*, 20:1385–1391, 1982.

[15] D. S. Dolling and S. M. Bogdonoff. Scaling of interactions of cylinders with supersonic turbulent boundary layers. *AIAA Journal*, 20:655–657, 1981.

[16] D. S. Dolling and S. M. Bogdonoff. Blunt fin-induced shock wave/turbulent boundary-layer interaction. *AIAA Journal*, 20:1674–1680, 1982.

[17] D. S. Dolling and P. E. Rodi. Upstream influence and separation scales in fin-induced shock turbulent boundary-layer interaction. *Journal of Spacecraft*, 25:101–108, 1988.

[18] W. H. Dorrance. *Viscous Hypersonic Flow*. McGraw & Hall, NewYork, 1962.

[19] E. R. G. Eckert. Engineering relations for skin friction and heat transfer to surfaces in high velocity flows. *Journal of Aeronautical Sciences*, 22:585–587, 1955.

[20] B. E. Edney. Temperature measurements in a hypersonic gun tunnel using heat transfer methods. *Journal of Fluid Mechanics*, 27:503–512, 1967.

[21] N. R. Fomison and J. L. Stollery. The effects of sweep and bluntness on a glancing shock wave turbulent boundary layer interaction. *AGARD Conference Proceedings*, CP-428, 1987.

[22] J. S. Fox, S. O'Byrne, A. F. P. Houwing, and A. Papinniemi. Fluorescence visualisation of the hypersonic flow establishment over a blunt fin. *Journal of Propulsion and Power*, 11:31–42, 2001.

[23] P. A. Gnoffo. Computational fluid dynamics technology for hypersonic applications. *NASA Technical Paper 23681-0001*, 2001.

[24] W. J. Gordon and C. A. Hall. Construction of curvilinear co-ordinate systems and applications to mesh generation. *International Journal for Numerical Methods in Engineering*, 7:461–477, 1973.

[25] F. Grasso, G. Leone, and J. M. Delery. Validation procedure for the analysis of shock-wave/boundary-layer interaction problems. *AIAA Journal*, 32(9):1820–1827, 1994.

[26] F. Grasso and M. Marini. Analysis of hypersonic shock-wave laminar boundary-layer interaction phenomena. *Computers and Fluids*, 25:561–581, 1996.

[27] A. G. Hammitt. The hypersonic viscous effect on a flat plate with finite leading edge. *Journal of Fluid Mechanics*, 5:242–256, 1959.

[28] Z. U. Haq. *Hypersonic Vehicle Interference Heating.* PhD thesis, University of Southampton, Southampton, 1993.

[29] R. S. Hiers and W. J. Loubsky. Effects of shock wave impingement on the heat-transfer on a cylinderical leading edge. *NASA TN D-3859*, 1967.

[30] M. S. Holden. A study of flow separation in regions of shock wave-boundary layer interaction in hypersonic flow. *AIAA Paper 78-1169*, 1978.

[31] B. R. Hollis, T. J. Horvath, S. A. Berry, H. H. Hamilton, and S. J. Alter. X-33 computational aeroheating predictions and comparisons with experimental data. *AIAA Paper 99-3559*, 1999.

[32] A. F. P. Houwing, D. R. Smith, J. S. Fox, and N. R. Mudford. Laminar boundary layer separtion at a fin-body junction in a hypersonic flow. *ShockWaves*, 11:31–42, 2001.

[33] C. M. Hung and P. G. Buning. Simulation of blunt-fin-induced shock-wave and turbulent boundary-layer interaction. *Journal of Fluid Mechanics*, 154:163–185, 1985.

[34] C. M. Hung and W. Kordulla. A time-split finite-volume algorithm for three-dimensional flowfield simulation. *AIAA Journal*, 31(1):64–71, 1984.

[35] C. M. Hung and S. S. Kurasaki. Thin-layer approximation for three-dimensional supersonic corner flows. *Computers and Fluids*, 25(2):421–431, 1996.

[36] F. T. Hung and J. M. Clauss. Three-dimensional protuberance interference in high speed flow. *Aerothermodynamics and planetary entry - Progress in Astronautics and Aeronautics*, 77:109–136, 1981.

[37] L. G. K. II, R. H. Korkegi, and L. C. L. C. Morton. Shock impingement caused by boundary-layer separation ahead of blunt-fin. *AIAA Journal*, 11:1363, 1973.

[38] P. Inc. *Gridgen User Manual Version 14*. Bedford. Texas, 1999.

[39] G. R. Inger. Spanwise propagation of upstream influence in conical swept-shock/boundary layer interactions. *AIAA Journal*, 25(2):287–293, 1987.

[40] Y. Kallinders and P. Vijayan. A 3d finite-volume scheme for the euler equations on adaptive tetrahedral grids. *Journal of Computational Physics*, 113:249–267, 1994.

[41] E. Katzer. On the lengthscales of laminar shock/boundary-layer interaction. *Journal of Fluid Mechanics*, 206:477–496, 1989.

[42] W. Kordulla and M. Vinokur. Efficient computation of volume in flow predictions. *AIAA Journal*, 21:917–918, 1983.

[43] R. H. Korkegi. Survey of viscous interactions associated with high mach number flight. *AIAA Journal*, 9:771–783, 1971.

[44] H. Kubota and J. L. Stollery. An experimental study of the interaction between a glacing shock wave and a turbulent boundary layer. *Journal of Fluid Mechanics*, 116:431–458, 1982.

[45] B. Lakshmanan and S. N. Tiwari. Investigation of three-dimensional separation at wing/body junctions in supersonic flows. *Journal of Aircraft*, 22:1564–1572, 1994.

[46] C. R. McClinton. X-43 scramjet power breaks the hypersonic barrier. *AIAA Paper 2006-1*, 2006.

[47] S. Navarro-Martinez. *Numerical Simulation of Laminar Flow Past Compression Ramps*. PhD thesis, University of Southampton, Southampton, 2002.

[48] NPARC. Geometry modelling and grid generation. In *Technical report, NASA*, 2000.

[49] G. C. Olsen and N. J. Roberts. Hydrogen film cooling with incident and swept-shock interactions in a mach 6.4 nitrogen free stream. *NASA TM 4603*, 1995.

[50] E. A. Price, P. W. Howard, and R. L. Stallings. Heat transfer measurements on a flat plate and attached fins at mach numbers 3.51 and 4.44. In *NASA TN D-3804*, 1964.

[51] P. J. Roache. Quantification of uncertainty in computational fluid dynamics. *Annual Review of Fluid Mechanics*, 29:123–160, 1997.

[52] A. G. Russell, Y. Hong, E. S. Gregory, and K. D. Doyle. Localized flow control by laser energy deposition applied to edney iv shock impingement and intersecting shocks. *AIAA Paper 2003*, 2003.

[53] P. H. Schuricht. *Liquid Crystal Thermography In High Speed Flows.* PhD thesis, University of Southampton, Southampton, 1999.

[54] R. Sedney. A survey of the effects of small protuberances on boundary-layer flows. *AIAA Journal*, 11:782–792, 1973.

[55] R. Sedney and C. W. J. Kitchens. The structure of three-dimensional separated flows in obstacle, boundary layer interactions. *AGARD-CP-168 on Flow Separation*, 168, 1975.

[56] J. L. Stollery. Some aspects of shock-wave boundary layer interaction at hypersonic speeds. In *17th ISSTSW*, 1989.

[57] J. F. Thompson, B. K. Soni, and N. P. Weatherill. *Handbook of Grid Generation.* CRC Press, 1999.

[58] M. Tobak and D. J. Peake. Topology of three-dimensional separated flows. *Annual Review of Fluid Mechanics*, 14:61–85, 1982.

[59] E. Turkel, R. C. Swanson, and V. N. Vatsa. Multgrid for hypersonic viscous two and three dimensional flows. In *Technical report, NASA*, 1991.

[60] O. R. Tutty, G. T. Roberts, and R. A. East. Numerical study of fin-body interference effects at hypersonic speeds. In *Proceedings at 2nd European Symposium on Aerothermodynamics for Space Vehicles*, 1994.

[61] M. R. Visbal. Structure of laminar juncture flows. *AIAA Journal*, 29:1273–1282, 1991.

[62] V. Viti. *Numerical Studies of the Jet Interaction Flowfield with a Main Jet and an Array of Smaller Jets*. PhD thesis, Virginia Polytechnic Institute and State University, 2002.

[63] D. M. Voitenko, A. I. Zubkov, and Y. A. Panov. The existence of supersonic zones in three-dimensional separated flows. *Journal of Fluid Dynamics*, 2:13–16, 1967.

[64] S. Walker and J. D. Schmisseur. C.f.d validation of shock-shock interaction flow fields. *AIAA Paper 2002-0436*, 2002.

[65] J. D. Watts and F. V. Olinger. Heat-transfer effects of surface protuberances on the x-15 airplane. *NASA TM X-1669*, 1964.

[66] J. C. Westkaemper. Turbulent boundary layer separation ahead of cylinders. *AIAA Journal*, 6:1352–1355, 1968.

[67] S. Yamamoto. Flow characteristics of unsteady three-dimensional type iv shock interference. *AIAA Paper 2000-2690*, 2000.

[68] S. Yamamoto and N. Takasu. Numerical study of unsteady shock/boundary-layer interaction induced by a blunt fin. *AIAA Paper 98-2815*, 1998.

[69] H. C. Yee. A class of explicit and implicit shock-capturing methods. *NASA TM 101088*, 1989.

[70] F. L. Young, L. G. Kaufmann, and R. H. Korkegi. Experimental investigation of interaction between blunt fin shock waves and adjacent boundary-layers at mach numbers 3 and 5. *Aerospace Research Laboratories*, ARL 68-0214, 1968.

Appendix A

Non-dimensionalisation

To derive non-dimensional quantities the physical magnitudes have been scaled by the corresponding free stream values which are denoted by the subscript (∞) while (L_{ref}) is the characteristic length of the flat plate.

Length

$$\frac{x}{L_{ref}}, \frac{y}{L_{ref}}, \frac{z}{L_{ref}} \tag{A.1}$$

Velocity

$$\frac{u}{U_\infty}, \frac{v}{V_\infty}, \frac{w}{W_\infty} \tag{A.2}$$

Time

$$\frac{t}{L_{ref}/U_\infty} \tag{A.3}$$

Density

$$\frac{\rho}{\rho_\infty} \tag{A.4}$$

Pressure

$$\frac{p}{\rho_\infty U_\infty^2} \tag{A.5}$$

Temperature

$$\frac{T}{T_\infty} \tag{A.6}$$

Specific energy

$$\frac{E}{U_\infty^2} \tag{A.7}$$

Viscosity

$$\frac{\mu}{\mu_\infty} \tag{A.8}$$

Specific heats

$$\frac{C_p}{U_\infty^2/T_\infty}, \frac{C_v}{U_\infty^2/T_\infty} \tag{A.9}$$

Appendix B

Numerics for Chapter 4

B.1 Navier Stokes equations

The Navier Stokes equations that describe the behavior of a compressible fluid can be written in conservative form as:

$$\frac{\delta U}{\delta t} + \frac{\delta F}{\delta x} + \frac{\delta G}{\delta y} + \frac{\delta H}{\delta z} = \frac{\delta F_v}{\delta x} + \frac{\delta G_v}{\delta y} + \frac{\delta H_v}{\delta z} \tag{B.1}$$

where (U) is the vector of conserved variables:

$$U = \begin{bmatrix} \rho \\ \rho u \\ \rho v \\ \rho w \\ \rho E \end{bmatrix} \tag{B.2}$$

and (F), (G) and (H) are the advection fluxes given by

$$F = \begin{bmatrix} \rho u \\ \rho u^2 + p \\ \rho uv \\ \rho uw \\ u(\rho E + p) \end{bmatrix} \tag{B.3}$$

$$G = \begin{bmatrix} \rho v \\ \rho uv + p \\ \rho v^2 + p \\ \rho vw \\ v(\rho E + p) \end{bmatrix} \tag{B.4}$$

$$H = \begin{bmatrix} \rho w \\ \rho uw \\ \rho vw \\ \rho w^2 + p \\ w(\rho E + p) \end{bmatrix} \tag{B.5}$$

Here (ρ) represents the density (u), (v) and (w) are the components of the velocity field, (E) is the total specific energy and (p) stands for pressure. To close the above set of relations, the pressure should be related with other thermodynamical properties through an equation of state. For the current study the relation is the ideal gas equation

$$p = (\gamma - 1)\Big(\rho E - \frac{1}{2}\rho(u^2 + v^2 + w^2)\Big) \tag{B.6}$$

where (γ) stands for the specific heat ratio which is a constant when dealing with perfect gases, the value of which for diatomic molecules is 1.4. From (Eqn B.1) (F_v), (G_v) and (H_v) represent the viscous fluxes given by

$$F_v = \begin{bmatrix} 0 \\ \xi_x\tau_{xx} + \xi_y\tau_{xy} + \xi_z\tau_{xz} \\ \xi_x\tau_{xy} + \xi_y\tau_{yy} + \xi_z\tau_{yz} \\ \xi_x\tau_{xz} + \xi_y\tau_{yz} + \xi_z\tau_{zz} \\ u\tau_{xx} + v\tau_{xy} + w\tau_{xz} + q_x \end{bmatrix} \tag{B.7}$$

$$G_v = \begin{bmatrix} 0 \\ \eta_x\tau_{xx} + \eta_y\tau_{xy} + \eta_z\tau_{xz} \\ \eta_x\tau_{xy} + \eta_y\tau_{yy} + \eta_z\tau_{yz} \\ \eta_x\tau_{xz} + \eta_y\tau_{yz} + \eta_z\tau_{zz} \\ u\tau_{yx} + v\tau_{yy} + w\tau_{yz} + q_y \end{bmatrix} \tag{B.8}$$

$$H_v = \begin{bmatrix} 0 \\ \zeta_x\tau_{xx} + \zeta_y\tau_{xy} + \zeta_z\tau_{xz} \\ \zeta_x\tau_{xy} + \zeta_y\tau_{yy} + \zeta_z\tau_{yz} \\ \zeta_x\tau_{xz} + \zeta_y\tau_{yz} + \zeta_z\tau_{zz} \\ u\tau_{zx} + v\tau_{zy} + w\tau_{zz} + q_z \end{bmatrix} \tag{B.9}$$

where the shear stress $(\tau_i j)$ can be related to the velocity field through the constants (λ) and (μ):

$$\begin{aligned} \tau_{xx} &= \lambda(u_x + v_y + w_z) + 2\mu u_x \\ \tau_{yy} &= \lambda(u_x + v_y + w_z) + 2\mu v_y \\ \tau_{zz} &= \lambda(u_x + v_y + w_z) + 2\mu w_z \\ \tau_{xy} &= \tau_{yx} = \mu(u_y + v_x) \\ \tau_{xz} &= \tau_{zx} = \mu(u_z + w_x) \\ \tau_{zy} &= \tau_{yz} = \mu(w_y + v_z) \end{aligned} \tag{B.10}$$

The components of the shear stress have been simplified using the Newtonian approximation for an isentropic medium. The Stokes hypothesis for the viscosities is also applied, suggesting a linear relation between the coefficients (λ) and (μ):

$$\lambda = \mu_b - \frac{2}{3}\mu \tag{B.11}$$

Where (μ) is the *coefficient of shear viscosity or dynamic viscosity and* and (μ_b) is the *coefficient of bulk viscosity.* Further simplification of the expression can be exacted by using molecular theory, with the hard sphere assumption, allowing ($\mu_b = 0$), reasonably accurate correlations have been found with experimental results. Therefore the relation between coefficients simplifies to ($\lambda = -2/3\mu$).

Using the simplification

$$\begin{aligned}
\frac{\partial}{\partial x} &= \xi_x \frac{\partial}{\partial \xi} + \eta_x \frac{\partial}{\partial \eta} + \zeta_x \frac{\partial}{\partial \zeta} \\
\frac{\partial}{\partial y} &= \xi_y \frac{\partial}{\partial \xi} + \eta_y \frac{\partial}{\partial \eta} + \zeta_y \frac{\partial}{\partial \zeta} \\
\frac{\partial}{\partial z} &= \xi_z \frac{\partial}{\partial \xi} + \eta_z \frac{\partial}{\partial \eta} + \zeta_z \frac{\partial}{\partial \zeta}
\end{aligned} \tag{B.12}$$

Therefore the resulting stress terms can be written in the following form:

$$\begin{aligned}
\tau_{xx} &= \tfrac{2}{3}\mu\Big[2\Big(\xi_x \tfrac{\partial u}{\partial \xi} + \eta_x \tfrac{\partial u}{\partial \eta} + \zeta_x \tfrac{\partial u}{\partial \zeta}\Big) - \Big(\xi_y \tfrac{\partial v}{\partial \xi} + \eta_y \tfrac{\partial v}{\partial \eta} + \zeta_y \tfrac{\partial v}{\partial \zeta}\Big) - \Big(\xi_z \tfrac{\partial w}{\partial \xi} + \eta_z \tfrac{\partial w}{\partial \eta} + \zeta_z \tfrac{\partial w}{\partial \zeta}\Big)\Big] \\
\tau_{yy} &= \tfrac{2}{3}\mu\Big[2\Big(\xi_y \tfrac{\partial v}{\partial \xi} + \eta_y \tfrac{\partial v}{\partial \eta} + \zeta_y \tfrac{\partial v}{\partial \zeta}\Big) - \Big(\xi_x \tfrac{\partial u}{\partial \xi} + \eta_x \tfrac{\partial u}{\partial \eta} + \zeta_x \tfrac{\partial u}{\partial \zeta}\Big) - \Big(\xi_z \tfrac{\partial w}{\partial \xi} + \eta_z \tfrac{\partial w}{\partial \eta} + \zeta_z \tfrac{\partial w}{\partial \zeta}\Big)\Big] \\
\tau_{zz} &= \tfrac{2}{3}\mu\Big[2\Big(\xi_z \tfrac{\partial w}{\partial \xi} + \eta_z \tfrac{\partial w}{\partial \eta} + \zeta_z \tfrac{\partial w}{\partial \zeta}\Big) - \Big(\xi_x \tfrac{\partial u}{\partial \xi} + \eta_x \tfrac{\partial u}{\partial \eta} + \zeta_x \tfrac{\partial u}{\partial \zeta}\Big) - \Big(\xi_y \tfrac{\partial v}{\partial \xi} + \eta_y \tfrac{\partial v}{\partial \eta} + \zeta_y \tfrac{\partial v}{\partial \zeta}\Big)\Big] \\
\tau_{xy} &= \mu\Big[\Big(\xi_y \tfrac{\partial u}{\partial \xi} + \eta_y \tfrac{\partial u}{\partial \eta} + \zeta_y \tfrac{\partial u}{\partial \zeta}\Big) + \Big(\xi_x \tfrac{\partial v}{\partial \xi} + \eta_x \tfrac{\partial v}{\partial \eta} + \zeta_x \tfrac{\partial v}{\partial \zeta}\Big)\Big] \\
\tau_{xz} &= \mu\Big[\Big(\xi_x \tfrac{\partial w}{\partial \xi} + \eta_x \tfrac{\partial w}{\partial \eta} + \zeta_x \tfrac{\partial w}{\partial \zeta}\Big) + \Big(\xi_z \tfrac{\partial u}{\partial \xi} + \eta_z \tfrac{\partial u}{\partial \eta} + \zeta_z \tfrac{\partial u}{\partial \zeta}\Big)\Big] \\
\tau_{yz} &= \mu\Big[\Big(\xi_z \tfrac{\partial v}{\partial \xi} + \eta_z \tfrac{\partial v}{\partial \eta} + \zeta_z \tfrac{\partial v}{\partial \zeta}\Big) + \Big(\xi_y \tfrac{\partial w}{\partial \xi} + \eta_y \tfrac{\partial w}{\partial \eta} + \zeta_y \tfrac{\partial w}{\partial \zeta}\Big)\Big]
\end{aligned} \tag{B.13}$$

The components of the heat transfer vector (q_x), (q_y) and (q_z) can be obtained through Fouriers's heat conduction law:

$$\begin{aligned}
q_x &= -\kappa \frac{\partial T}{\partial x} \\
q_y &= -\kappa \frac{\partial T}{\partial y} \\
q_z &= -\kappa \frac{\partial T}{\partial z}
\end{aligned} \tag{B.14}$$

where (κ) is the *coefficient of thermal conductivity*, or just *thermal conductivity* and (T) is the temperature. With this the last row of the flux vector can be expressed as:

$$\begin{aligned} &u\tau_{xx} + v\tau_{xy} + w\tau_{xz} + \kappa\left(\xi_x \frac{\partial T}{\partial \xi} + \eta_x \frac{\partial T}{\partial \eta} + \zeta_x \frac{\partial T}{\partial \zeta}\right) \\ &u\tau_{yx} + v\tau_{yy} + w\tau_{yz} + \kappa\left(\xi_y \frac{\partial T}{\partial \xi} + \eta_y \frac{\partial T}{\partial \eta} + \zeta_y \frac{\partial T}{\partial \zeta}\right) \\ &u\tau_{zx} + v\tau_{zy} + w\tau_{zz} + \kappa\left(\xi_z \frac{\partial T}{\partial \xi} + \eta_z \frac{\partial T}{\partial \eta} + \zeta_z \frac{\partial T}{\partial \zeta}\right) \end{aligned} \tag{B.15}$$

From molecular theory we can postulate that (κ) is proportional to (μ). If the specific heat at constant pressure (C_p) is constant , the Prandtl (Pr) remains constant at low temperatures and is given by the expression [3].

$$Pr = \frac{C_p \mu}{\kappa} \tag{B.16}$$

For the current study the (Pr) is 0.704, as used by Navarro-Martinez [47].

B.2 HLLC Riemann Solver

B.2.1 Average State

To estimate the average states (U^*), we need the contact wave speed (S_M), assuming that we know the velocities of the sonic wave (S_L) and (S_R). The normal velocity and pressure do not change across the contact discontinuity, therefore the normal velocity is equated to the wave speed:

$$S_M = q_l^* = q_r^* = q^* \tag{B.17}$$

and

$$p_l^* = p_r^* = p^* \tag{B.18}$$

where ($q = un_x + vn_y + wn_z$) is the velocity normal to the discontinuity. The region between the sonic waves has constant pressure (p^*) and normal velocity (q^*). To calculate the value of the contact wave speed, the integral form of the Euler equations (Eqn 3.23) across the Riemann fan should be solved, resulting in the following expression for the contact wave speed:

$$S_M = \frac{\rho_r q_r(S_R - q_r) - \rho_l q_l(S_L - q_l) + p_l - p_r}{\rho_r(S_R - q_r) - \rho_l(S_L - q_l)} \tag{B.19}$$

Once the contact wave speed is found, knowing the particle velocity from (Eqn B.17), we can apply the Rankine-Hugonoit conditions in each acoustic wave to find the average state. In the left wave, the jump relations are:

$$F_l^* - F_l = S_L(U_l^* - U_l) \tag{B.20}$$

In a general three dimension coordinate system the previous equation expands as follows:

$$S_L \begin{bmatrix} \rho_l^* \\ \rho_l^* u_l^* \\ \rho_l^* v_l^* \\ \rho_l^* w_l^* \\ e_l^* \end{bmatrix} - \begin{bmatrix} \rho_l^* q_l^* \\ \rho_l^* u_l^* q_l^* + p^* n_x \\ \rho_l^* v_l^* q_l^* + p^* n_y \\ \rho_l^* w_l^* q_l^* + p^* n_z \\ (e_l^* + p^*) q_l^* \end{bmatrix} = S_L \begin{bmatrix} \rho_l \\ \rho_l u_l \\ \rho_l v_l \\ \rho_l w_l \\ e_l \end{bmatrix} - \begin{bmatrix} \rho_l q_l \\ \rho_l u_l q_l + p_l n_x \\ \rho_l v_l q_l + p_l n_y \\ \rho_l w_l q_l + p_l n_z \\ (e_l + p_l) q_l \end{bmatrix} \tag{B.21}$$

Solution of the above set of equations is quite simple once the contact wave speeds are known, the first equation can be expressed as:

$$\rho_l^* = p_l \frac{S_L - q_l}{S_L - S_M} \tag{B.22}$$

Combining (Eqn B.21) and (Eqn B.22) we obtain the intermediate pressure ($p^* = p_l^* = p_r^*$).

$$p^* = \rho_l(q_L - S_l)(q_l - S_M) + p_l \tag{B.23}$$

Using the values of (ρ_l^*) and (p_l^*) derived from (Eqn B.22) and (Eqn B.23), we can define the solution for the intermediate-left state in its conserved variable form.

$$(\rho u)_l^* = \frac{(S_L - q_l)\rho u_l + (p^* - p_l)n_x}{S_L - S_M} \tag{B.24}$$

$$(\rho u)_l^* = \frac{(S_L - q_l)\rho v_l + (p^* - p_l)n_y}{S_L - S_M} \tag{B.25}$$

$$(\rho u)_l^* = \frac{(S_L - q_l)\rho w_l + (p^* - p_l)n_z}{S_L - S_M} \tag{B.26}$$

$$e_l^* = \frac{(S_L - q_l)\rho E_l - p_l q_l + p^* S_M}{S_L - S_M} \tag{B.27}$$

The procedure to compute the intermediate-right state is analogous to the left state. The results from (Eqn B.24) to (Eqn B.27), simply change the subscripts (l) or (L) to (r) and (R) respectively. Once the two intermediate states are found, the flux can be derived from (Eqn 3.27) and replaced in (Eqn 3.25).

B.2.2 Sonic Wave Speed Estimates

Before computing the intermediate states, an estimation of the sonic wave speeds is required. Following the suggestions of Batten *et al* [10], the wave estimates are:

$$S_L = min(q_l - c_l, \tilde{q} - \tilde{c}) \tag{B.28}$$

$$S_R = max(q_r + c_r, \tilde{q} + \tilde{c}) \tag{B.29}$$

where $(\tilde{q} = \tilde{u}n_x + \tilde{v}n_y + \tilde{w}n_z)$ and the average states ($\tilde{u}$,$\tilde{v}$ and $\tilde{w}$) are given by:

$$\tilde{u} = \frac{u_l + r_p u_r}{1 + r_p} \tag{B.30}$$

$$\tilde{v} = \frac{v_l + r_p v_r}{1 + r_p} \tag{B.31}$$

$$\tilde{w} = \frac{w_l + r_p w_r}{1 + r_p} \tag{B.32}$$

and the average sound speed:

$$\tilde{c}^2 = \frac{u_l + r_p u_r}{1 + r_p} \tag{B.33}$$

$$\tilde{H} = \frac{H_l + r_p H_r}{1 + r_p} \tag{B.34}$$

where (r_p) is the ratio of densities

$$r_p = \sqrt{p_r / p_l} \tag{B.35}$$

B.3 Transport properties

The transport properties considered in the study are the viscosity and the thermal conductivity, which generally are functions of the temperature and pressure. The viscosity models used in the present study are the Sutherland's law and the Lennard-Jones potentials. The Sutherland viscosity law assumes a rigid sphere model for the molecules, the relation is expressed as

$$\mu = \mu_\infty \left(\frac{T}{T_\infty} \right)^{\frac{3}{2}} \left(\frac{T_\infty + 110}{T + 110} \right) \tag{B.36}$$

The Lennard-Jones model provides a more accurate description of the viscosity, by taking into account the intermolecular forces between colliding molecules, and is commonly seen in the form

$$\mu = 2.6693 \times 10^{-6} \frac{\sqrt{mT}}{\sigma^2 \Omega_\mu} \tag{B.37}$$

where (m) is the gas species molecular weight, and (Ω_μ) is the viscosity collision integral while, quoting [1, 47], maybe expressed as a function of a reduced temperature (T^*)

$$\Omega_\mu = A{T^*}^{-B} + Ce^{-DT^*} + Ee^{-FT^*} \tag{B.38}$$

where $(A,\ B,\ C,\ D,\ E)$ and (F) are constants presented in Appendix C, while the reduced temperature is given as

$$T^* = \frac{T}{\epsilon_i/k} \tag{B.39}$$

The Lennard-Jones parameters, (ϵ_i/k) and (σ), depend on the molecular species involved (see Appendix C). This model, which is more accurate than Sutherlands law, can be used for more complex molecules.

B.4 Viscous Fluxes

The complete viscous fluxes (F_V) are presented in (Eqn B.40- B.43), to obtain (G_V) and (H_V), replace (ξ) with (η) and (ζ) respectively.

$$\begin{aligned}
F_{V_1} = {} & \tfrac{2}{3}\mu\Big[2\Big(\xi_x^2\tfrac{\partial u}{\partial \xi} + \xi_x\eta_x\tfrac{\partial u}{\partial \eta} + \xi_x\zeta_x\tfrac{\partial u}{\partial \zeta}\Big) - \Big(\xi_x\xi_y\tfrac{\partial v}{\partial \xi} + \xi_x\eta_y\tfrac{\partial v}{\partial \eta} + \xi_x\zeta_y\tfrac{\partial v}{\partial \zeta}\Big) \\
& - \Big(\xi_x\xi_z\tfrac{\partial w}{\partial \xi} + \xi_x\eta_z\tfrac{\partial w}{\partial \eta} + \xi_x\zeta_z\tfrac{\partial w}{\partial \zeta}\Big)\Big] + \mu\Big[\Big(\xi_y^2\tfrac{\partial u}{\partial \xi} + \xi_y\eta_y\tfrac{\partial u}{\partial \eta} + \xi_y\zeta_y\tfrac{\partial u}{\partial \zeta}\Big) \\
& + \Big(\xi_y\xi_x\tfrac{\partial v}{\partial \xi} + \xi_y\eta_x\tfrac{\partial v}{\partial \eta} + \xi_y\zeta_x\tfrac{\partial v}{\partial \zeta}\Big)\Big] + \mu\Big[\Big(\xi_z^2\tfrac{\partial u}{\partial \xi} + \xi_z\eta_x\tfrac{\partial u}{\partial \eta} + \xi_z\zeta_x\tfrac{\partial u}{\partial \zeta}\Big) \\
& + \Big(\xi_z\xi_x\tfrac{\partial w}{\partial \xi} + \xi_z\eta_x\tfrac{\partial w}{\partial \eta} + \xi_z\zeta_x\tfrac{\partial w}{\partial \zeta}\Big)\Big]
\end{aligned} \tag{B.40}$$

$$\begin{aligned}
F_{V_2} = {} & \mu\Big[\Big(\xi_x^2\tfrac{\partial v}{\partial \xi} + \xi_x\eta_x\tfrac{\partial v}{\partial \eta} + \xi_x\zeta_x\tfrac{\partial v}{\partial \zeta}\Big) + \Big(\xi_x\xi_y\tfrac{\partial u}{\partial \xi} + \xi_x\eta_y\tfrac{\partial u}{\partial \eta} + \xi_x\zeta_y\tfrac{\partial u}{\partial \zeta}\Big)\Big] \\
& + \tfrac{2}{3}\mu\Big[2\Big(\xi_y^2\tfrac{\partial v}{\partial \xi} + \xi_y\eta_y\tfrac{\partial v}{\partial \eta} + \xi_y\zeta_y\tfrac{\partial v}{\partial \zeta}\Big) - \Big(\xi_y\xi_x\tfrac{\partial u}{\partial \xi} + \xi_y\eta_x\tfrac{\partial u}{\partial \eta} + \xi_y\zeta_x\tfrac{\partial u}{\partial \zeta}\Big) \\
& - \Big(\xi_y\xi_z\tfrac{\partial w}{\partial \xi} + \xi_y\eta_z\tfrac{\partial w}{\partial \eta} + \xi_y\zeta_z\tfrac{\partial w}{\partial \zeta}\Big)\Big] \\
& + \mu\Big[\Big(\xi_z^2\tfrac{\partial v}{\partial \xi} + \xi_z\eta_z\tfrac{\partial v}{\partial \eta} + \xi_z\zeta_z\tfrac{\partial v}{\partial \zeta}\Big) + \Big(\xi_z\xi_y\tfrac{\partial w}{\partial \xi} + \xi_z\eta_y\tfrac{\partial w}{\partial \eta} + \xi_z\zeta_y\tfrac{\partial w}{\partial \zeta}\Big)\Big]
\end{aligned} \tag{B.41}$$

$$\begin{aligned}
F_{V_3} = {} & \mu\Big[\Big(\xi_x^2\tfrac{\partial w}{\partial \xi} + \xi_x\eta_x\tfrac{\partial w}{\partial \eta} + \xi_x\zeta_x\tfrac{\partial w}{\partial \zeta}\Big) + \Big(\xi_x\xi_z\tfrac{\partial u}{\partial \xi} + \xi_x\eta_z\tfrac{\partial u}{\partial \eta} + \xi_x\zeta_z\tfrac{\partial u}{\partial \zeta}\Big)\Big] \\
& + \mu\Big[\Big(\xi_y^2\tfrac{\partial w}{\partial \xi} + \xi_y\eta_y\tfrac{\partial w}{\partial \eta} + \xi_y\zeta_y\tfrac{\partial w}{\partial \zeta}\Big) + \Big(\xi_y\xi_z\tfrac{\partial v}{\partial \xi} + \xi_y\eta_z\tfrac{\partial v}{\partial \eta} + \xi_y\zeta_z\tfrac{\partial v}{\partial \zeta}\Big)\Big] \\
& + \tfrac{2}{3}\mu\Big[2\Big(\xi_z^2\tfrac{\partial w}{\partial \xi} + \xi_z\eta_z\tfrac{\partial w}{\partial \eta} + \xi_z\zeta_z\tfrac{\partial w}{\partial \zeta}\Big) - \Big(\xi_z\xi_x\tfrac{\partial u}{\partial \xi} + \xi_z\eta_x\tfrac{\partial u}{\partial \eta} + \xi_z\zeta_x\tfrac{\partial u}{\partial \zeta}\Big) \\
& - \Big(\xi_z\xi_y\tfrac{\partial v}{\partial \xi} + \xi_z\eta_y\tfrac{\partial v}{\partial \eta} + \xi_z\zeta_y\tfrac{\partial v}{\partial \zeta}\Big)\Big]
\end{aligned} \tag{B.42}$$

$$
\begin{aligned}
F_{V_4} = u\Bigg(&\tfrac{2}{3}\mu\Big[2\Big(\xi_x^2\tfrac{\partial u}{\partial\xi}+\xi_x\eta_x\tfrac{\partial u}{\partial\eta}+\xi_x\zeta_x\tfrac{\partial u}{\partial\zeta}\Big)-\Big(\xi_x\xi_y\tfrac{\partial v}{\partial\xi}+\xi_x\eta_y\tfrac{\partial v}{\partial\eta}+\xi_x\zeta_y\tfrac{\partial v}{\partial\zeta}\Big)\\
&-\Big(\xi_x\xi_z\tfrac{\partial w}{\partial\xi}+\xi_x\eta_z\tfrac{\partial w}{\partial\eta}+\xi_x\zeta_z\tfrac{\partial w}{\partial\zeta}\Big)\Big]\Bigg)+v\Bigg(\mu\Big[\Big(\xi_x^2\tfrac{\partial v}{\partial\xi}+\xi_x\eta_x\tfrac{\partial v}{\partial\eta}+\xi_x\zeta_x\tfrac{\partial v}{\partial\zeta}\Big)\\
&+\Big(\xi_x\xi_y\tfrac{\partial u}{\partial\xi}+\xi_x\eta_y\tfrac{\partial u}{\partial\eta}+\xi_x\zeta_y\tfrac{\partial u}{\partial\zeta}\Big)\Big]\Bigg)+w\Bigg(\mu\Big[\Big(\xi_x^2\tfrac{\partial w}{\partial\xi}+\xi_x\eta_x\tfrac{\partial w}{\partial\eta}+\xi_x\zeta_x\tfrac{\partial w}{\partial\zeta}\Big)\\
&+\Big(\xi_x\xi_z\tfrac{\partial u}{\partial\xi}+\xi_x\eta_z\tfrac{\partial u}{\partial\eta}+\xi_x\zeta_z\tfrac{\partial u}{\partial\zeta}\Big)\Big]\Bigg)-\kappa(\xi_x^2T_\xi+\xi_x\eta_xT_\eta+\xi_x\zeta_xT_\zeta)\\
&+u\Bigg(\mu\Big[\Big(\xi_y^2\tfrac{\partial u}{\partial\xi}+\xi_y\eta_y\tfrac{\partial u}{\partial\eta}+\xi_y\zeta_y\tfrac{\partial u}{\partial\zeta}\Big)+\Big(\xi_y\xi_x\tfrac{\partial v}{\partial\xi}+\xi_y\eta_x\tfrac{\partial v}{\partial\eta}+\xi_y\zeta_x\tfrac{\partial v}{\partial\zeta}\Big)\Big]\Bigg)\\
&+v\Bigg(\tfrac{2}{3}\mu\Big[2\Big(\xi_y^2\tfrac{\partial v}{\partial\xi}+\xi_y\eta_y\tfrac{\partial v}{\partial\eta}+\xi_y\zeta_y\tfrac{\partial v}{\partial\zeta}\Big)-\Big(\xi_y\xi_x\tfrac{\partial u}{\partial\xi}+\xi_y\eta_x\tfrac{\partial u}{\partial\eta}+\xi_y\zeta_x\tfrac{\partial u}{\partial\zeta}\Big)\\
&-\Big(\xi_y\xi_z\tfrac{\partial w}{\partial\xi}+\xi_y\eta_z\tfrac{\partial w}{\partial\eta}+\xi_y\zeta_z\tfrac{\partial w}{\partial\zeta}\Big)\Big]\Bigg)+w\Bigg(\mu\Big[\Big(\xi_y^2\tfrac{\partial w}{\partial\xi}+\xi_y\eta_y\tfrac{\partial w}{\partial\eta}+\xi_y\zeta_y\tfrac{\partial w}{\partial\zeta}\Big)\\
&+\Big(\xi_y\xi_z\tfrac{\partial v}{\partial\xi}+\xi_y\eta_z\tfrac{\partial v}{\partial\eta}+\xi_y\zeta_z\tfrac{\partial v}{\partial\zeta}\Big)\Big]\Bigg)-\kappa(\xi_y^2T_\xi+\xi_y\eta_yT_\eta+\xi_y\zeta_yT_\zeta)\\
&+u\Bigg(\mu\Big[\Big(\xi_z^2\tfrac{\partial u}{\partial\xi}+\xi_z\eta_z\tfrac{\partial u}{\partial\eta}+\xi_z\zeta_z\tfrac{\partial u}{\partial\zeta}\Big)+\Big(\xi_z\xi_x\tfrac{\partial w}{\partial\xi}+\xi_z\eta_x\tfrac{\partial w}{\partial\eta}+\xi_z\zeta_x\tfrac{\partial w}{\partial\zeta}\Big)\Big]\Bigg)\\
&+v\Bigg(\mu\Big[\Big(\xi_z^2\tfrac{\partial v}{\partial\xi}+\xi_z\eta_z\tfrac{\partial v}{\partial\eta}+\xi_z\zeta_z\tfrac{\partial v}{\partial\zeta}\Big)+\Big(\xi_z\xi_y\tfrac{\partial w}{\partial\xi}+\xi_z\eta_y\tfrac{\partial w}{\partial\eta}+\xi_z\zeta_y\tfrac{\partial w}{\partial\zeta}\Big)\Big]\Bigg)\\
&+w\Bigg(\tfrac{2}{3}\mu\Big[2\Big(\xi_z^2\tfrac{\partial w}{\partial\xi}+\xi_z\eta_z\tfrac{\partial w}{\partial\eta}+\xi_z\zeta_z\tfrac{\partial w}{\partial\zeta}\Big)-\Big(\xi_z\xi_x\tfrac{\partial u}{\partial\xi}+\xi_z\eta_x\tfrac{\partial u}{\partial\eta}+\xi_z\zeta_x\tfrac{\partial u}{\partial\zeta}\Big)\\
&-\Big(\xi_z\xi_y\tfrac{\partial v}{\partial\xi}+\xi_z\eta_y\tfrac{\partial v}{\partial\eta}+\xi_z\zeta_y\tfrac{\partial v}{\partial\zeta}\Big)\Big]\Bigg)-\kappa(\xi_z^2T_\xi+\xi_z\eta_zT_\eta+\xi_z\zeta_zT_\zeta)
\end{aligned}
\tag{B.43}
$$

The following terms in (F_v) can be divided into a format similar to,

$$
F_{v_{1,2..}} = F^{(\xi)}_{v_{1,2..}} + F^{(\eta)}_{v_{1,2..}} + F^{(\zeta)}_{v_{1,2..}} \tag{B.44}
$$

This allows the viscous fluxes to be broken down into the following format:

$$F_{V_1} = \overbrace{\left[\frac{2}{3}\mu\Big(2\xi_x^2\frac{\partial u}{\partial \xi} - \xi_x\xi_y\frac{\partial v}{\partial \xi} - \xi_x\xi_z\frac{\partial w}{\partial \xi}\Big) + \mu\Big(\xi_y^2\frac{\partial u}{\partial \xi} + \xi_y\xi_x\frac{\partial v}{\partial \xi}\Big) + \mu\Big(\xi_z^2\frac{\partial u}{\partial \xi} + \xi_z\xi_x\frac{\partial w}{\partial \xi}\Big)\right]}^{F_{V_1}^{(\xi)}}$$
$$+ \overbrace{\left[\frac{2}{3}\mu\Big(2\xi_x\eta_x\frac{\partial u}{\partial \eta} - \xi_x\eta_y\frac{\partial v}{\partial \eta} - \xi_x\eta_z\frac{\partial w}{\partial \eta}\Big) + \mu\Big(\xi_y\eta_y\frac{\partial u}{\partial \eta} + \xi_y\eta_x\frac{\partial v}{\partial \eta}\Big) + \mu\Big(\xi_z\eta_x\frac{\partial u}{\partial \eta} + \xi_z\eta_x\frac{\partial w}{\partial \eta}\Big)\right]}^{F_{V_1}^{(\eta)}}$$
$$+ \overbrace{\left[\frac{2}{3}\mu\Big(2\xi_x\zeta_x\frac{\partial u}{\partial \zeta} - \xi_x\zeta_y\frac{\partial v}{\partial \zeta} - \xi_x\zeta_z\frac{\partial w}{\partial \zeta}\Big) + \mu\Big(\xi_y\zeta_y\frac{\partial u}{\partial \zeta} + \xi_y\zeta_x\frac{\partial v}{\partial \zeta}\Big) + \mu\Big(\xi_z\zeta_x\frac{\partial u}{\partial \zeta} + \xi_z\zeta_x\frac{\partial w}{\partial \zeta}\Big)\right]}^{F_{V_1}^{(\zeta)}} \tag{B.45}$$

$$F_{V_2} = \overbrace{\left[\mu\Big(\xi_x^2\frac{\partial v}{\partial \xi} + \xi_x\xi_y\frac{\partial u}{\partial \xi}\Big) + \frac{2}{3}\mu\Big(2\xi_y^2\frac{\partial v}{\partial \xi} - \xi_y\xi_x\frac{\partial u}{\partial \xi} - \xi_y\xi_z\frac{\partial w}{\partial \xi}\Big) + \mu\Big(\xi_z^2\frac{\partial v}{\partial \xi} + \xi_z\xi_y\frac{\partial w}{\partial \xi}\Big)\right]}^{F_{V_2}^{(\xi)}}$$
$$+ \overbrace{\left[\mu\Big(\xi_x\eta_x\frac{\partial v}{\partial \eta} + \xi_x\eta_y\frac{\partial u}{\partial \eta}\Big) + \frac{2}{3}\mu\Big(2\xi_y\eta_y\frac{\partial v}{\partial \eta} - \xi_y\eta_x\frac{\partial u}{\partial \eta} - \xi_y\eta_z\frac{\partial w}{\partial \eta}\Big) + \mu\Big(\xi_z\eta_z\frac{\partial v}{\partial \eta} + \xi_z\eta_y\frac{\partial w}{\partial \eta}\Big)\right]}^{F_{V_2}^{(\eta)}}$$
$$+ \overbrace{\left[\mu\Big(\xi_x\zeta_x\frac{\partial v}{\partial \zeta} + \xi_x\zeta_y\frac{\partial u}{\partial \zeta}\Big) + \frac{2}{3}\mu\Big(2\xi_y\zeta_y\frac{\partial v}{\partial \zeta} - \xi_y\zeta_x\frac{\partial u}{\partial \zeta} - \xi_y\zeta_z\frac{\partial w}{\partial \zeta}\Big) + \mu\Big(\xi_z\zeta_z\frac{\partial v}{\partial \zeta} + \xi_z\zeta_y\frac{\partial w}{\partial \zeta}\Big)\right]}^{F_{V_2}^{(\zeta)}} \tag{B.46}$$

$$F_{V_3} = \overbrace{\left[\mu\Big(\xi_x^2\frac{\partial w}{\partial \xi} + \xi_x\xi_z\frac{\partial u}{\partial \xi}\Big) + \mu\Big(\xi_y^2\frac{\partial w}{\partial \xi} + \xi_y\xi_z\frac{\partial v}{\partial \xi}\Big) + \frac{2}{3}\mu\Big(2\xi_z^2\frac{\partial w}{\partial \xi} - \xi_z\xi_x\frac{\partial u}{\partial \xi} - \xi_z\xi_y\frac{\partial v}{\partial \xi}\Big)\right]}^{F_{V_3}^{(\xi)}}$$
$$+ \overbrace{\left[\mu\Big(\xi_x\eta_x\frac{\partial w}{\partial \eta} + \xi_x\eta_z\frac{\partial u}{\partial \eta}\Big) + \mu\Big(\xi_y\eta_y\frac{\partial w}{\partial \eta} + \xi_y\eta_z\frac{\partial v}{\partial \eta}\Big) + \frac{2}{3}\mu\Big(2\xi_z\eta_z\frac{\partial w}{\partial \eta} - \xi_z\eta_x\frac{\partial u}{\partial \eta} - \xi_z\eta_y\frac{\partial v}{\partial \eta}\Big)\right]}^{F_{V_3}^{(\eta)}}$$
$$+ \overbrace{\left[\mu\Big(\xi_x\zeta_x\frac{\partial w}{\partial \zeta} + \xi_x\zeta_z\frac{\partial u}{\partial \zeta}\Big) + \mu\Big(\xi_y\zeta_y\frac{\partial w}{\partial \zeta} + \xi_y\zeta_z\frac{\partial v}{\partial \zeta}\Big) + \frac{2}{3}\mu\Big(2\xi_z\zeta_z\frac{\partial w}{\partial \zeta} - \xi_z\zeta_x\frac{\partial u}{\partial \zeta} - \xi_z\zeta_y\frac{\partial v}{\partial \zeta}\Big)\right]}^{F_{V_3}^{(\zeta)}} \tag{B.47}$$

$$
\begin{aligned}
F_{V_4} = \overbrace{\Bigg[u\Bigg(\frac{2}{3}\mu\Big[2\xi_x^2\frac{\partial u}{\partial \xi} - \xi_x\xi_y\frac{\partial v}{\partial \xi} - \xi_x\xi_z\frac{\partial w}{\partial \xi}\Big] + \mu\Big[\xi_y^2\frac{\partial u}{\partial \xi} + \xi_y\xi_x\frac{\partial v}{\partial \xi}\Big] + \mu\Big[\xi_z^2\frac{\partial u}{\partial \xi} + \xi_z\xi_x\frac{\partial w}{\partial \xi}\Big]\Bigg)}^{F_{V_4}^{(\xi)}} \\
+v\Bigg(\mu\Big[\xi_x^2\tfrac{\partial v}{\partial \xi} + \xi_x\xi_y\tfrac{\partial u}{\partial \xi}\Big] + \tfrac{2}{3}\mu\Big[2\xi_y^2\tfrac{\partial v}{\partial \xi} - \xi_y\xi_x\tfrac{\partial u}{\partial \xi} - \xi_y\xi_z\tfrac{\partial w}{\partial \xi}\Big] + \mu\Big[\xi_z^2\tfrac{\partial v}{\partial \xi} + \xi_z\xi_y\tfrac{\partial w}{\partial \xi}\Big]\Bigg) + \\
w\Bigg(\mu\Big[\xi_x^2\tfrac{\partial w}{\partial \xi} + \xi_x\xi_z\tfrac{\partial u}{\partial \xi}\Big] + \mu\Big[\xi_y^2\tfrac{\partial w}{\partial \xi} + \xi_y\xi_z\tfrac{\partial v}{\partial \xi}\Big] + \tfrac{2}{3}\mu\Big[2\xi_z^2\tfrac{\partial w}{\partial \xi} - \xi_z\xi_x\tfrac{\partial u}{\partial \xi} - \xi_z\xi_y\tfrac{\partial v}{\partial \xi}\Big]\Bigg) \\
-\kappa T_\xi\Big(\xi_x^2 - \xi_y^2 - \xi_z^2\Big)\Bigg] + \\
\overbrace{\Bigg[u\Bigg(\frac{2}{3}\mu\Big[2\xi_x\eta_x\frac{\partial u}{\partial \eta} - \xi_x\eta_y\frac{\partial v}{\partial \eta} - \xi_x\eta_z\frac{\partial w}{\partial \eta}\Big] + \mu\Big[\xi_y\eta_y\frac{\partial u}{\partial \eta} + \xi_y\eta_x\frac{\partial v}{\partial \eta}\Big] + \mu\Big[\xi_z\eta_z\frac{\partial u}{\partial \eta} + \xi_z\eta_x\frac{\partial w}{\partial \eta}\Big]\Bigg)}^{F_{V_4}^{(\eta)}} \\
+v\Bigg(\mu\Big[\xi_x\eta_x\tfrac{\partial v}{\partial \eta} + \xi_x\eta_y\tfrac{\partial u}{\partial \eta}\Big] + \tfrac{2}{3}\mu\Big[2\xi_y\eta_y\tfrac{\partial v}{\partial \eta} - \xi_y\eta_x\tfrac{\partial u}{\partial \eta} - \xi_y\eta_z\tfrac{\partial w}{\partial \eta}\Big] + \mu\Big[\xi_z\eta_z\tfrac{\partial v}{\partial \eta} + \xi_z\eta_y\tfrac{\partial w}{\partial \eta}\Big]\Bigg) + \\
w\Bigg(\mu\Big[\xi_x\eta_x\tfrac{\partial w}{\partial \eta} + \xi_x\eta_z\tfrac{\partial u}{\partial \eta}\Big] + \mu\Big[\xi_y\eta_y\tfrac{\partial w}{\partial \eta} + \xi_y\eta_z\tfrac{\partial v}{\partial \eta}\Big] + \tfrac{2}{3}\mu\Big[2\xi_z\eta_z\tfrac{\partial w}{\partial \eta} - \xi_z\eta_x\tfrac{\partial u}{\partial \eta} - \xi_z\eta_y\tfrac{\partial v}{\partial \eta}\Big]\Bigg) \\
-\kappa T_\eta\Big(\xi_x\eta_x - \xi_y\eta_y - \xi_z\eta_z\Big)\Bigg] + \\
\overbrace{\Bigg[u\Bigg(\frac{2}{3}\mu\Big[2\xi_x\zeta_x\frac{\partial u}{\partial \zeta} - \xi_x\zeta_y\frac{\partial v}{\partial \zeta} - \xi_x\zeta_z\frac{\partial w}{\partial \zeta}\Big] + \mu\Big[\xi_y\zeta_y\frac{\partial u}{\partial \zeta} + \xi_y\zeta_x\frac{\partial v}{\partial \zeta}\Big] + \mu\Big[\xi_z\zeta_z\frac{\partial u}{\partial \zeta} + \xi_z\zeta_x\frac{\partial w}{\partial \zeta}\Big]\Bigg)}^{F_{V_4}^{(\zeta)}} \\
+v\Bigg(\mu\Big[\xi_x\zeta_x\tfrac{\partial v}{\partial \zeta} + \xi_x\zeta_y\tfrac{\partial u}{\partial \zeta}\Big] + \tfrac{2}{3}\mu\Big[2\xi_y\zeta_y\tfrac{\partial v}{\partial \zeta} - \xi_y\zeta_x\tfrac{\partial u}{\partial \zeta} - \xi_y\zeta_z\tfrac{\partial w}{\partial \zeta}\Big] + \mu\Big[\xi_z\zeta_z\tfrac{\partial v}{\partial \zeta} + \xi_z\zeta_y\tfrac{\partial w}{\partial \zeta}\Big]\Bigg) + \\
w\Bigg(\mu\Big[\xi_x\zeta_x\tfrac{\partial w}{\partial \zeta} + \xi_x\zeta_z\tfrac{\partial u}{\partial \zeta}\Big] + \mu\Big[\xi_y\zeta_y\tfrac{\partial w}{\partial \zeta} + \xi_y\zeta_z\tfrac{\partial v}{\partial \zeta}\Big] + \tfrac{2}{3}\mu\Big[2\xi_z\zeta_z\tfrac{\partial w}{\partial \zeta} - \xi_z\zeta_x\tfrac{\partial u}{\partial \zeta} - \xi_z\zeta_y\tfrac{\partial v}{\partial \zeta}\Big]\Bigg) \\
-\kappa T_\zeta\Big(\xi_x\zeta_x - \xi_y\zeta_y - \xi_z\zeta_z\Big)\Bigg]
\end{aligned}
\tag{B.48}
$$

Appendix C

Jacobian Matrices

C.1 HLLC Jacobians

The following Jacobians were obtained from Batten *et al* [6]; the notation is kept as in their original paper. The relevant Jacobians for the HLLC Riemann solver are:

$$\frac{\partial F_l^*}{\partial U_l} = \begin{bmatrix} \left(\frac{\partial \rho_l^*}{\partial U_l}\right)^T S_M + \left(\frac{\partial S_M}{\partial U_l}\right)^T \rho_l^* \\ \left(\frac{\partial (\rho u)_l^*}{\partial U_l}\right)^T S_M + \left(\frac{\partial S_M}{\partial U_l}\right)^T (\rho u)_l^* + \left(\frac{\partial p^*}{\partial U_l}\right)^T n_x \\ \left(\frac{\partial (\rho v)_l^*}{\partial U_l}\right)^T S_M + \left(\frac{\partial S_M}{\partial U_l}\right)^T (\rho v)_l^* + \left(\frac{\partial p^*}{\partial U_l}\right)^T n_y \\ \left(\frac{\partial (\rho w)_l^*}{\partial U_l}\right)^T S_M + \left(\frac{\partial S_M}{\partial U_l}\right)^T (\rho w)_l^* + \left(\frac{\partial p^*}{\partial U_l}\right)^T n_z \\ \left(\frac{\partial e_l^*}{\partial U_l} + \frac{\partial p^*}{\partial U_l}\right)^T S_M + (e_l^* + p^*)\left(\frac{\partial S_M}{\partial U_l}\right)^T \end{bmatrix} \tag{C.1}$$

$$\frac{\partial F_r^*}{\partial U_l} = \begin{bmatrix} \left(\frac{\partial \rho_r^*}{\partial U_r}\right)^T S_M + \left(\frac{\partial S_M}{\partial U_r}\right)^T \rho_r^* \\ \left(\frac{\partial (\rho u)_r^*}{\partial U_r}\right)^T S_M + \left(\frac{\partial S_M}{\partial U_r}\right)^T (\rho u)_r^* + \left(\frac{\partial p^*}{\partial U_r}\right)^T n_x \\ \left(\frac{\partial (\rho v)_r^*}{\partial U_r}\right)^T S_M + \left(\frac{\partial S_M}{\partial U_r}\right)^T (\rho v)_r^* + \left(\frac{\partial p^*}{\partial U_r}\right)^T n_y \\ \left(\frac{\partial (\rho w)_r^*}{\partial U_r}\right)^T S_M + \left(\frac{\partial S_M}{\partial U_r}\right)^T (\rho w)_r^* + \left(\frac{\partial p^*}{\partial U_r}\right)^T n_z \\ \left(\frac{\partial e_r^*}{\partial U_r} + \frac{\partial p^*}{\partial U_r}\right)^T S_M + (e_r^* + p^*)\left(\frac{\partial S_M}{\partial U_r}\right)^T \end{bmatrix} \tag{C.2}$$

the derivatives for the (S_M) vector can be derived from the definition of (S_M) from (Eqn B.19)

$$\frac{\partial S_M}{\partial U_l} = \tilde{\rho}^{-1} \begin{bmatrix} -q_l^2 + \psi_l(\gamma - 1)/2 + S_M S_L \\ n_x(2q_l - S_L - S_M) + (1 - \gamma)u_l \\ n_y(2q_l - S_L - S_M) + (1 - \gamma)v_l \\ n_z(2q_l - S_L - S_M) + (1 - \gamma)w_l \\ \gamma - 1 \end{bmatrix} \tag{C.3}$$

$$\frac{\partial S_M}{\partial U_r} = \tilde{\rho}^{-1} \begin{bmatrix} -q_r^2 + \psi_r(\gamma - 1)/2 + S_M S_R \\ n_x(2q_r - S_R - S_M) + (1 - \gamma)u_r \\ n_y(2q_r - S_R - S_M) + (1 - \gamma)v_r \\ n_z(2q_r - S_R - S_M) + (1 - \gamma)w_r \\ \gamma - 1 \end{bmatrix} \tag{C.4}$$

with $(\psi = u^2 + v^2 + w^2)$ and $(\tilde{\rho} = \rho_r(S_r - q_r) - \rho_l(S_l + q_l))$. To evaluate the remaining derivatives in (Eqn C.1 and Eqn C.2) we differentiate equation (Eqn B.23) with respect to (U_l) and (U_r), obtaining

$$\frac{\partial p^*}{\partial U_l} = \rho_l(S_L - q_l)\frac{\partial S_M}{\partial U_l} \tag{C.5}$$

$$\frac{\partial p^*}{\partial U_r} = \rho_r(S_R - q_r)\frac{\partial S_M}{\partial U_r} \tag{C.6}$$

The remainder of the terms in (Eqn C.1 and Eqn C.2) are obtained by simple algebraic manipulation:

$$\frac{\partial \rho_l^*}{\partial U_l} = \Omega_l \begin{bmatrix} S_L \\ -n_x \\ -n_y \\ -n_z \\ 0 \end{bmatrix} + \Omega_l \rho_l^* \frac{\partial S_M}{\partial U_l} \tag{C.7}$$

$$\frac{\partial \rho_l^*}{\partial U_r} = \Omega_l \rho_l^* \frac{\partial S_M}{\partial U_r} \tag{C.8}$$

$$\frac{\partial (\rho u)_l^*}{\partial U_l} = \Omega_l \begin{bmatrix} q_l u_l - n_x \psi(\gamma - 1)/2 \\ S_L - q_l + n_x(\gamma - 2)u_l \\ -u_l n_y + n_x(\gamma - 1)v_l \\ -u_l n_z + n_x(\gamma - 1)w_l \\ (1 - \gamma)n_x \end{bmatrix} + \Omega_l \Big(n_x \frac{\partial p^*}{\partial U_l} + (\rho u)_l^* \frac{\partial S_M}{\partial U_l} \Big) \tag{C.9}$$

$$\frac{\partial (\rho u)_l^*}{\partial U_r} = \Omega_l \Big(n_x \frac{\partial p^*}{\partial U_r} + (\rho u)_l^* \frac{\partial S_M}{\partial U_r} \Big) \tag{C.10}$$

$$\frac{\partial (\rho v)_l^*}{\partial U_l} = \Omega_l \begin{bmatrix} q_l v_l - n_y \psi(\gamma - 1)/2 \\ -v_l n_x + n_y(\gamma - 1)u_l \\ S_L - q_l + n_y(\gamma - 2)v_l \\ -v_l n_z + n_y(\gamma - 1)w_l \\ (1 - \gamma)n_y \end{bmatrix} + \Omega_l \Big(n_y \frac{\partial p^*}{\partial U_l} + (\rho v)_l^* \frac{\partial S_M}{\partial U_l} \Big) \tag{C.11}$$

$$\frac{\partial (\rho v)_l^*}{\partial U_r} = \Omega_l \Big(n_y \frac{\partial p^*}{\partial U_r} + (\rho v)_l^* \frac{\partial S_M}{\partial U_r} \Big) \tag{C.12}$$

$$\frac{\partial(\rho w)_l^*}{\partial U_l} = \Omega_l \begin{bmatrix} q_l w_l - n_z \psi(\gamma-1)/2 \\ -w_l n_x + n_z(\gamma-1)u_l \\ -w_l n_y + n_z(\gamma-1)v_l \\ S_L - q_l + n_z(\gamma-2)w_l \\ (1-\gamma)n_z \end{bmatrix} + \Omega_l \Big(n_z \frac{\partial p^*}{\partial U_l} + (\rho w)_l^* \frac{\partial S_M}{\partial U_l} \Big) \tag{C.13}$$

$$\frac{\partial(\rho w)_l^*}{\partial U_r} = \Omega_l \Big(n_z \frac{\partial p^*}{\partial U_r} + (\rho w)_l^* \frac{\partial S_M}{\partial U_r} \Big) \tag{C.14}$$

$$\frac{\partial e_l^*}{\partial U_l} = \Omega_l \begin{bmatrix} (e_l + p_l)q_l/\rho_l - q_l \psi(\gamma-1)/2 \\ -n_x(e_l+p_l)/\rho_l + (\gamma-1)u_l q_l \\ -n_y(e_l+p_l)/\rho_l + (\gamma-1)v_l q_l \\ -n_z(e_l+p_l)/\rho_l + (\gamma-2)w_l q_l \\ S_L - q_l \gamma \end{bmatrix} + \Omega_l \Big(\frac{\partial p^*}{\partial U_l} S_M + (p_l^* + e_l^*) \frac{\partial S_M}{\partial U_l} \Big) \tag{C.15}$$

$$\frac{\partial e_l^*}{\partial U_r} = \Omega_l \Big(\frac{\partial p^*}{\partial U_r} S_M + (p_l^* + e_l^*) \frac{\partial S_M}{\partial U_r} \Big) \tag{C.16}$$

In the case of $(S_M < 0)$, the resulting Jacobians $(\frac{\partial F_r^*}{\partial U_l})$ and $(\frac{\partial F_l^*}{\partial U_r})$ are simply obtained by replacing the subscripts $(l \longleftrightarrow r)$ and $(L \longleftrightarrow R)$ in all above equations. It is worth remembering that the acoustic wave speeds are frozen and not linearised. Further accuracy can be obtained by linearising the acoustic wave speeds (S_R) and (S_L). Batten *et al* [10] however concluded that the increase in convergence is not worth the extra computational cost by linearising the speeds. Therefore the wave speeds chosen are frozen.

C.2 Viscous Jacobians

Sections of the viscous Jacobians are taken from Batten *et al* [7] and the remainder of the terms are obtained by direct derivation of the viscous flux terms from Eqn 3.39.

$$\frac{\partial F_v}{\partial U_l} = \begin{bmatrix} 0 & 0 & 0 & 0 & 0 \\ \phi_{21} & \alpha_1 \frac{\partial \rho_\xi}{\partial \rho_l} & \beta_1 \frac{\partial \rho_\xi}{\partial \rho_l} & \beta_3 \frac{\partial \rho_\xi}{\partial \rho_l} & 0 \\ \phi_{31} & \beta_1 \frac{\partial \rho_\xi}{\partial \rho_l} & \alpha_2 \frac{\partial \rho_\xi}{\partial \rho_l} & \beta_2 \frac{\partial \rho_\xi}{\partial \rho_l} & 0 \\ \phi_{41} & \beta_3 \frac{\partial \rho_\xi}{\partial \rho_l} & \beta_2 \frac{\partial \rho_\xi}{\partial \rho_l} & \alpha_3 \frac{\partial \rho_\xi}{\partial \rho_l} & 0 \\ \phi_{51} & \phi_{52} & \phi_{53} & \phi_{54} & \alpha_4^* \frac{\partial E_\xi}{\partial \rho_l} \end{bmatrix} \tag{C.17}$$

the subscript (ξ) indicates a directional derivative along the (ξ) direction. (ϕ_{ij}) stands for a combination of derivatives given by

$$\phi_{21} = -\left(\alpha_1 \frac{\partial u_\xi}{\partial \rho_l} + \beta_1 \frac{\partial v_\xi}{\partial \rho_l} + \beta_3 \frac{\partial w_\xi}{\partial \rho_l} \right) \tag{C.18}$$

$$\phi_{31} = -\left(\beta_1 \frac{\partial u_\xi}{\partial \rho_l} + \alpha_2 \frac{\partial v_\xi}{\partial \rho_l} + \beta_2 \frac{\partial w_\xi}{\partial \rho_l} \right) \tag{C.19}$$

$$\phi_{41} = -\left(\beta_3 \frac{\partial u_\xi}{\partial \rho_l} + \beta_2 \frac{\partial v_\xi}{\partial \rho_l} + \alpha_3 \frac{\partial w_\xi}{\partial \rho_l} \right) \tag{C.20}$$

$$\phi_{51} = \alpha_4^* \frac{\partial E_\xi}{\partial \rho_l} + (\alpha_1 - \alpha_4^*) \frac{\partial u_\xi^2}{\partial \rho_l} + (\alpha_2 - \alpha_4^*) \frac{\partial v_\xi^2}{\partial \rho_l} + (\alpha_3 - \alpha_4^*) \frac{\partial w_\xi^2}{\partial \rho_l} + 2\beta_1 \frac{\partial u v_\xi}{\partial \rho_l} + 2\beta_2 \frac{\partial v w_\xi}{\partial \rho_l} + 2\beta_3 \frac{\partial u w_\xi}{\partial \rho_l} \tag{C.21}$$

$$\phi_{52} = (\alpha_1 - \alpha_4^*) \frac{\partial u_\xi}{\partial \rho_l} + \beta_1 \frac{\partial v_\xi}{\partial \rho_l} + \beta_3 \frac{\partial w_\xi}{\partial \rho_l} \tag{C.22}$$

$$\phi_{53} = (\alpha_2 - \alpha_4^*) \frac{\partial v_\xi}{\partial \rho_l} + \beta_1 \frac{\partial u_\xi}{\partial \rho_l} + \beta_2 \frac{\partial w_\xi}{\partial \rho_l} \tag{C.23}$$

$$\phi_{54} = (\alpha_3 - \alpha_4^*) \frac{\partial w_\xi}{\partial \rho_l} + \beta_3 \frac{\partial u_\xi}{\partial \rho_l} + \beta_2 \frac{\partial v_\xi}{\partial \rho_l} \tag{C.24}$$

where $(\alpha_4^* = \alpha / C_v)$, and the (α_i) and (β_i) are constants defined in (Eqn 3.40).

In the derivations of $(\frac{\partial F_v}{\partial U_r})$ the subscripts (l) should be changed by (r) in the above equations. Furthermore, to obtain the Jacobians to the fluxes in the (η) and (ζ) directions, the subscript (ξ) need to be replaced by (η) or (ζ).

C.3 Boundary conditions

C.3.1 Adiabatic Wall

The temperature boundary condition for an adiabatic wall is:

$$\frac{\partial T}{\partial \eta}\Big|_{wall} = 0 \tag{C.25}$$

The no-slip condition of the fluid particle at the boundary is expressed as

$$\mathbf{V}|_{wall} = 0 \tag{C.26}$$

Using the subscript (G) for ghost cell values, and 1 for the first cell adjacent to the boundary, the relationships for the primative variables in a first order approximation, are as follows:

$$\begin{aligned} p_G &= p_i \\ T_G &= T_i \\ u_G &= -u_i \\ v_G &= -v_i \\ w_G &= -w_i \end{aligned} \tag{C.27}$$

The resultant boundary matrix that relates (∂U_G) to (∂U_1) is

$$\mathcal{C}_{BC} = \begin{bmatrix} 1 & 0 & 0 & 0 & 0 \\ 0 & -1 & 0 & 0 & 0 \\ 0 & 0 & -1 & 0 & 0 \\ 0 & 0 & 0 & -1 & 0 \\ 0 & 0 & 0 & 0 & -1 \end{bmatrix} \tag{C.28}$$

C.3.2 Isothermal Wall

For an isothermal wall, the pressure gradient at the wall is zero.

$$\frac{\partial p}{\partial \eta}\Big|_{wall} = 0 \tag{C.29}$$

The temperature remains constant in the wall

$$T|_{wall} = T_{wall} \tag{C.30}$$

The no-slip condition remains as

$$\mathbf{V}|_{wall} = 0 \tag{C.31}$$

The resulting primitive variables are

$$\begin{aligned} p_G &= p_i \\ T_G &= 2T_{wall} - T_i \\ u_G &= -u_i \\ v_G &= -v_i \\ w_G &= -w_i \end{aligned} \tag{C.32}$$

The relation between densities is equal to:

$$r = \frac{\rho_G}{\rho_1} = \frac{T_1}{T_G} \tag{C.33}$$

By deriving the above equations in time, we obtain the relation between (∂U_G) and (∂U_1). To simplify the final matrix elements, we define some auxiliary variables as:

$$\begin{aligned}\beta &= \tfrac{1+r}{C_v T_G} \\ \varphi &= 2E_C - E_1 \\ \sigma &= 1 - r + \beta E_C\end{aligned} \tag{C.34}$$

where the kinetic energy (E_C) is equal for both ghost and real cells

$$E_C = \frac{1}{2}(u^2 + v^2 + w^2) \tag{C.35}$$

Finally the corresponding boundary matrix is:

$$\mathcal{C}_{BC} = \begin{bmatrix} r + \beta\varphi & -\beta u_1 & -\beta v_1 & -\beta w_1 & \beta \\ -\beta\varphi u_1 & \beta u_1^2 - r & \beta u_1 v_1 & \beta u_1 w_1 & -\beta u_1 \\ -\beta\varphi v_1 & \beta u_1 v_1 & \beta v_1^2 - r & \beta v_1 w_1 & -\beta w_1 \\ -\beta\varphi w_1 & \beta u_1 w - 1 & \beta v_1 w_1 & \beta w_1^2 - r & -\beta w_1 \\ (1 - r + \beta\varphi)E_C & -\sigma u_1 & -\sigma v_1 & -\sigma w_1 & 1 + \beta E_C \end{bmatrix} \tag{C.36}$$

C.3.3 Inflow

Inflow boundary conditions are defined by the hypersonic freestream and are imposed as follows

$$U_L = U_\infty \tag{C.37}$$

Because the inflow conditions do not change with time and are independent of the values on the inner flow, consequently the result is a null matrix

C.3.4 Outflow

Across the outflow boundary, all properties remain unaltered. The gradient in the normal direction becomes zero. This is reflected in the matrix as a unit-diagonal matrix.

$$\mathcal{C}_{BC} = \begin{bmatrix} 1 & 0 & 0 & 0 & 0 \\ 0 & 1 & 0 & 0 & 0 \\ 0 & 0 & 1 & 0 & 0 \\ 0 & 0 & 0 & 1 & 0 \\ 0 & 0 & 0 & 0 & 1 \end{bmatrix} \tag{C.38}$$

Appendix D

Gas Properties

Species	Molecular Weight $\times 10^3$(kg/kg-mole)	σ ($\dot{A}$)	$\frac{\epsilon}{\kappa}$ (K)
Ar	39.9480	3.542	93.9
O	15.9994	3.050	106.7
O_2	31.9988	3.467	106.7
N	14.0067	3.298	71.4
N_2	28.0134	3.798	71.4
NO	30.0061	3.492	116.7

Table D.1: Lennard-Jones parameters for transport coefficients, source [47]